Numerical Relativity beyond General Relativity

Thesis by
Maria Okounkova

In Partial Fulfillment of the Requirements for the
Degree of
Doctor of Philosophy in Physics

Caltech

CALIFORNIA INSTITUTE OF TECHNOLOGY
Pasadena, California

2019
Defended May 1st, 2019

Space may be the final frontier but it's made in a Hollywood basement
- Red Hot Chili Peppers, Californication

ACKNOWLEDGEMENTS

ABSTRACT

Einstein's theory of general relativity has passed all precision tests to date. At some length scale, however, general relativity (GR) must break down and be reconciled with quantum mechanics in a quantum theory of gravity (a beyond-GR theory). Binary black hole mergers probe the non-linear, highly dynamical regime of gravity, and gravitational waves from these systems may contain signatures of such a theory. In this thesis, we seek to make gravitational wave predictions for binary black hole mergers in a beyond-GR theory. These predictions can then be used to perform model-dependent tests of GR with gravitational wave detections.

We make predictions using numerical relativity, the practice of precisely numerically solving the equations governing spacetime. This allows us to probe the behavior of a binary black hole system through full inspiral, merger, and ringdown. We choose to work in dynamical Chern-Simons gravity (dCS), a higher-curvature beyond-GR effective field theory that couples spacetime curvature to a scalar field, and has motivations in string theory and loop quantum gravity. In order to obtain a well-posed initial value formalism, we perturb this theory around GR. We compute the leading-order behavior of the dCS scalar field in a binary black hole merger, as well as the leading-order dCS correction to the spacetime metric and hence gravitational radiation. We produce the first numerical relativity beyond-GR waveforms in a higher-curvature theory of gravity.

This thesis contains additional results, all of which harness the power of numerical relativity to test GR. We compute black hole shadows in dCS gravity, numerically prove the leading-order stability of rotating black holes in dCS gravity, and lay out a formalism for determining the start time of binary black hole ringdown using information from the strong-field region of a binary black hole simulation.

PUBLISHED CONTENT AND CONTRIBUTIONS

[1]   Maria Okounkova, Mark A. Scheel, and Saul A. Teukolsky. "Evolving Metric Perturbations in dynamical Chern-Simons Gravity". In: *Phys. Rev.* D99.4 (2019), p. 044019. DOI: 10.1103/PhysRevD.99.044019. arXiv: 1811.10713 [gr-qc].
M.O. conceived of the project, performed the analytical calculations, wrote the code, performed the simulations, analyzed the data, and wrote the manuscript.

[2]   Maria Okounkova, Mark A Scheel, and Saul A Teukolsky. "Numerical black hole initial data and shadows in dynamical Chern–Simons gravity". In: *Classical and Quantum Gravity* 36.5 (Feb. 2019), p. 054001. DOI: 10.1088/1361-6382/aafcdf.
M.O. conceived of the project, performed the analytical calculations, wrote the code, performed the simulations, analyzed the data, and wrote the manuscript.

[3]   Swetha Bhagwat et al. "On choosing the start time of binary black hole ringdowns". In: *Phys. Rev.* D97.10 (2018), p. 104065. DOI: 10.1103/PhysRevD.97.104065. arXiv: 1711.00926 [gr-qc].
M.O. conceived of the project jointly with S.B., and the two wrote the code, performed the analytical calculations, performed the computations, analyzed the data, and wrote the manuscript.

[4]   Maria Okounkova et al. "Numerical binary black hole mergers in dynamical Chern-Simons gravity: Scalar field". In: *Phys. Rev.* D96.4 (2017), p. 044020. DOI: 10.1103/PhysRevD.96.044020. arXiv: 1705.07924 [gr-qc].
M.O. performed the analytical calculations, wrote the code, performed the simulations, analyzed the data, and wrote the manuscript.

TABLE OF CONTENTS

C h a p t e r   1

INTRODUCTION

1.1 A century of general relativity

Over one hundred years ago, Albert Einstein put forth the theory of general relativity (GR), coupling spacetime to the matter and energy contained within [82].

In the century following this discovery, there was much progress in exploring the properties of this classical theory. The theory was found, for example, to contain black hole solutions [180]. Later, it was discovered that the theory contained *spinning* black hole solutions [112, 197]. Swiftly, scientists began to think not only about single black holes, but *binary* black hole systems. In binaries, two black holes orbit one another, inspiraling closer together through the emission of gravitational radiation, and ultimately merging in a violent, energetic process, to form one black hole. Theoretically computing the gravitational radiation (or *gravitational waves*) emitted by binary systems was of particular interest [135, 156]. The end of the century saw the first precise, numerical prediction of a full gravitational waveform from a binary black hole merger [161].

1.2 Gravity beyond general relativity

The same century, however, saw the development of quantum mechanics and quantum field theory as a description of nature. If the universe is ultimately quantum, then general relativity, a classical theory, does not fit into this picture as an appropriate theory of gravity. From a quantum field theory standpoint, general relativity is non-renormalizable. This means that in order to perform a perturbative expansion of GR, one needs an infinite number of parameters (unlike, for example, quantum electrodynamics, which requires only a few parameters, such as charges and masses).

This in turn led to various efforts to come up with a *quantum theory of gravity*. Such a theory would behave like general relativity at low energies (much like general relativity reduces to Newtonian gravity at low energies), but contain quantum effects at high energies. The most notable candidates for a theory of quantum gravity are string theory and loop quantum gravity. In string theory, in contrast to ordinary quantum field theory, the fundamental object is a one-dimensional string, rather than a point particle. The graviton, carrying the gravitational force, in turn corresponds

to a given mode of a string (cf. [41]). Loop quantum gravity, on the other hand, quantizes space and time, so that spacetime is no longer a classical field, but rather discrete at the Planck length, $\sim 10^{-35}$ meters (cf. [174]).

When considering physical theories, we must think about testable predictions. Since we know general relativity breaks down at high energies, let us consider predictions for astrophysical systems in the strong-field, dynamical regime of gravity, such as the merger of black holes.

Were we to directly work in a *full* quantum theory of gravity, these calculations would quickly become prohibitively complicated, if one could even formulate how to do them at all. Instead, we can work in *effective field theories*. These modify the Einstein-Hilbert action of general relativity, through the inclusion of classical terms that encompass high-energy quantum gravity effects, to produce a beyond-GR theory.

Beyond-GR effective field theories, thus, are valid at intermediate ranges, as they account for some high-energy effects, but not all, by virtue of being truncations at some energy. Astrophysical systems that probe the strong-field regime of gravity, such as binary black hole mergers, could potentially contain beyond-GR effects in this intermediate range.

Let us begin looking at the form of some beyond-GR effective field theories, by considering their (classical) actions. Let us start with the standard Einstein-Hilbert action of general relativity, which we will write as

$$S = \frac{1}{16\pi} \int d^4x \sqrt{-g} R, \tag{1.1}$$

where g_{ab} is the spacetime metric, g is its determinant, and R is the spacetime Ricci scalar. Beyond-GR theories will modify this action, whether by adding more terms or changing the form of the R term.

One class of effective field theories of gravity arises from considering actions with higher-order curvature terms added to the Einstein-Hilbert action. In this picture, general relativity becomes a lowest-order term in an action expanded in powers of all possible curvature invariants. In particular, let us focus on terms quadratic in the curvature (the leading-order correction). Adding quadratic-curvature terms to the Einstein-Hilbert action makes it renormalizable [186], thus solving our original problem. Of particular interest are the combinations

$$^*RR \equiv {}^*R^{abcd} R_{abcd}, \tag{1.2}$$

known as the Pontryagin scalar, and

$$R_{\text{GB}}^2 = R^2 - 4R_{ab}R^{ab} + R_{abcd}R^{abcd}, \tag{1.3}$$

known as the Gauss-Bonnet scalar. Both scalars appear in low-energy realizations of string theory [157, 18], and the Pontryagin scalar additionally appears in loop-quantum gravity [192, 134]. Hence, these are motivated by *underlying* theories of quantum gravity.

Coupling these quadratic curvature invariants to a scalar field ϑ creates a class of *quadratic gravity* theories, including Einstein-dilaton-Gauss-Bonnet gravity, with the action

$$S = \frac{1}{16\pi} \int \sqrt{-g}d^4x\, R - 2\nabla_a\vartheta\nabla^a\vartheta - V(\vartheta) + \alpha f(\vartheta)R_{\text{GB}}^2, \tag{1.4}$$

for some coupling function $f(\vartheta)$ and potential $V(\vartheta)$. Here, the first term is the familiar Einstein-Hilbert action of general relativity, the second and third terms correspond to a canonical stress-energy tensor for the scalar field, and the last term couples the scalar field to the Gauss-Bonnet spacetime curvature scalar. The quantity $\alpha^{1/2}$, meanwhile, is a coupling parameter with dimensions of length that determines the truncation of the effective field theory – the length scale below which quantum gravity effects become important.

Similarly, we can obtain dynamical Chern-Simons gravity, with the action

$$S = \frac{1}{16\pi} \int \sqrt{-g}d^4xR - 2\nabla_a\vartheta\nabla^b\vartheta - V(\vartheta) - \ell^2\vartheta\,{}^*RR. \tag{1.5}$$

Here, the fourth term couples the scalar field to the Pontryagin curvature quantity. The quantity ℓ in this case is a coupling parameter with dimensions of length that similarly denotes the length scale below which quantum gravity effects become important.

These theories contain terms motivated by full quantum gravity theories (namely string theory and loop-quantum gravity), and hence serve as classical approximations to some underlying quantum theory of gravity, truncated at second-order in curvature. One can, in theory, perform the same calculations outlined in Sec. 1.1 for these beyond-GR theories. Namely, one can make predictions for black hole metrics, perturbations to these metrics, and the behavior of binary black holes.

1.3 Testing general relativity in the strong-field regime

These physical theories, however, are nothing without experimental evidence, and significant effort has been made in the past century to test general relativity through

astrophysical observations [206]. Recall that we aim to test general relativity in the strong-field, towards a regime where quantum gravity effects could be important.

The strongest tests of general relativity were previously given by binary pulsar systems, including the notable Hulse-Taylor Pulsar, PSR B1913+16 [106]. These tests found consistency with Einstein's quadrupolar formula for gravitational wave emission at a 0.1% level and placed bounds on dipolar radiation, which does not occur in pure GR [205, 43].

However, binary pulsar observations are relatively *weak-field* compared to, for example, the merger of black holes and neutron stars, which at once probe the largest gravitational potentials and highest curvatures of any available astrophysical system (cf. Fig. 1 of [37]). Indeed, attempts to map binary pulsar observations onto constraints on quadratic gravity theories produce a relatively weak theoretical bound [214, 212].

It would take a century after the advent of general relativity to probe gravity in the strong-field regime. In 2015, the Laser Interferometer Gravitational-Wave Observatory (LIGO) made the first detection of gravitational waves from a binary black hole merger [10], probing the strong-field, dynamical regime of gravity for the first time. Together, LIGO and its sister detector, Virgo, have detected gravitational waves from ten binary black hole mergers in the $O(1-100)M_\odot$ range, and one binary neutron star merger [9, 8], with more detections at even higher experimental sensitivity on the way [3, 13].

Testing general relativity with gravitational wave observations: present

How can one test general relativity with gravitational wave observations? To look at the state of the art, let us turn to some of the tests in [14], the companion analysis testing general relativity for GW150914, the first LIGO detection [10].

One of the first tests one can perform is a simple *null test*, by checking the consistency of the null hypothesis (GR in this case) with the data. For GW150914, the most-probable GR waveform [12] was subtracted from the gravitational wave data from each detector, leaving a residual signal. If some loud, non-degenerate, unmodeled deviation from GR were present in the detected gravitational wave, then it would show up as a coherent signal between the two detector residuals. If, however, there were no deviations from GR, the residuals should contain only (uncorrelated) noise [70]. The residuals for GW140915 were not statistically distinguishable from noise, verifying the GR prediction for GW150914 to 4% [14].

The next null test one can perform investigates the post-merger portion of the

detected waveform. In general relativity, by the so-called no-hair theorem, (vacuum, asymptotically flat, stationary, axisymmetric, uncharged) black holes are completely characterized by just two parameters – their mass and spin [132, 135, 76, 94, 111]. In GR, after a binary black hole merger, the resulting single black hole enters the ringdown stage, where its gravitational wave spectrum is described by a linear superposition of damped sinusoids, known as quasi-normal modes (QNMs), which are paramterized by a damping time τ and frequency ω. By the no-hair theorem, these modes (in GR) purely depend on the mass M and spin χ of the final black hole. That is,

$$\left\{ \begin{array}{c} \chi \\ M \end{array} \right\} \leftrightarrow \left\{ \begin{array}{c} \omega \\ \tau \end{array} \right\}. \tag{1.6}$$

In some beyond-GR theories, however, black holes have additional *hair* – that is, there are additional parameters characterizing the ringdown stage and final remnant beyond the mass and spin. In this case, the QNM spectrum will differ from that predicted by GR.

While rigorously checking ringdown consistency with GR requires observing at least two modes for a given signal [94, 111], a weaker test was performed with GW150914 in [14], with just one mode. First, the most-probable GR waveform matching just the inspiral part of the gravitational wave signal was found. From the binary black hole parameters of this waveform, one can theoretically compute what the final mass and spin of the remnant black hole should be in GR [102, 201]. This mass and spin will then give unique predictions in GR for the damping time and frequency of the ringdown QNM spectrum. Thus, one can perform a consistency check between these theoretically predicted QNM parameters, and the QNM parameters measured by fitting damped sinusoids to the post-merger part of the detected signal. For GW150914, the 90% credible regions for the measured QNM parameters and the predicted QNM parameters for one mode overlapped, thus showing compatibility with GR. Such a test is also a *null test*, in that it checks the consistency of the signal with GR predictions (the null hypothesis), rather than using predictions for ringdown behavior from other, competing theories.

In addition to null tests, there are *parametrized* tests of general relativity one can perform with gravitational wave observations. In this case, the gravitational wave signal is tested against waveform models that have parametrized deviations from

GR. For example, in the Parametrized Post-Einsteinian (ppE) formalism [215, 71], the functional forms of the amplitude and phase of the gravitational wave signal are modified, and include some additional parameters. In [216], the authors used the ppE framework on GW150914 data to constraint various ppE parameters (and hence departures from GR). One can also modify the analytical form of the Post-Newtonian (PN) expansion, which describes the inspiral part of the gravitational wave signal. Extra terms (with extra parameters) are added to each order of the expansion (either one order at a time, or all together). In the LIGO GW150914 testing GR paper[14], the authors tested such a modified PN expansion against GW150914 data, finding no consistent departure from GR. These tests, however, only modify the inspiral part of the waveform, without considering the more-energetic merger phase.

In [15], the LIGO and Virgo collaborations used all of the LIGO and Virgo events [9] to test general relativity. In particular, they repeated the null test of subtracting the best-match waveform, and checking that parametrized deviations in PN coefficients were zero.[1] The data was not inconsistent with the predictions of GR, and constraints on deviations from GR decreased by a factor of ~ 2.

Testing general relativity with gravitational wave observations: future possibilities

We can in theory perform stronger tests of gravity than null and parametrized tests of general relativity. What if, in addition to best-match gravitational waveforms in general relativity, we had access to best-match gravitational waveforms in a theory beyond general relativity, such as dynamical Chern-Simons gravity? Then we can perform parameter estimation using the method currently used for general relativity [12] to find the best-match waveform in dynamical Chern-Simons gravity. In particular, dCS has an additional parameter, ℓ, which can (in theory) be measured. This match can then be compared to the match one gets with pure GR, using Bayesian model selection.

Parametrized tests, in a sense, do use a beyond-GR model. However, the merger regime in this case is not well understood. In fact, in [216], the authors discussed the theoretical implications of the GW150914 detection, including a ppE analysis, and argued that "the true potential for GW150914 to both rule out exotic objects and constrain physics beyond General Relativity is severely limited by the lack of

---

[1]There is a wealth of other tests of general relativity that can be performed with gravitational wave observations. We have summarized the tests relevant for the work presented in this thesis, but more information can be found in [43, 14, 15].

understanding of the coalescence regime in almost all relevant modified gravity theories."

A stronger test of gravity with gravitational wave observations then would require the use of gravitational waveforms in a beyond-GR theory.

Let us now discuss how to generate such beyond-GR waveforms. If we wish to perform an analysis with the same level of precision and accuracy as GR analyses, then we need access to waveforms of comparable accuracy. The most accurate gravitational waveforms [2, 1] come from numerical relativity, the practice of precisely solving the non-linear, highly-coupled partial differential equations governing the behavior of spacetime.[2] Binary black hole numerical relativity simulations, however can take on the order of weeks or months to compute. In order to find a best-match waveform as in [14, 12], data analysts must go through millions of waveforms. To produce a numerical relativity simulation for each on a short timescale would be infeasible. Thus, numerical relativity waveforms are used to calibrate waveform models that are faster to evaluate, including the Effective-One-Body model [191] used in [14, 12]. There is also growing interest in gravitational wave data analysis surrogate models, waveform models with NR level accuracy that are trained on NR waveforms [118, 49]. In each of these cases, however, we must first produce numerical relativity gravitational waveforms.

Our goal, thus, is to produce numerical relativity gravitational waveforms in a beyond-GR theory of gravity. This is the main topic of this thesis.

1.4 A brief introduction to numerical relativity

As stated before, numerical relativity (NR) is the practice of precisely solving the non-linear, highly coupled partial differential equations governing the behavior of spacetime. Without going into too much technical detail, let us take some time to give a brief overview of the subject. For an excellent primer on NR, see [40]. We will focus on numerical relativity in general relativity for now.

In analytical relativity, spacetime is characterized by a 4-dimensional spacetime metric, g_{ab}. General relativity is a *covariant theory*, in which all expressions, such as the Einstein field equations, hold true in any coordinate system [203, 64]. Spacetimes such as the Kerr and Schwarzschild black hole solutions are written

---

[2]Throughout this thesis, we use precisely this definition of numerical relativity. Some sources use "numerical relativity" to mean purely solving the Einstein field equations of general relativity numerically, including [40], while we mean solving any equations governing spacetime numerically, including the beyond-GR equations.

down in terms of 4-dimensional coordinates, often containing the full dependence on a time coordinate, t [203].

In numerical relativity, we are interested in situations where the full 4-dimensional spacetime is unknown. It is difficult, for example, to write down the entire spacetime of two merging binary black holes. Instead, in NR, we start with some initial conditions and *evolve* a spacetime. For example, we start with two black holes sitting far apart from each other, and evolve this configuration to see what happens with time.

In this picture, the 4-dimensional spacetime g_{ab} is decomposed into spacelike and timelike pieces. Namely, a 4-dimensional spacetime is *foliated* by a set of spatial slices $\{\Sigma_i\}$. The normal vector n^a to each spatial slice is timelike, and we use this vector to move in time from slice to slice. Each slice Σ_i is labeled by some coordinate time, t_i. On each slice Σ of a spacetime with spacetime metric g_{ab}, the timelike normal vector n^a induces a spatial metric on Σ, γ_{ab}, as

$$\gamma_{ab} = g_{ab} + n_a n_b \,. \tag{1.7}$$

We illustrate this picture in Fig. 1.1.

(a) Spacetime as seen by an analytical relativist (with one spatial dimension suppressed).

(b) Spacetime as seen by a numerical relativist (with one spatial dimension suppressed). The unit timelike normal vector n^a is shown schematically here, for one point on one slice. These is such a vector for each point on each slice.
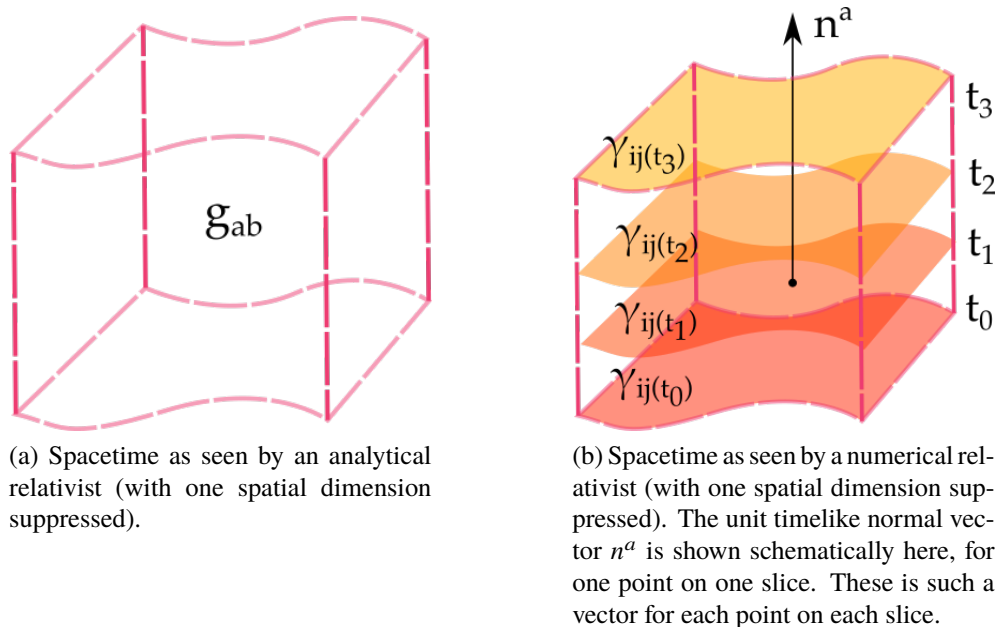
Figure 1.1

Now that we have sliced up the spacetime, let's think about the form the Einstein field equations take in this formalism, known as the 3+1 Arnowitt-Deser-Misner

(ADM) equations [28]. The equations take the form of two *elliptic constraint* equations that the metric must satisfy on each slice Σ_i, and two *hyperbolic evolution* equations governing how the metric data evolves from slice to slice. Satisfaction of the constraints means that the evolution is precisely solving the Einstein field equations.

In order to perform a simulation, we generate *initial data* for the metric (and its first derivatives) on an initial slice Σ_0 by solving the elliptic constraint equations. Then, these data are evolved using the hyperbolic evolution equations to obtain the metric on all subsequent slices. We show this schematically in Fig. 1.2. This constitutes the "simulation", and gives us the results.
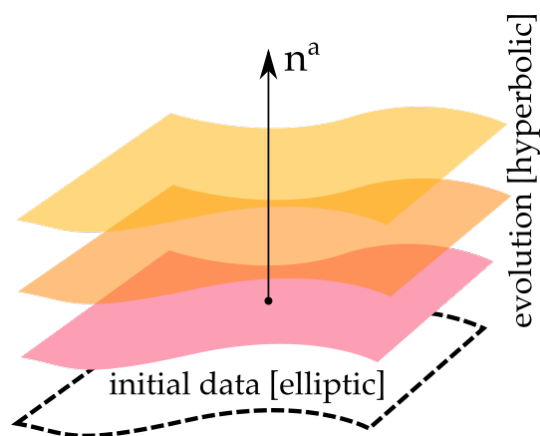
Figure 1.2: Schematic of initial data and evolution formalism.

However, performing this evolution is not so simple. In order to have a stable evolution, we must have a *well-posed initial value problem*. In this case, given an initial solution to a partial differential equation at some time, the solution cannot grow faster than exponentially. This is especially important in the context of numerical relativity, in which the numerical solutions to partial differential equations always have some level of numerical noise. What we want to guarantee is that if we add some numerical noise to an initial condition, we will not get a completely different solution to the problem at some later time.

The 3+1 ADM equations, however, are not well-posed, and performing an evolution using these equations will lead to numerical blow-up. It took some time to formulate the equations of general relativity in such a way as to guarantee that the initial value problem was well-posed. Some popular such formulations are the harmonic and generalized harmonic formalisms [67, 88, 162, 161, 121]. Indeed, it took almost four decades for the first numerical relativity simulation of a binary black hole

merger to be successfully performed [162, 161], mainly due to choosing appropriate evolution equations.

Recall additionally that the equations of general relativity are independent of the choice of coordinates. However, when performing a numerical simulation on a computational domain, we must specify a coordinate system. In particular, though GR as a theory is gauge invariant, we must specify a gauge for our numerical simulations. This leads to another complication – one must choose a satisfactory gauge in which to work [40].

Binary black hole simulations have their own unique challenges, beyond choosing appropriate evolution formulation and gauge. For example, we must determine how to numerically deal with the black hole singularities [104]. Additionally, while it is relatively simple to construct a computational grid for one stationary black hole, it is not so simple to a construct a grid that will faithfully be able to resolve two rapidly moving, merging black holes [179]. We must likewise have methods to find the black hole horizons numerically during a simulation (if desired or required) [98, 68, 53]. Finally, if the ultimate goal of a binary black hole simulation is to produce a gravitational waveform prediction, we must have methods for extracting this radiation [193, 56].

1.5 Pushing numerical relativity beyond general relativity

How does the picture of numerical relativity put forth in Sec. 1.4 change when we work not with general relativity, but a beyond-GR theory? Let us focus, as in this thesis, on a particular 4-dimensional theory of spacetime, namely dynamical Chern-Simons gravity.

We still foliate the spacetime into spatial slices as in Fig. 1.1. The 3+1 ADM equations, however, are equations for general relativity. We thus need to derive a set of constraint equations for initial data and evolution equations in dCS. However, it is believed that dCS does *not* have a well-posed initial value problem [74]. We thus cannot perform simulations of spacetime in the full dCS theory.

However, we know from Sec. 1.3 that deviations from general relativity, in the regime observable by gravitational waves, must be small. Thus, we can work *perturbatively* around GR, and perturb the equations governing dCS around an arbitrary GR solution, such as a binary black hole background. We expand both the spacetime metric and the dCS scalar field in powers of the coupling parameter, and collect the equations of motion at each order. This is known as an *order-reduction*

scheme.

The key to the order-reduction scheme is that GR is a quasilinear theory: the highest derivatives of the metric appear *linearly* in Einstein's equations. Accordingly, at each order in perturbation theory, the equations have the same *principal part* (leading-order derivative terms) as in general relativity. The principal part determines whether the equations have a well-posed initial value problem. Since we know how to formulate GR in a well-posed way, we can do the same for the order-reduced dCS equations, and obtain a well-posed evolution scheme.

At zeroth order in the coupling, we recover general relativity. At first order in the coupling, we see our first dCS correction to GR, namely in the scalar field dynamics. The GR background sources a leading-order dCS scalar field. At this order, there is no dCS modification to the metric. At second order, the GR background and the first-order dCS scalar field source a leading-order dCS metric perturbation. It is *this* field we are after, as it will give us the leading-order dCS modification to a gravitational waveform. We illustrate this system in Fig. 1.3.

In order to generate the leading-order dCS corrections to a binary black hole waveform, we must first be able to evolve a binary black hole system in GR (zeroth order). This problem has long been solved [2, 1]. However, we must now begin to add dCS modifications to the system.

Evolving the leading-order dCS scalar field

In order to obtain dCS corrections to the spacetime metric (and hence the gravitational waveform), we must first evolve the leading-order dCS scalar field, which sources this correction. This is the main objective of Chapter 2 of this thesis, where we develop a formalism and code to evolve the leading-order dCS scalar field on an arbitrary GR background.

We consider a variety of binary black hole systems with spin and compute (scalar) waveforms for the scalar field. The dominant radiation pattern of the scalar field during inspiral is quadrupolar, and we find good agreement with PN theory predictions for the inspiral phase [212]. However, unlike in PN theory, we evolve the system through merger and ringdown. In particular, we find a burst of dipolar scalar radiation at merger, a hitherto unknown phenomenon.

We use the scalar field to estimate the strength of the leading-order dCS correction to the *gravitational* radiation. We find that were LIGO to detect a GW150914-like system to an accuracy of 0.1 radians in the phase, the dCS coupling parameter would

{ Zeroth order } GR BBH Background

{ First order }
Leading-order dCS
Scalar Field

SOURCES

SOURCES

SOURCES

{ Second order }
Leading-order dCS
Metric Perturbation
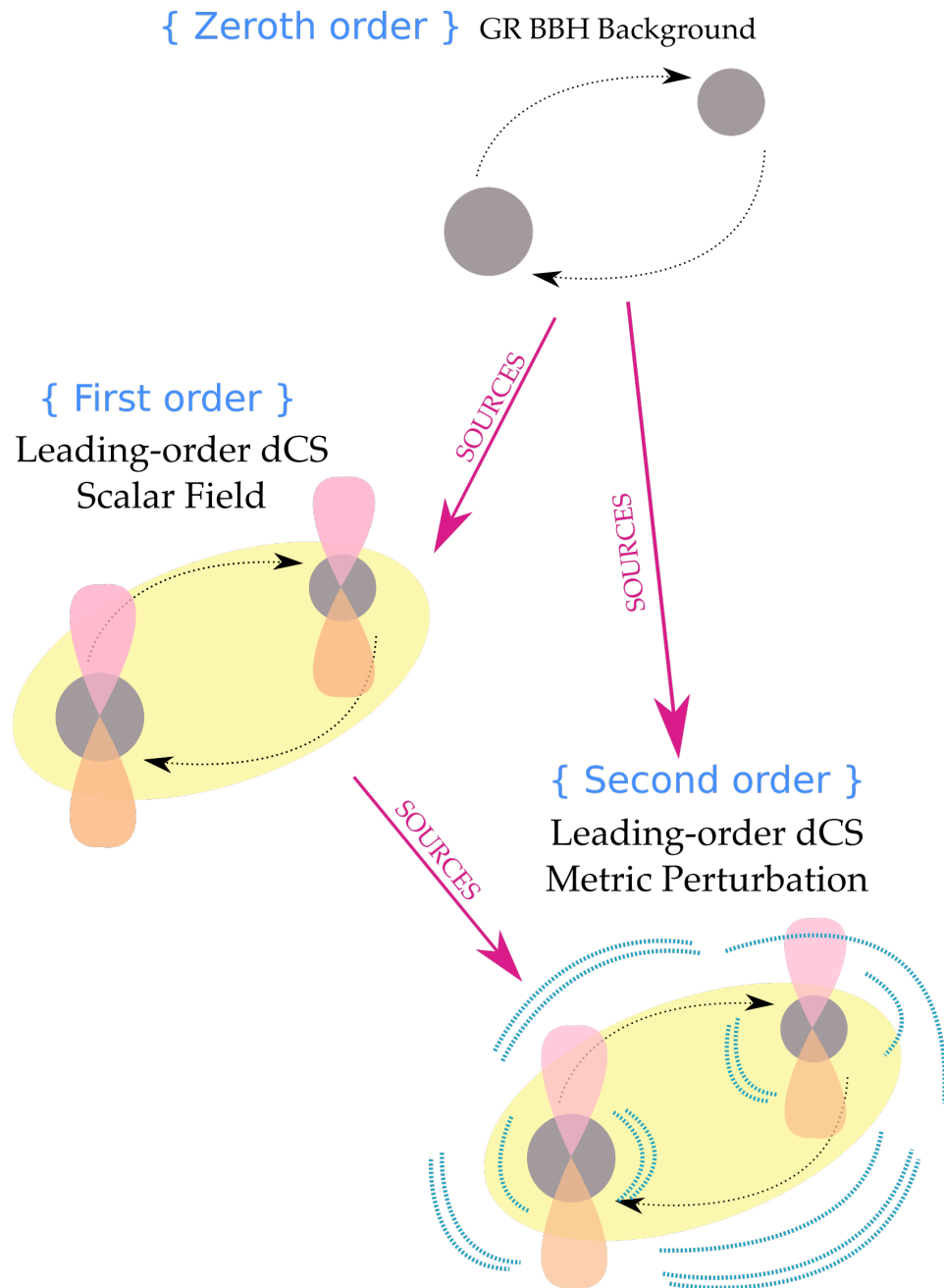
Figure 1.3: Illustration of the order-reduction scheme, which consists of perturbing the equations of dynamical Chern-Simons gravity about a GR background (an inspiraling, merging black hole binary in this case). The zeroth-order GR binary black hole background sources the (leading) first-order dCS scalar field (with no back-reaction on the GR background). This scalar field and the GR BBH background then source the (leading) second-order dCS metric perturbation (with no back-reaction onto the scalar field or the GR background) This in turn sources the dCS corrections to the gravitational waves at infinity.

be bounded by $\ell \lesssim \mathcal{O}(10)$ km, a result eight orders of magnitude stronger than that from solar-system tests [20].

Initial data for leading-order dCS spacetime metrics

If we wish to evolve the leading-order dCS metric perturbation sourced by the scalar field, we must first generate initial data for this metric perturbation. This is precisely the same step we must take for the GR background before a binary black hole evolution (cf. Fig. 1.2). This is the main focus of Chapter 3. Here, we outline a formalism for generating constraint-satisfying metric perturbations for a general source, on general GR background, and explore this is in the context of dCS.

While this framework is used to generate initial data for our dCS binary evolutions, we are also interested in looking at the leading-order dCS correction to a single, stationary, rotating black hole spacetime. The Kerr spacetime is not a solution of the full dCS theory. Thus, we expect the metric of a rotating black hole to differ from that of GR. We use this initial data formalism to compute the dCS correction to Kerr, for arbitrary spin. Since the spacetime is stationary, one slice of stationary initial data is all we need to obtain the full spacetime.

An interesting observable we can compute from this dCS black hole spacetime is the *black hole shadow*. If one were to take a picture of a black hole with a camera, the shadow is a dark region on the image corresponding to angles at which no photons reach the camera, because of light-bending and the presence of an event horizon. In general relativity, for a black hole with a given mass and spin, the shadow has a precise shape, and thus deviations from this predicted shape can be used to test the theory [136, 164, 136, 37]. The black hole shadow is of particular interest for the Event Horizon Telescope (EHT) [170, 85], a very long baseline interferometry array of radio telescopes that aims to image Sgr A*, the black hole at the center of the Milky Way galaxy, and has triumphantly imaged the black hole at the center of the M87 galaxy [80, 81].

In Chapter 3, we compute the black hole shadow in our dCS black hole spacetime for a variety of spins and dCS coupling parameters. We find that given the present ability of the EHT to measure the spin of Sgr A*, the dCS corrections would be within the margin of error due to the spin measurement, and thus not presently detectable. However, the dCS modifications to the shape of the shadow are *non-degenerate* with GR, meaning that in the limit of tight constraints on the spin measurement and high image resolution, one could differentiate dCS from GR.

Evolving leading-order dCS spacetime metrics

Given the initial data for some dCS system, our goal is now to evolve this data in time to obtain our full spacetime solution (cf. Fig. 1.2). This is the focus of Chapter 4. Recall that our evolution equations must be *well-posed* in order to be able to evolve the system. In this chapter, we derive well-posed evolution equations for a leading-order metric perturbation with arbitrary source on an arbitrary background.

In particular, we use this formalism to evolve the leading-order dCS metric perturbation sourced by the leading-order dCS scalar field on a rotating black hole background. The stability of rotating black holes in dCS is unknown [137, 90, 43]. By evolving this leading-order metric correction and showing that it remains constant in time, we showed that rotating black holes in dCS gravity are stable to second order.

Head-on binary black hole collisions in dCS gravity

Our next goal is to find the leading-order dCS correction to the gravitational waveforms from merging binary black hole systems in full numerical relativity. These waveforms will allow us to perform the model-dependent tests of general relativity we alluded to in Sec. 1.3.

We first consider the case of head-on collisions of binary black holes with spin. Head-on collisions, in which black holes do not orbit one another but rather directly smash into each other, are relatively simple systems, and they are fast simulations to perform. A head-on collision takes a fraction ($\sim 1/30$) of the time is takes an orbiting binary to merge, starting from the same initial separation. Thus, these serve as a perfect test-bed for our dCS metric perturbation evolution scheme given in Chapter 4.

While head-on collisions are not particularly relevant for astrophysical systems, they do cleanly probe the quasi-normal mode spectrum of the remnant spinning black hole [24, 23, 35, 181]. Thus, we can use the dCS correction to the gravitational waveform computed from such systems to learn about leading-order dCS modifications to the QNM spectrum of a spinning black hole.

This is the focus of Chapter 5 of this thesis. We perform binary black hole head-on collisions for a variety of spins, and produce the first numerical relativity beyond-GR gravitational waveforms in a higher-curvature theory of gravity. We measure the leading-order dCS corrections to the damping time and frequency of the quasi-normal mode spectrum, and find that these increase polynomially with spin.

Moreover, we find that for the cases we have considered, these modifications are non-degenerate with GR.

Full beyond-GR gravitational waveforms

Having demonstrated our ability to produce beyond-GR waveforms, or focus is next to add angular momentum to the system in order to produce beyond-GR waveforms appropriate for LIGO and future gravitational wave detectors.

In Chapter 6, we perform a numerical relativity simulation in order-reduced dCS for a binary black hole system consistent with the inferred parameters of GW150914 [12, 126]. We produce the first beyond-GR gravitational waveforms in a higher-curvature theory in full numerical relativity, through complete inspiral, merger, and ringdown. We find that the ringdown QNM spectrum is modified similarly to the head-on collision case (cf. Chapter 5), while the inspiral is modified with a beating frequency pattern, sourced by beating between the leading-order dCS scalar field and the GR binary black hole background (cf. Fig. 1.1).

Using numerical relativity to test the no-hair theorem

The final chapter of this thesis, Chapter 7, considers another use-case for numerical relativity in testing general relativity.

Recall from Sec. 1.3 that one of the tests we can perform with gravitational wave observations is a test of the *no-hair theorem*, which involves the ringdown portion of the gravitational wave signal. One can also perform a test, (as in [14] for GW150914) to simply look for the least-damped quasi-normal mode in the ringdown portion of the signal, and check that its parameters are consistent with those predicted by GR. *Ringdown*, in this case, refers precisely to the regime where the gravitational wave can be described as a set of *linear* QNM perturbations on a stationary black hole background. After merger, the spacetime around the resulting single black hole can still potentially contain non-linearities – it takes some time after merger to settle into the ringdown regime.

In order to perform a no-hair theorem or least-damped QNM test, we must thus choose a portion of the post-merger gravitational waveform that is truly within this ringdown regime. If we start our test too early in the gravitational waveform, then our analysis will contain systematic errors from trying to model something that is non-linear as linear. In fact, the post-merger analysis for GW150914 [14] saw precisely such an effect. When the authors started the analysis close to merger,

the 90% credible region for the inferred QNM parameters did *not* overlap with that predicted by GR and QNM perturbation theory. However, when the analysis window was shifted to a later time, where the ringdown description was more faithful, the regions overlapped.

How should we choose the start time of ringdown? Past authors have used properties of numerical relativity gravitational waveforms to estimate this regime [110, 44, 124, 33]. However, in a numerical relativity simulation, we have access not only to the computed gravitational waveform, but also *the whole spacetime itself* (cf. Fig. 1.2). Thus, when asking ourselves questions about the amount of non-linearity present in the waveform, we can instead turn directly to the associated strong-field region in the simulation.

In Chapter 7, we offer a numerical-relativity based approach to choosing the start time of binary black hole ringdown. We use various algebraic and geometric quantities put forth in [93, 187] that measure *Kerrness*, or closeness to a Kerr spacetime on a given spatial slice. We present a formalism to associate the values of the Kerrness measures to the amount of non-linearity present in the spacetime. We see that as the post-merger numerical relativity simulation progresses, each spatial slice gets closer and closer to a linearly perturbed Kerr spacetime, with fewer and fewer non-linearities. We derive a prescription for then mapping this information onto the gravitational waveform from the simulation.

The result thus gives a gravitational waveform with a measure of the amount of non-linearity (let's call it ε) at each time on the post-merger part of the waveform. This ε can thus act as a systematic error measure on a ringdown analysis, for it denotes precisely how much non-linearity is contaminating a linear analysis. We produced such a result for the numerical relativity simulation of GW140915 used in the LIGO detection paper [11]. Our analysis found that the start times of ringdown chosen in the testing GR companion paper [14] were too early, as the spacetime still contained a fair amount of non-linearity. Subsequent, independent studies on testing GR with binary black hole ringdowns explicitly confirmed our results [123, 65, 57].

1.6 Looking forward

Our motivation for all of the projects presented in this thesis can be summarized by the following: we know that at some length scale, general relativity must break down and be reconciled with quantum mechanics in a beyond-GR theory of gravity.
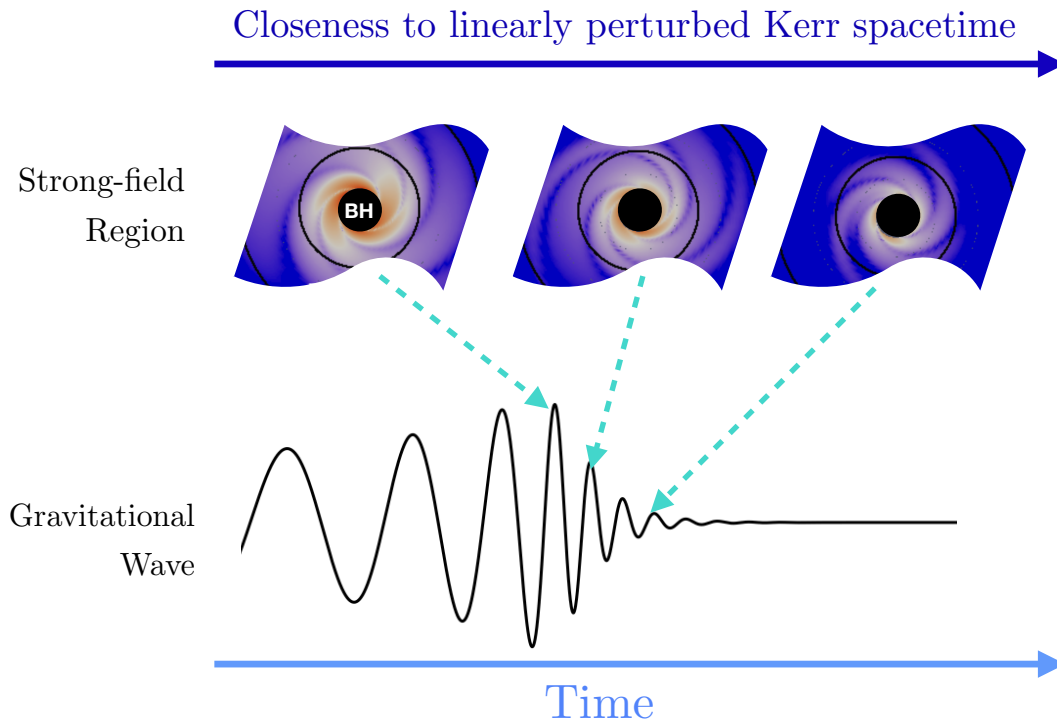
Figure 1.4: Schematic of the method of determining the start time of binary black hole ringdown, as discussed in Chapter 7. Time moves from the left to the right. The top figures show snapshots of the strong-field region around the final black hole (denoted BH) on three spatial time-slices. We show a Kerrness measure on the on slice, which in time settles to a value consistent with that of a linearly perturbed Kerr spacetime. How close the strong-field region is to the linear regime can then be mapped onto the gravitational waveform. This information on the gravitational waveform can then be used to inform the start time of ringdown, which requires being in a linear regime.

Merging binary black holes probe the strong-field, non-linear, dynamical regime of gravity, and gravitational waves from these systems could perhaps contain signatures of such a theory.

Our goal of generating precise beyond-GR gravitational waveforms using numerical relativity is to try to probe such signatures (or show their absence) using model-dependent tests of general relativity. Similarly, our goal of using numerical relativity to inform the start time of binary black hole ringdown is aimed to be able to precisely probe beyond-GR signatures in the post-merger signal.

There is much work to be done. We need to generate more dCS waveforms in order to perform a model-dependent test of GR with gravitational wave detector data. We must generate enough waveforms to produce a dCS surrogate model for rapid parameter estimation (cf. Sec. 1.3). Luckily, this can be done with our present code.

We also need our waveforms to be more accurate. Gravitational wave detectors with higher singal-to-noise ratios (for some systems) than LIGO, such as the Laser Interferometer Space Antenna (LISA), will come online in this century [27, 22]. Numerical relativists need to make sure that general relativity and beyond-GR waveforms are at the level of accuracy where numerical errors in the waveform are lower than the level of noise on the detectors. This should be feasible with future codes [114].

We need to consider other beyond-GR theories of gravity, in addition to dynamical Chern-Simons theory. The techniques and code that we have generated and used in Chapters 2, 3, 4, 5, and 6 can be used for Einstein-dilaton-Gauss-Bonnet gravity (cf. Eq. 1.4), and other higher-curvature effective field theories, by simply changing the source term.

The past century has seen the triumph of general relativity, and perhaps the coming century can see beyond it.

Chapter 2

NUMERICAL BINARY BLACK HOLE MERGERS IN DYNAMICAL CHERN-SIMONS GRAVITY: SCALAR FIELD

[1]   Maria Okounkova et al. "Numerical binary black hole mergers in dynamical Chern-Simons gravity: Scalar field". In: *Phys. Rev.* D96.4 (2017), p. 044020. DOI: 10.1103/PhysRevD.96.044020. arXiv: 1705.07924 [gr-qc].

Abstract

Testing general relativity in the non-linear, dynamical, strong-field regime of gravity is one of the major goals of gravitational wave astrophysics. Performing precision tests of general relativity (GR) requires numerical inspiral, merger, and ringdown waveforms for binary black hole (BBH) systems in theories beyond GR. Currently, GR and scalar-tensor gravity are the only theories amenable to numerical simulations. In this article, we present a well-posed perturbation scheme for numerically integrating beyond-GR theories that have a continuous limit to GR. We demonstrate this scheme by simulating BBH mergers in dynamical Chern-Simons gravity (dCS) to linear order in the perturbation parameter. We present mode waveforms and energy fluxes of the dCS pseudoscalar field from our numerical simulations. We find good agreement with analytic predictions at early times, including the absence of pseudoscalar dipole radiation. We discover new phenomenology only accessible through numerics: a burst of dipole radiation during merger. We also quantify the self-consistency of the perturbation scheme. Finally, we estimate bounds that GR-consistent LIGO detections could place on the new dCS length scale, approximately $\ell \lesssim O(10)$ km.

2.1   Introduction

General relativity has been observationally and experimentally tested for almost a century, and has been found consistent with all precision tests to date [206]. But no matter how well a theory has been tested, it may be invalidated at any time when pushed to a new regime. Indeed, there are many theoretical reasons to believe that general relativity (GR) cannot be the ultimate description of gravity, from non-renormalizability to the black hole information problem.

Moreover, from the empirical standpoint, all *precision* tests of GR to date have been in the slow-motion, weak-curvature regime. With the Laser Interferometer Gravitational Wave Observatory (LIGO) now detecting the coalescence of compact binary systems [10, 5, 16], we finally have direct access to the non-linear, dynamical, strong-field regime of gravity. This is an arena where GR lacks precision tests, and it may give clues to a theory beyond GR. The LIGO collaboration has already used the detections of GW150914, GW151226, and GW170104 to perform some tests of GR [14, 16], but these are not yet very precise: a model-independent test gives 96% agreement with GR.

Both black hole (BH) and neutron star (NS) binaries probe the strong-field regime. However, NSs have the added complication that the equation of state of dense nuclear matter is presently unknown. Until more is known about the equation of state, we must rely on binary black holes (BBHs) for precision tests of GR. Yunes, Yagi, and Pretorius argued [216] that the lack of understanding of BBH merger in beyond-GR theories severely limits the ability to constrain gravitational physics using GW150914 and GW151226. Thus, to perform tests of GR with BBHs, we require inspiral, merger, and ringdown waveform predictions for these systems, which can only come from numerical simulations.

To date, BBH simulations have only been performed in GR and scalar-tensor gravity [43] (note that BBHs in massless scalar-tensor gravity will be identical to GR, under ordinary initial and boundary conditions). There are a huge number of beyond-GR theories [43], and for the vast majority of them, there is no knowledge of whether there is a well-posed initial value formulation, a necessity for numerical simulations. Indeed, there is evidence that dynamical Chern-Simons gravity, the beyond-GR theory we use here as an example, lacks a well-posed initial value formulation [74].

Our goal is to numerically integrate BBH inspiral, merger, and ringdown in theories beyond GR that are viable but that do not necessarily have a well-posed initial value problem. This goal is relevant even for those only interested in parametric, model-independent tests, because there is presently no theory guidance for late-inspiral and merger waveforms in theories beyond GR.

We are only interested in theories that are sufficiently "close" to GR: for a theory to be viable, it has to be able to pass all the tests that GR has passed. This motivates an effective field-theory (EFT) approach. We assume that there is a high-energy theory whose low-energy limit gives GR plus "small" corrections. The effective theory

of GR with corrections does not need to capture arbitrarily short-distance physics. Such a theory is valid up to some cutoff, and modes shorter than this distance scale are said to be outside of the regime of validity of the EFT. The EFT only needs to be well-posed for the modes within the regime of validity. This can be accomplished with perturbation theory.

We present a perturbation scheme for numerically integrating beyond-GR theories that limit to GR. For such a theory, we perturb it about GR in powers of the small coupling parameter. We collect equations of motion at each order in the coupling, creating a tower of equations, with each level inheriting the same principal part as the background GR system. The well-posedness of the initial value problem in GR [203] thus ensures the well-posedness of this framework, even if the "full" underlying theory may not have a well-posed initial value formulation.

In this study, we apply our perturbation framework to BBH mergers in dynamical Chern-Simons gravity (dCS) [18] to linear order in perturbation theory. This theory involves a pseudoscalar field coupled to the parity-odd Pontryagin curvature invariant with a small coupling parameter, and at linear order gives a scalar field evolving on a GR BBH background.

There are a number of theoretical motivations for considering dynamical Chern-Simons. The dCS interaction arises when cancelling gravitational anomalies in chiral theories in curved spacetime [72, 79, 21], including the famous Green-Schwarz anomaly cancellation in string theory [95] when compactified to four dimensions [18, 157, 158]. DCS also arises in loop quantum gravity when the Barbero-Immirzi parameter is allowed to be a spacetime field [192, 134]. From an EFT standpoint, dCS is the lowest-mass-dimension correction that has a parity-odd interaction. All other EFTs at the same mass dimension have parity-even interactions, so the phenomenology of dCS is distinct [212]. The dCS interaction was also included in Weinberg's EFT of inflation [204].

From a practical standpoint, there are already a large number of dCS results in the literature that we can compare against [214, 212, 210, 209, 211, 117, 184], including post-Newtonian (PN) calculations for the BBH inspiral. One of the more important results is that scalar dipole radiation is highly suppressed in dCS during the inspiral [212]. Dipole radiation is present in scalar-tensor theory and Einstein-dilaton-Gauss-Bonnet (EdGB), and enters with two fewer powers of the orbital velocity (i.e. 1 PN order earlier) than the leading quadrupole radiation of GR. This leads to gross modifications of the inspiral, but dCS avoids this problem because

the dipole is suppressed. As a result, the perturbative treatment of dCS will be valid for a longer period of inspiral than scalar-tensor or EdGB.

The paper is organized as follows. Sec. 2.2 covers the analytical and numerical formalisms. More specifically, in Sec. 2.2 we introduce dynamical Chern-Simons, and in Sec. 2.2 we present the perturbation scheme, which is valid for any theory with a continuous limit to GR. We discuss the numerical scheme in Sec. 2.2 (some numerical details are in the Appendix). We present the results of numerically implementing this formalism in dCS on three different binary mergers in Sec. 2.3. Sec. 2.3 reviews some previously-known analytic phenomenology of the BBH inspiral problem in dCS. Sec. 2.3 presents the waveform results, and 2.3 presents the energy fluxes, both including comparison to PN. In Sec. 2.3 we use the numerical results to assess the validity of the perturbation scheme. In Sec. 2.3 we use the numerical results to estimate the detectability of dCS and the bounds that could be placed by LIGO detections. We conclude and discuss in Sec. 2.4, and lay out plans for future work.

2.2 Formalism

Throughout this paper, we set $c = 1$ and $\hbar = 1$ so that $[M] = [L]^{-1}$. Since there will be more than one length scale, we explicitly include factors of the reduced Planck mass $m_{\mathrm{pl}}^{-2} = 8\pi G$ and the "bare" gravitational length GM, though quantities in our code are non-dimensionalized with $GM = 1$. Latin letters in the middle of alphabet $\{i, j, k, l, m, n\}$ are (3-dimensional) spatial indices, while Latin letters in the beginning of the alphabet $\{a, b, c, d\}$ refer to (4-dimensional) spacetime indices. We follow the sign conventions of [203], and g_{ab} refers to the 4-dimensional spacetime metric, with signature $(- + + +)$, and with ∇ its Levi-Civita connection.

Action and equations of motion

The method we present in this paper applies to a large number of beyond-GR theories that have a continuous limit to GR, but for concreteness we focus on dCS. We start with the four-dimensional action

$$I = \int d^4x \sqrt{-g} \left[L_{\mathrm{EH}} + L_{\vartheta} + L_{\mathrm{int}} + L_{\mathrm{mat}} + \ldots \right], \tag{2.1}$$

where the omitted terms $(\ldots)$ are above the cutoff of our EFT treatment. Here g without indices is the determinant of the metric, L_{EH} is the Einstein-Hilbert Lagrangian, L_{ϑ} is the Lagrangian of a minimally coupled (pseudo-)scalar field ϑ (also referred to in the literature as the axion), L_{int} is a beyond-GR interaction

between ϑ and curvature terms, and L_{mat} is the Lagrangian for ordinary matter. In this paper, we are considering a binary black hole (BBH) merger in dCS, so we ignore L_{mat}.

Explicitly, these action terms are given by

$$L_{\text{EH}} = \frac{m_{\text{pl}}^2}{2} R, \qquad\qquad L_{\vartheta} = -\tfrac{1}{2}(\partial\vartheta)^2, \qquad (2.2a)$$

$$L_{\text{int}} = -\frac{m_{\text{pl}}}{8}\ell^2\vartheta \,^*RR. \qquad\qquad\qquad (2.2b)$$

Here the Ricci scalar of g_{ab} is R. With our unit system, $[g] = [L]^0$, coordinates carry dimensions of length, $[x] = [L]^1$, and note that the scalar field ϑ has been canonically normalized, $[\vartheta] = [L]^{-1}$. We have omitted any potential $V(\vartheta)$, so ϑ is massless and long-ranged, as appropriate for a "gravitational" degree of freedom. In the interaction Lagrangian L_{int}, the scalar field ϑ is coupled to the 4-dimensional Pontryagin density (also known as the Chern-Pontryagin density) $^*RR$,

$$^*RR \equiv \,^*R^{abcd}R_{abcd} = \tfrac{1}{2}\epsilon^{abef}R_{ef}{}^{cd}R_{abcd}, \qquad (2.3)$$

where ϵ_{abcd} is the fully antisymmetric Levi-Civita tensor.

The coupling strength of this interaction is governed by the new parameter ℓ with dimensions of length. This parameter takes on specific values if this EFT arises from the low-energy limit of certain string theories [95] or to cancel gravitational anomalies [21, 157, 158]. However, here we simply take it as a "small" coupling parameter. In the limit that $\ell \to 0$, we recover general relativity with a massless, minimally coupled scalar field.

The coupling parameter conventions vary throughout the literature. To enable comparisons, we express the couplings of a number of works in terms of our conventions. To put Yagi et al. [212] into our conventions, use

$$\kappa^{\text{YSYT}} = \frac{1}{2}m_{\text{pl}}^2, \qquad \alpha_4^{\text{YSYT}} = -\frac{m_{\text{pl}}\ell^2}{8}, \qquad \beta^{\text{YSYT}} = 1. \qquad (2.4)$$

To convert Alexander and Yunes [18] into our conventions,

$$\kappa^{\text{AY}} = \frac{1}{2}m_{\text{pl}}^2, \qquad \alpha_4^{\text{AY}} = +\frac{m_{\text{pl}}\ell^2}{2}, \qquad \beta^{\text{AY}} = 1. \qquad (2.5)$$

To compare with McNees et al. [133], use

$$\kappa^{\text{MSY}} = m_{\text{pl}}^{-1}, \qquad\qquad \alpha^{\text{MSY}} = +\frac{\ell^2}{2}. \qquad (2.6)$$

The conventions of Stein [184] agree with ours (except for an inconsequential sign change in the definition of $^*RR$, which is compensated for by an additional sign everywhere $^*RR$ appears).

Below we will perform an expansion in powers of ℓ^2. To simplify matters, we insert a dimensionless formal order-counting parameter ε that will keep track of powers of ℓ^2. Expanding in a dimensionless parameter ensures that field quantities at different orders have the same length dimension.

Specifically, we replace the action in Eq. (2.1) with

$$I_\varepsilon = \int d^4x \sqrt{-g} \left[L_{\text{EH}} + L_\vartheta + \varepsilon L_{\text{int}} + L_{\text{mat}} + \ldots \right],$$ (2.7)

a one-parameter family of actions parameterized by ε. Formally, we recover the action in Eq. (2.1) when $\varepsilon = 1$.

Varying the action Eq. (2.7) with respect to the scalar field, we have the sourced wave equation

$$\Box \vartheta = \varepsilon \frac{m_{\text{pl}}}{8} \ell^2 \, {}^*RR,$$ (2.8)

where $\Box = \nabla_a \nabla^a$ is the d'Alembertian operator. Varying with respect to the metric gives the corrected Einstein field equations,

$$m_{\text{pl}}^2 G_{ab} + m_{\text{pl}} \varepsilon \ell^2 C_{ab} = T_{ab}^\vartheta + T_{ab}^{\text{mat}},$$ (2.9)

where G_{ab} is the Einstein tensor of g_{ab}, and the tensor C_{ab} includes first and second derivatives of ϑ, and second and *third* derivatives of the metric,

$$C_{ab} \equiv \epsilon_{cde(a} \nabla^d R_{b)}{}^c \nabla^e \vartheta + {}^*R^c{}_{(ab)}{}^d \nabla_c \nabla_d \vartheta.$$ (2.10)

Since we are focusing on BBH mergers, $T_{ab}^{\text{mat}} = 0$. The scalar field's stress-energy tensor T_{ab}^ϑ is given by the expression for a canonical, massless Klein-Gordon field,

$$T_{ab}^\vartheta = \nabla_a \vartheta \nabla_b \vartheta - \frac{1}{2} g_{ab} \nabla_c \vartheta \nabla^c \vartheta.$$ (2.11)

From here forward we will drop the superscript ϑ.

The "full" system of equations for dCS is thus the pair of Eqs. (2.8) and (2.9).

Perturbation scheme

Because C_{ab} in Eq. (2.9) contains third derivatives of the metric, the "full" system of equations for dCS likely lacks a well-posed initial value formulation [74]. In the language of particle physics, this is equivalent to the appearance of ghost modes above a certain momentum scale [77].

From the EFT point of view, though, the ghost modes and ill-posedness are nothing more than the breakdown of the regime of validity of the theory, which should be valid for long wavelength modes in the decoupling limit $\ell \to 0$. To excise the ghost modes and arrive at a well-posed initial value formulation, we expand about $\varepsilon = 0$, which is simply GR coupled to a massless minimally-coupled scalar field and certainly has a well-posed initial value problem [203]. As a result, all higher orders in ε will inherit the well-posedness of the zeroth-order theory by inheriting the principal parts of the differential equations.

We begin this order-reduction scheme by expanding the metric and scalar field in power series in ε,[1]

$$g_{ab} = g_{ab}^{(0)} + \sum_{k=1}^{\infty} \varepsilon^k h_{ab}^{(k)}, \tag{2.12a}$$

$$\vartheta = \sum_{k=0}^{\infty} \varepsilon^k \vartheta^{(k)}. \tag{2.12b}$$

Note that since ε is dimensionless, each $\vartheta^{(k)}$ has the same units as ϑ, and similarly for $h_{ab}^{(k)}$. This expansion is now inserted into the field equations, which are likewise expanded in powers of ε, and we collect orders homogeneous in ε^k, as below. This results in a "tower" of systems of equations that must be solved at progressively increasing orders in ε. This scheme is quite general and should apply to any theory that has a continuous limit to GR.

Order ε^0

Zeroth order comes from taking $\varepsilon \to 0$, which simply gives the system of GR coupled to a massless, minimally coupled scalar field,

$$m_{\text{pl}}^2 G_{ab}[g^{(0)}] = T_{ab}^{(0)}, \tag{2.13a}$$

$$\Box^{(0)} \vartheta^{(0)} = 0, \tag{2.13b}$$

---

[1]Note that this is not a Taylor series, since there is no factor of $1/k!$ in the kth term. These factors must be tracked if using standard perturbation theory, e.g. with the `xPert` package [208, 58].

where $G_{ab}[g^{(0)}]$ is the Einstein tensor of the background metric $g^{(0)}$, $\Box^{(0)}$ is the associated d'Alembert operator, and $T^{(0)}$ is the stress-energy of $\vartheta^{(0)}$. This system certainly has a well-posed initial value problem.

Because of the explicit presence of ε in front of L_{int} in the action [Eq. (2.7)], C_{ab} does not appear in the metric equation (2.13a), and the Pontryagin source does not appear on the right-hand side of the scalar equation (2.13b). These terms have been pushed to one order higher and will appear below.

On general grounds, we expect that any initially non-vanishing scalar field will radiate away within a few dynamical times. Similarly, if we start with a $\vartheta^{(0)} = 0$ initial condition and impose purely outgoing boundary conditions, $\vartheta^{(0)}$ will remain zero throughout the entire simulation. Therefore, rather than simulating a vanishingly small $\vartheta^{(0)}$, we simply analytically assume that $\vartheta^{(0)} = 0$.

Therefore, at order $O(\varepsilon^0)$, the system will simply be

$$G_{ab}[g^{(0)}] = 0, \tag{2.14}$$

and the solution will be

$$(g^{(0)}, \vartheta^{(0)}) = (g^{\text{GR}}, 0), \tag{2.15}$$

where g^{GR} is a GR solution to the BBH inspiral-merger-ringdown problem.

Order ε^1

Continuing to linear order in ε, we find the system

$$m_{\text{pl}}^2 G_{ab}^{(1)}[h^{(1)}; g^{(0)}] = -m_{\text{pl}}\ell^2 C_{ab}^{(0)} + T_{ab}^{(1)}, \tag{2.16a}$$

$$\Box^{(0)}\vartheta^{(1)} + \Box^{(1)}\vartheta^{(0)} = \tfrac{m_{\text{pl}}}{8}\ell^2 [^*RR]^{(0)}. \tag{2.16b}$$

As noted above, the explicit presence of ε in the action (2.7) and equations of motion [(2.8) and (2.9)] lead to $C^{(0)}$ and $[^*RR]^{(0)}$ appearing in these ε^1 equations strictly as source terms. By construction, the principal part of this differential system is the same as the principal part of the $O(\varepsilon^0)$ system, and thus it inherits its well-posedness property. This is true at all higher orders in perturbation theory.

Here, $G^{(1)}[h^{(1)}; g^{(0)}]$ is the linearized Einstein operator, built with the covariant derivative $\nabla^{(0)}$ compatible with $g^{(0)}$, acting on the metric deformation $h^{(1)}$. The d'Alembert operator receives the correction $\Box^{(1)}$, which depends on the metric deformation $h^{(1)}$. The quantity $C_{ab}^{(0)}$ is the same as the definition given in Eq. (2.10),

evaluated on the background quantities $(g^{(0)}, \vartheta^{(0)})$. Similarly, $[^*RR]^{(0)}$ is the Pontryagin density evaluated on the background spacetime metric $g^{(0)}$. Finally, $T_{ab}^{(1)}$ is the first-order perturbation to the stress-energy tensor; since T_{ab} is quadratic in ϑ, $T_{ab}^{(1)}$ has pieces both linear and quadratic in $\vartheta^{(0)}$ (the quadratic-in-$\vartheta^{(0)}$ pieces are linear in $h^{(1)}$).

The crucial property at this order is that both $C^{(0)}$ and $T^{(1)}$ are built from pieces linear and quadratic in $\vartheta^{(0)}$. At order $O(\varepsilon^0)$, we found that $\vartheta^{(0)} = 0$. Therefore, when evaluated on the $O(\varepsilon^0)$ solution [Eq. (2.15)], these both vanish,

$$C_{ab}^{(0)}[\vartheta^{(0)} = 0] = 0, \qquad\qquad T_{ab}^{(1)}[\vartheta^{(0)} = 0] = 0. \qquad (2.17)$$

Therefore, at order $O(\varepsilon^1)$ in perturbation theory, evaluating on the background solution, we have the system

$$m_{\mathrm{pl}}^2 G_{ab}^{(1)}[h^{(1)}; g^{(0)}] = 0, \qquad (2.18a)$$

$$\Box^{(0)}\vartheta^{(1)} = \tfrac{m_{\mathrm{pl}}}{8}\ell^2 [^*RR]^{(0)}. \qquad (2.18b)$$

In the metric perturbation equation (2.18a), starting with $h^{(1)} = 0$ initial conditions and imposing purely outgoing boundary conditions will enforce $h^{(1)} = 0$ throughout the entire simulation. Similarly, we can argue that small perturbations of $h^{(1)}$ would radiate away on a few dynamical times, since there is no potential to confine the metric perturbations. Once again, rather than simulating a vanishingly small field, we will just analytically assume that $h^{(1)} = 0$. Therefore, at order $O(\varepsilon^1)$, there is no metric deformation, and the system is only Eq. (2.18b), driven by the background system (2.14) which generates the source term $[^*RR]^{(0)}$.

Order ε^2

This perturbation scheme can be extended to any order desired. Although this paper reports only on work extending through $O(\varepsilon^1)$, we sketch the derivation of $O(\varepsilon^2)$, since that is the lowest order where a metric deformation is sourced.

Schematically, the system at $O(\varepsilon^2)$, after accounting for the vanishing of $\vartheta^{(0)}$ and $h^{(1)}$, is

$$m_{\mathrm{pl}}^2 G_{ab}^{(1)}[h^{(2)}] = -m_{\mathrm{pl}}\ell^2 C_{ab}^{(1)}[\vartheta^{(1)}] + T_{ab}^{(2)}[\vartheta^{(1)}, \vartheta^{(1)}], \qquad (2.19a)$$

$$\Box^{(0)}\vartheta^{(2)} = 0. \qquad (2.19b)$$

The operator $C^{(1)}[\vartheta^{(1)}]$ is linear in its argument, and $T^{(2)}[\vartheta^{(1)}, \vartheta^{(1)}]$ is linear in each slot. Various other combinations have vanished. In (2.19a), vanishing source terms

were quadratic in $h^{(1)}$ or built from the product of $h^{(1)} \times \vartheta^{(1)}$. In (2.19b), $\ell^2[^*RR]^{(1)}$ is proportional to $h^{(1)}$ and thus vanishes, as do terms such as $\Box^{(1)}\vartheta^{(1)}$ (linear in $h^{(1)}$) and $\Box^{(2)}\vartheta^{(0)}$ (linear in $\vartheta^{(0)}$).

We leave detailed discussion of order $O(\varepsilon^2)$ to future work [144].

Summary and scaling

Let us briefly summarize the perturbative order-reduction scheme and discuss the scaling of different orders. The system at orders ε^0 and ε^1 is

$$O(\varepsilon^0): \qquad G_{ab}[g^{(0)}] = 0, \qquad\qquad \vartheta^{(0)} = 0, \qquad (2.20a)$$

$$O(\varepsilon^1): \qquad \Box^{(0)}\vartheta^{(1)} = \frac{m_{\text{pl}}}{8}\ell^2[^*RR]^{(0)}, \qquad h^{(1)} = 0, \qquad (2.20b)$$

and if we were to continue to $O(\varepsilon^2)$,

$$O(\varepsilon^2): \qquad G^{(1)}_{ab}[h^{(2)}] = m_{\text{pl}}^{-2}T^{\text{eff}}_{ab}, \qquad\qquad \vartheta^{(2)} = 0, \qquad (2.20c)$$

where T^{eff}_{ab} may be determined from the right hand side of Eq. (2.19a).

Zeroth order (2.20a) is just vacuum GR, which has no intrinsic scale. As is very common in numerical relativity simulations, the coordinates used in the simulation are dimensionless and in units of the total ADM mass, $X^a = x^a/(GM)$. This means that ∇ may be non-dimensionalized by pulling out a factor of $(GM)^{-1}$, Riemann may be non-dimensionalized by pulling out a factor of $(GM)^{-2}$, etc.

Meanwhile, the new length scale and coupling parameter ℓ enters at first order. If we non-dimensionalize the derivative operator and curvature tensors in Eq. (2.20b), we will find

$$(GM)^{-2}\Box^{(0)}\vartheta^{(1)} = \frac{m_{\text{pl}}}{8}\ell^2(GM)^{-4}[^*RR]^{(0)}. \qquad (2.21)$$

We therefore define the dimensionless scalar field Ψ via

$$\vartheta^{(1)} = \frac{m_{\text{pl}}}{8}\left(\frac{\ell}{GM}\right)^2 \Psi. \qquad (2.22)$$

Then Ψ will satisfy

$$\Box^{(0)}\Psi = [^*RR]^{(0)}. \qquad (2.23)$$

Thus the analytic dependence of $\vartheta^{(1)}$ on (ℓ/GM) has been extracted. The solution Ψ can later be scaled to reconstruct $\vartheta^{(1)}$ for any allowable value of (ℓ/GM).

All of the results that we present will be given in terms of powers of the dimensionless coupling (ℓ/GM). We will also compare to known post-Newtonian results [211], that were presented in terms of α_4^{YSYT}. To perform the comparison, we use the conversion given in Eq. (2.4).

Finally, though we do not address $O(\varepsilon^2)$ simulations in this paper, we should still study how $h^{(2)}$ scales with ℓ and (GM). Since the perturbative scheme preserves the units of length of fields, $[h^{(k)}] = [g] = [L]^0$ is already dimensionless; however, it still depends on (ℓ/GM) in a specific way. When we move to units in which we measure lengths and times in units of (GM), we find it is appropriate to define a scaled metric deformation Υ via

$$h_{ab}^{(2)} \equiv \left(\frac{\ell}{GM}\right)^4 \Upsilon_{ab}. \tag{2.24}$$

Then this dimensionless quantity Υ will satisfy an equation that is schematically

$$\nabla^2 \Upsilon + \text{L.O.T.} \sim (\nabla\Psi)^2 + (\nabla\Psi)(\nabla R) + (\nabla^2\Psi)R, \tag{2.25}$$

where L.O.T. stands for lower order terms, and all derivatives and curvatures are $O(\varepsilon^0)$ dimensionless quantities.

Numerical scheme

For the order ε^1 part of the order reduction scheme, our overall goal is to solve Eq. (2.23) on a dynamical background metric. We co-evolve the metric and the scalar field, where Eq. (2.23) is driven by Eq. (2.20a). The whole system is simulated using the Spectral Einstein Code (SpEC) [198], which uses the generalized harmonic formulation of general relativity in a first-order, constraint-damping system [121] in order to ensure well-posedness and hence numerical stability. We have added a scalar field module that is similarly a first-order, constraint-damping system, following [105], as outlined in App. 2.A.

The code uses pseudospectral methods on an adaptively-refined grid [128, 189], and thus numerical convergence with resolution of both the metric variables and the scalar field is exponential. We demonstrate the numerical convergence of the scalar field in App. 2.A.

The initial data for the binary black hole background is a superposition of two Kerr-Schild black holes with a Gaussian roll-off of the conformal factor around each black hole [129]. The initial data for the scalar field is similarly given by a superposition

of approximate dCS solutions around isolated black holes, and is given in more detail in Sec. 2.3.

The metric equations are evolved in a damped harmonic gauge [190, 120], with excision boundaries just inside the apparent horizons [104, 177], and minimally-reflective, constraint-preserving boundary conditions on the outer boundary [172]. The scalar field system, meanwhile, uses purely outgoing boundary conditions modified to reduce the influx of constraint violations into the computational domain [105].

The Pontryagin density source term $^*RR$ is computed throughout the simulation in a 3+1 split from the available spatial quantities as outlined in App. 2.B.

2.3 Results

Background: Phenomenology of binary black hole inspirals in dCS

To give the proper context for our numerical results, we first review the previously-known phenomenology relevant to this problem. Analytical and numerical results are known for isolated black holes in the decoupling limit, and analytical results are known for the binary black hole problem in the decoupling limit and at slow velocities ($v/c \ll 1$).

Any spherically-symmetric metric will have vanishing Pontryagin density.[2] Thus the Schwarzschild solution with vanishing scalar field is already a solution to the "full" dCS system. An isolated spinning black hole in dCS, however, is not given by the Kerr solution of GR [61, 214, 116, 210]; the scalar field is sourced, and the metric acquires corrections. Analytical results for the leading-order, small-coupling corrections to the Kerr metric have been found in the slow-rotation approximation ($a \ll M$) [214, 116, 210, 131]. Additionally, numerical results have been found for the scalar field for general rotation [117, 183]. The leading-order correction to Kerr is dipolar scalar hair, while the scalar monopole vanishes. This vanishing scalar monopole means that scalar dipole radiation is heavily suppressed in dCS. At a large radius away from an isolated black hole labeled by A, the dipolar scalar field goes

---

[2]This is straightforward to verify with a computer algebra system, using the canonical form for a spherically symmetric metric, $ds^2 = -e^{2\alpha(t,r)}dt^2 + e^{2\beta(t,r)}dr^2 + r^2 d\Omega^2$. Since it is true in this coordinate system, it is true in general. This is also proven in App. A of [97] following a tensorial approach. Finally, one can appeal to a symmetry argument. If the metric is invariant under an $O(3)$ isometry, then the curvature tensor and $^*RR$, being tensorial objects built only from g, must also be invariant under this symmetry. Therefore, $^*RR$ must be a constant on each 2-sphere. The group $O(3)$ also contains the reflection symmetry, sending points to their antipodes. The metric is invariant under this reflection, but $^*RR$ must flip sign, as it is a pseudo-scalar. But then we must have $^*RR = -^*RR$, so $^*RR = 0$.

as

$$\vartheta_A^{(1)} = \frac{\mu_A^i n_A^i}{R_A^2},$$ (2.26)

where R_A is the distance from black hole A, n_A^i is the spatial unit vector pointing away from BH A, and μ_A^i is the scalar dipole moment of the BH. This scalar dipole moment is given by [212]

$$\mu_A^i = -\frac{5}{2} \frac{m_{\mathrm{pl}} \ell^2}{8} \chi_A^i,$$ (2.27)

where χ_A^i is the dimensionless spin vector of black hole A, $\chi_A^i = J_A^i / GM_A^2$ (this factor of G in the denominator arises from our usage of natural units, where angular momentum is dimensionless, $[J] = [L]^0$, in units of $\hbar$).

The dCS binary inspiral problem in the post-Newtonian regime ($v \ll c$) was first treated by Yagi et al. [212]. When two spinning BHs with scalar dipole hair are placed in proximity with each other, the hair is responsible for a number of effects. First, there is a correction to the binding energy due to the dipole-dipole interaction. Second, as the BHs orbit each other, the net *quadrupole* of the binary system has a time derivative on the orbital timescale. The binary's combined dipole moment is also time-varying, but only on the spin-precession timescale, so it is heavily suppressed. Thus in the far zone of the binary, the scalar field exhibits predominantly quadrupole and higher radiation, and no $l = 0$ monopole radiation.

The dominant far-zone multipole moments for the scalar field have $|m| = l - 1$ with $l \geq 2$ and the $l = 1$ modes radiate on the spin-precession timescale. To make comparing to PN simpler, we are simulating aligned-spin systems, so the $l = 1$ mode will in fact be non-radiative at early times. Yagi et al. [212] gave expressions for the scalar field $\vartheta^{(1)}$ due to spinning and non-spinning binaries, presented in terms of symmetric tracefree (STF) tensors. In most numerical relativity work, however, we decompose fields into spherical harmonics,

$$\vartheta^{(1)\mathrm{FZ}} = \sum_{lm} Y_{lm}(\theta, \varphi) \vartheta_{l,m}^{(1)\mathrm{FZ}}.$$ (2.28)

Using [52], we convert the STF expressions from [212, 185] into spherical harmonics at extraction radius R for a *spin-aligned* binary, when the post-Newtonian

Name	$\frac{m_1}{m_2}$	χ_1	χ_2	$\Omega_0(GM)$	$\frac{t_{\text{Merger}}}{GM}$	$\frac{t_{\text{RD}}}{GM}$	$\frac{m_{\text{Final}}}{M}$	χ_{Final}
Spin 0.3	3.0	0.30	0.30	0.0163	5841	764	0.96	0.68
Spin 0.1	3.0	0.10	0.10	0.0164	5452	817	0.97	0.59
Spin 0.0	3.0	0.00	0.00	0.0190	3457	697	0.97	0.54

Table 2.1: Parameters of numerical runs. Each run was performed at low, medium, and high resolutions. We give the mass ratio m_1/m_2 where the subscripts label the black holes. All of the spins are aligned in the z-direction, so we give the $\hat{z}$ component of the dimensionless spin vector $\vec{\chi}_A$ for each black hole. The initial orbital frequency is Ω_0. Initial orbital parameters were chosen so that the eccentricity was below 5×10^{-4}. The time simulated to merger is t_{Merger}, and the amount of ringdown simulated thereafter is t_{RD}, both in units of GM. The final mass of the remnant black hole is m_{Final}, in units of M. The remnant spins are in the z-direction, and thus we give the $\hat{z}$ component χ_{Final} of the dimensionless spin.

approximation is valid (the early inspiral), giving

$$
\vartheta_{1,0}^{(1)\text{FZ}} = \sqrt{\frac{4\pi}{3}} \frac{1}{R^2} (\mu_1 + \mu_2),
$$

(2.29)

$$
\vartheta_{2,1}^{(1)\text{FZ}} = \sqrt{\frac{2\pi}{15}} \frac{1}{R} \left(\mu_1 \frac{m_2}{M} - \mu_2 \frac{m_1}{M} \right) \omega (GM\omega)^{1/3} e^{-i\phi},
$$

$$
\vartheta_{3,2}^{(1)\text{FZ}} = \sqrt{\frac{32\pi}{105}} \frac{1}{R} \left(\mu_1 \frac{m_2^2}{M^2} + \mu_2 \frac{m_1^2}{M^2} \right) \omega (GM\omega)^{2/3} i e^{-2i\phi}.
$$

Here $\phi = \phi(t)$ is the orbital phase, $\omega = \omega(t) = \dot{\phi}$ is the orbital frequency, m_A is the mass of each black hole, $M = m_1 + m_2$ is the total mass,[3] and μ_A is the z component (the only component since this calculation is for a spin-aligned binary) of the scalar dipole moment from Eq. (2.27). Note that the $(1,0)$ mode is time-independent (and hence non-radiative), since we are focusing on spin-aligned systems.

The behavior of the scalar field during the late inspiral and merger was previously unknown and is part of the motivation for the present numerical study.

Scalar field waveforms

We performed three numerical simulations in this formalism, each at low, medium, and high numerical resolutions, with parameters given by Table 2.1. We chose three values for the BHs' dimensionless spins of 0.0, 0.1, and 0.3, to qualitatively see the

---

[3] In PN literature, m is often used as the total mass. We use M here in order to be consistent with numerical relativity literature.

effect of spin on the physics, and to allow for comparison with analytical calculations. While SpEC can simulate very high spins [177], the analytics we compare against use the small-spin expansion and stop at linear order in spin. Therefore the $O(\chi^2)$ errors should be at most $\sim 30\%$ of the $O(\chi)$ effects we compare against. Similarly, while modeling spin precession is possible [148], it is not the focus of this study, and thus we have eliminated this complication by aligning all of the spins with the orbital angular momentum.

As mentioned in Sec. 2.3, the scalar field around an isolated, slowly spinning black hole in dCS is approximately a dipole. We use this analytic approximation as the basis for our initial data, as mentioned in Sec. 2.2. The initial scalar field is a superposition of two slow-rotation dipole solutions (since all of the dimensionless spins are ≤ 0.3), one around each black hole. We apply a boost to account for the initial velocity of each black hole. As our scalar field evolution system is first-order (see App. 2.A), we also initialize the variables corresponding to the spatial and time derivatives of Ψ to the analytical derivatives of the approximate dipole solution. For the non-spinning simulation, we set the initial value of Ψ and its derivatives to zero.

We plot mode-decomposed waveforms extracted from the highest resolution simulations of the three simulations in Figs. 2.1, 2.2, and 2.3. Each figure shows the $(l = 2, m = 2)$ mode of the Newman-Penrose quantity Ψ_4 decomposed into spin-weight -2 spherical harmonics, and the dominant $(l, m = l - 1)$ modes of the scalar $\vartheta^{(1)}$ for $l = 1, 2, 3$, along with the PN comparisons from Eq. (2.29).

We immediately see that at early times, there is good qualitative agreement between the numerical waveforms and the PN predictions, with the $(l = 2, m = 1)$ mode dominating, as expected. In the PN formulas of Eq. (2.29), we used the instantaneous coordinate orbital frequency and phase calculated from the black hole trajectories for ω and ϕ. Since the starting phase is arbitrary, we perform a phase alignment (by eye) between the numerical results and the PN waveforms.

As expected, because the spins are not precessing, there is no dipole radiation at early times. The offset away from zero seen in the $(l = 1, m = 0)$ panel of Fig. 2.1 is a real physical effect: it is due to the combined dipole moments of the two individual black holes and their orbital angular momentum. After merger, the $l = 1$ moment settles down to a new non-zero value (below the resolution of this figure) determined by the spin of the final black hole, again via Eq. (2.27). In between, there is a burst of scalar dipole radiation. This is a newly discovered phenomenon that could not have been computed with analytic post-Newtonian calculations. Scalar monopole
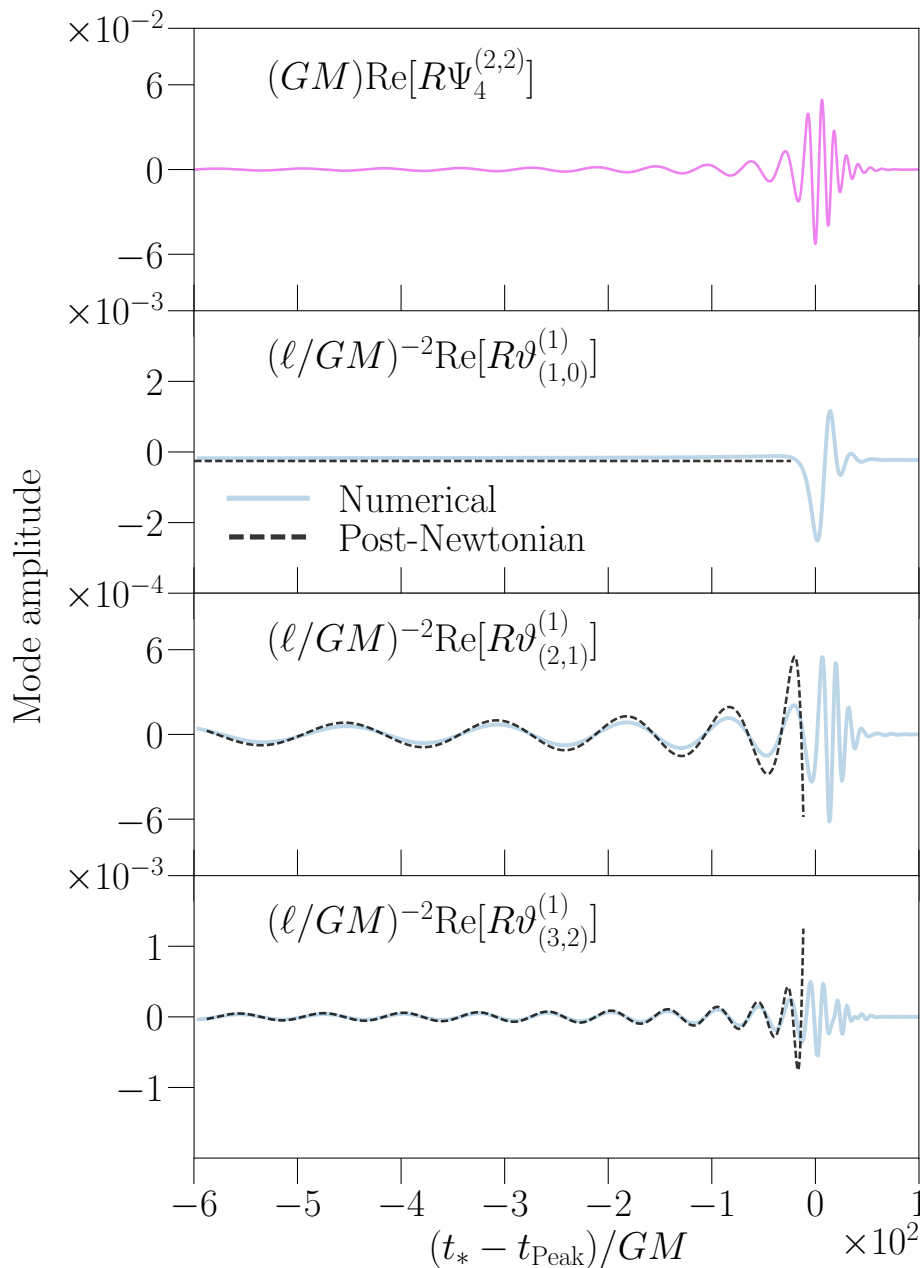
Figure 2.1: Waveforms for simulation with spin $\chi = 0.3\hat{z}$ on each black hole. The top panel shows the real part of the $(l = 2, m = 2)$ mode of the spin-weight -2 spherical harmonic decomposition of the Newman-Penrose scalar Ψ_4, extracted at a (large enough) radius of $R = 290\,GM$. This serves as a proxy for the gravitational waveform. The lower three panels show the $(1,0)$, $(2,1)$ and $(3,2)$ scalar spherical harmonic modes of the scalar $\vartheta^{(1)}$ at $R = 300\,GM$. The numerical values from the simulation are shown by the solid blue curves, while the PN calculations are shown by the dashed black curves. The time axis corresponds to the approximate retarded time (simulation time minus extraction radius) minus the merger time, which is computed as the time of peak amplitude of $\Psi_4^{(2,2)}$.
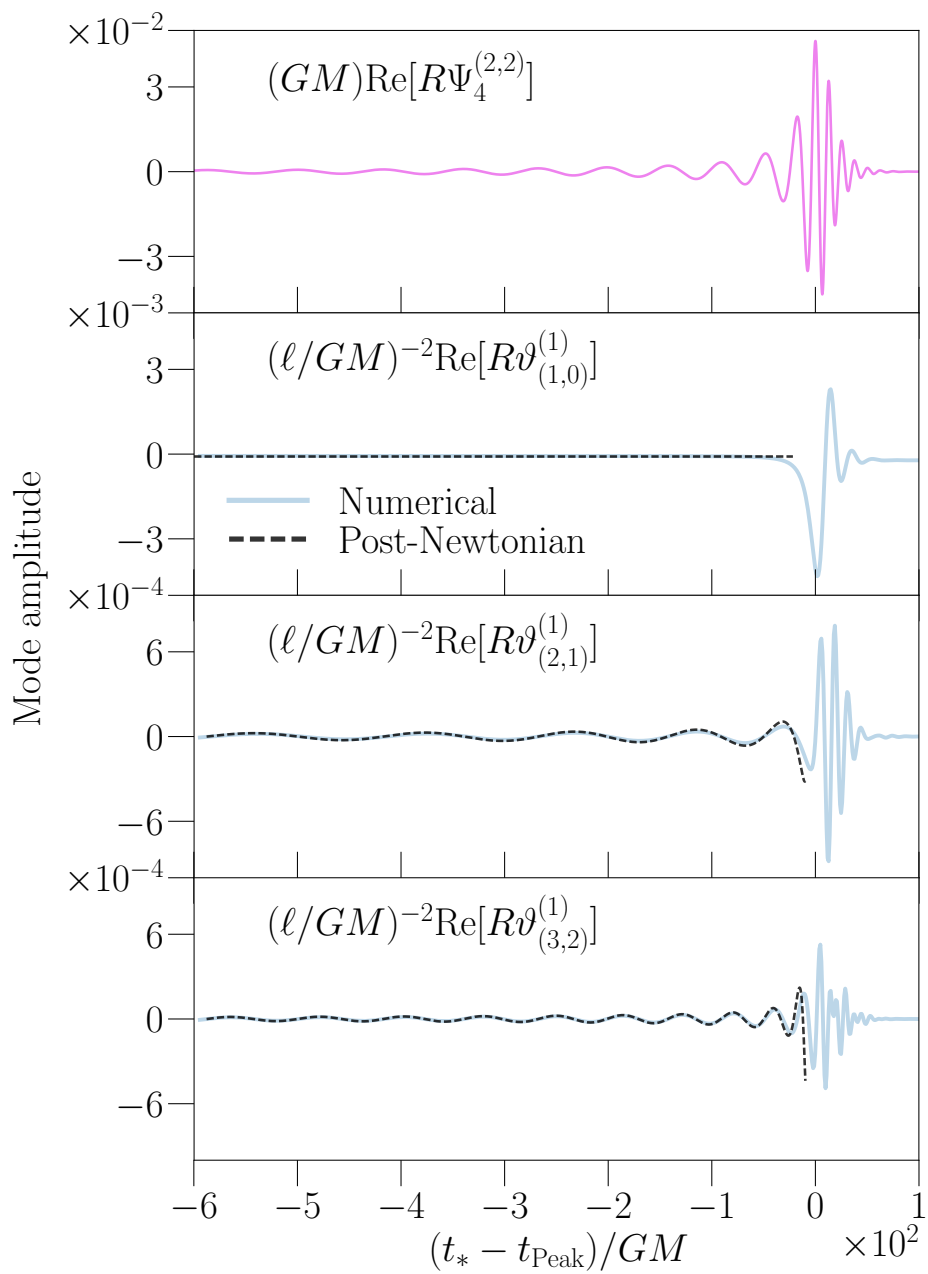
Figure 2.2: Similar to Fig. 2.1, but with spin $\chi = 0.1\hat{z}$ on each BH.
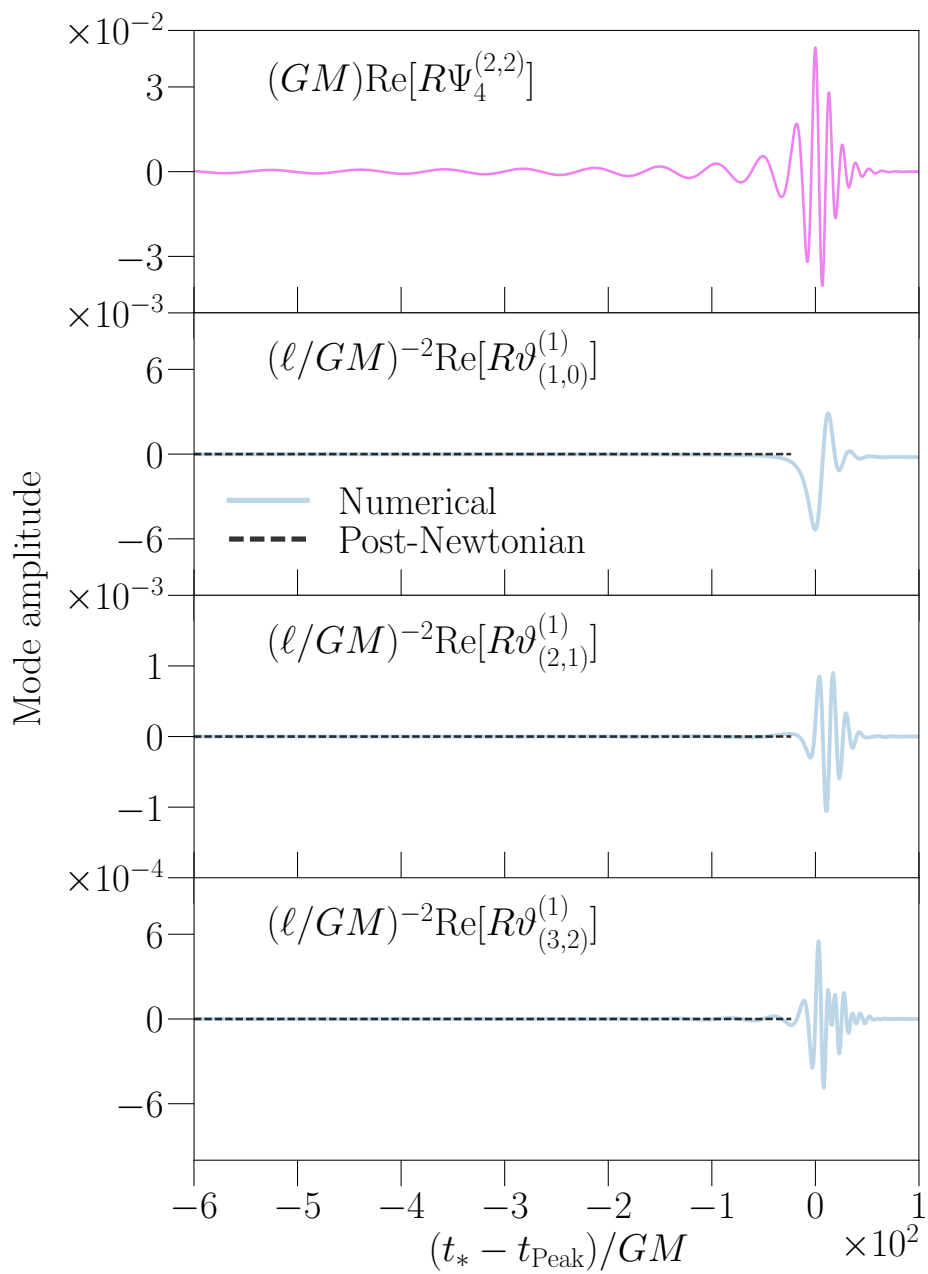
Figure 2.3: Similar to Fig. 2.1, but with no spin on either BH.

radiation, meanwhile, is consistent with zero within the numerical errors of the simulation.

Energy fluxes

Having solved for the scalar field $\vartheta^{(1)}$, we can evaluate physical quantities such as its stress-energy tensor, Eq. (2.11). From $T_{ab}^{(\vartheta)}$, we can compute the energy flux through some 2-sphere S_R^2 at coordinate radius R via

$$\dot{E}^{(\vartheta)} = \int_{S_R^2} T_{ab}^{(\vartheta)} n^a dS^b \,. \tag{2.30}$$

Here n^a is the timelike unit normal to the spatial slice, and dS^b is the proper area element of S_R^2, i.e. $dS^b = N^b \sqrt{\gamma} dA$, where N^b is the spacelike unit normal to S_R^2, γ is the determinant of the induced 2-metric, and dA is the coordinate area element.

Like the metric and scalar field, we similarly expand $T_{ab}^{(\vartheta)}$ and $\dot{E}^{(\vartheta)}$ in powers of ε,

$$T_{ab}^{(\vartheta)} = \sum_{k=0}^{\infty} \varepsilon^k T_{ab}^{(\vartheta,k)} \,, \qquad\qquad \dot{E}^{(\vartheta)} = \sum_{k=0}^{\infty} \varepsilon^k \dot{E}^{(\vartheta,k)} \,, \tag{2.31}$$

where each $\dot{E}^{(\vartheta,k)}$ includes the appropriate orders of both the scalar field and metric. Since $\vartheta^{(0)} = 0$ and $T_{ab}^{(\vartheta)}$ is quadratic in ϑ, we have $T_{ab}^{(\vartheta,0)} = T_{ab}^{(\vartheta,1)} = 0$, and similarly $\dot{E}^{(\vartheta,0)} = \dot{E}^{(\vartheta,1)} = 0$. The first non-vanishing order is $T_{ab}^{(\vartheta,2)}$, which is given by

$$T_{ab}^{(\vartheta,2)} = \nabla_a \vartheta^{(1)} \nabla_b \vartheta^{(1)} - \frac{1}{2} g_{ab} \nabla_c \vartheta^{(1)} \nabla^c \vartheta^{(1)} \,. \tag{2.32}$$

Using the results of the simulations, we compute $T_{ab} n^a$, interpolate it onto surfaces of fixed coordinate radius R, compute $T_{ai} n^a N^i$ by contracting with the normal, and perform spectral integration with the induced area element to obtain $\dot{E}^{(\vartheta,2)}$. That is, we compute

$$\dot{E}^{(\vartheta,2)}(R) = \int_{S_R^2} T_{ai}^{(\vartheta,2)} n^a N^i \sqrt{\gamma} dA \,. \tag{2.33}$$

We also compute the energy flux at order $(\ell/GM)^0$, which for vanishing $\vartheta^{(0)}$ consists purely of the background gravitational energy flux, as (c.f. [175])

$$\dot{E}^{(0)} = \lim_{R \to \infty} \frac{R^2}{16\pi G} \int_{S_R^2} \left| \int_{-\infty}^{t} \Psi_4 dt' \right|^2 d\Omega \,, \tag{2.34}$$

where numerically we set the lower bound of the time integral to the start of the simulation, assuming there was comparatively little radiation before the start.
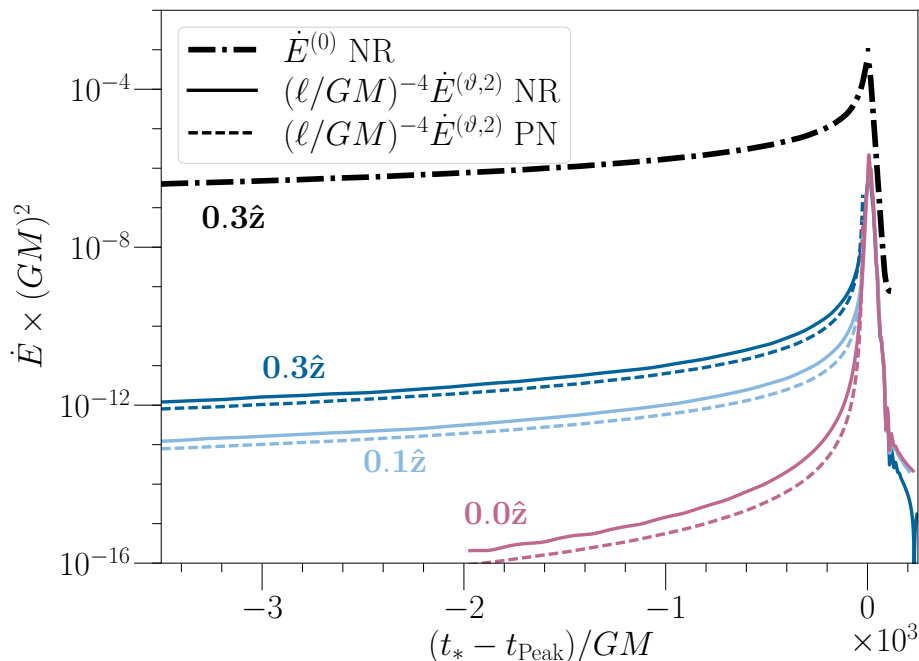
Figure 2.4: Order $(\ell/GM)^0$ and $(\ell/GM)^4$ energy fluxes, as a function of time, aligned at the peak of $\Psi_4^{(2,2)}$. We plot the order $(\ell/GM)^4$ numerical scalar energy flux extracted at $R = 300\,GM$ [colored solid lines; Eq. (2.33)] and the corresponding post-Newtonian approximation [dashed lines, Eqs. (2.35) and (2.36)], for the highest resolution of each simulation. We also plot the energy flux at order $(\ell/GM)^0$, which consists solely of the background gravitational radiation [Eq. (2.34)], for the spin 0.3 simulation (dot-dashed black line); the GW flux is the same order of magnitude for all three spin configurations. The $O(1)$ ratio between PN and numerics is likely due to the PN fluxes only including $l = 2$, whereas numerical quantities are computed with all modes up to $l = 8$.

We plot the numerical values of $\dot{E}^{(\vartheta,2)}(R)$ and $\dot{E}^{(0)}(R)$ in Fig. 2.4, keeping (spin-weighted) spherical harmonics up through $l = 8$. We check for the convergence of the flux quantities with increasing extraction radius, and present the results at $R = 300\,GM$, which agree with the results at $R = 200\,GM$.

In Fig. 2.4 we also plot a post-Newtonian approximation to $\dot{E}^{(\vartheta,2)}$. This is computed using the far-zone PN solution for $\vartheta^{(1)}$ from [212], which only includes the $l = 2$ quadrupole radiation. We impose circular orbits and aligned spins, convert to our conventions via Eq. (2.4), and re-insert the appropriate factors of G. The result for at least one non-zero spin is

$$\dot{E}_{\text{PN}}^{(\vartheta,2)} = -\frac{5}{1536G}\left(\frac{\ell}{GM}\right)^4 \left(\tfrac{m_2}{M}\chi_1 - \tfrac{m_1}{M}\chi_2\right)^2 (GM\omega)^{14/3}, \qquad (2.35)$$

and for two non-spinning black holes,

$$\dot{E}_{\text{PN}}^{(\vartheta,2)} = -\frac{2}{15G}\left(\frac{\ell}{GM}\right)^4 \eta^2 \frac{\delta m^2}{M^2}(GM\omega)^8 \,. \tag{2.36}$$

In these expressions, χ_A is the dimensionless spin of black hole A, $\eta = m_1 m_2/M^2$ is the symmetric mass ratio, and $\delta m = m_1 - m_2$ is the mass difference.

Although the gravitational flux at order $(\ell/GM)^0$ is by far the largest energy flux, the scalar field flux at order $(\ell/GM)^4$ sharply increases before merger. The spin contributions are dominant, as the scalar flux for the spin-0 simulation is comparatively small until the merger, when nonlinearities become very important. At early times, our fully numerical results qualitatively agree with the PN results of [212], validating our and their calculations. We expect the $O(1)$ ratio between PN and full numerics in Fig. 2.4 stems from the PN expressions (2.35), (2.36) only including $l = 2$, whereas our numerics include all modes up through $l = 8$.

Regime of validity

Since this method is perturbative, we expect that it breaks down, or, becomes invalid, at some point. There are two types of breakdown. First, at every instant of time, there is the question of whether the series converges. We expect that the series should only converge when $\ell \ll GM$, and we assess this in Sec. 2.3. Second, over much longer times, there will be a secular drift between the perturbative solution and the "true" solution, so that the two solutions become out of phase. We assess the dephasing below in Sec. 2.3.

Instantaneous validity

The perturbative scheme is valid pointwise at every instant in time if the series for the metric (2.12a) and scalar (2.12b) are convergent. Roughly, we can assess this by comparing the magnitudes of successive terms in the series. As shown in Sec. 2.2, up through order ε^2, the metric and scalar are expanded as

$$g_{ab} = g_{ab}^{(0)} + \varepsilon^2 h_{ab}^{(2)} + O(\varepsilon^3), \tag{2.37a}$$

$$\vartheta = \varepsilon\vartheta^{(1)} + O(\varepsilon^3) \,. \tag{2.37b}$$

Thus we cannot assess the convergence of ϑ without going to $O(\varepsilon^3)$, but at $O(\varepsilon^2)$ we can compare the magnitudes of $g_{ab}^{(0)}$ and $h_{ab}^{(2)}$. A rough condition for convergence is that

$$\left\|h_{ab}^{(2)}\right\| \lesssim \left\|g_{ab}^{(0)}\right\|, \tag{2.38}$$
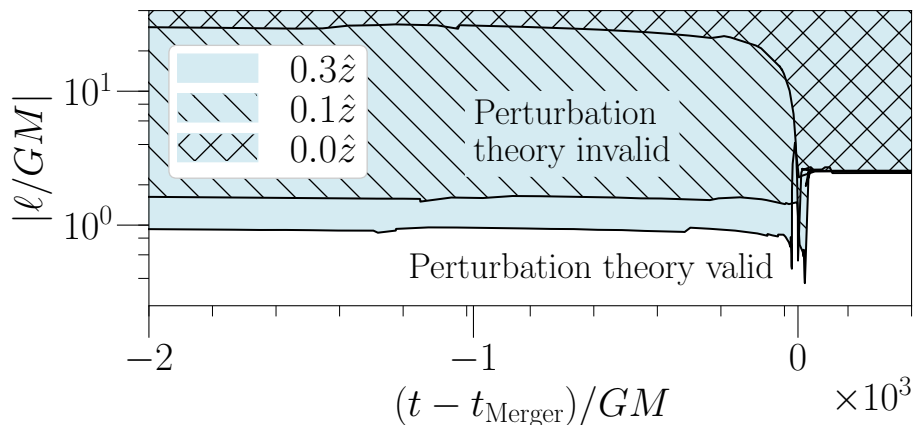
Figure 2.5: Estimate of instantaneous regime of validity of perturbation theory for each of the binary black hole configurations in this study, as a function of coordinate time relative to merger. Perturbation theory in powers of $|\ell/GM|$ is invalid in the shaded region above each curve. The maximum allowed value of $|\ell/GM|$ comes from Eq. (2.42). The jaggedness at early times is due to p-refinement of the spectral subdomains causing points to cross the mask outside of apparent horizons. The jump near time of merger is due to formation of the common horizon. After merger, the remnant black hole governs $|\ell/GM|_{\text{max}}$. Since all simulations have comparable remnant spins (see Table 2.1), the final values of valid $|\ell/GM|$ are similar.

where $\|\cdot\|$ is an L^2 norm.

The magnitude of $h_{ab}^{(2)}$ depends on the strength of the coupling parameter ℓ, as discussed in Sec. 2.2, via $h_{ab}^{(2)} = (\ell/GM)^4 \Upsilon_{ab}$, where Υ_{ab} is independent of ℓ. Thus we translate Eq. (2.38) into a condition on the maximum allowed value of ℓ/GM,

$$\left| \frac{\ell}{GM} \right|_{\text{max}} \sim C \left(\frac{\left\| g_{ab}^{(0)} \right\|}{\| \Upsilon_{ab} \|} \right)_{\text{min}}^{1/4}, \tag{2.39}$$

where C is some factor of order unity, and on the right-hand side, the ratio is evaluated pointwise, and then the minimum is taken over the domain outside of the apparent horizons, at each coordinate time. At values of ℓ/GM larger than this estimate, we expect the perturbative approach fails to converge somewhere in the spacetime.

In these order ε^1 simulations, we have not simulated Υ_{ab}. We can, however, make scaling estimates from its schematic equation of motion, Eq. (2.25). The source term $m_{\text{pl}} \ell^2 C_{ab}^{(1)}$ should be of the same order of magnitude as $T_{ab}^{(2)}$ (which we do

compute in the simulations), so, to within an order of magnitude, we estimate

$$\Box^{(0)}\Upsilon \sim T_{ab}[\Psi], \tag{2.40}$$

$$\frac{1}{L^2}\|\Upsilon_{ab}^{(2)}\| \sim \|T_{ab}[\Psi]\|. \tag{2.41}$$

Here L is a characteristic curvature length scale, and $T_{ab}[\Psi]$ is shorthand for the "stress-energy" $T_{ab}[\Psi] = \nabla_a\Psi\nabla_b\Psi - \frac{1}{2}g_{ab}(\nabla\Psi)^2$. Therefore, we estimate the allowed value for ℓ/GM as

$$\left|\frac{\ell}{GM}\right|_{\max} \sim CL^{-1/2}\left(\frac{\left\|g_{ab}^{(0)}\right\|}{\|T_{ab}[\Psi]\|}\right)_{\min}^{1/4}. \tag{2.42}$$

We plot this estimate in Fig. 2.5 for each of the spin configurations considered in this study. During inspiral, the curvature is highest around the smaller black hole, so we let $L = \min(Gm_1, Gm_2)$. After merger, we let $L = Gm_{\text{Final}}$ (see Table 2.1 for values).

We can compare our estimates for the regime of validity $|\ell/GM|_{\max}$ to those computed in Stein [184]. Stein computed $|\ell/Gm|_{\max}$ of a stationary, isolated black hole as a function of χ of the body, using methods that are independent of ours. At late times, we find direct agreement, at the 5% level, by setting $C = (32)^{1/4} \approx 2.38$. At early times, after including a factor of M/m_2 to convert from $|\ell/GM|$ to $|\ell/Gm_2|$, we again find agreement. At early times, the low-spin simulation has a very large regime of validity, because the Pontryagin density is small, and hence Chern-Simons effects are also small. However, approaching the time of merger, orbital motion and nonlinearities source enough energy density in the scalar field to restrict the regime of validity of $|\ell/GM|$ to order unity.

Secular validity (dephasing)

The true physical system at $\varepsilon > 0$ radiates energy more quickly than the GR-only ($\varepsilon = 0$) solution that we are using as the background for perturbation theory. As a result, the true solution will inspiral more quickly, so the orbital phase will have a *secularly* growing deviation away from the background. A post-Newtonian scaling estimate (see below) says that the standard solution will break down over a secular timescale of order $T_{\text{sec}} \sim T_{\text{RR}}^{\text{GR}}(\ell/GM)^{-2}v^{-2}$, where $T_{\text{RR}}^{\text{GR}}$ is the radiation-reaction timescale in GR. This scaling $(\ell/GM)^{-2}$ is characteristic of singular perturbation theory [42, 66, 89].

If the length of a detected gravitational waveform is long compared to the secular breakdown time, then we will need a method to extend the secular regime of validity of the calculation—for example, multiple-scale analysis (MSA) [42] or the dynamical renormalization group [66, 89]. We save this issue for future work. Here, we will estimate the dephasing time (secular breakdown time).

Let us focus on quasi-circular, adiabatic inspirals. Similarly to the scalar field and metric variables in Eqs. (2.12a) and (2.12b), we can expand the accumulated orbital phase $\phi(t)$ and the orbital frequency $\omega(t) = \dot{\phi}(t)$ of the binary in powers of ε,

$$\phi = \phi^{(0)} + \varepsilon\phi^{(1)} + \varepsilon^2\phi^{(2)} + O(\varepsilon^3), \tag{2.43}$$

$$\omega = \omega^{(0)} + \varepsilon\omega^{(1)} + \varepsilon^2\omega^{(2)} + O(\varepsilon^3), \tag{2.44}$$

where $\phi^{(0)}$ corresponds to the phase of the binary in pure GR, and $\phi^{(1)}$ contains the dCS corrections at order ε^1 and so on. Since the metric deformation at $O(\varepsilon^1)$ vanishes, the phase correction at $O(\varepsilon^1)$ also vanishes, $\phi^{(1)} = 0 = \omega^{(1)}$. The first non-vanishing orbital phase correction is

$$\Delta\phi \equiv \phi^{(2)}. \tag{2.45}$$

We can use $\Delta\phi$ to assess the secular regime of validity, and in Sec. 2.3 we will also use it to assess the detectability of dynamical Chern-Simons.

We do not have $\Delta\phi$ directly from the simulation, as we do not evolve the ε^2 system. However, we can estimate it from previously-known analytical results combined with numerical quantities available during the simulation.

Consider the local-in-time expansion of the orbital phase correction $\Delta\phi$ around any "alignment time" t_0,

$$\Delta\phi(t) = \Delta\phi(t_0) + (t - t_0)\frac{d\Delta\phi}{dt}\Big|_{t=t_0} \tag{2.46}$$

$$+ \frac{1}{2}(t - t_0)^2\frac{d^2\Delta\phi}{dt^2}\Big|_{t=t_0} + O(t - t_0)^3,$$

$$\Delta\phi(t) = \Delta\phi(t_0) + (t - t_0)\omega^{(2)}(t_0) \tag{2.47}$$

$$+ \frac{1}{2}(t - t_0)^2\frac{d\omega^{(2)}}{dt}\Big|_{t=t_0} + O(t - t_0)^3.$$

If our simulation had started at reference time t_0, then we would have $\Delta\phi(t_0) = 0$. The linear piece $(t - t_0)\omega^{(2)}(t_0)$ corresponds to a perturbative, instantaneous frequency shift, which is completely degenerate with a renormalization of the physical mass

$M(\varepsilon)$ in terms of the "bare" mass $M(\varepsilon = 0)$. Therefore, the constant and linear pieces of this expansion are not observable.

However, the curvature $\frac{1}{2}(t - t_0)^2 d\omega^{(2)}/dt|_{t=t_0}$ cannot be redefined or scaled away. Therefore, within a sufficiently short window of time around the alignment time t_0, the deformation to the orbital phase is given by

$$\Delta\phi = \frac{1}{2}(t - t_0)^2 \frac{d\omega^{(2)}}{dt}\bigg|_{t=t_0} + O((t - t_0)^3). \tag{2.48}$$

We use this to define the perturbative secular time $T_{\text{sec}}(t_0)$ at any instant t_0 via

$$1 \approx \Delta\phi = \frac{1}{2}T_{\text{sec}}^2 \frac{d\omega^{(2)}}{dt}\bigg|_{t=t_0}, \tag{2.49}$$

$$T_{\text{sec}} \equiv \left(\frac{1}{2}\frac{d\omega^{(2)}}{dt}\bigg|_{t=t_0}\right)^{-1/2}, \tag{2.50}$$

roughly the time to dephase by order one radian.

Thus we need to estimate $d\omega^{(2)}/dt$ from our simulation. Under the assumption of quasi-circular, adiabatic orbits, there is a one-to-one correspondence between the orbital frequency ω and orbital energy E. In other words, there exists a function of one variable, $E(\omega)$ or $\omega(E)$. Therefore, from the chain rule, we can find the time derivative

$$\frac{d\omega}{dt} = \frac{d\omega}{dE}\frac{dE}{dt} = \frac{dE/dt}{dE/d\omega}. \tag{2.51}$$

This depends on the conservative sector through the frequency-dependence of orbital energy, $dE/d\omega$, and on the dissipative sector through the radiated power, dE/dt. Just as with the frequency, we expand the orbital energy in powers of ε,

$$E = E^{(0)} + \varepsilon E^{(1)} + \varepsilon^2 E^{(2)} + O(\varepsilon^3). \tag{2.52}$$

We can then use this to expand Eq. (2.51) in powers of ε. The $O(\varepsilon^2)$ piece is given by

$$\frac{d\omega^{(2)}}{dt} = \frac{d\omega^{(0)}}{dt}\left[\frac{dE^{(2)}/dt}{dE^{(0)}/dt} - \frac{dE^{(2)}/d\omega}{dE^{(0)}/d\omega}\right]. \tag{2.53}$$

The prefactor $d\omega^{(0)}/dt$ is simply the background (GR) evolution of the orbital frequency. The first term in square brackets in Eq. (2.53) comes from the dissipative sector of the dynamics, since it depends on the radiated power $dE^{(2)}/dt$. The second term, meanwhile, comes from the conservative sector, as it depends on the

correction to the orbital energy $E^{(2)}(\omega)$. Both of the factors in square brackets scale as $(\ell/GM)^4 v^4$ [212, 211] for BBHs with spin. Plugging this scaling into Eq. (2.50) recovers $T_{\text{sec}} \sim T_{\text{RR}}^{\text{GR}}(\ell/GM)^{-2} v^{-2}$.

We find it useful to rewrite $dE^{(0)}/d\omega$ in the second term using the chain rule (2.51) to give

$$\frac{d\omega^{(2)}}{dt} = \frac{d\omega^{(0)}/dt}{dE^{(0)}/dt} \left[\frac{dE^{(2)}}{dt} - \frac{d\omega^{(0)}}{dt} \frac{dE^{(2)}}{d\omega} \right] . \tag{2.54}$$

Now we can discuss how to evaluate these factors from our numerical simulation and previously-known analytical results. The background energy flux $dE^{(0)}/dt$ comes from the numerical simulation via Eq. (2.34). We also have the background frequency evolution $d\omega^{(0)}/dt$ from the numerical simulation, via a time derivative of the coordinate orbital frequency.

The two $O(\varepsilon^2)$ quantities require approximations. In the dissipative sector, there are two contributions to $dE^{(2)}/dt$: the first from scalar radiation, and the second from gravitational radiation. We expect these to be the same order of magnitude. Since we do not have access to the gravitational radiation, we approximate that to within an order of magnitude,

$$\dot{E}^{(2)} \approx \dot{E}^{(\vartheta,2)}, \tag{2.55}$$

where $\dot{E}^{(\vartheta,2)}$ was given in Eq. (2.33). This is further justified during the inspiral, where the $O(\varepsilon^2)$ dissipative correction due to gravitational waves is higher-PN than the scalar radiation [212].

In the conservative sector, we can approximate $E^{(2)}(\omega)$ from a post-Newtonian calculation [211, 185]. The (PN-approximate) correction to the orbital energy $E^{(2)}$ also has two pieces: the scalar binding energy and the metric-deformation binding energy. Again we are going to make an approximation and ignore the metric deformation piece, approximating

$$E^{(2)}(\omega) \approx E_{\text{DD}}^{(\vartheta,2)}, \tag{2.56}$$

where $E_{\text{DD}}^{(\vartheta)}$ is the scalar dipole-dipole interaction. After accounting for a missing minus sign in [211, 185], this is given by

$$E_{\text{DD}}^{(\vartheta,2)} = 4\pi \frac{3\mu_1^i \mu_2^j n_{\langle ij \rangle}^{12}}{r_{12}^3} \tag{2.57}$$

$$= \frac{4\pi}{r_{12}^3} \left[3(\mu_1 \cdot n_{12})(\mu_2 \cdot n_{12}) - (\mu_1 \cdot \mu_2) \right] , \tag{2.58}$$
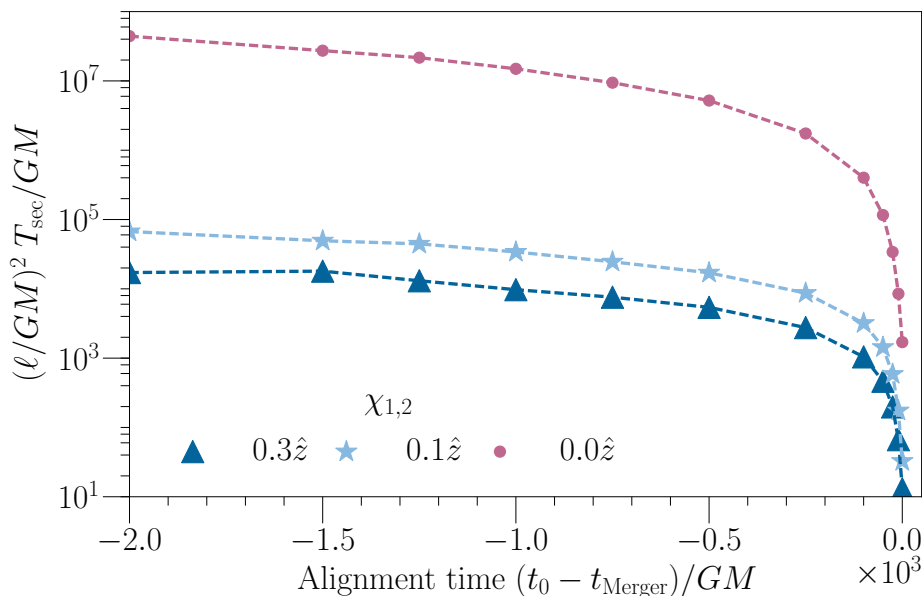
Figure 2.6: Estimate of secular regime of validity from dephasing time T_{sec}, Eq. (2.50). The perturbative scheme is valid within a sufficiently short time window $|t - t_0| \ll T_{\text{sec}}$ about an alignment time t_0. For longer times, multiple-scale analysis or renormalization will be needed to extend the regime of validity. The dephasing time is parametrically longer than the GR radiation reaction time, $T_{\text{sec}} \sim T_{\text{RR}}^{\text{GR}}(\ell/GM)^{-2}v^{-2}$. As expected it shrinks toward merger, remaining nonzero.

where again μ_A^i is the scalar dipole moment given in Eq. (2.27). In our case, the spins are in the $\hat{z}$ direction, so the $(\mu_A \cdot n_{12})$ term vanishes. To leading PN order, we use the Kepler relation $\omega^2 = GM/r_{12}^3$ and obtain

$$E_{\text{DD}}^{(\vartheta,2)} = 4\pi\omega^2(GM)^{-1}\mu_1\mu_2 \tag{2.59}$$

$$\frac{dE_{\text{DD}}^{(\vartheta,2)}}{d\omega} = 8\pi\omega(GM)^{-1}\mu_1\mu_2, \tag{2.60}$$

where μ_A now refers to the $\hat{z}$ component. For ω, we again use the coordinate orbital frequency from the simulation.

To summarize this calculation: we are approximating the secular breakdown time T_{sec} [Eq. (2.50)] by assuming a quasi-circular, adiabatic inspiral, and thus we compute $d\omega^{(2)}/dt$, Eq. (2.54). We approximate the dissipation $\dot{E}^{(2)}$ from only the scalar flux, Eq. (2.55). We approximate the conservative correction $E^{(2)}(\omega)$ from the post-Newtonian scalar dipole-dipole interaction, Eq. (2.56).

In Fig. 2.6, we plot $(\ell/GM)^2 T_{\text{sec}}(t_0)$, the time to secularly dephase by about ~ 1 radian, around various alignment times t_0. We have checked that at early times,

this numerical estimate agrees with an analytic PN estimate. As expected, T_{sec} is parametrically longer than the GR radiation-reaction time. The time window for secular validity shrinks approaching merger, but does not vanish.

The value of T_{sec}, and hence secular regime of validity, is smallest near merger. For the spin 0.3 simulation, just before merger, we find the time to dephase by about 1 radian from the GR background is $T_{\text{sec}} \sim 15\, GM(\ell/GM)^{-2}$. If Advanced LIGO detects a gravitational waveform of length, say, $200\, GM$, then a perturbative calculation without MSA/renormalization would be valid for $(\ell/GM) \lesssim 1/4$. For longer waveforms or larger values of (ℓ/GM), MSA or renormalization would be required. However, larger values of (ℓ/GM) will be very close to the limit on the instantaneous regime of validity, Fig. 2.5.

Detectability and bounds estimates

We now turn to the issue of how well Advanced LIGO/Virgo would be able to detect or bound the effects of dynamical Chern-Simons gravity from observations of a binary black hole merger. As we do not yet have metric waveforms [that arise at $O(\varepsilon^2)$], we make order-of-magnitude projections of detectability and bounds from the dephasing estimates in the previous section.

Suppose that LIGO detects a gravitational waveform similar to one of those we have simulated, with approximately 5 cycles of inspiral in band before merger—similar to GW150914 [10], with a total mass approximately $M \approx 60 M_\odot$. Such a detection would come with errors due to noise and calibration uncertainty; let us define the overall waveform phase uncertainty σ_ϕ. Let us further assume that the dCS corrections to the full waveform are not degenerate with redefining "bare" binary parameters. Upon detection, there are two distinct possibilities: (i) the detected waveform is consistent with GR predictions; or (ii) the detection is inconsistent with any point in the GR parameter space.

In the case of consistency, we would be able to place bounds on the size of ℓ. Crudely, we would be able to say

$$\Delta\phi_{\text{gw}} = 2\Delta\phi \lesssim \sigma_\phi, \tag{2.61}$$

where the factor of two comes from the gravitational wave being at twice the orbital frequency. If we have consistency with GR, then the quadratic approximation for $\Delta\phi$ in Eq. (2.48) holds.
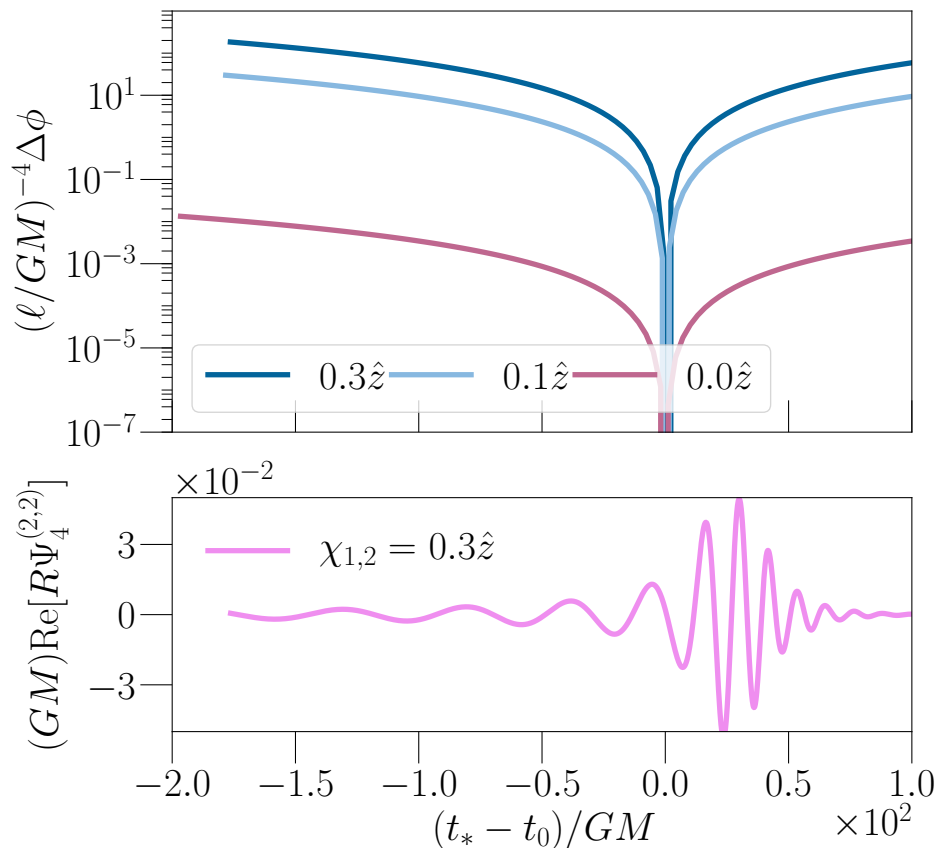
Figure 2.7: Estimated orbital phase difference (top) for the three different simulations as a function of time, given by the quadratic approximation Eq. (2.48). We choose the alignment time t_0 to be when the common apparent horizon forms, the last time when we have access to the orbital frequency. From $\Delta\phi$ we can estimate how large ℓ must be for a detectable deviation from GR, or project bounds on ℓ for GR-consistent detections. For reference, we also plot the gravitational waveform (bottom) from the spin 0.3 simulation, with approximately 5 cycles of inspiral before merger. This is approximately how many cycles were seen in GW150914 [10]. The two other simulations' gravitational waveforms are similar.

We plot the quadratic approximation to the orbital phase difference (relative to GR) in Fig. 2.7. By taking the maximum value of $\Delta\phi$ over the length of the waveform, and taking into account the scaling with $(\ell/GM)^4$, we can derive a projected bound on ℓ. For example, from the spin 0.3 simulation and $M \approx 60M_\odot$, we would find

$$\left(\frac{\ell}{GM}\right) \lesssim 0.13 \left(\frac{\sigma_\phi}{0.1}\right)^{1/4} \qquad \text{or} \qquad \ell \lesssim 11 \text{ km} \left(\frac{\sigma_\phi}{0.1}\right)^{1/4}, \qquad (2.62)$$

and from the spin 0.1 simulation,

$$\left(\frac{\ell}{GM}\right) \lesssim 0.2 \left(\frac{\sigma_\phi}{0.1}\right)^{1/4} \qquad \text{or} \qquad \ell \lesssim 18 \text{ km} \left(\frac{\sigma_\phi}{0.1}\right)^{1/4}. \qquad (2.63)$$

The spin 0.0 simulation would only give $(\ell/GM) \lesssim 1.4(\sigma_\phi/0.1)^{1/4}$. Such a bound would be past the instantaneous regime of validity limit during merger for this simulation (see Fig. 2.5). It is not internally self-consistent to use this perturbative result to claim a constraint on the regime past perturbative validity, so conservatively, no statement can be made. The higher spin simulations do not suffer from this problem.

These bounds forecasts can immediately be turned around into detectability forecasts. We can forecast that dynamical Chern-Simons corrections would be detectable in an $M \approx 60M_\odot$ binary with parameters consistent with our spin 0.3 simulation if $\ell \gtrsim 11$ km, and similarly for the spin 0.1 simulation if $\ell \gtrsim 18$ km.

We can draw three simple lessons on detectability and bounds from these results. First, better phase sensitivity (smaller σ_ϕ) is an obvious way to improve the odds of detectability, or place stronger bounds. This comes from improved detector sensitivity, but also from higher signal-to-noise ratio (SNR) events. Second, at fixed phase sensitivity, lower-mass events would be better than higher mass events, to a point. Lower mass events obviously have smaller GM, but they also spend more time in band, and thus have more time for dephasing. There is a tradeoff, though, because lower mass events are quieter, and also because most of the dephasing comes right before merger—so the mass must be high enough for merger to be in band. Finally, we can easily see that higher spin systems would lead to stronger constraints or a better chance of detecting dCS effects.

Let us compare our projected bounds to those appearing previously in the literature. Ali-Haïmoud and Chen [20] used solar system data from Gravity Probe B and the LAGEOS satellites to constrain the characteristic length scale to $\ell \lesssim 10^8$ km. Yagi, Yunes, and Tanaka [210] found a similar bound from table-top experiments. This is comparable to the curvature radius in the solar system.

Yunes and Pretorius [214] applied a precession calculation from the extreme mass-ratio limit to PSR J0737–3039 to estimate a constraint of $\ell \lesssim 10^4$ km. However, this calculation missed some effects (such as the scalar binding energy), and the mass ratio of PSR J0737–3039 is very close to 1. Moreover, the curvature radius at the surface of one of the NSs in this system should be order ~ 10 km, which means there is room between $10 - 10^4$ km where ℓ could be large compared to the curvature length, and thus the calculation would not be internally self-consistent. Yagi, Stein, Yunes, and Tanaka [211] performed a more careful analysis, using post-Newtonian theory for binary NS systems. They concluded that even PSR J0737–3039, with its high orbital velocity and exquisite timing, would not be able to yield a constraint on dCS for the foreseeable future, and that gravitational wave measurements would be the best hope.

Yagi, Yunes, and Tanaka [209] used post-Newtonian calculations to project the level of constraints that might arise from second and third generation GW detectors. If next-generation detectors such as Einstein Telescope [167] were to observe binary black hole inspirals consistent with GR, then YYT project a bound of $\ell \lesssim O(10 - 100)$ km. Second-generation ground-based detectors could place a similar constraint. The only caveat here is that YYT use post-Newtonian estimates, stopping at the ISCO frequency, for systems that would be seen not only in the inspiral, but also in the merger and ringdown, where PN is invalid. The additional SNR contributed by merger and ringdown will likely improve constraints.

Stein and Yagi [185] projected a number of constraints on ℓ based on both pericenter precession in pulsar binaries and gravitational wave measurements. For a LIGO detection of a $(10 + 11)M_\odot$ BBH inspiral, consistent with GR, at an SNR of 30, they projected a bound on the order of $\ell \lesssim 10$ km. Note that this is the same order of magnitude as the projected bound we estimate here.

Finally, Stein [184] projected a bound based on the observations of the black hole candidate GRO J1655–40. Assuming observations were consistent with GR, Stein projected a constraint of $\ell \lesssim 22$ km. However, such a constraint would require (for example) accretion disk modeling in the presence of the dCS correction, which has not been simulated.

2.4   Discussion and future work

In this study, we have performed the first fully nonlinear inspiral, merger, and ringdown numerical simulations of a binary black hole system in dynamical Chern-

Simons gravity. These are the first BBH simulations in a theory besides general relativity and standard scalar-tensor gravity. BBH in scalar-tensor is identical to that in GR, unless one imposes an external scalar field gradient [103, 46]. Therefore, these are also the first numerical simulations in a theory where the BBH dynamics differ from GR under ordinary initial and boundary conditions.

The "full" equations of motion for dCS, and many other corrections to GR, probably lack a well-posed initial value formulation. This is not an obstacle if the corrections are treated as being a low-energy effective field theory. In Sec. 2.2, we formulated a perturbation scheme which guarantees a well-posed initial value problem. We stress that this scheme is applicable not just to dCS, but also any deformation of general relativity which has a continuous limit to GR.

We performed fully nonlinear numerical simulations through order $O(\varepsilon^1)$ in the perturbation scheme. We simulated binaries with mass ratio $q = 3$ and aligned spins with equal dimensionless spin parameters $\chi_1 = \chi_2$, taking on three values, $\chi = 0.0, 0.1, 0.3$. The background (ε^0) metric radiation and perturbative (ε^1) scalar radiation waveforms are presented in Sec. 2.3. We found good agreement with PN waveform predictions [212, 211] during the early inspiral.

We have also discovered new phenomenology in dCS. In agreement with PN predictions, dCS does not suffer from dipole radiation during the early inspiral. However, during merger, there is a burst of dipole radiation. This phenomenon can only be studied with full numerical simulations.

We extracted energy fluxes in Sec. 2.3, finding good agreement with PN at early times. We found that the scalar field's $O(\varepsilon^2)$ energy flux during the inspiral was approximately $10^{-6}(\ell/GM)^4$ times smaller than the corresponding $O(\varepsilon^0)$ (GR) energy flux for the highest spin simulation, rising to a $10^{-3}(\ell/GM)^4$ fraction of GR during merger. This energy flux enters into our detectability estimate.

Since we use a perturbative scheme, it is important to understand where perturbation theory breaks down. In Sec. 2.3, we estimated the maximum values of ℓ/GM for the perturbation theory to be convergent at each time during the simulation. During the inspiral and ringdown, the regime of validity agrees with estimates from [184]. The tightest bound on the instantaneous regime of validity comes during merger and is comparable for spinning and non-spinning black hole mergers, close to $\ell/GM \lesssim 1$.

The additional radiation in the scalar field $\vartheta^{(1)}$ leads to a secular drift in orbital phase between the "true" orbital dynamics and the GR background from which we

perturb. Therefore, even if perturbation theory is instantaneously under control, the perturbative solution will dephase after a sufficiently long time. We numerically estimated this dephasing time in Sec. 2.3, and it agrees with post-Newtonian scaling at early times. At times approaching merger, the dephasing time becomes shorter, but remains nonzero.

This dephasing calculation served as the basis for estimating detectability and predicting bounds that LIGO would be able to place on ℓ, in Sec. 2.3. For $q = 3$, $M \approx 60 M_\odot$, and aligned dimensionless spins of $\chi_1 = \chi_2 = 0.3$, we estimated that a GR-consistent detection would yield a bound of

$$\ell \lesssim 11 \text{ km} \left(\frac{\sigma_\phi}{0.1}\right)^{1/4} , \tag{2.64}$$

where σ_ϕ is LIGO's statistical phase uncertainty on the detected waveform, which depends on the SNR of the detection. Conversely, any ℓ above this value would be detectable by LIGO. Lower spins lead to poorer detectability and/or bounds. Better bounds come from three places: (i) improved phase sensitivity (higher SNR), (ii) lower mass events (while keeping merger in band), and (iii) higher spin systems.

Future work

The natural next step in this program is to continue to the order ε^2 system, as outlined in Sec. 2.2. This is the lowest order where gravitational radiation is modified, and would involve solving for $h_{ab}^{(2)}$, which is sourced by $g_{ab}^{(0)}$ and $\vartheta^{(1)}$.

With the solution for the deformation to the metric $h_{ab}^{(2)}$, we will be able to directly compare dCS predictions against LIGO data. We will also have a more complete assessment of the convergence of the perturbation scheme.

Comparing dCS predictions against LIGO data will yield the first direct bounds on the theory from the strong-field, dynamical regime of gravity. To do so will involve extending GR parameter estimation [202] with one additional parameter, ℓ, which will be simultaneously inferred or constrained from the data.

A complete analysis would involve thorough exploration of the 7-dimensional parameter space of quasicircular BBHs (mass ratio and two spin vectors; the ℓ dependence is analytic in the perturbative approach). For example, in this work, we have focused on aligned-spin binaries in order to simplify comparisons with analytic predictions. The scalar energy flux in the case of misaligned binaries may be an order of magnitude larger than in the spin-aligned case (see [212] and the erratum). Building a surrogate waveform model [51, 50] would simultaneously allow for an efficient

exploration of parameter space and efficient parameter estimation/constraints with LIGO data.

The standard perturbation theory approach we used here will be sufficient if we find that the dephasing time is long compared to LIGO signals. However, if we need to extend the secular regime of validity, some form of multiple-scale analysis [42] or dynamical renormalization group [66, 89] approach will be required.

Finally, let us emphasize that our approach is not limited to dynamical Chern-Simons gravity: dCS is a proof of principle. Any theory with a continuous limit to GR can be treated with the same scheme, and reusing a large fraction of the code. In particular, we will consider EdGB and a class of theories proposed in [83]. Switching from dCS to another theory will only involve changing source terms that appear on the right hand sides of the differential equations we are solving numerically.

2.A   Scalar field evolution formulation

In this appendix, we discuss the numerical evolution scheme for a (massless) Klein-Gordon field, denoted by the code variable Ψ, in greater detail. This is an update of the system described in [105], which did not include the "$\gamma_1 \gamma_2$" constraint-damping term (see below). The basic equation we are simulating is

$$\Box \Psi = S, \tag{2.65}$$

for some prescribed source term S (in this work, the source term is the Pontryagin density $^*RR$).

We first review the 3+1 ADM formalism for the foliation of a spacetime into spatial slices, as used in numerical relativity [40]. We decompose the metric as

$$g_{ab} = \gamma_{ab} - n_a n_b, \tag{2.66}$$

where g_{ab} is the spacetime metric, n_a is a timelike unit one-form normal to the spatial slice with $n_a n^a = -1$, and γ_{ab} is the induced spatial metric and projector, with $n^a \gamma_{ab} = 0$. In ADM variables, the timelike unit normal can be written in terms of a lapse, α, and shift β^i, as $n^a = (\alpha^{-1}, -\alpha^{-1}\beta^i)$.

We work with the Spectral Einstein Code (SpEC), which uses the generalized harmonic formulation of general relativity, and evolves a symmetric-hyperbolic first-order system of metric variables g_{ab}, $\Phi_{iab} = \partial_i g_{ab}$ and $\Pi_{ab} = -n^c \partial_c g_{ab}$ [121].

We similarly define a set of first-order variables for the scalar field Ψ as

$$\Phi_i = \partial_i \Psi, \tag{2.67}$$

$$\Pi = -n^a \partial_a \Psi = -\alpha^{-1}(\partial_t \Psi - \beta^i \partial_i \Psi). \tag{2.68}$$

From these definitions and the equality of mixed partial derivatives, we can create a system of constraints which vanish in the continuum limit, and which an accurate evolution of the system will satisfy to within some tolerance:

$$C_i^{(1)} = \partial_i \Psi - \Phi_i, \tag{2.69}$$

$$C_i^{(2)} = [ijk]\partial_j \Phi_k. \tag{2.70}$$

In Eq. (2.70) the indices j, k are summed and $[ijk]$ is the completely antisymmetric Levi-Civita *symbol*, with $[123] = +1$.

The evolution equation (2.65) thus becomes a set of first-order time evolution equations for $\{\Psi, \Phi_i, \Pi\}$. However, in order to prevent numerical errors in the constraints from making the evolution unstable, we follow what is done in the metric system and add specific multiples of the constraints to the evolution equations. These combinations of constraints are chosen so as to ensure that the system is symmetric hyperbolic and that the constraints are damped out, ensuring a well-posed evolution scheme. The evolution equation for Ψ is thus

$$\partial_t \Psi = -\alpha\Pi + \beta^m[\partial_m \Psi + \gamma_1(\partial_m \Psi - \Phi_m)], \tag{2.71}$$

where the first terms come from the definitions of Φ_i and Π, and the last term is a constraint damping term with coefficient γ_1. The evolution equation for Φ_i is

$$\begin{aligned}
\partial_t \Phi_k = &-\alpha[\partial_k \Pi + \gamma_2(\Phi_k - \partial_k \Psi)] \\
&- \Pi\partial_k\alpha + \beta^m\partial_m\Phi_k + \Phi_m\partial_k\beta^m,
\end{aligned} \tag{2.72}$$

where the term with γ_2 is a constraint damping term, and all other terms come from definitions of the first-order variables and equality of mixed partial derivatives. Finally, the evolution equation for Π is

$$\begin{aligned}
\partial_t \Pi = &\,\alpha\Pi K + \beta^m\partial_m\Pi + \alpha\Phi_m\Gamma^m \\
&+ \gamma_1\gamma_2\beta^m(\partial_m\Psi - \Phi_m) \\
&- \alpha g^{mn}\partial_n\Phi_m - g^{mn}\Phi_n\partial_m\alpha \\
&+ \alpha S,
\end{aligned} \tag{2.73}$$

where K is the trace of the extrinsic curvature, $\Gamma^m \equiv g^{ab}\Gamma^m{}_{ab}$ is a specific contraction of the Christoffel connection coefficients, S is the source term, and the $\gamma_1\gamma_2$ term is the appropriate constraint-damping term to keep the system symmetric hyperbolic.

This "$\gamma_1\gamma_2$" term was not included in the previous description [105], but it is required if both γ_1 and γ_2 are non-zero. The parameters γ_1 and γ_2 play the same role in the damping and characteristic analysis of this Klein-Gordon system as they do in the generalized harmonic system [121]. Specifically, in order for the constraint $C_i^{(1)}$ to be damped, we must have $\gamma_2 > 0$ (satisfying the constraint $C_i^{(1)}$ implies satisfaction of the constraint $C_i^{(2)}$). The choice $\gamma_1 = -1$ makes the system linearly degenerate. In practice, we set the values of γ_1 and γ_2 to match those of the generalized harmonic evolution of the metric variables, so that the characteristic speeds of the metric and scalar field systems agree.

The scalar field variables, like the metric variables, are represented spectrally. In order to reduce the amount of numerical noise in the system, we apply the same filters we use for the metric variables to the scalar field system, namely filtering the top 4 tensor spherical harmonics and using an exponential Chebyshev filter for the radial piece.

In order to assess the accuracy of the simulations, we evaluate the constraints that the generalized harmonic evolution system must satisfy [121], as well as the constraints for the first-order scalar field system given by Eqs. (2.69) and (2.70). We combine these constraints, contracting with a Euclidean metric to give a constraint energy as

$$C^2 = C_i^{(1)}C_i^{(1)} + C_j^{(2)}C_j^{(2)} . \tag{2.74}$$

Since the code is spectral, we check for exponential convergence of these constraint energies as we increase the number of angular and radial basis functions per subdomain (and hence the resolution). We plot the convergence of the L^∞ norm of the constraint energies for the highest spin simulation of this study, which has the greatest level of constraint violation, in Fig. 2.8. We find that the error decreases exponentially with resolution. The lower spin simulations have similar qualitative behavior.

2.B Pontryagin density in 3+1 split

Since numerical relativity computations are formulated in a 3+1 split, we must compute the scalar field's source term—the Pontryagin density—in terms of 3-
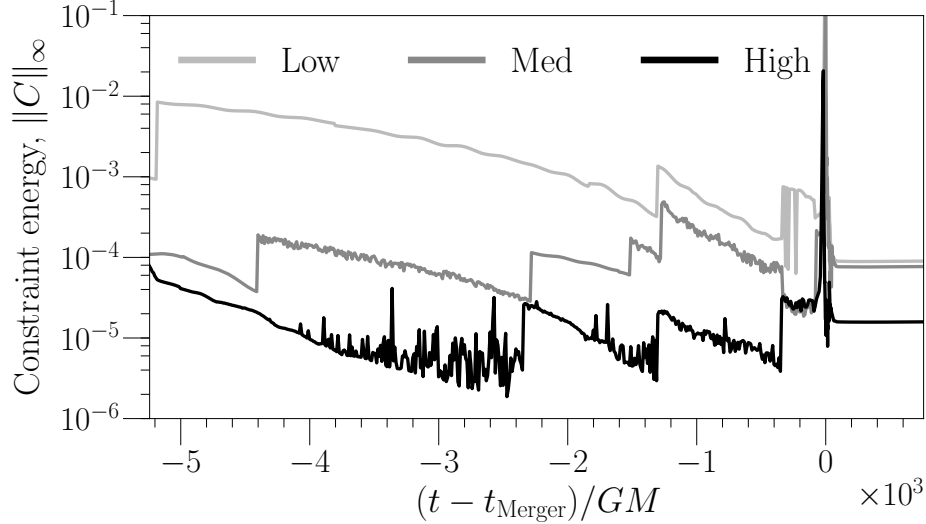
Figure 2.8: Numerical error convergence for the highest spin (0.3 $\hat{z}$) simulation performed in this study, which shows the greatest level of constraint violation. We plot the L^∞ norm of the constraint energy defined in Eq. (2.74) for the low, medium and high numerical resolutions (adding a constant number of angular and radial basis functions to increase resolution). Note that these constraints are not normalized, but the relative error between the levels shows exponential convergence. The constraint energy increases at merger, which also happens in the metric evolution system, and is consistent with other BBH simulations.

dimensional quantities. First, it is straightforward to verify

$$^*RR \equiv {}^*R^{abcd} R_{abcd} = {}^*C^{abcd} C_{abcd}, \tag{2.75}$$

where C_{abcd} is the Weyl tensor, and its left dual is $^*C^{abcd} \equiv \frac{1}{2}\epsilon^{abef} C_{ef}{}^{cd}$. Thus we do not need to consider all of Riemann, but only its trace-free part, Weyl. The Pontryagin density is completely insensitive to the Ricci part of curvature.

In a 4-dimensional numerical relativity simulation, it is especially convenient to decompose Weyl into its electric and magnetic parts, defined as

$$E_{ab} \equiv + C_{acbd}n^c n^d, \tag{2.76}$$

$$B_{ab} \equiv - {}^*C_{acbd}n^c n^d. \tag{2.77}$$

The minus sign in (2.77) follows the conventions of [151, 140] and the implementation in SpEC [198], though much of the literature has a plus sign. From the symmetries of Weyl, the two tensors E_{ab} and B_{ab} are both symmetric ($E_{ab} = E_{(ab)}$ and $B_{ab} = B_{(ab)}$), purely spatial ($E_{ab}n^a = 0 = B_{ab}n^a$), and trace-free ($E^a{}_a = 0 = B^a{}_a$). We may also write an inversion formula for Weyl in terms of E_{ab} and B_{ab} (thanks to

Alfonso García-Parrado for bringing this inversion formula to our attention),

$$C_{abcd} = \boxed{\begin{smallmatrix} a & c \\ b & d \end{smallmatrix}}[4E_{ac}(\gamma_{bd} + n_b n_d) - \epsilon_{ab}{}^e n_d B_{ce}] \,, \tag{2.78}$$

where the operator $\boxed{\begin{smallmatrix} a & c \\ b & d \end{smallmatrix}}$ is a projector that imposes the symmetries of the Riemann tensor ($R_{abcd} = R_{[ab][cd]} = R_{cdab}$). Here we have the induced 3-dimensional volume element,

$$\epsilon_{abc} \equiv n^d \epsilon_{dabc} \,, \qquad\qquad \epsilon_{abcd} = -4n_{[a}\epsilon_{bcd]} \,. \tag{2.79}$$

For coordinate component calculations, we use the conventions where $\epsilon_{abcd} = +\sqrt{-g}[abcd]$ where $[abcd]$ is the alternating *symbol*, with $[0123] = +1$ (see e.g. [135]). We also have $\epsilon^{abcd} = -[abcd]/\sqrt{-g}$, and similar conventions for the 3-dimensional volume element: $\epsilon_{abc} = \sqrt{\gamma}[abc]$ and $\epsilon^{abc} = [abc]/\sqrt{\gamma}$ (this makes use of the identity $\sqrt{-g} = \alpha\sqrt{\gamma}$).

With this above decomposition, it is easy to verify that the Pontryagin density can be expressed simply in terms of the electric and magnetic parts of Weyl,

$$^*RR = -16E_{ab}B^{ab} \,. \tag{2.80}$$

Thus all that remains is to compute E_{ab} and B_{ab} from other quantities. Finding these expressions for E and B comes from the standard Gauss-Codazzi-Mainardi (GCM) equations (see [40] for a didactic explanation). After using the GCM equations, for the electric Weyl tensor we find

$$E_{ab} = K_{ab}K^c{}_c - K_a{}^c K_{bc} + {}^{(3)}R_{ab} \tag{2.81}$$
$$- \frac{1}{2}\gamma_a{}^c\gamma_b{}^{d\,(4)}R_{cd} - \frac{1}{2}\gamma_{ab}\gamma^{cd\,(4)}R_{cd} + \frac{1}{3}\gamma_{ab}{}^{(4)}R \,.$$

Here ${}^{(3)}R_{ab}$ is the spatial 3-Ricci tensor while ${}^{(4)}R_{ab}$ is the 4-Ricci tensor, and K_{ab} is the extrinsic curvature of the spacelike hypersurface. The second line of (2.81) contains 4-Ricci terms which would vanish if the 4-metric was Ricci-flat, for example if it solves the Einstein equations in vacuum. These terms were not included in e.g. [115].

Meanwhile, for the magnetic Weyl tensor we find the simple expression

$$B_{ab} = -\epsilon_{cd(a}D^c K_{b)}{}^d \,, \tag{2.82}$$

where D_a is the covariant derivative induced on the 3-surface which is compatible with the 3-metric, $D_a\gamma_{bc} = 0$.

C h a p t e r   3

NUMERICAL BLACK HOLE INITIAL DATA AND SHADOWS IN DYNAMICAL CHERN-SIMONS GRAVITY

[1]   Maria Okounkova, Mark A Scheel, and Saul A Teukolsky. "Numerical black hole initial data and shadows in dynamical Chern–Simons gravity". In: *Classical and Quantum Gravity* 36.5 (Feb. 2019), p. 054001. DOI: 10.1088/1361-6382/aafcdf.

Abstract

We present a scheme for generating first-order metric perturbation initial data for an arbitrary background and source. We then apply this scheme to derive metric perturbations in order-reduced dynamical Chern-Simons gravity (dCS). In particular, we solve for metric perturbations on a black hole background that are sourced by a first-order dCS scalar field. This gives us the leading-order metric perturbation to the spacetime in dCS gravity. We then use these solutions to compute black hole shadows in the linearly perturbed spacetime by evolving null geodesics. We present a novel scheme to decompose the shape of the shadow into multipoles parametrized by the spin of the background black hole and the perturbation parameter ε^2. We find that we can differentiate the presence of a pure Kerr spacetime from a spacetime with a dCS perturbation using the shadow, allowing in part for a null-hypothesis test of general relativity. We then consider these results in the context of the Event Horizon Telescope.

3.1   Introduction

Einstein's theory of general relativity (GR) has passed all precision tests to date [206]. In particular, model-independent tests using binary black hole merger data from the Laser Interferometry Gravitational Wave Observatory (LIGO) are consistent with GR at the 96% confidence level [16, 14, 216].

However, at some length scale, GR must be reconciled with quantum mechanics in a theory of quantum gravity. Black holes and black hole binaries probe the strong-field, non-linear, high-curvature regime of gravity, and thus observations of these

systems might contain signatures of quantum gravity. Our goal is to predict these signatures.

We know from the first LIGO detections that deviations from GR are small, and thus rather than considering black holes in a fully quantum theory, we can calculate their properties in *effective field theories* (EFTs). These theories involve adding perturbative quantum-gravity-motivated terms to the Einstein-Hilbert action of general relativity. Since these theories are classical, we can hope to apply the numerical tools used to study GR (a classical theory) to these quantum-gravity-motivated theories.

One such EFT is dynamical Chern-Simons gravity (dCS), which modifies the action of GR through the inclusion of a scalar field coupled to spacetime curvature [18]. In particular, this theory has motivations in string theory [95], loop quantum gravity [192, 134], and inflation [204]. The full effective field theory, however, most likely does not have a well-posed initial value formulation [74]. However, we can expand the theory around general relativity in order to guarantee a well-posed system of equations at each order [146]. This is in part justified by the first LIGO detection, which found deviations from GR in black hole systems to be small [14]. In a previous study, we investigated the leading-order behavior of the dCS scalar field in a binary black hole system, quantifying the amount by which gravitational waves in dCS gravity would differ from those in pure GR [146].

In this study, we numerically compute *metric perturbations* in dCS. In other words, we calculate to leading order the modifications to a pure GR spacetime due to the presence of the dCS scalar field. Such modifications will be required, for example, as initial data to perform binary black hole simulations involving a dCS metric perturbation. We thus produce and test a formalism for generating metric perturbation initial data based on the extended conformal thin sandwich formalism (cf. [40] for a review). Previous studies have considered such modifications, but we present the first such formalism that can be used in the binary black hole case [214, 210, 133, 73, 62, 29].

In addition to LIGO, an instrument coming online that will have the power to probe the strong-field regime of gravity is the Event Horizon Telescope (EHT). The primary goal of this instrument (a very long baseline interferometry array of radio telescopes) is to image black hole event horizons, including those of Sgr A*, the black hole at the center of the Milky Way galaxy, and the black hole of the center of the M87 galaxy [170, 85]. The EHT in part has the power to image the *black hole shadow*, a dark region on the image corresponding to angles at which

no photons reach the observer because of light-bending and the presence of an event horizon. The shadow, for a black hole with a given mass and spin, has a precise shape predicted by GR, and thus deviations from this shape can be used to test the theory [136, 164, 136]. Since the paths of photons are determined by the spacetime itself, resolving the shadow corresponds to directly probing the metric of the spacetime and hence, is a metric test of GR. Moreover, predictions for black hole shadows exist in other theories of gravity. Thus one can go beyond performing a null-hypothesis test of GR and instead test specific theories. Additionally, since the mass of Sgr A* is $\sim 10^6 \, M_\odot$, whereas the masses of black holes observed by LIGO are $\sim 10 \, M_\odot$, the EHT probes gravity on a wholly new scale [37].

Given dCS metric perturbations, our goal is to compute the black hole shadow in a dCS-modified spacetime, and quantify the effects (including degeneracies) on the shape of the shadow as a function of mass, spin, and the dCS coupling parameter. We can then estimate whether the EHT would be able to resolve these deviations.

Roadmap and conventions

This chapter is organized as follows. In Sec. 3.2, we derive and provide all of the equations for the formalism for generating metric perturbation initial data. In Sec. 3.3, we specifically apply this formalism to black holes in dCS gravity, presenting convergent initial data results. In Sec. 3.4, we present results using stationary dCS metric perturbation initial data to calculate black hole shadows. We conclude in Sec. 3.5.

We set $G = c = 1$ throughout. Quantities are given in terms of units of M, the ADM mass of the system. Latin letters in the beginning of the alphabet $\{a, b, c, d \ldots\}$ denote 4-dimensional spacetime indices, while Latin letters in the middle of the alphabet $\{i, j, k, l \ldots\}$ denote 3-dimensional spatial indices. ψ_{ab} refers to the spacetime metric, while g_{ij} refers to the spatial metric from a 3+1 decomposition with corresponding timelike unit normal one-form n_a (cf. [40] for a review of the 3+1 ADM formalism).

3.2 Solving for general metric perturbation initial data
Overview

In standard numerical general relativity, initial data is often generated using the extended conformal thin sandwich formalism [69, 154, 129, 127, 149]. A thorough review of this method is presented in [40], and a derivation is presented in [153]. This formalism decomposes the 3+1 ADM Hamiltonian and momentum constraints,

as well as the equation for the time derivative of the extrinsic curvature, to generate a set of elliptic equations to numerically solve for initial data.

Recall that in the 3+1 decomposition, the constraints and time derivative of the extrinsic curvature are given as

$$R + K^2 - K_{ij}K^{ij} = 16\pi\rho, \tag{3.1}$$

$$D_j(K^{ij} - g^{ij}K) = 8\pi S^i, \tag{3.2}$$

$$\partial_t K_{ij} = \alpha(R_{ij} - 2K_{ij}K^k{}_j + KK_{ij}) - D_i D_j \alpha \tag{3.3}$$

$$- 8\pi\alpha(S_{ij} - \frac{1}{2}g_{ij}(S - \rho)) + \beta^k \partial_k K_{ij} + K_{ik}\partial_j\beta^k + K_{kj}\partial_i\beta^k,$$

where g_{ij} is the spatial metric with corresponding covariant derivative D_i, α is the lapse, and β^i is the shift. K_{ij} is the extrinsic curvature with trace K, and R_{ij} is the spatial Ricci tensor with trace R. The matter terms ρ, S^i, S_{ij}, and S are defined with respect to the stress-energy tensor T_{ab} and timelike unit normal one-form n_a as

$$\rho \equiv n_a n_b T^{ab}, \tag{3.4}$$

$$S^i \equiv -g^{ij} n^a T_{aj}, \tag{3.5}$$

$$S_{ij} \equiv g_{ia} g_{jb} T^{ab}, \tag{3.6}$$

$$S \equiv g^{ij} S_{ij}, \tag{3.7}$$

where the time-space components of the spatial metric are given via $g_{ab} \equiv \psi_{ab} + n_a n_b$ for spacetime metric ψ_{ab}.

The extended conformal thin sandwich formalism involves writing the spatial metric in terms of a conformal metric $\bar{g}_{ij}$ as

$$g_{ij} = \psi^4 \bar{g}_{ij}, \tag{3.8}$$

where ψ is known as the conformal factor. Additionally, the time derivative of the spatial metric is decomposed as

$$u_{ij} = \partial_t g_{ij} - \frac{2}{3}g_{ij}(-\alpha K + D_i \beta^i), \tag{3.9}$$

where the function u_{ij} is related to the time derivative of the conformal metric as

$$u_{ij} = \psi^4 \bar{u}_{ij}, \tag{3.10}$$

with

$$\bar{u}_{ij} \equiv \partial_t \bar{g}_{ij}. \tag{3.11}$$

In this formalism, the extrinsic curvature is decomposed into traceless and trace parts as

$$K_{ij} = A_{ij} + \frac{1}{3}g_{ij}K, \tag{3.12}$$

where A_{ij} is the traceless part of K_{ij} and is conformally transformed as

$$A_{ij} = \psi^{-2}\bar{A}_{ij}, \tag{3.13}$$

with

$$\bar{A}^{ij} = \frac{\psi^7}{2\alpha\psi}((\bar{L}\beta)^{ij} - \bar{u}^{ij}), \tag{3.14}$$

$$(\bar{L}\beta)^{ij} \equiv \bar{D}^i\beta^j + \bar{D}^j\beta^i - \frac{2}{3}\bar{g}^{ij}\bar{D}_k\beta^k. \tag{3.15}$$

Here, $\bar{D}_i$ refers to the covariant derivative with respect to the conformal metric, $\bar{g}_{ij}$.

Having defined all of these quantities, we can now recast Eqs. (3.1), (3.2), and (3.3) to give an elliptic equation for the conformal factor,

$$\bar{D}^2\psi - \frac{1}{8}\psi\bar{R} - \frac{1}{12}\psi^5 K^2 + \frac{1}{8}\psi^{-7}\bar{A}_{ij}\bar{A}^{ij} = -2\pi\psi^5\rho, \tag{3.16}$$

an elliptic equation for the shift,

$$(\bar{\Lambda}_L\beta)^i - (\bar{L}\beta)^{ij}\bar{D}_j\ln\bar{\alpha} = \bar{\alpha}\bar{D}_j(\bar{\alpha}^{-1}\bar{u}^{ij}) + \frac{4}{3}\bar{\alpha}\psi^6\bar{D}^i K + 16\pi\bar{\alpha}\psi^{10}S^i, \tag{3.17}$$

and an elliptic equation for $\alpha\psi$,

$$\bar{D}^2(\alpha\psi) = \alpha\psi(\frac{7}{8}\psi^{-8}\bar{A}_{ij}\bar{A}^{ij} + \frac{5}{12}\psi^4 K^2 + \frac{1}{8}\bar{R} \tag{3.18}$$
$$+ 2\pi\psi^4(\rho + 2S)) - \psi^5\partial_t K + \psi^5\beta^i\bar{D}_i K.$$

Here, $\bar{\alpha} \equiv \psi^{-6}\alpha$ is the densitized lapse, $\bar{R}$ is the conformal Ricci scalar computed for $\bar{g}_{ij}$, and $(\bar{\Lambda}_L\beta)^i$ is the vector Laplacian (cf. [40]).

In the extended conformal thin sandwich formalism, we are freely allowed to specify

$$\boxed{\text{Free data: } \bar{g}_{ij}, \bar{u}_{ij}, K, \partial_t K}, \tag{3.19}$$

and solve for the variables

$$\boxed{\text{Solved data: } \psi, \beta^i, \alpha\psi}. \tag{3.20}$$

We are interested in solving for initial data for linear metric perturbations of the form

$$\psi_{ab} \rightarrow \psi_{ab} + \Delta\psi_{ab}. \tag{3.21}$$

In order to solve for perturbed initial data, we will perturb the extended conformal thin sandwich equations. Our overall goal is to perturb each of these equations to linear order, which will give us elliptic equations for the perturbed variables with the same principal part as the background equations. Throughout, we will denote by ΔX the first-order (linear) perturbation to some variable X. We perturb each of the variables as

$$\psi \rightarrow \psi + \Delta\psi, \tag{3.22}$$

$$\beta^i \rightarrow \beta^i + \Delta\beta^i, \tag{3.23}$$

$$\alpha\psi \rightarrow \alpha\psi + (\alpha\Delta\psi + \Delta\alpha\psi), \tag{3.24}$$

and solve for $\Delta\psi$, the perturbation to the conformal factor, $\Delta\beta^i$, the perturbation to the shift, and

$$\Delta C \equiv \Delta(\alpha\psi) = \alpha\Delta\psi + \Delta\alpha\psi, \tag{3.25}$$

the perturbation to the lapse times the conformal factor.

The equations will additionally involve perturbing metric quantities to first order, such as

$$\bar{g}_{ij} \rightarrow \bar{g}_{ij} + \Delta\bar{g}_{ij}, \tag{3.26}$$

$$\bar{u}_{ij} \rightarrow \bar{u}_{ij} + \Delta\bar{u}_{ij}, \tag{3.27}$$

$$K \rightarrow K + \Delta K, \tag{3.28}$$

$$\partial_t K \rightarrow \partial_t K + \partial_t \Delta K, \tag{3.29}$$

where $\Delta\bar{u}_{ij} \equiv \partial_t \Delta\bar{g}_{ij}$. We outline these terms in more detail in 3.A.

Much like we have the solved data and free data in the extended conformal thin sandwich formalism, we will have

$$\boxed{\text{Perturbed free data: } \Delta\bar{g}_{ij}, \Delta\bar{u}_{ij}, \Delta K, \partial_t \Delta K}, \tag{3.30}$$

and

$$\boxed{\text{Perturbed solved data: } \Delta\psi, \Delta\beta^i, \Delta C}. \tag{3.31}$$

Perturbed initial data formalism

We now perturb Eqs. (3.16), (3.17), and (3.18) to obtain elliptic equations for $\Delta\psi$, $\Delta\beta^i$, and ΔC. Each of these equations involves the perturbations to the extended conformal thin sandwich quantities. For example, the equations will include the first-order perturbation to $\bar{A}^{ij}$ (defined in Eq. (3.14)), denoted $\Delta\bar{A}^{ij}$. We leave the derivations of the perturbations to all of the extended conformal thin sandwich quantities to 3.A and present the perturbations to the elliptic equations for $\Delta\psi$, $\Delta\beta^i$, and ΔC here.

Perturbed equations

Perturbing Eq. (3.16) yields an elliptic equation for $\Delta\psi$. We obtain

$$
\begin{aligned}
0 = {} & -\bar{D}^2\Delta\psi - \Delta(\bar{D}^2)\psi \qquad\qquad\qquad\qquad\qquad\qquad (3.32) \\
& + \frac{1}{8}\Delta\psi\bar{R} + \frac{1}{8}\psi\Delta\bar{R} + \frac{5}{12}\psi^4\Delta\psi K^2 + \frac{1}{6}\psi^5 K\Delta K \\
& + \frac{7}{8}\psi^{-8}\Delta\psi\bar{A}_{ij}\bar{A}^{ij} - \frac{1}{8}\psi^{-7}(\Delta\bar{A}_{ij}\bar{A}^{ij} + \bar{A}_{ij}\Delta\bar{A}^{ij}) \\
& - 2\pi(5\psi^4\Delta\psi\rho + \psi^5\Delta\rho),
\end{aligned}
$$

where $\bar{D}^2\Delta\psi$ is the principal part of this perturbed equation.

Perturbing Eq. (3.18) yields an elliptic equation for ΔC. Since this equation is longer, we will do it piece by piece, splitting the original expression as

$$
0 = \underbrace{-\bar{D}^2(\alpha\psi)}_{\text{Principal part}} + \underbrace{\alpha\psi\left(\frac{7}{8}\psi^{-8}\bar{A}_{ij}\bar{A}^{ij} + \frac{5}{12}\psi^4 K^2 + \frac{1}{8}\bar{R}\right)}_{\text{Non-matter terms}} \qquad (3.33)
$$

$$
\underbrace{-\psi^5\partial_t K + \psi^5\beta^i\bar{D}_i K}_{\text{Non-matter terms}} + \underbrace{\alpha\psi 2\pi\psi^4(\rho + 2S)}_{\text{Matter terms}}.
$$

Perturbing the **Matter terms**, we obtain

$$
\begin{aligned}
\Delta(C \text{ Matter terms}) = {} & 2\pi(\Delta C\psi^4(\rho + 2S) + 4\alpha\psi\psi^3\Delta\psi(\rho + 2S) \qquad (3.34) \\
& + \alpha\psi\psi^4(\Delta\rho + 2\Delta S)).
\end{aligned}
$$

Next, perturbing the **Non-matter terms**, we obtain

$$\Delta(C \text{ Non-matter terms}) = \Delta C \left(\frac{7}{8} \psi^{-8} \bar{A}_{ij} \bar{A}^{ij} + \frac{5}{12} \psi^4 K^2 + \frac{1}{8} \bar{R} \right) \tag{3.35}$$

$$+ \alpha\psi(-7\psi^{-9}\Delta\psi \bar{A}_{ij}\bar{A}^{ij} + \frac{7}{8}\psi^{-8}(\Delta\bar{A}_{ij}\bar{A}^{ij} + \bar{A}_{ij}\Delta\bar{A}^{ij})$$

$$+ \frac{5}{3}\psi^3\Delta\psi K^2 + \frac{5}{6}\psi^4 K\Delta K + \frac{1}{8}\Delta\bar{R})$$

$$- 5\psi^4\Delta\psi\,\partial_t K - \psi^5\partial_t\Delta K$$

$$+ 5\psi^4\Delta\psi\,\beta^i\bar{D}_i K + \psi^5\Delta\beta^i\bar{D}_i K + \psi^5\beta^i\bar{D}_i\Delta K \,.$$

Finally, for the perturbation to the **principal part**, we obtain

$$\Delta(C \text{ Principal part}) = -\bar{D}^2(\Delta C) - \Delta(\bar{D}^2)(\alpha\psi), \tag{3.36}$$

where the first term gives us the principal part for the perturbed equation. We combine these terms into an overall elliptic equation for ΔC

$$\Delta(C \text{ Principal part}) + \Delta(C \text{ Non-matter terms}) + \Delta(C \text{ Matter terms}) = 0, \tag{3.37}$$

where the perturbed terms are given in Eqs. (3.36), (3.34), and (3.35).

In order to complete our system of equations, we perturb Eq. (3.17) to obtain an equation for $\Delta\beta^i$. In practice, we solve the momentum constraint with the principal part

$$-\alpha\psi\bar{D}_j\left(\frac{1}{\alpha\psi}(\bar{L}\beta)^{ij}\right), \tag{3.38}$$

where the momentum constraint has been rewritten using as

$$0 = -\alpha\psi\bar{D}_j\left(\frac{1}{\alpha\psi}(\bar{L}\beta)^{ij}\right) \tag{3.39}$$

$$+ \bar{D}_j\bar{u}^{ij} - \frac{14\alpha\psi}{\psi^8}\bar{A}^{ij}\bar{D}_j\psi - \bar{u}^{ij}\frac{\bar{D}_j\alpha\psi}{\alpha\psi} + \frac{4}{3}\frac{\alpha\psi}{\psi}\bar{D}^i K$$

$$+ 16\pi\alpha\psi\psi^3 S^i \,.$$

For simplicity, we split up Eq. (3.39) as

$$0 = \underbrace{-\alpha\psi \bar{D}_j \left(\frac{1}{\alpha\psi} (\bar{L}\beta)^{ij} \right)}_{\text{Principal part}} \tag{3.40}$$

$$\underbrace{+ \bar{D}_j \bar{u}^{ij} - \frac{14\alpha\psi}{\psi^8} \bar{A}^{ij} \bar{D}_j \psi - \bar{u}^{ij} \frac{\bar{D}_j \alpha\psi}{\alpha\psi} + \frac{4}{3} \frac{\alpha\psi}{\psi} \bar{D}^i K}_{\text{Non-matter terms}}$$

$$\underbrace{+ 16\pi\alpha\psi\psi^3 S^i}_{\text{Matter terms}} .$$

Perturbing the **Matter terms**, we obtain

$$\Delta(\beta^i \text{ Matter terms}) = 16\pi (\Delta C \psi^3 S^i + 3\alpha\psi\psi^2 \Delta\psi S^i + \alpha\psi\psi^3 \Delta S^i) . \tag{3.41}$$

Perturbing the **Non-matter terms** gives

$$\Delta(\beta^i \text{ Non-matter terms}) = \Delta(\bar{D})_j \bar{u}^{ij} + \bar{D}_j \Delta\bar{u}^{ij} \tag{3.42}$$

$$- \frac{14\Delta C}{\psi^8} \bar{A}^{ij} \bar{D}_j \psi + \frac{112\alpha\psi}{\psi^9} \Delta\psi \bar{A}^{ij} \bar{D}_j \psi$$

$$- \frac{14\alpha\psi}{\psi^8} (\Delta\bar{A}^{ij} \bar{D}_j \psi + \bar{A}^{ij} \bar{D}_j \Delta\psi)$$

$$- \Delta\bar{u}^{ij} \frac{\bar{D}_j \alpha\psi}{\alpha\psi} - \frac{\bar{u}^{ij}}{\alpha\psi} \bar{D}_j \Delta C + \bar{u}^{ij} \Delta C \frac{\bar{D}_j \alpha\psi}{(\alpha\psi)^2}$$

$$+ \frac{4}{3} \frac{\Delta C}{\psi} \bar{D}^i K - \frac{4}{3} \frac{\alpha\psi}{\psi^2} \Delta\psi \bar{D}^i K$$

$$+ \frac{4}{3} \frac{\alpha\psi}{\psi} (\Delta(\bar{D})^j K + \bar{D}^i \Delta K) .$$

Finally, perturbing the **Principal part** gives

$$\Delta(\beta^i \text{ Principal part}) = - \alpha\psi \bar{D}_j \left(\frac{1}{\alpha\psi} ((\bar{L}\Delta\beta)^{ij} + (\Delta(\bar{L})\beta)^{ij}) \right) \tag{3.43}$$

$$- \Delta(\bar{D})_j (\bar{L}\beta)^{ij} + \frac{(\bar{L}\beta)^{ij}}{\alpha\psi} \bar{D}_j \Delta C - (\bar{L}\beta)^{ij} \frac{\Delta C}{(\alpha\psi)^2} \bar{D}_j \alpha\psi .$$

Our overall elliptic equation for $\Delta\beta^i$ is

$$\Delta(\beta^i \text{ Principal part}) + \Delta(\beta^i \text{ Non-matter terms}) + \Delta(\beta^i \text{ Matter terms}) = 0, \tag{3.44}$$

where the perturbed terms are given in Eqs. (3.43), (3.41), and (3.42).

Thus, we have derived a set of three second-order, elliptic equations for $\Delta\psi$, ΔC, and $\Delta\beta^i$. We solve Eq. (3.32) for $\Delta\psi$, Eq. (3.37) for ΔC, and Eq.(3.44) for $\Delta\beta^i$. The

principal parts of all of these equations are the same as in the unperturbed extended conformal thin sandwich equations. Thus, for numerical solutions, we can reuse the preconditioning matrices and linearized operators that are used in the unperturbed equations. The specific details of the numerical computation can be found in [154].

Reconstructing perturbed data

Given solutions of the equations from the previous section for $\Delta\psi, \Delta C, \Delta\beta^i$, as well as the perturbed free data and background data, we now wish to reconstruct Δg_{ij}, the full perturbed spatial metric, and $\partial_t \Delta g_{ij}$, its time derivative. This allows us to construct $\Delta\psi_{ab}$, the perturbation to the spacetime metric, and its time derivative, $\partial_t \Delta\psi_{ab}$. We detail this procedure in 3.B.

Constraint satisfaction

Writing down the perturbed initial data equations is only the first half of the problem. In practice, we need to make sure that solving them produces data that satisfies the Hamiltonian and momentum constraints. In the unperturbed case, we simply check that Eqs. (3.1) and (3.2) are satisfied. In the perturbed case, since we are computing a *linear perturbation*, we do not expect the full, non-linear constraints to be satisfied. Rather, the first-order linearization of these constraints should hold. We thus perturb these constraints to give

$$\Delta H \equiv \Delta R + 2K\Delta K - \Delta K_{ij}K^{ij} - K_{ij}\Delta K^{ij} - 16\pi\Delta\rho, \qquad (3.45)$$

for the perturbed Hamiltonian constraint, and

$$\begin{aligned} \Delta M_i \equiv\ & \Delta g^{jk}(D_j K_{ki} - D_i K_{jk}) \\ & + g^{jk}(\Delta(D)_j K_{ki} - \Delta(D)_i K_{jk} + D_j \Delta K_{ki} - D_i \Delta K_{jk}) - 8\pi\Delta S_i \end{aligned} \qquad (3.46)$$

for the perturbed momentum constraint. Constraint-satisfying perturbed initial data will thus have $\Delta H = 0$ and $\Delta M_i = 0$.

In practice, these conditions will never be exactly satisfied, but we can check that these quantities tend toward zero with increasing numerical resolution. In our case, we use a spectral code [198], and thus the constraint violation converges to zero exponentially. In order to give meaning to the level of constraint violation, we normalize each constraint by the magnitude of the fields contained therein.

Boundary conditions

Before solving elliptic equations for metric perturbations for a generic source ΔT_{ab}, we must impose boundary conditions. Specifically, we must impose conditions on $\Delta\psi$, ΔC, and $\Delta\beta^i$ at spatial infinity ($R \to \infty$). In our spectral code [198], we excise the black hole singularities from the computational domain via a surface that conforms to the apparent horizon (or is slightly inside the apparent horizon) [104]. Thus, for a background containing a black hole, we must specify boundary conditions on the excision surface. In the case of a black hole binary, there are two such excision surfaces, one for each hole, and thus we must specify boundary conditions on each of them.

Let us now consider the boundary conditions we would impose in the case where the background spacetime contains a single black hole. First, the matter distribution, and hence the source of the perturbation, should decay at least as fast as $1/R^2$ as $R \to \infty$. Thus, we can choose the conditions

$$\Delta\psi|_{r\to\infty} = 0, \tag{3.47}$$

$$\Delta\beta^i|_{r\to\infty} = 0, \tag{3.48}$$

$$\Delta C|_{r\to\infty} = 0. \tag{3.49}$$

These conditions agree with the perturbed boundary conditions for an isolated black hole spacetime given in [69, 154]. In practice, we extend the (finite) outer domain to $R = 10^{14}\,M$, more than sufficient to satisfy these conditions.

For conditions on the inner boundaries, which correspond to apparent horizons, we impose the set of apparent horizon boundary conditions for ψ, α, and β^i given in [69, 154]. The conditions ensure that the surface has zero expansion and has a desired value for the spin. In our case, we can perturb these apparent horizon boundary conditions to give conditions on $\Delta\psi$, ΔC, and $\Delta\beta^i$.

Specifically, for the unperturbed boundary conditions, the condition on ψ corresponds to setting the expansion of the surface to be zero, the condition on β^i corresponds to setting the spin and also setting the shear of the null rays on the horizon to be zero, while the condition on α is physically unconstrained and can be set with a Dirichlet condition. The condition on ψ takes the form

$$0 = -\bar{P}^i\partial_i\psi - B\psi + \frac{1}{8}\frac{\psi^4}{\alpha\psi}(C_{ij})(\bar{L}\beta^{ij} - u^{ij}) + \frac{\psi^3}{12}C^{ij}\bar{g}_{ij}K, \tag{3.50}$$

where

$$N \equiv \sqrt{\bar{g}^{ij}\hat{n}_i\hat{n}_j}\,, \tag{3.51}$$

$$\bar{P}^i \equiv \frac{\hat{n}_j\bar{g}^{ij}}{N}\,, \tag{3.52}$$

with $\hat{n}^i$ being the normal vector to the inner boundary, and

$$C^{ij} \equiv \bar{g}^{ij} - \bar{P}^i\bar{P}^j\,, \tag{3.53}$$

$$B \equiv \frac{1}{4N}(C^{ij})(\partial_j\hat{n}_i - \bar{\Gamma}^l_{ij}\hat{n}_l)\,. \tag{3.54}$$

When perturbing this condition, we must consider what to do with the perturbation to $\hat{n}^i$. If we set $\Delta\hat{n}^i = 0$, then the excision surface corresponds to a horizon for the background, and the overall shape of the surface is not perturbed. By choosing a non-zero $\Delta\hat{n}^i$, we can, for example, set the expansion of the background metric plus the first-order metric perturbation to zero, and hence have the surface correspond to a linearly perturbed horizon. In this study, we set $\Delta\hat{n}^i = 0$ for simplicity.

Perturbing Eq. (3.50), we thus obtain

$$\begin{aligned}
0 =\ & -\Delta\bar{P}^i\partial_i\psi - \bar{P}^i\partial_i\Delta\psi - \Delta B\psi - B\Delta\psi \tag{3.55}\\
& + \frac{1}{2}\frac{\psi^3\Delta\psi}{\alpha\psi}(C_{ij})(\bar{L}\beta^{ij} - u^{ij})\\
& - \frac{1}{8}\frac{\psi^4}{(\alpha\psi)^2}\Delta C(C_{ij})(\bar{L}\beta^{ij} - u^{ij})\\
& + \frac{1}{8}\frac{\psi^4}{\alpha\psi}(\Delta C_{ij})(\bar{L}\beta^{ij} - u^{ij})\\
& + \frac{1}{8}\frac{\psi^4}{\alpha\psi}(C_{ij})(\Delta(\bar{L}\beta^{ij}) - \Delta u^{ij})\\
& + \frac{\psi^2\Delta\psi}{4}C^{ij}\bar{g}_{ij}K + \frac{\psi^3}{12}\Delta C^{ij}\bar{g}_{ij}K + \frac{\psi^3}{12}C^{ij}\Delta\bar{g}_{ij}K\\
& + \frac{\psi^3}{12}C^{ij}\bar{g}_{ij}\Delta K
\end{aligned}$$

on the excision surface, where

$$\Delta N = \frac{1}{2N}\Delta\bar{g}^{ij}\hat{n}_i\hat{n}_j\,, \tag{3.56}$$

$$\Delta\bar{P}^i = \frac{\hat{n}_j\Delta\bar{g}^{ij}}{N} - \frac{\hat{n}_j\bar{g}^{ij}}{N^2}\Delta N\,, \tag{3.57}$$

$$\Delta C^{ij} = \Delta\bar{g}^{ij} - \Delta\bar{P}^i\bar{P}^j - \bar{P}^i\Delta\bar{P}^j\,, \tag{3.58}$$

$$\Delta B = -\frac{1}{4N^2}\Delta N(C^{ij})(\partial_j\hat{n}_i - \bar{\Gamma}^l_{ij}\hat{n}_l)\,, \tag{3.59}$$

$$+ \frac{1}{4N}(\Delta C^{ij})(\partial_j\hat{n}_i - \bar{\Gamma}^l_{ij}\hat{n}_l)$$

$$+ \frac{1}{4N}(C^{ij})(-\Delta\bar{\Gamma}^l_{ij}\hat{n}_l)\,.$$

Next, the background boundary condition on β^i takes the form

$$0 = \beta^i - \frac{1}{\psi^3}\frac{\hat{n}_j g^{ij}}{N}\alpha\psi - \xi^i \tag{3.60}$$

on the inner boundary. Here, ξ^i is the vector

$$\xi^i = \Omega_x X^i + \Omega_y Y^i + \Omega_z Z^i\,, \tag{3.61}$$

where Ω_i corresponds to the components of the orbital angular momentum, and X^i, Y^i, and Z^i have the form

$$X^i = (0, -z, y)\,, \tag{3.62}$$

$$Y^i = (z, 0, -x)\,, \tag{3.63}$$

$$Z^i = (-y, x, 0)\,. \tag{3.64}$$

Now, when we perturb this condition, we must consider how to perturb Ω_i. Setting this to a non-zero value gives a spin to the metric perturbation as well.

Perturbing Eq. (3.60), we thus obtain

$$0 = \Delta\beta^i + 3\frac{1}{\psi^4}\Delta\psi\frac{\hat{n}_j g^{ij}}{N}\alpha\psi \tag{3.65}$$

$$- \frac{1}{\psi^3}\frac{\hat{n}_j\Delta g^{ij}}{N}\alpha\psi$$

$$+ \frac{1}{\psi^3}\frac{\hat{n}_j g^{ij}}{N^2}\Delta N\alpha\psi$$

$$- \frac{1}{\psi^3}\frac{\hat{n}_j g^{ij}}{N}\Delta C$$

$$- \Delta\xi^i$$

on the excision surface, where $\Delta\xi^i$ is the vector

$$\Delta\xi^i = \Delta\Omega_x X^i + \Delta\Omega_y Y^i + \Delta\Omega_z Z^i \,. \tag{3.66}$$

The Dirichlet boundary condition on α, meanwhile, can be perturbed to give a Dirichlet boundary condition on ΔC. However, we are already solving Eq. (3.55) for $\Delta\psi$, and thus to uncouple these equations, we can instead try to drive $\Delta\alpha$ to some desired value $\Delta\alpha_{\text{Desired}}$ on the excision surface via the Dirichlet condition

$$0 = \Delta C - (\Delta\psi\alpha + \psi\Delta\alpha_{\text{Desired}}) \,. \tag{3.67}$$

We can generalize the isolated black hole case to a binary black hole case by applying Eqs. (3.55), (3.65), and (3.67) to each excision surface corresponding to a horizon and applying a boost in the case of an initial velocity.

Summary

Thus, in order to generate metric perturbation initial data given some source ΔT_{ab} and background spacetime metric ψ_{ab}, we solve the elliptic equations given in Sec. 3.2 for $\Delta\psi$, ΔC, and $\Delta\beta^i$. We then apply the formulae in Sec. 3.2 to construct $\Delta\psi_{ab}$, the perturbed spacetime metric for these variables. For the case where the background is an isolated black hole, we can apply the perturbed version of the horizon boundary conditions on $\Delta\psi$, ΔC, and $\Delta\beta^i$ given in Sec. 3.2. In order to generate stationary data on an isolated black hole background, we choose $\Delta\Omega_i$ in Eq. (3.65) to be equal to the Ω_i of the background.

Note that, as outlined in Sec. 3.2, we have the freedom to choose $\Delta\bar{g}_{ij}$, $\Delta\bar{u}_{ij}$, ΔK, and $\partial_t\Delta K$. To simplify the calculation in the isolated black hole case, we choose $\Delta\bar{g}_{ij} = 0$, and thus $\Delta g_{ij} = 4\psi^3\Delta\psi\bar{g}_{ij}$. For stationarity, we choose $\Delta\bar{u}_{ij} = 0$ and $\partial_t\Delta K = 0$ to set as many time derivatives to zero as possible. We similarly choose $\Delta K = 0$.

3.3 Solving for metric perturbations in dCS

Order reduction scheme

We now turn to applying the method for solving for metric perturbation initial data outlined in Sec. 3.2 to isolated black holes in dynamical Chern-Simons (dCS) gravity. The dCS action for a metric ψ_{ab} and scalar field ϑ is given by

$$\int d^4x\sqrt{-\psi}\left(\frac{m_{\text{pl}}^2}{2}R - \frac{1}{2}(\partial\vartheta)^2 - \frac{m_{\text{pl}}}{8}\ell^2\vartheta \,{}^*RR\right), \tag{3.68}$$

where ℓ is a coupling constant with dimensions of length,

$$^*RR \equiv {}^*R^{abcd}R_{abcd} \tag{3.69}$$

is the Pontryagin density, where $^*R^{abcd} = \frac{1}{2}\epsilon^{abef}R_{ef}{}^{cd}$ is the dual of the Riemann tensor and $\epsilon^{abcd} \equiv -[abcd]/\sqrt{-\psi}$ is the fully-antisymmetric Levi-Civita tensor, and $m_{\rm pl}$ is the Planck mass.

Varying the action in Eq. (3.68), we obtain a sourced wave equation for the scalar field,

$$\Box\vartheta = \frac{m_{\rm pl}\ell^2}{8}\,{}^*RR\,, \tag{3.70}$$

where $\Box \equiv \nabla_a\nabla^a$ is the d'Alembertian operator. For the metric, we obtain a corrected Einstein field equation

$$m_{\rm pl}^2 G_{ab} + m_{\rm pl}\ell^2 C_{ab} = T_{ab}\,, \tag{3.71}$$

where T_{ab} is the kinetic stress-energy tensor of ϑ,

$$T_{ab} = \nabla_a\vartheta\nabla_b\vartheta - \frac{1}{2}\psi_{ab}\nabla_c\vartheta\nabla^c\vartheta\,, \tag{3.72}$$

and

$$C_{ab} \equiv \epsilon_{cde(a}\nabla^d R_{b)}{}^c\nabla^e\vartheta + {}^*R^c{}_{(ab)}{}^d\nabla_c\nabla_d\vartheta\,. \tag{3.73}$$

Note that C_{ab} contains third derivatives of the metric, and thus these equations of motion must likely not have a well-posed initial value problem [74]. However, in the perturbation limit, we can solve these equations of motion using an *order reduction scheme*, expanding the metric and scalar field in powers of a parameter ε that counts powers of ℓ^2:

$$\psi_{ab} = \psi_{ab}^{(0)} + \sum_{k=1}^{\infty}\varepsilon^k h_{ab}^{(k)}\,, \tag{3.74}$$

$$\vartheta = \sum_{k=0}^{\infty}\varepsilon^k\vartheta^{(k)}\,. \tag{3.75}$$

The key is that at each order of this scheme, we will obtain equations of motion with the same principal part as GR. Perturbing around GR is justified in part by the first LIGO detection, which showed that deviations from GR in black hole systems are small [14].

At zeroth order in ε, we obtain for our equations of motion

$$m_{\mathrm{pl}}^2 G_{ab}[\psi^{(0)}] = T_{ab}^{(0)}, \tag{3.76}$$

$$\Box^{(0)}\vartheta^{(0)} = 0, \tag{3.77}$$

where $T_{ab}^{(0)}$ is the stress-energy tensor constructed from $\vartheta^{(0)}$. Since the zeroth order scalar field has no source, we can take $\vartheta^{(0)} = 0$. This is turn means that the equation for the metric at zeroth order is a pure GR Einstein field equation.

At first order, meanwhile, we obtain the equation

$$\Box^{(0)}\vartheta^{(1)} = \frac{m_{\mathrm{pl}}}{8}\ell^2 [\,{}^*RR]^{(0)} \tag{3.78}$$

for the first-order scalar field $\vartheta^{(1)}$ and the equation

$$m_{\mathrm{pl}}^2 G_{ab}[h^{(1)}] = -m_{\mathrm{pl}}\ell^2 C_{ab}^{(0)} + T_{ab}^{(1)} \tag{3.79}$$

for the first-order metric perturbation, where G_{ab} is the Einstein-Hilbert operator of the background acting on the metric perturbation. Here, $C_{ab}^{(0)}$ is the background value of the tensor defined in Eq. (3.73), and $T_{ab}^{(1)}$ is the first-order perturbation to the stress-energy tensor given in Eq. (3.72). However, both $C_{ab}^{(0)}$ and $T_{ab}^{(1)}$ are linear in $\vartheta^{(0)}$, which vanishes, and hence $-m_{\mathrm{pl}}\ell^2 C_{ab}^{(0)} + T_{ab}^{(1)}$, the RHS of Eq. (3.79) vanishes, leaving an unsourced metric perturbation,

$$m_{\mathrm{pl}}^2 G_{ab}[h^{(1)}] = 0. \tag{3.80}$$

Thus, at first order in ε, $h^{(1)} = 0$, there is no modification to the metric, and the scalar field is governed by Eq. (3.78). Indeed, in [146], we evolved this ε^1 system on a binary black hole background.

We now turn to order ε^2, where we obtain a metric perturbation sourced by $\vartheta^{(1)}$. Specifically, we obtain

$$m_{\mathrm{pl}}^2 G_{ab}[h^{(2)}] = -m_{\mathrm{pl}}\ell^2 C_{ab}^{(1)}[\vartheta^{(1)}] + T_{ab}^{(2)}[\vartheta^{(1)}, \vartheta^{(1)}]. \tag{3.81}$$

Here, the first term on the right-hand side is the perturbed C-tensor formed from the background metric and the non-vanishing first-order scalar field $\vartheta^{(1)}$ (and hence is non-zero). The second term is the second-order perturbation to the stress-energy tensor, quadratic in $\vartheta^{(1)}$, and hence also non-zero.

To simplify the equations and to more easily use the results of the previous section, it is useful to define a new variable Ψ by

$$\vartheta^{(1)} \equiv \frac{m_{\mathrm{pl}}}{8}\ell^2 \Psi, \tag{3.82}$$

which gives, at first-order

$$\Box\Psi = {}^*RR\,. \tag{3.83}$$

Here all metric variables now correspond to the background (in other words, ${}^*RR = [{}^*RR]^{(0)}$, for example). Similarly, let $\Delta\psi_{ab}$ correspond to the second-order metric perturbation by defining

$$h_{ab}^{(2)} \equiv \frac{\ell^4}{8}\Delta\psi_{ab}\,. \tag{3.84}$$

The equation for the metric perturbation is thus

$$G_{ab}[\Delta\psi_{ab}] = T_{ab}^{\rm eff}(\Psi), \tag{3.85}$$

where

$$T_{ab}^{\rm eff}(\Psi) \equiv -C_{ab}(\Psi) + \frac{1}{8}T_{ab}(\Psi)\,. \tag{3.86}$$

We can then write the C-tensor and matter terms in the form

$$C_{ab}(\Psi) = \epsilon_{cde(a}\nabla^d R_{b)}{}^c\nabla^e\Psi + {}^*R^c{}_{(ab)}{}^d\nabla_c\nabla_d\Psi\,, \tag{3.87}$$

$$T_{ab}(\Psi) = \nabla_a\Psi\nabla_b\Psi - \frac{1}{2}\psi_{ab}\nabla_c\Psi\nabla^c\Psi\,. \tag{3.88}$$

The first term of C_{ab} vanishes when working on a vacuum GR background.

Thus, $\Delta\psi_{ab}$ is governed by the Einstein tensor and is a perturbation off a GR background of the form $\psi_{ab} \to \psi_{ab} + \Delta\psi_{ab}$ with source $T_{ab}^{\rm eff}$. Comparing this to Eq. (3.21), we can thus use the formalism developed in Sec. 3.2 to solve for $\Delta\psi_{ab}$ sourced by $T_{ab}^{\rm eff}$ on a black hole background.

Scalar field initial data

Before solving for $\Delta\psi_{ab}$, however, we need a scalar field Ψ on a black hole background that obeys Eq. (3.83). Moreover, in order to obtain stationary data for $\Delta\psi_{ab}$, we require that Ψ is stationary. Rather than attempting to find an analytical solution, we use the numerical solution for Ψ computed using the methods in [184]. This solution is valid for any spin. However, this solution is expressed in Boyer-Lindquist coordinates, which are singular at the horizon, and thus we transform to Kerr-Schild coordinates. The transformation to Kerr-Schild coordinates is given, e.g., in [135].

We check that the solution for Ψ is constraint satisfying, and moreover that it is stationary. Note that the solution given in [184] has its own inherent resolution in

terms of the number of radial and angular basis functions. Including more radial basis functions in this solution increases its stationarity. We interpolate the solution onto our grid, generally with a different resolution.

Given this solution for Ψ, we then construct the perturbed source terms of Eqs. (3.115), (3.116), (3.117), and (3.118) using $\Delta T_{ab} = T_{ab}^{\text{eff}}$ computed from Ψ via Eq. (3.86).

dCS metric perturbation results

Given these source terms, we then apply the formalism developed in Sec. 3.2 to solve for $\Delta\psi_{ab}$. We verify that our results are convergent by checking the perturbed constraints given in Sec. 3.2. We solve for the data on a set of nested spherical shells extending from the apparent horizon to $R = 10^{14} M$, all with equal numbers of spectral collocation points. Fig. 3.1 presents the behavior of the normalized, perturbed Hamiltonian and momentum constraints with increasing resolution. The figure shows the exponential convergence of the constraints to zero as the numerical resolution increases. Higher spins in Kerr-Schild coordinates require more grid points to fully resolve the solution, and thus have a slower level of convergence. Recall likewise that we wish to solve for stationary initial data. In practice, the stationarity converges with increasing resolution. However, at the same numerical resolution, a lower spin will have a greater stationarity, as measured by $\|\Delta g_{ij}\|/\|g_{ij}\|$, than a higher spin. Thus, when comparing quantities across spins in practice, we choose resolutions that give the same level of non-stationarity to mitigate these spin-dependent effects.

In summary, we have constraint-satisfying data for the second-order metric perturbation in order-reduced dCS gravity. In Fig. 3.2, we plot the profiles for the scalar field Ψ as well as the conformal factor $\Delta\psi$.

The extended conformal thin sandwich formalism can potentially suffer from ill-posedness and non-uniqueness problems if the equations do not have a positive-definite linearization [39, 202]. In our case, however, we do not see the appearance of non-unique solutions.

3.4 Physics with dCS metric perturbations

We now consider what physics we can extract from these solutions for $\Delta\psi_{ab}$ in dCS.
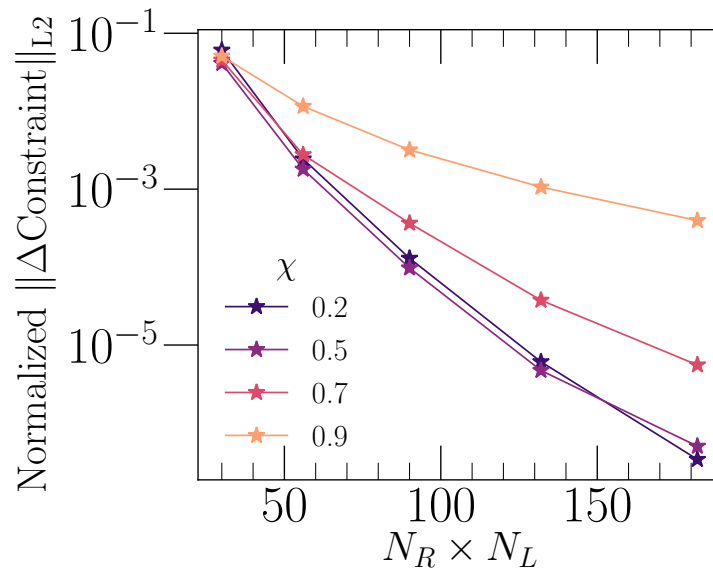
Figure 3.1: Convergence of the perturbed constraints with resolution for a metric perturbation $\Delta\psi_{ab}$ on a Kerr background with given dimensionless spin χ. We evaluate the constraints on the entire numerical grid. The horizontal axis is the number of radial basis functions N_R times angular basis functions N_L in a representative subdomain of our numerical grid. As this number increases, the constraint violation exponentially converges to zero. Higher-spin black holes require more grid points to achieve the same level of constraint satisfaction in the metric perturbation as lower-spin black holes, just as for the unperturbed background spacetime.

Regime of validity

To second order, the perturbed metric takes the form

$$\psi_{ab} \rightarrow \psi_{ab} + \varepsilon^2 \Delta\psi_{ab} \tag{3.89}$$

where ε^2 determines the amplitude of the metric perturbation. For the perturbative scheme to be valid, we require that $\|\psi_{ab}\| \gtrsim \|\varepsilon^2 \Delta\psi_{ab}\|$, where $\|\,\|$ denotes the L2 norm of the field. The values of ε^2 that satisfy this condition define the *regime of validity*. We can measure this value of ε^2 by comparing the magnitudes of ψ_{ab} and $\Delta\psi_{ab}$ as

$$\varepsilon^2_{\max} = 0.1 \left(\|\frac{\psi_{ab}}{\Delta\psi_{ab}}\| \right)_{\min}. \tag{3.90}$$

Here the ratio is taken pointwise on the domain, we have chosen a constant 0.1 for the comparison, and we find a global minimum (the minimum is close to the horizon, where the perturbation is the largest). We plot the results in Fig. 3.3, where
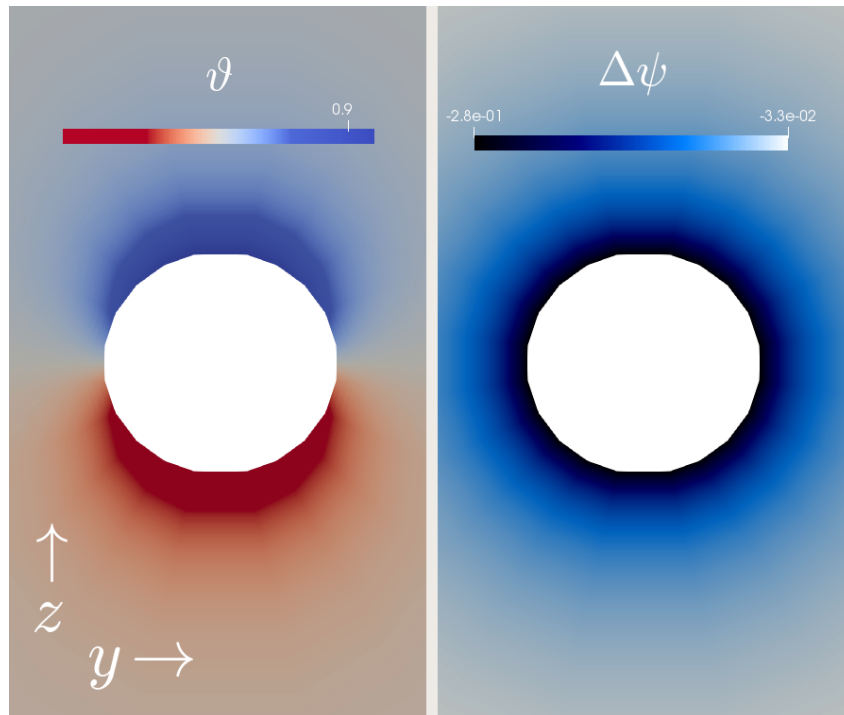
Figure 3.2: Plot of the numerical solution for Ψ from [184] (left) and perturbed conformal factor $\Delta\psi$ (right) on a spin $\chi = 0.6$ black hole background, shown in the y-z plane. Note that the solution is axisymmetric about the z-axis.

for lower spins, larger values of ε^2 are allowed. Recall that ε counts powers of ℓ^2/GM, and thus we can map this regime of validity result to ℓ as well.

Black hole shadows

One application of this initial data framework is to study modifications to the black hole shadow. Observing black hole shadows explores an entirely new scale of gravitational curvature and thus can test GR in a wholly new way [37]. Since looking at the shadow effectively involves observing the behavior of test particles (photons) moving on geodesics in the spacetime, observing the shadows of stationary black holes serves as a *metric test* of GR.

EHT capabilities and previous work

Let us first review the capabilities of the Event Horizon Telescope (EHT) for detecting black hole shadows. The EHT is a very long baseline interferometry array of radio telescopes around the world that aims to generate images of the black hole at the center of the Milky Way galaxy, Sgr A*, as well as that of the M87 galaxy, with horizon-scale resolution. Electromagnetic images show not the actual horizon,
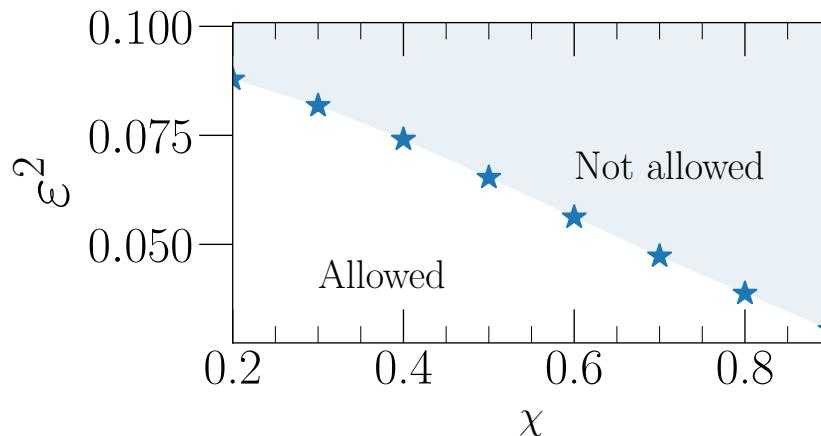
Figure 3.3: Evaluation of the regime of validity as given by Eq. (3.90), for various values of spin. The top region is not allowed by perturbation theory, while the bottom region is allowed. The stars denote the values of χ at which we have evaluated Eq. (3.90). We can compare this to the regime of validity figure given in [184].

but the region external to the light ring at $3GM/c^2$, which serves as a probe of the black hole shadow [85]. Resolving Sgr A* requires an angular resolution of $\mathcal{O}(10)$ microarcseconds (μas) [164]. Once complete, the array should have resolutions of up 23 μas at 230 GHz and 15 μas at 345 GHz [170]. The size of Sgr A*'s visible event horizon is predicted to be $\sim 50\,\mu$as [84], with the photon ring contributing to $1-10\%$ of the total flux [75].

Actually predicting what black hole images will look like for Sgr A* and M87, however, requires simulating the matter around the black hole using GRMHD simulations (cf. [164] for a review). However, as the shadow only depends on the black hole spacetime, the shadow is not affected by the presence of matter [166]. Nevertheless, observing the shadow free from obscuration due to the accretion onto the black hole (and gravitational lensing thereof) is a technical challenge. Additionally, interstellar scattering affects the resolution of the image [164]. In this study, we only consider null rays and the scalar field around a black hole otherwise in vacuum when probing the shadow, and thus do not include the matter effects.

How well can the edge of the shadow be detected? Psaltis et al. [166] took advantage of the fact that the black hole shadow produces some of the steepest gradients in an image, and applied various edge-finding algorithms to locate the shadow. In practice, thus, it is possible to extract to an extent an edge corresponding roughly to the black hole shadow to within $\sim 9\%$, assuming a given scattering kernel.

How well can current algorithms measure the properties of the black hole shadow of Sgr A*? Fig. 13 of Psaltis et al. [164] shows a combined posterior distribution for the black hole quadrupole moment q and the black hole spin a for a hypothetical observation of Sgr A*. If the black hole is Kerr, then there should be a unique point in this space for each mass and spin on the curve $q = -a^2$. EHT observations give a wide curve in the q-a space, while constraints from spin measurements from stars and pulsars around Sgr A* provide tighter constraints. Nevertheless, the spin in this posterior can only be predicted to an accuracy of $\sigma_a \sim 0.1$.

Previous studies have calculated (without considering matter effects) black hole shadows in alternative theories of gravity (see [84] and [164] for a review). Additionally, Ref. [108] reviews the detectability of effective *deviation parameters* from otherwise GR predictions.

Computing the shadow

We now compute the second-order deviation to the black hole shadow in order-reduced dynamical Chern-Simons gravity. Recall that we have solved for a metric perturbation $\Delta\psi_{ab}$ around an isolated black hole of a given spin. We can then add it to the background metric ψ_{ab} via a coupling parameter ε^2 that lies in the regime of validity outlined in Sec. 3.4. The overall metric is thus

$$\psi_{ab}^{\text{pert}} \equiv \psi_{ab} + \varepsilon^2 \Delta\psi_{ab}. \tag{3.91}$$

We compute the dCS black hole shadow in this metric, which will be correct to second order. Note that since we have solved for stationary data, we only need to evolve geodesics on one time slice to trace the shadow, as all of the slices will be the same. Note also that since the shadow is a physical observable, we do not need to worry about gauge effects.

To probe the shadow, we use the geodesic integration methods (and corresponding code) outlined in [54] and [53]. We refer the reader to those papers for a technical discussion. Schematically, we start geodesics from a camera some $C = O(10)\,M$ away from the black hole and integrate them backwards in time. The geodesics that make it to past null infinity (which we approximate as a distance of $2C$ from the black hole in order to avoid integrating geodesics to infinity) are labeled as not in the shadow, while the geodesics that converge onto the horizon determine the edge of the shadow. The code has built-in refinement, and with increasing resolution more geodesics are added along the shadow edge.

Analyzing the shadow

We now present a novel way to analyze the black hole shadow as computed from evolving null geodesics. Note that there exist previously-proposed methods of analyzing the shadow [17]. Given the shadow edge in the x-y plane of the camera (also known as the *image plane*), parameterized as two functions $x(\theta)$ and $y(\theta)$ where θ is the angle about some chosen center, we can Fourier decompose the shadow edge as

$$x(\theta) = a_0 + \sum_{n=1}^{N} a_n \cos(n\theta), \tag{3.92}$$

$$y(\theta) = b_0 + \sum_{n=1}^{N} b_n \sin(n\theta), \tag{3.93}$$

up to some number N of fitting coefficients. We define a measure of the power in each Fourier mode as

$$f_n \equiv \sqrt{a_n^2 + b_n^2}. \tag{3.94}$$

In this procedure, one must take precautions in defining the axes and the origin for θ. Suppose we have an image of a black hole shadow. For simplicity, assume that the spin axis has no component normal to the plane of the camera, but has some arbitrary orientation in that plane. Given such an image, we can find a line about which the image has a reflection symmetry. Let this be the x-axis (in the case of $\chi = 0$, we can take any axis).

Next, we need to define an origin $\{x_0, y_0\}$ in the x-y plane from which to measure the angle θ. For y_0, we can simply choose $y_0 = 0$ since we have defined $y = 0$ to be the axis of reflection symmetry. For x_0, however, we need to be more careful. In the $\chi = 0$ case, for example, one can choose an x_0 such that the decomposition has an artificially non-zero $n = 2$ multipole. Thus, we choose x_0 to be the point at which the value of f_2 is minimized. We show the result of this procedure in Fig. 3.4.

We also check that the values of the coefficients given in the decomposition (3.94) converge with resolution. We show a quantitative convergence analysis in Fig. 3.5. We check convergence for each shadow we analyze, for a given χ and ε^2.

The $n = 0$ multipole refers to the coordinate location of the shadow center in the plane of the camera, which is not gauge-invariant and hence not meaningful. The $n = 1$ multipole corresponds to the "size" of the shadow and is proportional to
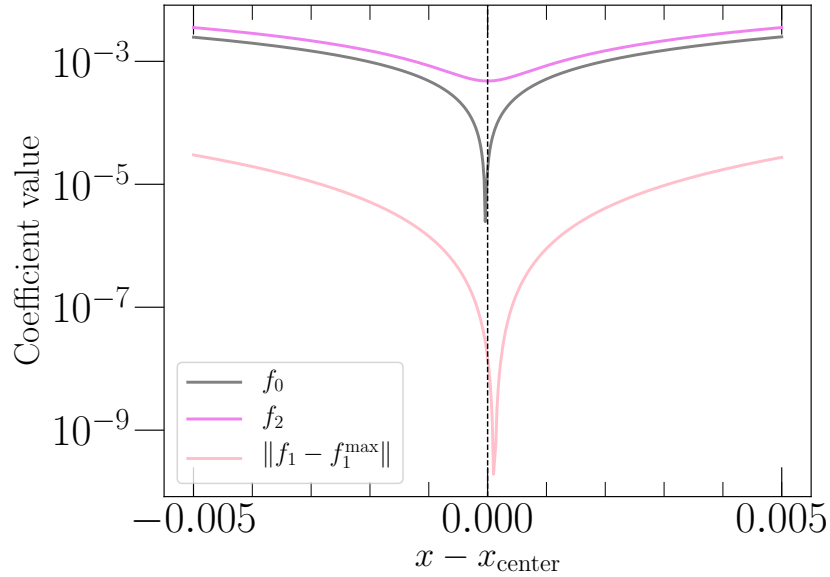
Figure 3.4: Results of our procedure for designating the center (and hence the origin for the angle θ) of a black hole shadow for $\chi = 0.9$ and $\varepsilon^2 = 0$. We find the central value of x by minimizing the recovered $n = 2$ multipole for each trial value. Here, we plot in the dashed black line the optimal value of x. We see that when x is chosen to minimize $n = 2$, it also minimizes the artificial $n = 0$ multipole. Note that the minimum value of the $n = 2$ multipole is finite, as the shadow shape is non-spherical. Additionally, we plot the difference between the $n = 1$ multipole and its maximum value, finding that it attains the maximum near but not at the optimum center value as the shape is not exactly spherical.

both the mass of the black hole and the distance to the camera. Thus, the value of the $n = 1$ multipole is not meaningful as there is a mass-distance degeneracy. However, dividing all of the $n > 1$ multipoles f_n by f_1 gives normalized values that are independent of the mass and distance, and in the $\varepsilon^2 = 0$ case, only dependent on the dimensionless spin. We have verified this numerically by changing the mass of the black hole, and checking that the normalized $n > 1$ coefficients remain the same. We thus focus our attention on the $n > 1$ multipoles normalized by f_1, which have physical meaning.

Now, in the presence of a nonzero ε, we still apply this same procedure (orienting on the axis of reflection symmetry, finding the center by minimizing f_2, then dividing through by f_1). Note that in this case, we expect the higher multipoles to have a different dependence on χ and now ε. We will need to observe at least two multipoles to perform a consistency check with the $\varepsilon = 0$ case, or to estimate ε and
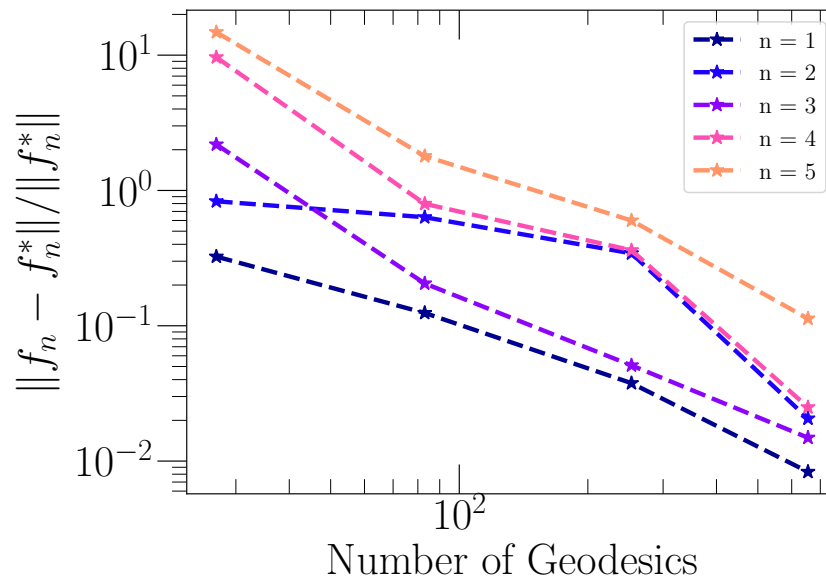
Figure 3.5: Convergence of the shadow multipoles with resolution for a spin $\chi = 0.9$ black hole for $\varepsilon^2 = 0$. For each multipole ($n = 1$ to $n = 5$), we plot the normalized difference of the value of the multipole from the highest resolution value (denoted as f_n^*), as a function of resolution. Here, the x-axis corresponds to the number of geodesics that converge onto the horizon when integrated backwards in time, and hence are used to image the black hole shadow. As we increase this resolution, the normalized differences from the highest resolution value decrease. We see that the higher multipoles, which take more geodesics to resolve, converge more slowly than the lower multipoles.

χ if we find $\varepsilon \neq 0$.

Results

Let us now analyze the black hole shadow using the procedure outlined in this section for various dimensionless spins χ of the background black hole and perturbation parameters ε^2. In accordance with the feasibility study shown in Fig. 13 of [164], we concentrate our attention on spins of $\chi = 0.6$. In Fig. 3.6, we plot the black hole shadow for $\chi = 0.6$ for $\varepsilon^2 = 0$ (i.e., the shadow as predicted by GR) and $\varepsilon^2 = 0.05$, the maximal value allowed by the regime of validity. Additionally, we plot the GR shadows for $\chi = 0.7$ and $\chi = 0.9$ black holes. We see that shifting the spin away from 0.6 has a greater effect than adding a dCS perturbation. Given the $\sigma_a \sim 0.1$ spread in the recovered spin for the trial EHT measurement in Ref. [164], it is informative to compare the effect of increasing χ by 0.1 versus increasing ε^2
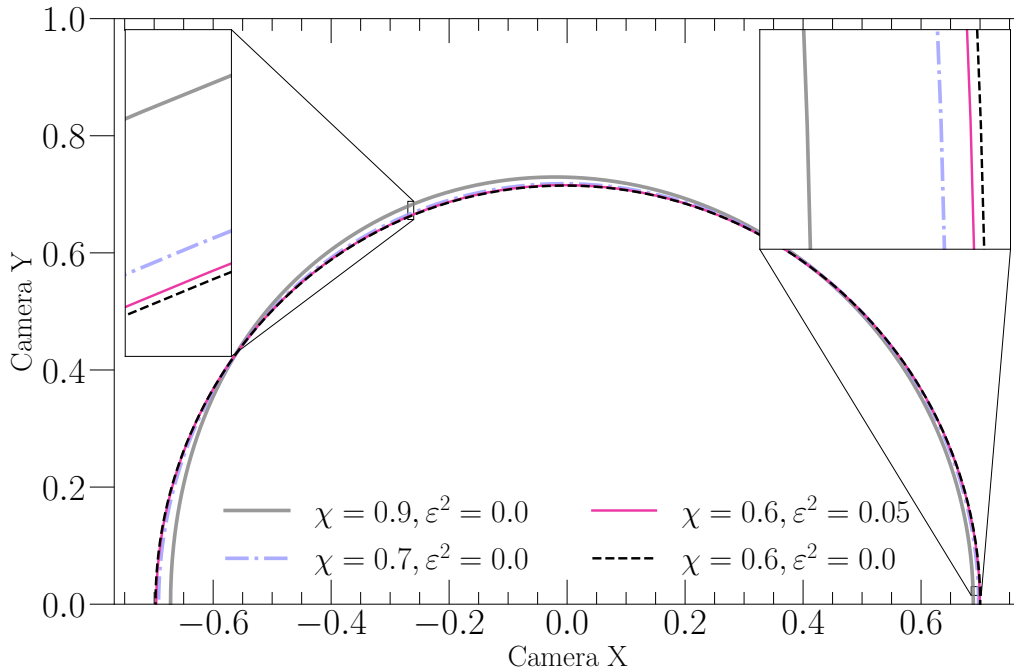
Figure 3.6: Visualization of black hole shadows. The x- and y-axes correspond to camera coordinates for a camera resolving the black hole, and thus are not physically meaningful. The shape of each shadow has been normalized by its overall "size" as given by the $n = 1$ multipole. Likewise, each shadow has been centered according the procedure described in this paper. We plot the shadow for spin of $\chi = 0.6$, with dCS perturbation parameters $\varepsilon^2 = 0$ and $\varepsilon^2 = 0.05$, the maximum allowed within the regime of validity. Zooming in, we see a difference in the two shadows. However, increasing the spin to $\chi = 0.7$ without a dCS perturbation (and even $\chi = 0.9$) has a stronger effect on the shape of the shadow. We have checked that increasing the resolution of the shadow by integrating more geodesics has a smaller effect than aforementioned the physical effects.

to its maximum valid value at a given χ. We see that the effect increasing ε^2 on the visual shape of the shadow is less than the effect from increasing χ.

We can quantitatively analyze the shape of the shadow by considering the values of f_2/f_1 and f_3/f_1, the two dominant normalized multipoles. Considering again spins around $\chi = 0.6$, we plot the values of these multipoles with increasing ε^2 in Figs. 3.7a and 3.7b. We see that, for a given spin, as we increase ε^2, the values of f_2/f_1 and f_3/f_1 linearly deviate away from the $\varepsilon^2 = 0$, GR prediction. Since the shadow, with the mass normalized away, is dependent only on χ and ε^2 in dCS, we can map

$$\{\chi, \varepsilon^2\} \rightarrow \{f_2/f_1, f_3/f_1\}, \tag{3.95}$$
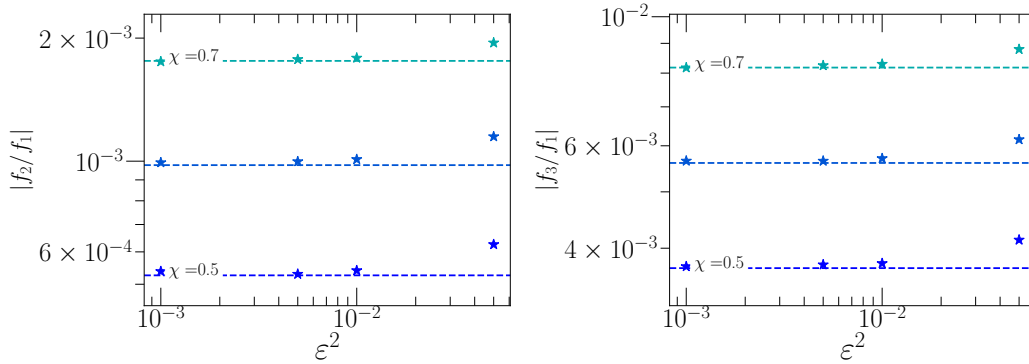
Figure 3.7: Values of the f_2 and f_3 coefficients of the black hole shadow, as calculated using the methods outlined in Sec. 3.4. Each coefficient is normalized by f_1, which corresponds to the size of the shadow. Each dashed line shows the $\varepsilon^2 = 0$ value of the coefficient, corresponding to an unperturbed GR black hole, for spins $\chi = 0.5$, $\chi = 0.6$, and $\chi = 0.7$ (as labeled on the plot). Since the shadow in GR becomes less spherical with increasing spin, it is consistent that the f_2 and f_3 coefficients, which correspond to non-spherical multipoles, increase with spin. For each spin, we also plot the values of the multipoles when we introduce a dCS perturbation of the form $\psi_{ab} + \varepsilon^2 \Delta\psi_{ab}$. As we increase ε^2 (up to a value given by the regime of validity of perturbation theory), we see that these coefficients increase as well, in a power-law fashion. We have checked that increasing the resolution of the shadow by integrating more geodesics leads to convergent results for the multipoles and does not affect the results on the scale presented here.

for each choice of χ and ε^2.

While the mapping shown in Eq. (3.95) is unique for each $\{\chi, \varepsilon^2\}$ pair, it may not be invertible. In other words, degeneracies may exist such that a given pair $\{f_2/f_1, f_3/f_1\}$ can be generated by more than one combination of $\{\chi, \varepsilon^2\}$. In particular, this degeneracy can spoil a GR null hypothesis test using the shadow. Suppose there exists a spin χ_a and $\varepsilon_a^2 \neq 0$ combination such that the corresponding f_2/f_1 and f_3/f_1 values are equal to those of a χ_b and $\varepsilon_b^2 = 0$ shadow. Then, we would not be able to distinguish a black hole with a dCS perturbation from a Kerr black hole with a different spin.

We explore this potential degeneracy in Fig. 3.8. Using the $\varepsilon^2 = 0$ values of f_2/f_1 and f_3/f_1 for various spins, we trace out a curve in this multipolar parameter space. This curve is solely parametrized by spin χ, and any deviation away from this curve corresponds to some additional, non-Kerr effects. We call this the "Kerr" curve. Then, considering $\chi = 0.6$ and neighboring spins, we consider the effect of adding an $\varepsilon^2 = 0.05$ dCS perturbation. We see that in the presence of $\varepsilon^2 \neq 0$, the

multipolar values deviate away from the Kerr curve. In other words, we do not have a χ-ε^2 degeneracy. This in turn makes a GR null-hypothesis test possible using dCS shadows. On the other hand, we can also see from the figure that it may be difficult to distinguish various $\{\chi, \varepsilon^2 \neq 0\}$ pairs. However, since ε^2 is a universal parameter, observing more and more black hole shadows in practice should statistically narrow the value.

Let us now consider these results in the context of the EHT capabilities outlined in Sec. 3.4. We claim, given our investigation of the shape of the shadow, that precisely quantifying χ and ε^2 for Sgr A*, for example, may be infeasible with the current EHT resolution. Given that observations can yield a spread of as much as 0.2 in the spin, and given that we have seen that dCS effects for the maximum allowed values of ε^2 are smaller than a 0.1 increase in the spin, it will be difficult to observe such a deviation with the EHT. However, increasing the resolution of EHT shadow edge observations will allow us to perhaps probe these small effects, in part to perform an analysis to check for $\varepsilon^2 = 0$ consistency, or at least bound large values of ε^2.

Suppose that an external measurement of the mass of Sgr A* was available. Because the size of the shadow on the camera depends not only on mass but also on distance, we would need to have a measurement of the distance of Sgr A* as well. In this case, we would not need to normalize all of $f_{>1}$ coefficients by f_1, since the mass would be known. However, the f_1 multipole is independent of spin, and thus a deviation of the f_1 multipole predicted from an independent measurement of the mass and distance of Sgr A* could point to a non-GR signature. Such an analysis was performed, for example in [166].

On the other hand, suppose there were an independent measurement of the spin of Sgr A* from pulsars [165], with tighter constraints than the example shown in Ref. [164]. If χ was known precisely from pulsar measurements, then we would simply use the value of the dominant multipole f_3 to observe deviations from the predicted value in the case of $\varepsilon^2 = 0$. Fig. 3.7b shows the value of f_3 away from its predicted GR value for a spin of $\chi = 0.6$, for example. Knowing precisely the value of χ would thus allow us to constrain the value of ε^2 in the ε^2 - f_3 space. However, we must be careful in noting that this would only serve as a null-hypothesis test of GR, as inferring χ from pulsar measurements (presently) assumes that GR is the underlying model.
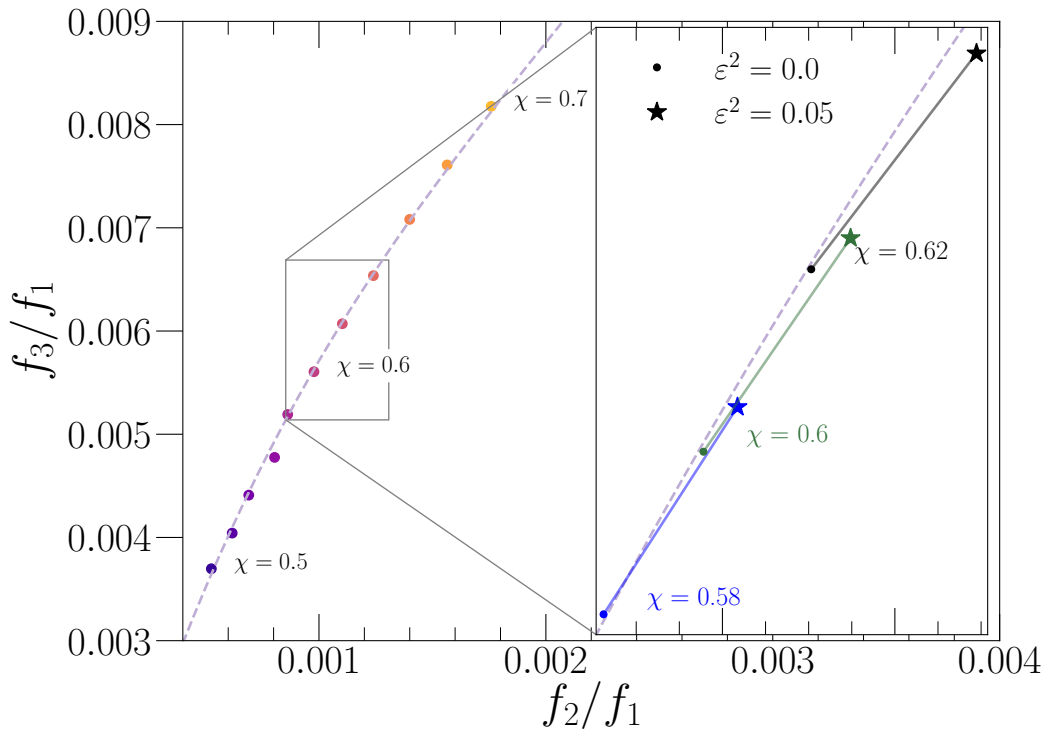
Figure 3.8: Normalized black hole shadow coefficients of the $n = 2$ (x-axis) and $n = 3$ (y-axis) multipoles. These correspond to the dominant non-spherical multipoles. The figure explores degeneracies in the χ-ε space. In the **(left)** panel, we plot the coefficient values for $\varepsilon^2 = 0$ for a variety of spins from $\chi = 0.5$ to $\chi = 0.7$. We additionally plot a curve (dashed line) that we have fit for all of the $\varepsilon^2 = 0$ coefficient values over a broader range of spins ($\chi = 0.1$ to $\chi = 0.9$). This line is the Kerr curve in the f_2-f_3 space. In the **(right)** panel, we introduce dCS perturbations. We plot again the Kerr curve, and consider coefficient values for spins of 0.58, 0.6, and 0.62. We see that when we introduce a dCS perturbation of strength $\varepsilon^2 = 0.05$, the values of the coefficients deviate from the Kerr curve. The fact that the perturbed values do not lie on the Kerr curve gives us a handle on the amount of degeneracy in the χ-ε space. We have checked that these effects are convergent with increasing the resolution of the shadow by integrating more geodesics.

3.5 Conclusion

In this chapter, we have presented a method for numerically generating metric perturbation initial data (Sec. 3.2), applied it to dynamical Chern-Simons gravity (Sec. 3.3), and investigated black hole shadows in the presence of dCS metric perturbations (Sec. 3.4).

The metric perturbation initial data computation is fully general, meaning that given some metric perturbation source, background spacetime, and boundary conditions (as well as specifying a choice of the free data), we can produce constraint-convergent first-order metric perturbation results. In particular, we can easily extend the dCS initial data results for a single black hole presented in this paper to the binary case. We can also, for example, apply this initial data formalism to explore linear versus non-linear metric perturbations in a standard Kerr spacetime, as our metric perturbation data is constraint-satisfying to first order (for example, to compare to the metric perturbation data used in [78] and [47]).

Future work in this program involves evolving dCS initial metric perturbations. This is done following the order-reduction scheme (cf. Sec.3.3 and [146]), which guarantees well-posedness, as each order in the scheme has the same principal part as the general relativity background. One possibility is to evolve a single spinning black hole to see if it is stable. A second is for the binary black hole case. There, we can evolve the metric perturbation sourced by the dCS scalar field and generate perturbed gravitational waveforms, thus performing the next step of the program outlined in [146].

3.A Perturbed extended conformal thin sandwich quantities

In this appendix, we derive the first-order perturbations to all of the extended conformal thin sandwich quantities, which enter into Eqs. (3.32), (3.44), and (3.37).

First, the perturbation to the inverse of the conformal spatial metric is

$$\Delta \bar{g}^{ij} = -\bar{g}^{ik} \bar{g}^{jm} \Delta \bar{g}_{km} \,. \tag{3.96}$$

We can use this to obtain the useful identities

$$\Delta V_i = \Delta \bar{g}_{ij} V^j + \bar{g}_{ij} \Delta V^j \,, \tag{3.97}$$

$$\Delta F^{kl} = \Delta \bar{g}_{ki} \bar{g}_{lj} F^{ij} + \bar{g}_{ki} \Delta \bar{g}_{lj} F^{ij} + \bar{g}_{ki} \bar{g}_{lj} \Delta F^{ij} \,, \tag{3.98}$$

$$\Delta F = \Delta \bar{g}^{ij} F_{ij} + \bar{g}^{ij} \Delta F_{ij} \,, \tag{3.99}$$

for vectors V^i with perturbation ΔV^i and tensor F_{ij} with trace F and perturbation ΔF_{ij}.

The covariant derivative operator $\bar{D}$ will also have a perturbation. We perturb the Christoffel symbols corresponding to $\bar{g}_{ij}$ to obtain

$$\Delta\bar{\Gamma}^i_{jk} = \frac{1}{2}\Delta\bar{g}^{il}(\partial_k\bar{g}_{lj} + \partial_j\bar{g}_{lk} - \partial_l\bar{g}_{jk}) + \frac{1}{2}\bar{g}^{il}(\partial_k\Delta\bar{g}_{lj} + \partial_j\Delta\bar{g}_{lk} - \partial_l\Delta\bar{g}_{jk})\,. \tag{3.100}$$

This in turn gives the useful perturbed derivative identities

$$\Delta(\bar{D})_i S = 0, \tag{3.101}$$

$$\Delta(\bar{D})^i S = \Delta\bar{g}^{ij}\bar{D}_j S, \tag{3.102}$$

$$\Delta(\bar{D}^2)S = \Delta\bar{g}^{ij}\partial_i\partial_j S - \Delta\bar{g}^{ij}\bar{\Gamma}^l_{ij}\partial_l S - \bar{g}^{ij}\Delta\bar{\Gamma}^l_{ij}\partial_l S \tag{3.103}$$

$$\Delta(\bar{D})_i V^j = \Delta\bar{\Gamma}^i_{jk}V^k, \tag{3.104}$$

$$\Delta(\bar{D})_i V_j = \Delta\bar{\Gamma}^k_{ij}V_k, \tag{3.105}$$

$$\Delta(\bar{D})^i V^j = \Delta\bar{g}^{ik}\bar{D}_k V^j + \bar{g}^{ik}\Delta\bar{\Gamma}^j_{kl}V^l, \tag{3.106}$$

$$\Delta(\bar{D})_k F_{ij} = -\Delta\bar{\Gamma}^m_{ki}F_{mj} - \Delta\bar{\Gamma}^m_{kj}F_{im}, \tag{3.107}$$

$$\Delta(\bar{D})_k F^{ij} = \Delta\bar{\Gamma}^i_{km}F^{mj} + \Delta\bar{\Gamma}^j_{km}F^{im}, \tag{3.108}$$

for any scalars S with perturbation ΔS, vectors V^i, with perturbation ΔV^i, and tensor F_{ij}, with perturbation ΔF_{ij}. The parentheses in expressions such as $\Delta(\bar{D}^2)S$ refer to the perturbation on just the derivative operator.

Then we can compute the perturbation to the spatial Ricci tensor as

$$\Delta\bar{R}_{ij} = \partial_m\Delta\bar{\Gamma}^m_{ij} - \frac{1}{2}(\partial_i\Delta\bar{\Gamma}^m_{mj} + \partial_j\Delta\bar{\Gamma}^m_{mi}) \tag{3.109}$$

$$+ \Delta\bar{\Gamma}^m_{ij}\bar{\Gamma}^n_{nm} - \Delta\bar{\Gamma}^m_{in}\bar{\Gamma}^n_{mj} + \bar{\Gamma}^m_{ij}\Delta\bar{\Gamma}^n_{nm} - \bar{\Gamma}^m_{in}\Delta\bar{\Gamma}^n_{mj}\,.$$

and $\Delta\bar{R}$ can then be computed using Eq. (3.99).

Meanwhile, the perturbation to $\bar{L}\beta^{ij}$, defined in Eq. (3.15), is

$$\Delta(\bar{L}\beta)^{ij} = \Delta(\bar{D})^i\beta^j + \bar{D}^i\Delta\beta^j + \Delta(\bar{D})^j\beta^i + \bar{D}^j\Delta\beta^i \tag{3.110}$$

$$- \frac{2}{3}\Delta\bar{g}^{ij}\bar{D}_k\beta^k - \frac{2}{3}\bar{g}^{ij}(\Delta(\bar{D})_k\beta^k + \bar{D}_k\Delta\beta)^k\,.$$

For simplicity, we can group the terms with the background derivative operators operating on $\Delta\beta^i$, defining

$$\Delta(\bar{L}\beta)^{ij} = (\bar{L}\Delta\beta)^{ij} + (\Delta\bar{L}\beta)^{ij}, \tag{3.111}$$

where

$$(\bar{L}\Delta\beta)^{ij} \equiv \bar{D}^i\Delta\beta^j + \bar{D}^j\Delta\beta^i - \frac{2}{3}\bar{g}^{ij}\bar{D}_k\Delta\beta^k, \tag{3.112}$$

and

$$(\Delta(\bar{L})\beta)^{ij} \equiv \Delta(\bar{D})^i\beta^j + \Delta(\bar{D})^j\beta^i - \frac{2}{3}\Delta\bar{g}^{ij}\bar{D}_k\beta^k - \frac{2}{3}\bar{g}^{ij}\Delta(\bar{D})_k\beta^k. \tag{3.113}$$

Finally, the perturbation to $\bar{A}^{ij}$, defined in Eq. (3.14), is

$$\Delta\bar{A}^{ij} = 7\frac{\psi^6\Delta\psi}{2\alpha\psi}((\bar{L}\beta)^{ij} - \bar{u}^{ij}) - \frac{\psi^7}{2(\alpha\psi)^2}\Delta C((\bar{L}\beta)^{ij} - \bar{u}^{ij}) \tag{3.114}$$

$$+ \frac{\psi^7}{2\alpha\psi}(\Delta(\bar{L}\beta)^{ij} - \Delta\bar{u}^{ij}).$$

The perturbations to the source terms given in Eqs. (3.4) (3.5) (3.6) and (3.7) are

$$\Delta\rho \equiv \Delta n_a n_b T^{ab} + n_a \Delta n_b T^{ab} + n_a n_b \Delta T^{ab}, \tag{3.115}$$

$$\Delta S^i \equiv -\Delta g^{ij}n^a T_{aj} - g^{ij}\Delta n^a T_{aj} - g^{ij}n^a\Delta T_{aj}, \tag{3.116}$$

$$\Delta S_{ij} \equiv \Delta g_{ia}g_{jb}T^{ab} + g_{ia}\Delta g_{jb}T^{ab} + g_{ia}g_{jb}\Delta T^{ab}, \tag{3.117}$$

$$\Delta S \equiv \Delta g^{ij}S_{ij} + g^{ij}\Delta S_{ij}. \tag{3.118}$$

For a vacuum background ($T_{ab} = 0$), these terms simplify to give

$$\Delta\rho \equiv n_a n_b \psi^{ac}\psi^{bd}\Delta T_{cd} = n^a n^b \Delta T_{ab}, \tag{3.119}$$

$$\Delta S^i \equiv -g^{ij}n^a\Delta T_{aj}, \tag{3.120}$$

$$\Delta S_{ij} \equiv \Delta T_{ij}, \tag{3.121}$$

$$\Delta S \equiv g^{ij}\Delta S_{ij}. \tag{3.122}$$

Note that all of the above terms use the background variables without applying a conformal transformation.

3.B Reconstructing the perturbed spacetime metric

In this appendix, we detail how to reconstruct the (non-conformal) spatial metric, Δg_{ij}, and its time derivative, $\partial_t \Delta g_{ij}$, from the perturbed extended conformal thin sandwich variables solved for in Sec. 3.2. This in turn allows us to construct the perturbation to the spacetime metric, $\Delta\psi_{ab}$, and its time derivative, $\partial_t\Delta\psi_{ab}$.

We obtain, perturbing Eq. (3.8)

$$\Delta g_{ij} = \psi^4 \Delta \bar{g}_{ij} + 4\psi^3 \Delta \psi \bar{g}_{ij}, \tag{3.123}$$

and

$$\Delta g^{ij} = \psi^{-4} \Delta \bar{g}_{ij} - 4\psi^{-5} \Delta \psi \bar{g}^{ij}. \tag{3.124}$$

For u_{ij}, we perturb Eq. (3.10) to give

$$\Delta u_{ij} = \psi^4 \Delta \bar{u}_{ij} + 4\psi^3 \Delta \psi \bar{u}_{ij}, \tag{3.125}$$

which is in turn related to $\partial_t \Delta g_{ij}$ through perturbing Eq. (3.9) to give

$$\Delta u_{ij} = \partial_t \Delta g_{ij} - \frac{2}{3} \Delta g_{ij}(-\alpha K + D_i \beta^i) \tag{3.126}$$
$$- \frac{2}{3} g_{ij}(-\Delta \alpha K + \Delta(D)_i \beta^i - \alpha \Delta K + D_i \Delta \beta^i).$$

Finally, the perturbed extrinsic curvature ΔK_{ij} can be reconstructed from ΔK and the solved variables following Eqs. (3.12) and (3.13) as

$$\Delta K_{ij} = \Delta A_{ij} + \frac{1}{3}(\Delta g_{ij} K + g_{ij} \Delta K), \tag{3.127}$$

where

$$\Delta A_{ij} = \psi^{-2} \Delta \bar{A}_{ij} - 2\psi^{-3} \Delta \psi \bar{A}_{ij}. \tag{3.128}$$

In addition to Δg_{ij} and $\partial_t \Delta g_{ij}$, some applications, such as computing the black hole shadow, require the perturbation to the full spacetime metric $\psi_{ab} \to \psi_{ab} + \Delta \psi_{ab}$ and its time derivative $\partial_t \Delta \psi_{ab}$. We thus construct the spacetime metric perturbation as

$$\Delta \psi_{ab} = \begin{pmatrix} -2\alpha \Delta \alpha + \Delta \beta_m \beta^m + \beta_m \Delta \beta^m & \Delta \beta_i \\ \Delta \beta_j & \Delta g_{ij} \end{pmatrix}. \tag{3.129}$$

For the time derivative, given by applying the chain rule to the terms in Eq. (3.129), we need to specify the time derivatives of β^i, α, $\Delta \beta^i$, and $\Delta \alpha$. For the background case, we can freely specify $\partial_t \beta^i = 0$ and $\partial_t \alpha = 0$ [40]. We can apply the same principle to the perturbed data, and freely set $\partial_t \Delta \alpha = 0$ and $\partial_t \Delta \beta^i = 0$. For a stationary background ($\partial_t \psi_{ab} = 0$, where ∂_t is a linear combination to Killing vector fields), we obtain

$$\partial_t (\Delta \beta_m \beta^m + \beta_m \Delta \beta^m) \tag{3.130}$$
$$= \partial_t (\Delta g_{mi} \beta^i \beta^m + g_{mi} \Delta \beta^i \beta^m + g_{mi} \beta^i \Delta \beta^m)$$
$$= \partial_t \Delta g_{mi} \beta^i \beta^m,$$

and thus

$$\partial_t \Delta \psi_{ab} = \begin{pmatrix} \partial_t \Delta g_{ij} \beta^i \beta^j & \partial_t \Delta g_{ij} \beta^j \\ \partial_t \Delta g_{ij} \beta^i & \partial_t \Delta g_{ij} \end{pmatrix}. \tag{3.131}$$

C h a p t e r   4

EVOLVING METRIC PERTURBATIONS IN DYNAMICAL CHERN-SIMONS GRAVITY AND THE STABILITY OF ROTATING BLACK HOLES IN DYNAMICAL CHERN-SIMONS GRAVITY

[1]   Maria Okounkova, Mark A. Scheel, and Saul A. Teukolsky. "Evolving Metric Perturbations in dynamical Chern-Simons Gravity". In: *Phys. Rev.* D99.4 (2019), p. 044019. DOI: 10.1103/PhysRevD.99.044019. arXiv: 1811.10713 [gr-qc].

Abstract

The stability of rotating black holes in dynamical Chern-Simons gravity (dCS) is an open question. To study this issue, we evolve the leading-order metric perturbation in order-reduced dynamical Chern-Simons gravity. The source is the leading-order dCS scalar field coupled to the spacetime curvature of a rotating black hole background. We use a well-posed, constraint-preserving scheme. We find that the leading-order metric perturbation numerically exhibits linear growth, but that the level of this growth converges to zero with numerical resolution. This analysis shows that spinning black holes in dCS gravity are numerically stable to leading-order perturbations in the metric.

4.1   Introduction

Einstein's theory of general relativity (GR) has passed all precision tests to date, and binary black hole observations from the Laser Interferometry Gravitational Wave Observatory (LIGO) have given a roughly 96% agreement with GR [206, 14]. At some scale, however, GR must be reconciled with quantum mechanics in a quantum theory of gravity. Black hole systems can potentially illuminate signatures of quantum gravity, as they probe the strong-field, non-linear, high-curvature regime of gravity.

While several null-hypothesis and parametrized tests of GR with LIGO observations have been performed [14, 216], an open problem is the simulation of binary black holes through full inspiral, merger, and ringdown in a beyond-GR theory. Waveform

predictions from such simulations would allow us to perform *model-dependent* tests, and to parametrize the behavior at merger in beyond-GR theories.

From the first LIGO detections, we know that deviations from GR are presently not detectable. It is reasonable to assume that this is because any such deviations are less than about a 4% effect. While it is possible that the signal-to-noise ratio from the merger itself is currently too small to rule out larger deviations at the horizon, we will not consider this possibility here. Accordingly, rather than simulating black holes in a full quantum theory of gravity, we can consider *effective field theories*. These modify the classical Einstein-Hilbert action of GR through the inclusion of classical terms encompassing quantum gravity effects. One such theory is dynamical Chern-Simons (dCS) gravity, which adds a scalar field coupled to spacetime curvature to the Einstein-Hilbert action, and has origins in string theory, loop quantum gravity, and inflation [18, 95, 192, 134, 204].

The well-posedness of the initial value problem in full, non-linear dCS gravity is unknown [74]. However, we can work in an *order-reduction scheme*, in which we perturb the dCS scalar field and metric about a GR background. At each order, the equations of motion are well-posed (cf. [146]). In this study, we investigate the behavior of the leading-order dCS metric perturbation, sourced by the leading-order dCS scalar field coupled to the spacetime curvature of a GR background.

The stability of rotating black holes in dCS gravity is unknown [137, 90, 43]. In this study, we numerically test the leading-order stability of rotating dCS black holes by evolving the leading-order dCS metric perturbation on a rotating black hole GR background. Since the background (and the leading-order dCS scalar field) are stationary, the dCS metric perturbation should remain stationary if rotating dCS black holes are stable.

This question of stability is of broader importance to our goal of simulating the leading-order dCS metric perturbation of a binary black hole spacetime, in order to produce beyond-GR gravitational waveforms. If rotating black holes in dCS are not stable to leading order, and the metric perturbation grows in time, then we know that we would not be able to simulate black hole binaries in this theory. Specifically, the metric perturbations around each black hole would grow in time during inspiral, and similarly for the final black hole after merger, thus spoiling the evolution.

Roadmap and conventions

This chapter is organized as follows. In Sec. 4.2, we present the equations of motion of dCS that we aim to evolve in this study. In Sec. 4.3, we derive and present a formalism for stably evolving linear metric perturbations on an arbitrary background, so that we may evolve the leading-order dCS metric perturbation. In Sec. 4.4, we apply this formalism to evolve the leading-order dCS metric perturbation on a rotating black hole background. We discuss our findings in Sec. 4.5.

We set $G = c = 1$ throughout. Quantities are given in terms of units of M, the ADM mass of the background. Latin letters in the beginning of the alphabet $\{a, b, c, d \ldots\}$ denote 4-dimensional spacetime indices, while Latin letters in the middle of the alphabet $\{i, j, k, l, \ldots\}$ denote 3-dimensional spatial indices. g_{ab} refers to the spacetime metric, while γ_{ij} refers to the spatial metric from a 3+1 decomposition with corresponding timelike unit normal one-form n_a (cf. [40] for a review of the 3+1 ADM formalism).

4.2 Dynamical Chern-Simons gravity

Dynamical Chern-Simons gravity modifies the Einstein-Hilbert action of GR through the inclusion of a scalar field ϑ, coupled to spacetime curvature as

$$ S \equiv \int d^4x \sqrt{-g} \left(\frac{m_{\mathrm{pl}}^2}{2} R - \frac{1}{2}(\partial \vartheta)^2 - \frac{m_{\mathrm{pl}}}{8} \ell^2 \vartheta \, {}^*RR \right) . \tag{4.1} $$

The first term in the action is the familiar Einstein-Hilbert action of general relativity, with the Planck mass denoted by m_{pl}. The second term in the action is a kinetic term for the scalar field. The third term, meanwhile, couples ϑ to spacetime curvature via the Pontryagin density,

$$ {}^*RR \equiv {}^*R^{abcd} R_{abcd} , \tag{4.2} $$

where ${}^*R^{abcd} = \frac{1}{2} \epsilon^{abef} R_{ef}{}^{cd}$ is the dual of the Riemann tensor, and $\epsilon^{abcd} \equiv -[abcd]/\sqrt{-g}$ is the fully antisymmetric Levi-Civita tensor. This coupling is governed by a coupling constant ℓ, which has dimensions of length. ℓ physically represents the length scale below which quantum gravity effects become important. One may also include stress-energy terms in this action for additional fields (such as matter terms in a neutron-star spacetime, for example), though we do not write them here.

Varying the dCS action with respect to ϑ gives a sourced wave equation for the scalar field,

$$\Box\vartheta = \frac{m_{\rm pl}}{8}\ell^2 \, {}^*RR\,, \tag{4.3}$$

where $\Box = \nabla_a\nabla^a$ is the d'Alembertian operator. Varying the action with respect to the metric g_{ab} gives

$$m_{\rm pl}^2 G_{ab} + m_{\rm pl}\ell^2 C_{ab} = T_{ab}^\vartheta\,, \tag{4.4}$$

where

$$C_{ab} \equiv \epsilon_{cde(a}\nabla^d R_{b)}{}^c\nabla^e\vartheta + {}^*R^c{}_{(ab)}{}^d\nabla_c\nabla_d\vartheta\,, \tag{4.5}$$

and T_{ab}^ϑ is the stress energy tensor for a canonical, massless Klein-Gordon field

$$T_{ab}^\vartheta = \nabla_a\vartheta\nabla_b\vartheta - \frac{1}{2}g_{ab}\nabla_c\vartheta\nabla^c\vartheta\,. \tag{4.6}$$

It is the inclusion of C_{ab} in Eq. (4.4) that modifies the equation of motion for the metric from that of a metric in GR sourced by a scalar field.

C_{ab}, as given in Eq. (4.5), contains third derivatives of the metric, thus modifying the principal part of the equation of motion for γ_{ab} from that of GR. Because of the presence of these third-derivative terms, it is unknown whether dCS has a well-posed initial value formulation [74].

However, one can expand the scalar field and metric about a GR background as

$$g_{ab} = g_{ab}^0 + \sum_{k=1}^\infty \varepsilon^k h_{ab}^{(k)}\,, \tag{4.7}$$

$$\vartheta = \sum_{k=0}^\infty \varepsilon^k \vartheta^{(k)}\,, \tag{4.8}$$

where ε is an order-counting parameter. At each order in ε, one recovers an equation of motion with the same principal part as GR. This is known as an *order-reduction scheme*, and has been previously implemented in [146] and [143].

In this scheme, ε^0 simply gives the Einstein field equations of general relativity for $g_{ab}^{(0)}$, with no source term for $\vartheta^{(0)}$, which we can thus set to zero. At first order, we obtain a wave equation for the leading-order scalar field,

$$\Box^{(0)}\vartheta^{(1)} = {}^*RR^{(0)}\,, \tag{4.9}$$

where $\Box^{(0)}$ is the d'Alembertian operator of the background, and $RR^{(0)}$ is the Pontryagin density of the background. At this order, the metric perturbation $h_{ab}^{(1)}$ is unsourced, and thus we set it to zero. At order ε^2, the metric perturbation $h_{ab}^{(2)}$ is sourced by the leading-order scalar field $\vartheta^{(1)}$ coupled to spacetime curvature as

$$m_{\text{pl}}^2 G_{ab}^{(0)}[h_{ab}^{(2)}] = -m_{\text{pl}}\ell^2 C_{ab}^{(1)}\vartheta^{(1)} + \frac{1}{8}T_{ab}^{(\vartheta(1))}, \tag{4.10}$$

where $G_{ab}^{(0)}$ is the Einstein field equation operator of the background, and

$$T_{ab}^{(\vartheta(1))} \equiv \nabla_a^{(0)}\vartheta^{(1)}\nabla_b^{(0)}\vartheta^{(1)} - \frac{1}{2}g_{ab}^{(0)}\nabla_c^{(0)}\vartheta^{(1)}\nabla^{c(0)}\vartheta^{(1)}, \tag{4.11}$$

where $\nabla_a^{(0)}$ denotes the covariant derivative associated with $g_{ab}^{(0)}$. Meanwhile,

$$\begin{aligned}
C_{ab}^{(1)} &\equiv \epsilon_{cde(a}\nabla^{d(0)}R_{b)}{}^{c(0)}\nabla^{e(0)}\vartheta^{(1)} \\
&+ {}^*R^c{}_{(ab)}{}^{d(0)}\nabla_c^{(0)}\nabla_d^{(0)}\vartheta^{(1)}.
\end{aligned} \tag{4.12}$$

Note that though $C_{ab}^{(1)}$ contains third derivatives of the background metric $g_{ab}^{(0)}$, it does not contain derivatives of $h_{ab}^{(2)}$, and hence does not contribute to the principal part of Eq. (4.10). We can thus write the RHS of Eq. (4.10) in terms of an effective stress energy tensor,

$$T_{ab}^{\text{eff}(1)} \equiv -m_{\text{pl}}\ell^2 C_{ab}^{(1)}\vartheta^{(1)} + \frac{1}{8}T_{ab}^{(\vartheta(1))}. \tag{4.13}$$

Let us write Eq. (4.10) in a more illuminating way, as

$$\begin{aligned}
m_{\text{pl}}^2 G_{ab}^{(0)}[h_{ab}^{(2)}] &= \frac{1}{8}T_{ab}^{(\vartheta(1))} \\
&- m_{\text{pl}}\ell^2\Big(\epsilon_{cde(a}\nabla^{d(0)}R_{b)}{}^{c(0)}\nabla^{e(0)}\vartheta^{(1)} \\
&+ {}^*R^c{}_{(ab)}{}^{d(0)}\nabla_c^{(0)}\nabla_d^{(0)}\vartheta^{(1)}\Big)\vartheta^{(1)}.
\end{aligned} \tag{4.14}$$

As mentioned previously, it is the inclusion of the second term on the right-hand side of Eq. (4.14) that differentiates the equation of motion for the leading-order metric perturbation in dynamical Chern-Simons theory from that of a simple metric perturbation sourced by a scalar field in general relativity.

Our goal, thus, is to evolve the leading-order metric perturbation $h_{ab}^{(2)}$, sourced by $T_{ab}^{\text{eff}(1)}$. Because this is the leading-order metric perturbation, we only need to work in linear theory. We will thus develop a numerical scheme for stably evolving first-order metric perturbations on an arbitrary GR background with arbitrary source.

From here on, we simplify the notation, writing

$$h_{ab}^{(2)} \equiv \frac{\ell^4}{8} \Delta g_{ab}, \quad \vartheta^{(1)} \equiv \frac{m_{\rm pl}}{8} \ell^2 \Psi, \tag{4.15}$$

and thus

$$T_{ab}^{\rm eff}(\Psi) \equiv -C_{ab}(\Psi) + \frac{1}{8} T_{ab}(\Psi), \tag{4.16}$$

$$C_{ab}(\Psi) \equiv \epsilon_{cde(a} \nabla^d R_{b)}{}^c \nabla^e \Psi + {}^*R^c{}_{(ab)}{}^d \nabla_c \nabla_d \Psi, \tag{4.17}$$

$$T_{ab}(\Psi) = \nabla_a \Psi \nabla_b \Psi - \frac{1}{2} g_{ab} \nabla_c \Psi \nabla^c \Psi, \tag{4.18}$$

with the overall evolution equation

$$G_{ab}^{(1)}[\Delta g_{ab}] = T_{ab}^{\rm eff}(\Psi). \tag{4.19}$$

4.3 Evolving metric perturbations

Our goal now is to outline a formalism to evolve the leading-order metric perturbation in dCS, following Eq. (4.19). In this section, we derive a more general formalism for evolving leading-order metric perturbations on an arbitrary GR background with arbitrary source, which we will apply to rotating black holes in dCS in Sec. 4.4.

Generalized harmonic formalism

The formalism that we will use to evolve metric perturbations is based on the generalized harmonic formalism [121]. This formulation is a generalization of the well-known harmonic formulation of Einstein's equations, and has seen great success in evolving binary black hole mergers [87, 162, 161, 121]. This well-posed formalism involves expressing the gauge freedom in terms of a (nearly) freely specifiable gauge source function

$$H_a = g_{ab} \nabla_c \nabla^c x^b = -\Gamma_a, \tag{4.20}$$

where $\Gamma_a = g^{bc} \Gamma_{abc}$ for the Christoffel symbol derived from g_{ab}, and ∇_c is the corresponding spacetime covariant derivative. Here, H_a is known as the gauge source function, and is a fixed function of coordinates x^a and g_{ab} (but not derivatives of g_{ab}). In particular, setting $H_a = 0$ corresponds to a harmonic gauge. This framework has seen success in numerical relativity, including the simulation of black hole binaries [162, 161, 178].

In this study, we will consider the first-order formulation of the generalized harmonic formalism given in [121]. This involves evolving the spacetime metric g_{ab}, along

with variables Π_{ab} and Φ_{iab} corresponding to its time and spatial derivatives defined as

$$\Phi_{iab} \equiv \partial_i g_{ab}, \tag{4.21}$$

$$\Pi_{ab} \equiv -n^c \partial_c g_{ab}, \tag{4.22}$$

where n^c is the timelike unit normal vector to slices of constant time t.

For simplicity, we will combine these into a single 4-dimensional variable κ_{abc}, defined as

$$\kappa_{0ab} \equiv \Pi_{ab} = -n^c \partial_c g_{ab}, \tag{4.23}$$

$$\kappa_{iab} \equiv \Phi_{iab} = \partial_i g_{ab}. \tag{4.24}$$

Note that κ_{abc} does not obey the tensor transformation law.

In addition to being first order, the formalism given in [121] is also *constraint-damping*. It includes terms proportional to $\partial_i g_{ab} - \kappa_{iab}$, for example; these terms are chosen so that small violations of constraints are driven toward zero. Here, $\partial_i g_{ab}$ is the derivative of g_{ab} taken numerically, while κ_{iab} is the first-order variable corresponding to the spatial derivative of the metric. Terms are added to the evolution equations with (spatially-dependent) multiplicative constants $\gamma_0, \gamma_1, \gamma_2$ to ensure symmetric-hyperbolicity and that the relations in Eqs. (4.20), (4.23) and (4.24) are obeyed.

The first-order, symmetric-hyperbolic, constraint-damping evolution equations for the metric are given by

$$\partial_t g_{ab} = (1 + \gamma_1)\beta^k \partial_k g_{ab} - \alpha \kappa_{0ab} - \gamma_1 \beta^i \kappa_{iab}, \tag{4.25}$$

$$\partial_t \kappa_{iab} = \beta^k \partial_k \kappa_{iab} - \alpha \partial_i \kappa_{0ab} + \alpha \gamma_2 \partial_i g_{ab} - \alpha \gamma_2 \kappa_{iab} \tag{4.26}$$

$$+ \frac{1}{2}\alpha n^c n^d \kappa_{icd} \kappa_{0ab} + \alpha \gamma^{jk} n^c \kappa_{ijc} \kappa_{kab},$$

and

$$\partial_t \kappa_{0ab} = \beta^k \partial_k \kappa_{0ab} - \alpha \gamma^{ki} \partial_k \kappa_{iab} + \gamma_1 \gamma_2 \beta^k \partial_k g_{ab} \qquad (4.27)$$
$$+ 2\alpha g^{cd}(\gamma^{ij} \kappa_{ica} \kappa_{jdb} - \kappa_{0ca} \kappa_{0db}$$
$$- g^{ef} \Gamma_{ace} \Gamma_{bdf})$$
$$- 2\alpha \nabla_{(a} H_{b)} - \frac{1}{2} \alpha n^c n^d \kappa_{0cd} \kappa_{0ab}$$
$$- \alpha n^c \kappa_{0ci} \gamma^{ij} \kappa_{jab}$$
$$+ \alpha \gamma_0 [2\delta^c{}_{(a} n_{b)} - g_{ab} n^c](H_c + \Gamma_c)$$
$$- \gamma_1 \gamma_2 \beta^i \kappa_{iab} - 2\alpha S_{ab} .$$

In the last equation, S_{ab} is a source term related to trace-reverse of the stress-energy tensor T_{ab} as

$$S_{ab} = 8\pi(T_{ab} - \frac{1}{2}T g_{ab}), \qquad (4.28)$$

where $T = g^{ab}T_{ab}$. In the above, $\nabla_a H_b$ is defined as $\partial_a H_b - \Gamma^d{}_{ab} H_d$, as if H_a were a one-form (which it is not).

Linearized generalized harmonic formalism

Our goal in this study is to evolve first-order metric perturbations on a GR background. Given a background $\{g_{ab}, \kappa_{abc}\}$, we perturb it to first order as

$$g_{ab} \rightarrow g_{ab} + \Delta g_{ab}, \qquad (4.29)$$

$$\kappa_{abc} \rightarrow \kappa_{abc} + \Delta \kappa_{abc} . \qquad (4.30)$$

From here on, ΔA will always refer to the linear perturbation to a variable A.

The evolution equations for Δg_{ab} and $\Delta \kappa_{abc}$ can be derived by linearizing Eqs. (4.25), (4.26), and (4.27), and keeping terms to first order. The resulting equations will be a first-order formulation. The symmetric hyperbolicity of these equations is guaranteed because the perturbation equations will have the same principal part as the background system. The linearized system is also constraint damping, as the associated *constraint evolution system* has the same linear part as in the constraint-damping unperturbed system (cf. Eqs. 17 – 21 in [121]). More importantly, the equations for Δg_{ab} and $\Delta \kappa_{abc}$ will have the same principal part as the equations for g_{ab} and κ_{abc}, as we shall see.

Linearizing Eqs. (4.25), (4.26), and (4.27) involves computing terms like $\Delta \alpha$, $\Delta \beta^i$, the first-order perturbations to the lapse and shift. In the following section, we thus

derive expressions for these terms in terms of the fundamental variables Δg_{ab} and $\Delta \kappa_{abc}$.

Linearized variables

To compute Δg^{ab}, we can use the identity $g^{ab} g_{bc} = \delta^a_c$ to give

$$\Delta g^{ad} = -g^{cd} g^{ab} \Delta g_{bc} \,. \tag{4.31}$$

For the perturbation to the lapse, $\Delta \alpha$, the shift, $\Delta \beta^i$, the lower-indexed shift, $\Delta \beta_i$, and the spatial metric $\Delta \gamma_{ij}$ and $\Delta \gamma^{ij}$, we recall that the spacetime metric is decomposed in the 3+1 ADM formalism as

$$g_{ab} = \begin{pmatrix} -\alpha^2 + \beta_l \beta^l & \beta_i \\ \beta_j & \gamma_{ij} \end{pmatrix} \tag{4.32}$$

$$g^{ab} = \begin{pmatrix} -\alpha^{-2} & \alpha^{-2} \beta^i \\ \alpha^{-2} \beta^j & \gamma^{ij} - \alpha^{-2} \beta^i \beta^j \end{pmatrix} \,. \tag{4.33}$$

Recall that spatial quantities are raised and lowered with γ_{ij}, the spatial metric. When we perturb all 10 independent components of g_{ab}, we can find what all of the linearized quantities are in terms of g_{ab} and Δg_{ab}. We begin with perturbing g_{0i} to find $\Delta \beta_i$:

$$\Delta \beta_i = \Delta g_{0i} \,. \tag{4.34}$$

Similarly, we can perturb g_{ij} to obtain:

$$\Delta \gamma_{ij} = \Delta g_{ij} \,. \tag{4.35}$$

We can now use g^{00} to obtain

$$\Delta \alpha = \frac{1}{2} \alpha^3 \Delta g^{00} \,. \tag{4.36}$$

Next, using $\gamma^{ij} \gamma_{jk} = \delta^i_k$, we find

$$\Delta \gamma^{im} = -\gamma^{mk} \gamma^{ij} \Delta \gamma_{jk} \,. \tag{4.37}$$

From this, we can compute $\Delta \beta^i$ as

$$\Delta \beta^i = \Delta \gamma^{ij} \beta_j + \gamma^{ij} \Delta \beta_j \,. \tag{4.38}$$

Finally, we need to compute Δn^a and Δn_a, the perturbed time-like unit normal vector and one-form. We can use the expressions for n^a and n_a in terms of the lapse and shift to obtain the perturbed quantities (cf. [40]). We compute

$$\Delta n_a = (-\Delta \alpha, 0, 0, 0) \,. \tag{4.39}$$

and

$$\Delta n^a = (-\alpha^{-2}\Delta\alpha, \alpha^{-2}\Delta\alpha\beta^i - \alpha^{-1}\Delta\beta^i).$$ (4.40)

In order to check constraint satisfaction (as will be discussed in Sec. 4.3), we will also need to obtain the perturbation to γ_a^b. We obtain (cf. Eq. 2.30 in [40]),

$$\Delta\gamma^a{}_b = \Delta n^a n_b + n^a \Delta n_b.$$ (4.41)

Thus, we have obtained all of the necessary perturbed quantities to perturb the generalized harmonic expressions as well as the constraint expressions that we can obtain from Δg_{ab}. In the next section, we describe the quantities that we can obtain from $\Delta\kappa_{abc}$.

Referring back to Eq. (4.27), we also need to find expressions for $\Delta\Gamma_{abc}$, the first-order perturbation to the connection compatible with g_{ab}, as well as the first-order perturbation to its trace, $\Delta\Gamma_a$. First, let's compute the perturbation to $\Delta\Gamma_{abc}$. By definition,

$$\Gamma_{abc} = \frac{1}{2}(\partial_b g_{ac} + \partial_c g_{ab} - \partial_a g_{bc}).$$ (4.42)

However, in order to preserve hyperbolicity in the evolution equations, all instances of $\partial_a g_{bc}$ appearing in Γ_{abc} are replaced with κ_{abc} according to Eqs. (4.23) and (4.24) [121], thus giving

$$\begin{aligned}
\Gamma_{abc} = \frac{1}{2}\Big(&(1 - \delta_b^0)\kappa_{bac} + \delta_b^0(-\alpha\kappa_{0ac} + \beta^i\kappa_{iac}) \\
&+ (1 - \delta_c^0)\kappa_{cab} + \delta_c^0(-\alpha\kappa_{0ab} + \beta^i\kappa_{iab}) \\
&- (1 - \delta_a^0)\kappa_{abc} - \delta_a^0(-\alpha\kappa_{0bc} + \beta^i\kappa_{ibc})\Big)
\end{aligned}$$ (4.43)

where the Kronecker delta symbol δ_b^a picks out the spatial indices $\{1, 2, 3\}$ versus time indices $\{0\}$.

We can perturb Eq. (4.43) to give

$$\begin{aligned}
\Delta\Gamma_{abc} = \frac{1}{2}\Big(&(1 - \delta_b^0)\Delta\kappa_{bac} \\
&+ \delta_b^0(-\Delta\alpha\kappa_{0ac} - \alpha\Delta\kappa_{0ac} + \Delta\beta^i\kappa_{iac} + \beta^i\Delta\kappa_{iac}) \\
&+ (1 - \delta_c^0)\Delta\kappa_{cab} \\
&+ \delta_c^0(-\Delta\alpha\kappa_{0ab} - \alpha\Delta\kappa_{0ab} + \Delta\beta^i\kappa_{iab} + \beta^i\Delta\kappa_{iab}) \\
&- (1 - \delta_a^0)\Delta\kappa_{abc} \\
&- \delta_a^0(-\Delta\alpha\kappa_{0bc} - \alpha\Delta\kappa_{0bc} + \Delta\beta^i\kappa_{ibc} + \beta^i\Delta\kappa_{ibc})\Big)
\end{aligned}$$ (4.44)

Now, for $\Gamma^a{}_{bc} \equiv g^{ad}\Gamma_{dbc}$, we compute the corresponding perturbations (for future use) via

$$\Delta\Gamma^a{}_{bc} = \Delta g^{ad}\Gamma_{dbc} + g^{ad}\Delta\Gamma_{dbc} \,. \tag{4.45}$$

For the trace of $\Gamma_a \equiv g^{bc}\Gamma_{abc}$, we compute

$$\Delta\Gamma_a = \Delta g^{bc}\Gamma_{abc} + g^{bc}\Delta\Gamma_{abc} \,, \tag{4.46}$$

where $\Delta\Gamma_{abc}$ is as above, and Δg^{bc} is given in Eq. (4.31).

The generalized harmonic gauge source term, H_a, will also have a perturbation, ΔH_a. However, ΔH_a, like H_a, is freely specifiable, with the caveat that it can only depend on g_{ab} and Δg_{ab} but no derivatives of g_{ab} or Δg_{ab}. Throughout this study we will choose a *freezing* gauge condition: we set ΔH_a from the initial data $\Delta H_a = \Delta\Gamma_a(t = 0)$, and keep it at this constant value throughout the evolution.

Eq. (4.27) has a $\nabla_a H_b$ term. Perturbing this quantity, we obtain

$$\Delta(\nabla_a H_b) = \partial_a\Delta H_b - \Delta g^{cd}\Gamma_{dab}H_c \tag{4.47}$$
$$- g^{cd}(\Delta\Gamma_{dab}H_c + \Gamma_{dab}\Delta H_c) \,.$$

Perturbed initial data

Suppose we are given initial data in the form $\{\Delta g_{ab}, \partial_t\Delta g_{ab}, \partial_i\Delta g_{ab}\}$. Perturbing Eqs. (4.23) and (4.24), we can relate $\Delta\kappa_{abc}$ to derivatives of Δg_{ab}:

$$\Delta\kappa_{0ab} = -\Delta n^c\partial_c g_{ab} - n^c\partial_c\Delta g_{ab} \,, \tag{4.48}$$

$$\Delta\kappa_{iab} = \partial_i\Delta g_{ab} \,, \tag{4.49}$$

where Δn^c is computed from Δg_{ab} using Eq. (4.40).

Source terms

In order to source the metric perturbation, we require a perturbation to the stress energy tensor, ΔT_{ab}. This will appear in the perturbed evolution equations through ΔS_{ab}, the perturbation to S_{ab} defined in Eq. (4.28), as

$$\Delta S_{ab} = 8\pi(\Delta T_{ab} - \frac{1}{2}(\Delta T g_{ab} + T\Delta g_{ab})) \,, \tag{4.50}$$

$$\Delta T = \Delta g^{ab}T_{ab} + g^{ab}\Delta T_{ab} \,. \tag{4.51}$$

For a vacuum background, we obtain the simpler form

$$\Delta S_{ab} = 8\pi(\Delta T_{ab} - \frac{1}{2}g_{ab}g^{cd}\Delta T_{cd})\,. \tag{4.52}$$

Perturbed evolution equations

We have now derived the first-order perturbations to all of the variables in Eqs. (4.25), (4.26), and (4.27). We next perturb these equations to linear order, in order to obtain evolution equations for Δg_{ab} and $\Delta \kappa_{abc}$.

We begin by perturbing Eq. (4.25) to obtain

$$\begin{aligned}
\partial_t \Delta g_{ab} = {} & (1 + \gamma_1)(\Delta\beta^k \partial_k g_{ab} + \beta^k \partial_k \Delta g_{ab}) \\
& - \Delta\alpha\kappa_{0ab} - \alpha\Delta\kappa_{0ab} \\
& - \gamma_1\Delta\beta^i \kappa_{iab} - \gamma_1\beta^i \Delta\kappa_{iab}\,.
\end{aligned} \tag{4.53}$$

Next, we perturb Eq. (4.26) to give

$$\begin{aligned}
\partial_t \Delta\kappa_{iab} = {} & \Delta\beta^k \partial_k \kappa_{iab} + \beta^k \partial_k \Delta\kappa_{iab} \\
& - \Delta\alpha\partial_i\kappa_{0ab} - \alpha\partial_i\Delta\kappa_{0ab} \\
& + \Delta\alpha\gamma_2\partial_i g_{ab} + \alpha\gamma_2\partial_i\Delta g_{ab} \\
& + \frac{1}{2}\Delta\alpha n^c n^d \kappa_{icd}\kappa_{0ab} + \frac{1}{2}\alpha\Delta n^c n^d \kappa_{icd}\kappa_{0ab} \\
& + \frac{1}{2}\alpha n^c \Delta n^d \kappa_{icd}\kappa_{0ab} + \frac{1}{2}\alpha n^c n^d \Delta\kappa_{icd}\kappa_{0ab} \\
& + \frac{1}{2}\alpha n^c n^d \kappa_{icd}\Delta\kappa_{0ab} \\
& + \Delta\alpha\gamma^{jk} n^c \kappa_{ijc}\kappa_{kab} + \alpha\Delta\gamma^{jk} n^c \kappa_{ijc}\kappa_{kab} \\
& + \alpha\gamma^{jk}\Delta n^c \kappa_{ijc}\kappa_{kab} + \alpha\gamma^{jk} n^c \Delta\kappa_{ijc}\kappa_{kab} \\
& + \alpha\gamma^{jk} n^c \kappa_{ijc}\Delta\kappa_{kab} \\
& - \Delta\alpha\gamma_2\kappa_{iab} - \alpha\gamma_2\Delta\kappa_{iab}\,.
\end{aligned} \tag{4.54}$$

Finally, we perturb Eq. (4.27) to obtain

$$
\begin{aligned}
\partial_t \Delta\kappa_{0ab} = {} & \Delta\beta^k \partial_k \kappa_{0ab} + \beta^k \partial_k \Delta\kappa_{0ab} \\
& - \Delta\alpha\gamma^{ki}\partial_k\kappa_{iab} - \alpha\Delta\gamma^{ki}\partial_k\kappa_{iab} \\
& - \alpha\gamma^{ki}\partial_k\Delta\kappa_{iab} \\
& + \gamma_1\gamma_2\Delta\beta^k\partial_k g_{ab} + \gamma_1\gamma_2\beta^k\partial_k\Delta g_{ab} \\
& + 2\Delta\alpha g^{cd}(\gamma^{ij}\kappa_{ica}\kappa_{jdb} - \kappa_{0ca}\kappa_{0db} - g^{ef}\Gamma_{ace}\Gamma_{bdf}) \\
& + 2\alpha\Delta g^{cd}(\gamma^{ij}\kappa_{ica}\kappa_{jdb} - \kappa_{0ca}\kappa_{0db} - g^{ef}\Gamma_{ace}\Gamma_{bdf}) \\
& + 2\alpha g^{cd}(\Delta\gamma^{ij}\kappa_{ica}\kappa_{jdb} - \Delta\kappa_{0ca}\kappa_{0db} - \Delta g^{ef}\Gamma_{ace}\Gamma_{bdf}) \\
& + 2\alpha g^{cd}(\gamma^{ij}\Delta\kappa_{ica}\kappa_{jdb} - \kappa_{0ca}\Delta\kappa_{0db} - g^{ef}\Delta\Gamma_{ace}\Gamma_{bdf}) \\
& + 2\alpha g^{cd}(\gamma^{ij}\kappa_{ica}\Delta\kappa_{jdb} - g^{ef}\Gamma_{ace}\Delta\Gamma_{bdf}) \\
& - 2\Delta\alpha\nabla_{(a}H_{b)} - 2\alpha\Delta\nabla_{(a}H_{b)} \\
& - \frac{1}{2}\Delta\alpha n^c n^d \kappa_{0cd}\kappa_{0ab} - \frac{1}{2}\alpha\Delta n^c n^d \kappa_{0cd}\kappa_{0ab} \\
& - \frac{1}{2}\alpha n^c \Delta n^d \kappa_{0cd}\kappa_{0ab} - \frac{1}{2}\alpha n^c n^d \Delta\kappa_{0cd}\kappa_{0ab} \\
& - \frac{1}{2}\alpha n^c n^d \kappa_{0cd}\Delta\kappa_{0ab} \\
& - \Delta\alpha n^c \kappa_{0ci}\gamma^{ij}\kappa_{jab} - \alpha\Delta n^c \kappa_{0ci}\gamma^{ij}\kappa_{jab} \\
& - \alpha n^c \Delta\kappa_{0ci}\gamma^{ij}\kappa_{jab} - \alpha n^c \kappa_{0ci}\Delta\gamma^{ij}\kappa_{jab} \\
& - \alpha n^c \kappa_{0ci}\gamma^{ij}\Delta\kappa_{jab} \\
& + \Delta\alpha\gamma_0[2\delta^c{}_{(a}n_{b)} - g_{ab}n^c](H_c + \Gamma_c) \\
& + \alpha\gamma_0[2\delta^c{}_{(a}\Delta n_{b)} - \Delta g_{ab}n^c](H_c + \Gamma_c) \\
& + \alpha\gamma_0[-g_{ab}\Delta n^c](H_c + \Gamma_c) \\
& + \alpha\gamma_0[2\delta^c{}_{(a}n_{b)} - g_{ab}n^c](\Delta H_c + \Delta\Gamma_c) \\
& - \gamma_1\gamma_2\Delta\beta^i \kappa_{iab} - \gamma_1\gamma_2\beta^i\Delta\kappa_{iab} \\
& - 2\Delta\alpha S_{ab} - 2\alpha\Delta S_{ab} \,.
\end{aligned}
\tag{4.55}
$$

Constraint Equations

In order to check the numerical performance of the evolution equations given in the previous section, we evaluate a set of four perturbed constraints that Δg_{ab} and $\Delta\kappa_{abc}$ must satisfy. These functions are zero analytically, and we will check their convergence to zero with increasing numerical resolution.

The 1-index constraint (cf. [121]) is the gauge constraint

$$C_a = H_a + \Gamma_a, \tag{4.56}$$

which measures the numerical accuracy of the generalized harmonic evolution (cf. Eq. (4.20)). We perturb this to get the constraint

$$\Delta C_a \equiv \Delta H_a + \Delta\Gamma_a, \tag{4.57}$$

where ΔH_a is the gauge source function for the metric perturbation evolution.

The 3-index constraint evaluates the difference between the numerical derivative of g_{ab} and κ_{iab}, the first-order variable encoding the spatial derivative of the metric as

$$C_{iab} = \partial_i g_{ab} - \kappa_{iab}. \tag{4.58}$$

Perturbing this, we obtain

$$\Delta C_{iab} = \partial_i \Delta g_{ab} - \Delta\kappa_{iab}. \tag{4.59}$$

The 4-index constraint concerns the commutation of partial derivatives as

$$C_{ijab} \equiv 2\partial_{[i}\kappa_{j]ab}. \tag{4.60}$$

Perturbing this, we obtain

$$\Delta C_{ijab} \equiv 2\partial_{[i}\Delta\kappa_{j]ab}. \tag{4.61}$$

Finally, the 2-index constraint is derived from the Hamiltonian and momentum constraints, as well as the 3-index constraint. The constraint and its perturbation are too lengthy to reproduce here, and so we have written them in Appendix 4.A.

Thus, when performing an evolution, we evaluate the right-hand sides of Eqs. (4.57), (4.59), (4.61), and (4.80), and check that they converge to zero with increasing numerical resolution. In particular, as we use a spectral code, we expect exponential convergence with resolution [198].

In order to show that the constraints themselves are convergent, rather than the absolute values of the metric variables simply getting smaller, we can normalize the constraints by the absolute values of the metric fields they contain. For example, for a constraint of the form $A + B$, we normalize it by dividing by $\sqrt{A^2 + B^2}$. The question arises of whether we should normalize the constraints pointwise, or whether we should compute the norm of each constraint and its normalization factor over the entire domain and then divide the norms. Since we will evolve a localized metric perturbation, there will be regions in the domain with Δg_{ab} nearly zero, so we choose to first compute norms and then divide them.

Characteristic variables

All of the discussion so far has centered on fundamental variables Δg_{ab} and $\Delta \kappa_{abc}$. However, in order to implement boundary conditions, it is useful to instead consider *characteristic fields*. These can be used to measure the characteristic speeds and to construct boundary conditions.

The characteristic fields are the eigenvectors of the principal part of the evolution equations (cf. [121] for an example derivation). The characteristic speeds are the corresponding eigenvalues. For the generalized harmonic system, the characteristic variables on a surface with spatial normal vector $\hat{n}^i$ take the form

$$u^0_{ab} = g_{ab}, \tag{4.62}$$

$$u^{1\pm}_{ab} = \kappa_{0ab} \pm \hat{n}^i \kappa_{iab} - \gamma_2 g_{ab}, \tag{4.63}$$

$$u^2_{iab} = (\delta_i{}^k - \hat{n}_i \hat{n}^k) \kappa_{kab}. \tag{4.64}$$

The principal parts of the linearized equations (cf. Sec 4.3) are

$$\partial_t \Delta g_{ab} - (1 + \gamma_1) \beta^k \partial_k \Delta g_{ab} \simeq 0, \tag{4.65}$$

$$\partial_t \Delta \kappa_{0ab} - \beta^k \partial_k \Delta \kappa_{0ab} \tag{4.66}$$
$$+ \alpha \gamma^{ki} \partial_k \Delta \kappa_{iab} - \gamma_1 \gamma_2 \beta^k \partial_k \Delta g_{ab} \simeq 0,$$

$$\partial_t \Delta \kappa_{iab} - \beta^k \partial_k \Delta \kappa_{iab} \tag{4.67}$$
$$+ \alpha \partial_i \Delta \kappa_{0ab} - \gamma_2 \alpha \partial_i \Delta g_{ab} \simeq 0.$$

These are exactly those of the generalized harmonic system, and hence the characteristic fields and speeds will be the same. Thus, the characteristic fields of the linearized system are simply

$$\Delta u^0_{ab} = \Delta g_{ab}, \tag{4.68}$$

$$\Delta u^{1\pm}_{ab} = \Delta \kappa_{0ab} \pm \hat{n}^i \Delta \kappa_{iab} - \gamma_2 \Delta g_{ab}, \tag{4.69}$$

$$\Delta u^2_{iab} = (\delta_i{}^k - \hat{n}_i \hat{n}^k) \Delta \kappa_{kab}. \tag{4.70}$$

The reverse transformation from characteristic variables to fundamental variables is then

$$\Delta g_{ab} = \Delta u^0_{ab}, \tag{4.71}$$

$$\Delta \kappa_{0ab} = \frac{1}{2} (\Delta u^{1+}_{ab} + \Delta u^{1-}_{ab}) + \gamma_2 \Delta u^0_{ab}, \tag{4.72}$$

$$\Delta \kappa_{iab} = \frac{1}{2} \hat{n}_i (\Delta u^{1+}_{ab} - \Delta u^{1-}_{ab}) + \Delta u^2_{iab}. \tag{4.73}$$

As in the generalized harmonic system, the characteristic speed for Δu^0_{ab} is $-(1 + \gamma_1)n_k\beta^k$, the speed for $\Delta u^{1\pm}_{ab}$ is $-n_k\beta^k \pm \alpha$, and the speed for Δu^2_{iab} is $-n_k\beta^k$.

Boundary Conditions

In the previous section, we derived the characteristic fields for the linearized system. In order to complete the evolution system, we must include boundary conditions for these characteristic fields. All of our numerical evolutions include a finite outer boundary, and we choose to use a freezing boundary condition, which sets

$$P(d\Delta u^{(a)}/dt) = 0, \tag{4.74}$$

where $\Delta u^{(a)}$ is a perturbation to a characteristic field and P refers to the characteristic projection onto the surface. Though more sophisticated conditions are available, especially for computing accurate gravitational radiation (cf. [115, 172, 173]), we find that the freezing boundary condition is sufficient for our purposes, especially since the characteristics are initially purely outgoing (out of the computational domain).

When simulating metric perturbations on a spacetime containing one or more black holes, we exclude the region just inside the apparent horizon from the computational domain [104]. This forms a topologically spherical inner boundary. However, there should be no characteristics entering the computational domain from the horizon, and thus we do not need to specify a condition at the inner boundary.

Code Tests

Because of the complexity of Eqs. (4.25), (4.26), and (4.27), we perform a series of code tests. These code tests contain no new physics, but rather check that the evolution equations have been implemented correctly. We present the results of these tests in Appendix 4.B.

4.4 Evolving dCS metric perturbations

We now apply the formalism given in Sec. 4.3 to dynamical Chern-Simons gravity. Specifically, we aim to test the stability of rotating black holes in dCS by evolving the leading-order metric perturbation, Δg_{ab}, governed by Eq. (4.19), on a rotating black hole background. In GR, this background is given by the Kerr metric. Recall from Eqs. (4.16), (4.17), and (4.18), that it is precisely the inclusion of $C_{ab}(\Psi)$ in the effective stress energy tensor that differentiates dynamical Chern-Simons gravity, where the scalar field is coupled to spacetime curvature via $^{*}RR$, from a simple metric perturbation sourced by a scalar field in GR.

Implementation details

In [143], we derived stationary initial data for Δg_{ab} on a Kerr background sourced by the spacetime curvature of the Kerr background coupled to a stationary field Ψ obeying $\Box \Psi = \, ^{*}RR$. [184]. Using these data, we construct $\Delta \kappa_{abc}$ following Eqs. (4.49) and (4.48). The source term ΔS_{ab} described in Sec. 4.3 is computed from Ψ using $T_{ab}^{\mathrm{eff}}(\Psi)$ in Eq. (4.16).

Our computational domain is a set of eleven nested spherical shells, with more shells centered near the horizon and fewer shells further out. The boundary of the innermost shell conforms to the apparent horizon of the background black hole, and the outer boundary is at $R = 200\,M$. We repeat simulations at three different numerical resolutions determined by a parameter labeled "low", "medium", or "high"; each shell has 5 radial spectral basis points and 6 angular spectral basis points at the lowest resolution, with one more radial and angular basis point added for each increase in our resolution parameter.

We evolve $\{\Delta g_{ab}, \Delta \kappa_{abc}\}$ using the equations in Sec. 4.3 using a spectral code [198]. We apply filtering to the spectral scheme in order to minimize the growth of high-frequency modes [190]. We choose damping parameters γ_0 and γ_2 to be larger close to the horizon, where the metric perturbation is greatest, as shown in Fig. 4.1. We choose $\gamma_1 = -1$ as in Ref. [121].

Results

In Fig. 4.2, we present the perturbed constraint violation for a spin $\chi = 0.1$ background using the expressions derived in Sec. 4.3. We see that the constraints remain roughly constant in time and are exponentially convergent. We check the constraint convergence for every simulation. Note that as we increase the spin, more spectral coefficients are needed to achieve the same level of constraint violation.
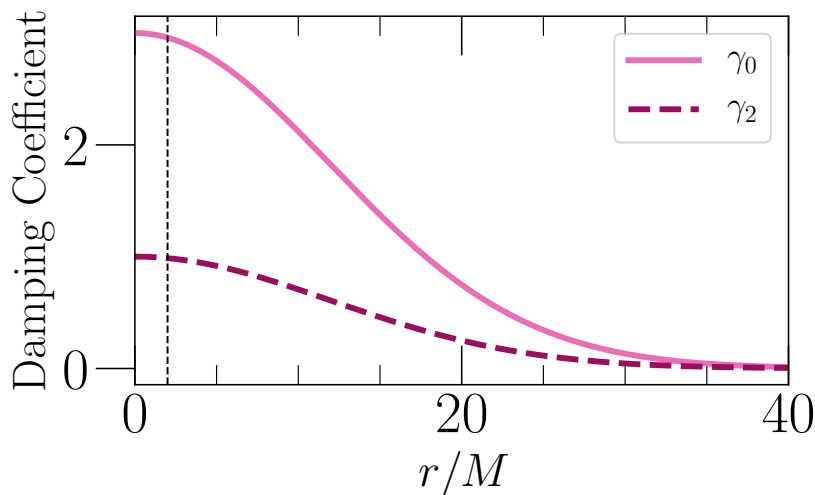
Figure 4.1: Constraint damping functions γ_0 and γ_2 used to evolve metric perturbations on a Kerr background. The functions are largest where the metric perturbation source has the highest value, and exponentially decay to $R \to \infty$. While the functions extend to $R = 0$, the computational domain terminates outside the apparent horizon inner boundary (here shown by the black dashed line at $R = 2\,M$ in the case of Schwarzschild).

In Fig. 4.3, we present the behavior of the norm of the metric perturbation with time for $\chi = 0.1$ for low, medium, and high resolution. We see that as we increase resolution, Δg_{ab} becomes more constant in time. Note that the specific value of $\|\Delta g_{ab}\|$ (~ 0.86 in Fig. 4.3) should be a function of χ, the spin of the back hole. However, though expressions for this functional dependence exist in the slow and rapid rotation limits [214, 116], and as post-Newtonian expansions [29], no closed-form, analytical expression for the functional dependence is known.

Fig. 4.4 similarly shows the behavior of the metric perturbation for $\chi = 0.6$. This case is particularly interesting, as it corresponds roughly to the final spin of the post-merger black holes in [146]. We thus conclude that were we to also simulate metric perturbations in that study, we could stably evolve metric perturbations through ringdown.

For a more quantitative analysis, we show the time derivative of the norm of Δg_{ab} in Figs. 4.5, 4.6, and 4.7, for $\chi = 0.1$, $\chi = 0.6$, and $\chi = 0.9$, for three different resolutions. Initially, there is some junk radiation (unphysical spurious radiation) present on the domain, so the first $\sim 150\,M$ (corresponding to the computational domain radius) of each figure can be ignored.
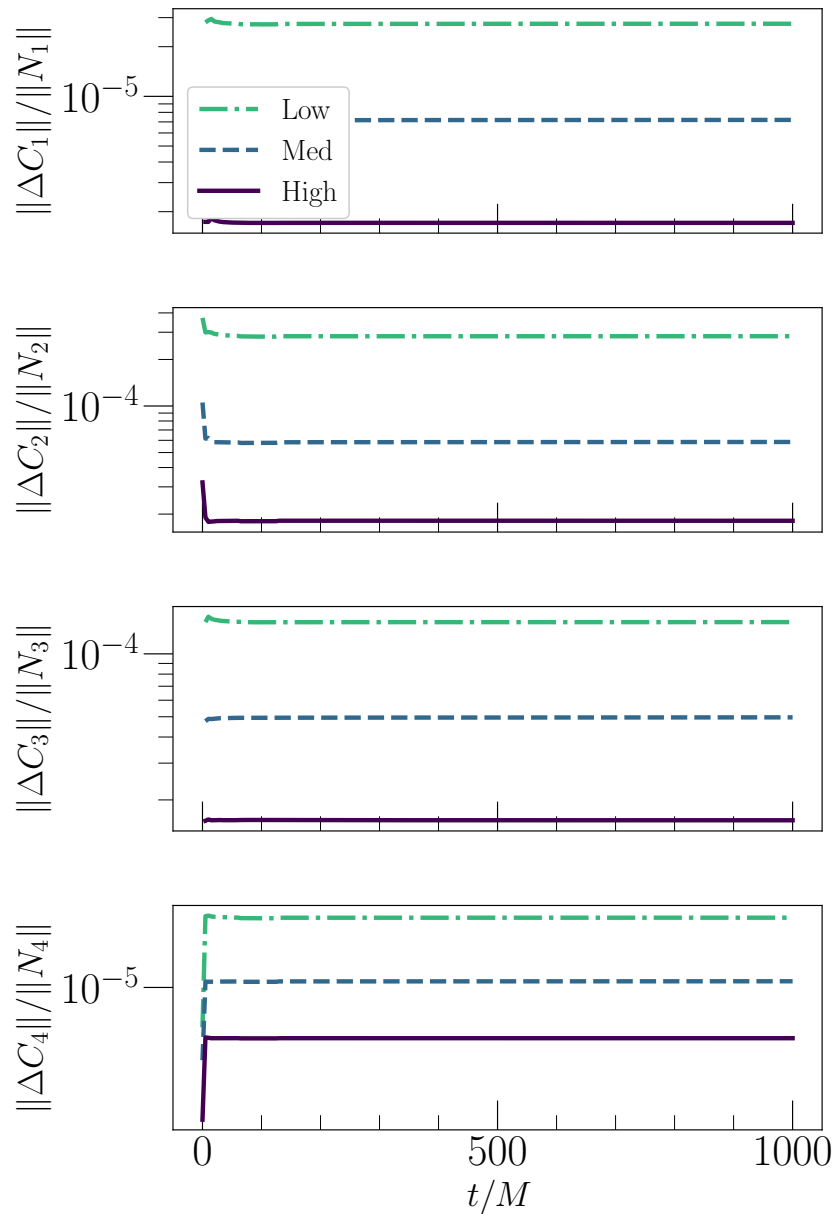
Figure 4.2: Behavior of the perturbed constraints given in Sec. 4.3 for a dCS perturbation on a Kerr background with $\chi = 0.1$. For each constraint ΔC_A, we compute the L2 norm of the constraint over the entire computational domain ($\|\Delta C_1\|$ for the 1-index constraint, for example) and divide by the L2 norm of its normalization factor ($\|N_A\|$) (cf. Sec. 4.3). We see that the constraints remain constant in time and are exponentially convergent with resolution.
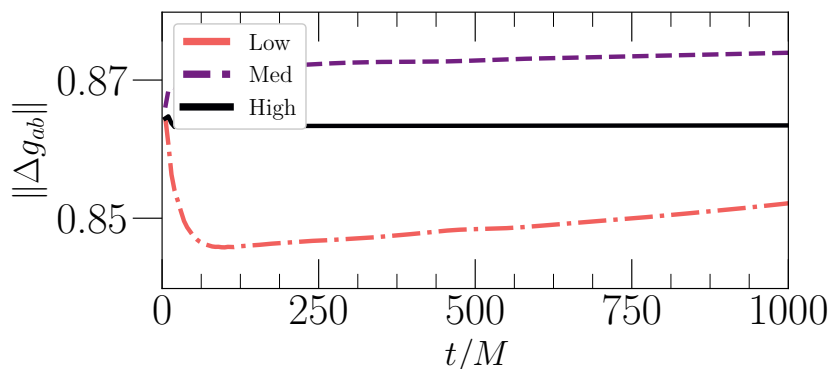
Figure 4.3: Metric perturbation Δg_{ab} on a Kerr background with $\chi = 0.1$. We present the behavior at low, medium, and high resolutions, and find that we increase the numerical resolution, the level of linear growth in time decreases.
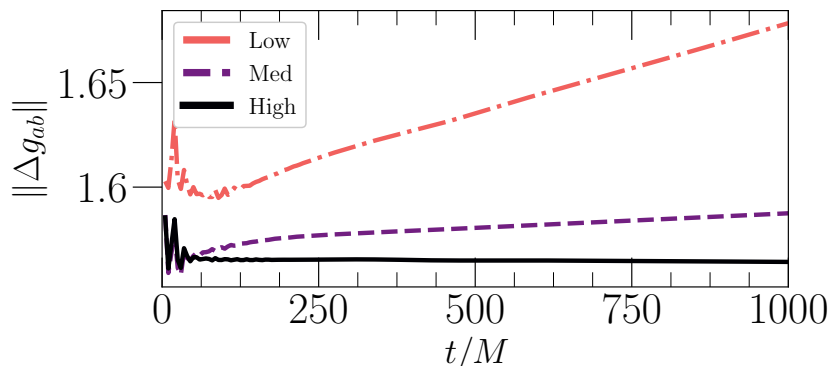
Figure 4.4: Similar to Fig. 4.3, but for spin of $\chi = 0.6$. For each resolution, we use the initial data for Δg_{ab} we have solved for at that resolution, and hence Δg_{ab} has different initial values depending on resolution. We have checked that these initial values converge to the highest-resolution result.

We see that after the junk radiation has left the domain, the normalized time derivative decreases with numerical resolution, staying at a low level of $\sim 10^{-6}$ at the highest resolution[1]. Let us examine this result more carefully. The metric perturbation, as shown for example in Fig. 4.3, exhibits linear growth in time. However, the lower numerical resolutions exhibit more linear growth than higher numerical resolutions. As shown in Fig. 4.5, we see that with increasing numerical resolution, this linear growth converges exponentially towards zero. Thus, this linear growth is

---

[1]Higher spins require higher resolutions to achieve the same level of numerical accuracy in Kerr-Schild coordinates, and thus the values of the time derivatives at the same numerical resolution increase slightly with spin.

a numerical artifact and, in the limit of infinite resolution, will be zero. Thus, we must evolve the metric perturbation at a high enough resolution such that the linear growth is small enough for our purposes.

How long do we need to evolve Δg_{ab} to be confident in the stability of the field? Practically, NR gravitational waveforms typically contain $100 - 200\,M$ of ringdown signal [139], as did the simulations we performed in [146]. Thus, we certainly require stability on timescales of $\mathcal{O}(100)\,M$. Binary black hole simulation initial data is comprised of an approximate superposition of two black hole metrics [127]. Thus, in the early inspiral, the spacetime is similar to that of two black holes, with a dCS metric perturbation isolated around each black hole. While binary black hole simulations typically start $\sim 5,000$ to $10,000\,M$ before merger (cf. [139]), at some point in the inspiral, strong-field dynamics take over and the spacetime is no longer a superposition of two Kerr black holes. Thus, we are interested in timescales of $\mathcal{O}(1000)\,M$, to be able to simulate the early inspiral. For one resolution, we have also evolved Δg_{ab} on a $\chi = 0.1$ background for $10,000\,M$ (but only 1000M of evolution is shown in Fig. 4.5). We find that the metric perturbation exhibits similar behavior on these timescales (the time derivative of the perturbed metric, $\partial_t \Delta g_{ab}$, remains at a constant level for at least $10,000\,M$).

Let us now discuss the origin of the linearly growing mode (a zero-frequency mode). One possibility is that it is present in the initial data for the metric perturbation, as it is in the spectrum of the differential operator. For the simulations shown in Figs. 4.5, 4.6, and 4.7, the evolution for each numerical resolution has its own initial data, which is solved for independently on a grid of that resolution. Thus, if the presence of the mode is purely due to the initial data, we would expect different resolutions to display various levels of linear growth, which we indeed see. To further test this hypothesis, we can instead solve for initial data for Δg_{ab} only at the highest resolution, and *interpolate* this onto the lower-resolution grids to use for the evolution. In Fig. 4.8, we show the results of this procedure. We see that all three resolutions have roughly the same amount of linear growth, suggesting that the zero-frequency mode is seeded by the initial data, rather than spontaneously appearing during the evolution. Note that the growth is at the level of the highest resolution, which is still finite, and hence the growth is non-zero. This in turn tells us that in order to achieve the requisite level of numerical stability, we can use higher-resolution initial data and perform our simulations at lower resolutions.
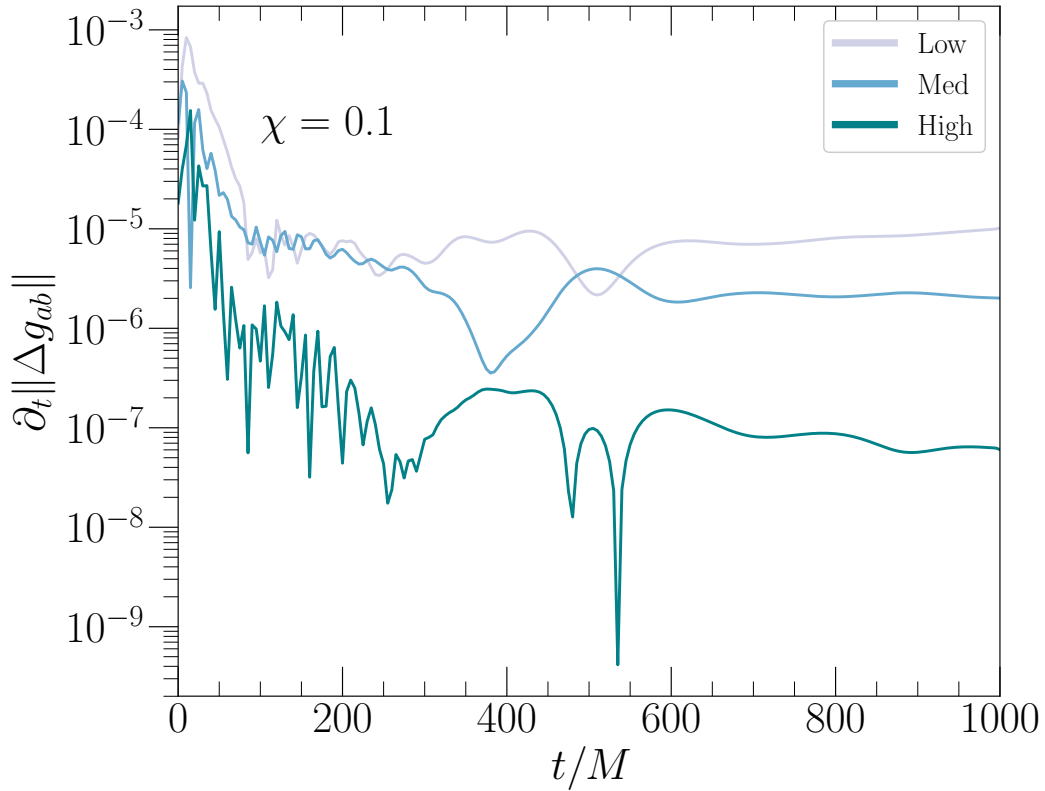
Figure 4.5: Behavior of the derivative of the norm of the metric perturbation with time for a background with spin $\chi = 0.1$. We plot $\partial_t \|\Delta g_{ab}\|$, the time derivative of the norm of the metric perturbation. Each line corresponds to a different resolution. We see that after an initial period of junk radiation, the time derivative is convergent towards zero with increasing numerical resolution.
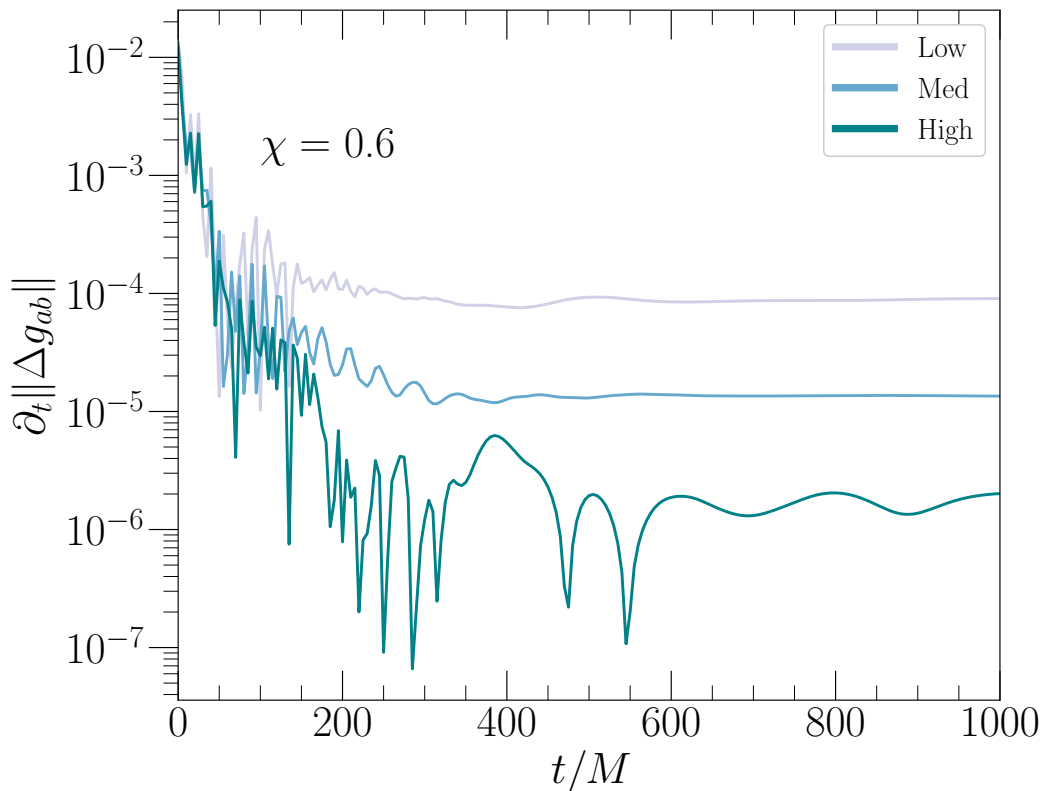
Figure 4.6: Similar to Fig. 4.5, but for spin $\chi = 0.6$.

4.5 Results and discussion

In this chapter, we have aimed to test the stability of rotating black holes in dCS gravity to leading order. We have worked in order-reduced dCS, in which we perturb the dCS scalar field and metric around a GR background. We have evolved the leading-order dCS metric perturbation, sourced by the leading-order dCS scalar field coupled to the spacetime curvature of the GR background (Sec. 4.4). We used a fully general, first-order, constraint-damping metric perturbation evolution scheme based on the generalized harmonic formalism of general relativity (Sec. 4.3). We found that the dCS metric perturbation exhibits linear growth in time, but that the level of linear growth converges towards zero with increasing numerical resolution.

The linear stability analysis presented in this paper shows that black holes in dCS gravity are numerically stable to leading-order perturbations in the metric. The leading-order (first non-vanishing) metric perturbation in dCS gravity occurs at second order, and thus the linear stability presented corresponds to stability at second order in the dCS order-reduction scheme. Previous studies have explored
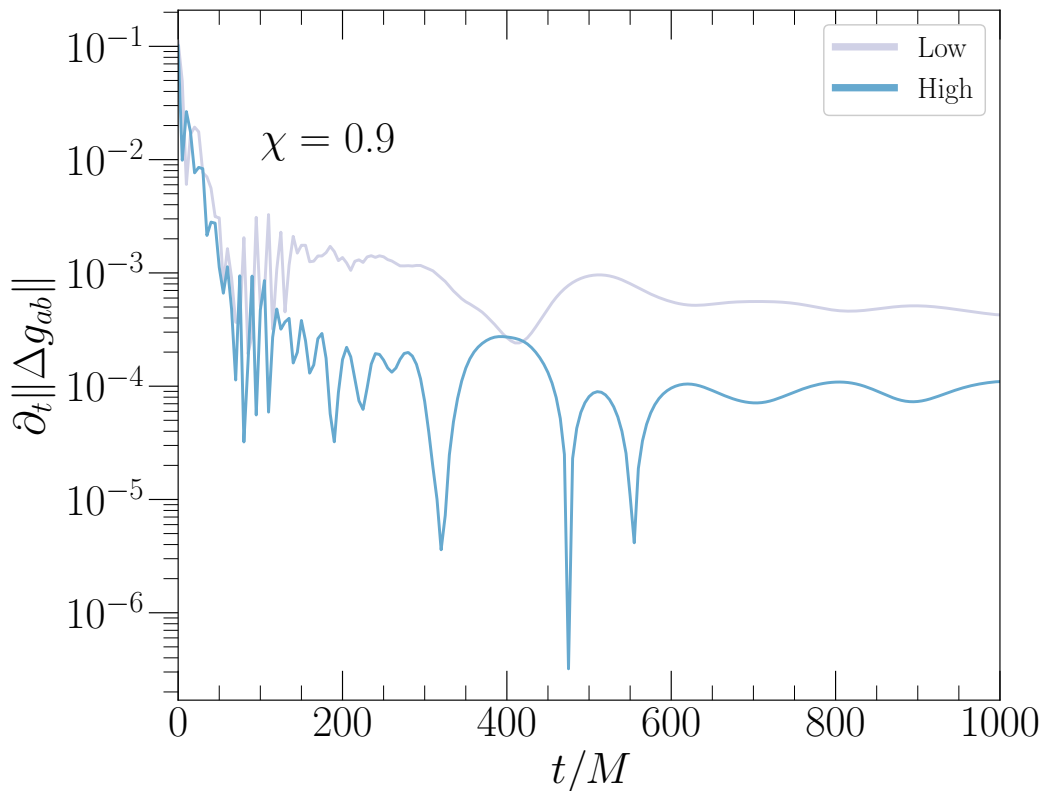
Figure 4.7: Similar to Fig. 4.5, but for spin $\chi = 0.9$.

the question of black hole stability in dCS gravity [137, 90, 43], but this is the first study to explore the behavior of metric perturbations on a spinning background with non-zero source.

Linear theory has no scale, and thus the results presented in this paper can be applied to any coupling parameter ε^2 such that, to second order, the dCS metric is $g_{ab} + \varepsilon^2 \Delta g_{ab}$. However, for the perturbative scheme to be valid, we must choose ε^2 such that $\|\varepsilon^2 \Delta g_{ab}\| \lesssim \|g_{ab}\|$ (cf. [184] and [143] for a quantitative analysis of allowed values of ε^2).

The stability of our simulations makes us confident that we can evolve dCS metric perturbations in a binary black hole spacetime without numerical instabilities. We can use a superposition of the dCS scalar field initial data given in [184] and the dCS metric perturbation initial data formalism and code used in [143] to generate initial data for scalar field Ψ and perturbed metric variables Δg_{ab} and $\Delta \kappa_{abc}$. We can then evolve the scalar field as we previously have in [146] and use this $\Psi(t)$ to source the evolution of Δg_{ab}. While we have used a stationary gauge as determined by
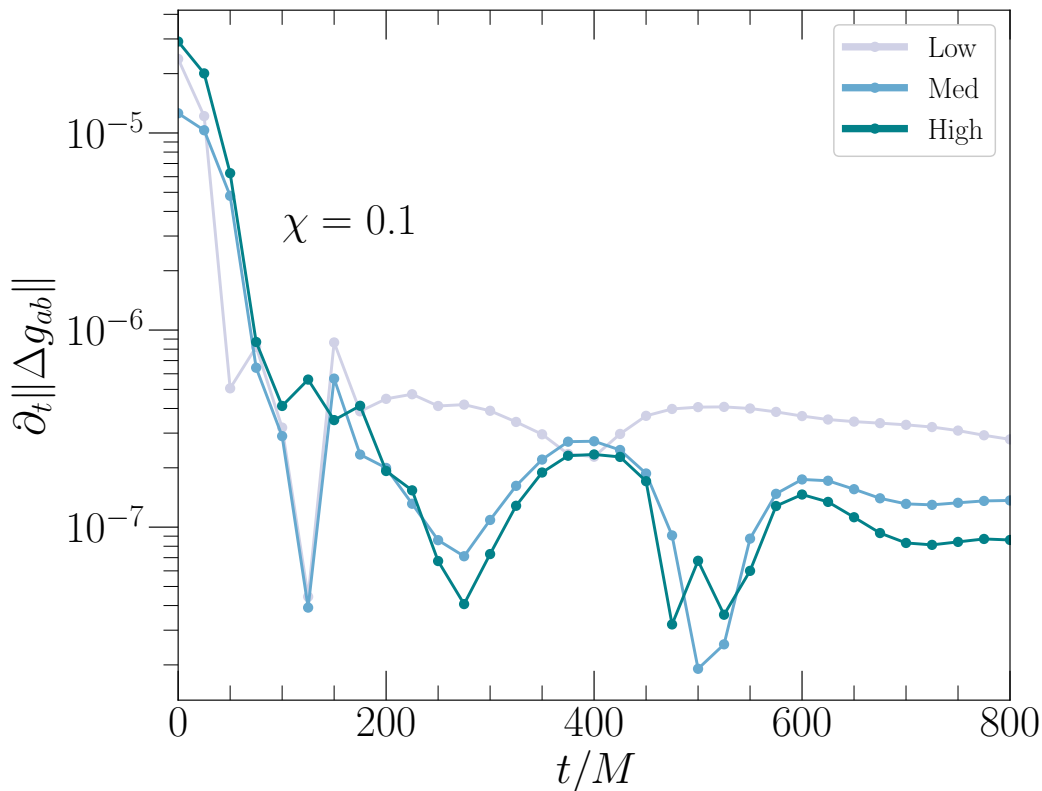
Figure 4.8: The structure of this figure is similar to that of Fig. 4.5. However, in this case, we solve for the initial data for Δg_{ab} purely at the "High" resolution. We interpolate this data onto the "Low" and "Medium" resolution grids to give initial data at these resolutions. We see that as the simulation progresses, the linear growth in Δg_{ab} remains at roughly the same level for all resolutions. This suggests that the zero-frequency mode in Δg_{ab} is present in and due to the resolution of the initial data, rather than spontaneously appearing during the evolution.

$\Delta H_a = \Delta \Gamma_a(t = 0)$ in this work, we also have the option of rolling into a perturbed damped harmonic gauge during the binary evolution (cf. [189]).

4.A   Perturbed 2-index constraint

In this appendix, we derive perturbations to the generalized harmonic constraint C_{ab}. This constraint corresponds to a combination of the Hamiltonian and momentum constraints, and includes terms proportional to the constraint C_{iab} (cf. Eq. (4.58)) that are added in order to simplify the evolution equations for the constraints [121]. The constraint C_{ab} is defined in Eqs. 43 and 44 of [121], in which the time components C_{0a} are called $\mathcal{F}_a$. The expressions in [121] do not contain stress-energy source

terms, but we include these terms here. In particular,

$$C_{0a} \equiv \mathcal{F}_a - 2n^b S_{ba} + n_a S_{bc} g^{bc}, \tag{4.75}$$

where $\mathcal{F}_a$ is the expression from [121].

In terms of the variable κ_{abc}, the spatial part of the 2-index constraint is

$$\begin{aligned}
C_{ia} \equiv\ & \gamma^{jk} \partial_j \kappa_{ika} - \frac{1}{2} \gamma^j{}_a g^{cd} \partial_j \kappa_{icd} + n^b \partial_i \kappa_{0ba} \tag{4.76} \\
& - \frac{1}{2} n_a g^{cd} \partial_i \kappa_{0cd} + \partial_i H_a + \frac{1}{2} g^j{}_a \kappa_{jcd} \kappa_{ief} g^{ce} g^{df} \\
& + \frac{1}{2} \gamma^{jk} \kappa_{jcd} \kappa_{ike} g^{cd} n^e n_a \\
& - \gamma^{jk} \gamma^{mn} \kappa_{jma} \kappa_{ikn} \\
& + \frac{1}{2} \kappa_{icd} \kappa_{0be} n_a \left(g^{cb} g^{de} + \frac{1}{2} g^{be} n^c n^d \right) \\
& - \kappa_{icd} \kappa_{0ba} n^c \left(g^{bd} + \frac{1}{2} n^b n^d \right) \\
& + \frac{1}{2} \gamma_2 \left(n_a g^{cd} - 2 \delta^c_a n^d \right) C_{icd},
\end{aligned}$$

and the time part is the lengthy expression

$$
\begin{aligned}
C_{0a} \equiv\ & -2n^b S_{ba} + n_a S_{bc} g^{bc} \tag{4.77} \\
& + \frac{1}{2} g_a^i g^{bc} \partial_i \kappa_{0bc} - \gamma^{ij} \partial_i \kappa_{0ja} - \gamma^{ij} n^b \partial_i \kappa_{jba} \\
& + \frac{1}{2} n_a g^{bc} \gamma^{ij} \partial_i \kappa_{jbc} + n_a \gamma^{ij} \partial_i H_j \\
& + g_a^i \kappa_{ijb} \gamma^{jk} \kappa_{kcd} \left(g^{bd} n^c - \frac{1}{2} g^{cd} n^b \right) \\
& - g_a^i n^b \partial_i H_b + \gamma^{ij} \kappa_{icd} \kappa_{jba} g^{bc} n^d \\
& - \frac{1}{2} n_a \gamma^{ij} \gamma^{mn} \kappa_{imc} \kappa_{njd} g^{cd} \\
& - \frac{1}{4} n_a \gamma^{ij} \kappa_{icd} \kappa_{jbe} g^{cb} g^{de} + \frac{1}{4} n_a \kappa_{0cd} \kappa_{0be} g^{cb} g^{de} \\
& - \gamma^{ij} H_i \kappa_{0ja} - n^b \gamma^{ij} \kappa_{0bi} \kappa_{0ja} \\
& - \frac{1}{4} g_a^i \kappa_{icd} n^c n^d \kappa_{0be} g^{be} + \frac{1}{2} n_a \kappa_{0cd} \kappa_{0be} g^{ce} n^d n^b \\
& + g_a^i \kappa_{icd} \kappa_{0be} n^c n^b g^{de} - \gamma^{ij} \kappa_{iba} n^b \kappa_{0je} n^e \\
& - \frac{1}{2} \gamma^{ij} \kappa_{icd} n^c n^d \kappa_{0ja} - \gamma^{ij} H_i \kappa_{jba} n^b \\
& + g_a^i \kappa_{icd} H_b g^{bc} n^d \\
& + \gamma_2 \left(\gamma^{id} C_{ida} - \frac{1}{2} g_a^i g^{cd} C_{icd} \right) \\
& + \frac{1}{2} n_a \kappa_{0cd} g^{cd} H_b n^b - n_a \gamma^{ij} \kappa_{ijc} H_d g^{cd} \\
& + \frac{1}{2} n_a \gamma^{ij} H_i \kappa_{jcd} g^{cd} \,.
\end{aligned}
$$

Perturbing Eq. (4.76) to obtain the perturbation to the spatial part of the 2-index constraint, we find

$$\Delta C_{ia} \equiv \Delta\gamma^{jk}\partial_j\kappa_{ika} + \gamma^{jk}\partial_j\Delta\kappa_{ika} - \frac{1}{2}\Delta\gamma^j{}_a g^{cd}\partial_j\kappa_{icd} - \frac{1}{2}\gamma^j{}_a\Delta g^{cd}\partial_j\kappa_{icd} \quad (4.78)$$

$$- \frac{1}{2}\gamma^j{}_a g^{cd}\partial_j\Delta\kappa_{icd} + \Delta n^b\partial_i\kappa_{0ba} + n^b\partial_i\Delta\kappa_{0ba}$$

$$- \frac{1}{2}\Delta n_a g^{cd}\partial_i\kappa_{0cd} - \frac{1}{2}n_a\Delta g^{cd}\partial_i\kappa_{0cd}$$

$$- \frac{1}{2}n_a g^{cd}\partial_i\Delta\kappa_{0cd} + \partial_i\Delta H_a$$

$$+ \frac{1}{2}\Delta g^j{}_a\kappa_{jcd}\kappa_{ief}g^{ce}g^{df} + \frac{1}{2}g^j{}_a\Delta\kappa_{jcd}\kappa_{ief}g^{ce}g^{df}$$

$$+ \frac{1}{2}g^j{}_a\kappa_{jcd}\Delta\kappa_{ief}g^{ce}g^{df} + \frac{1}{2}g^j{}_a\kappa_{jcd}\kappa_{ief}\Delta g^{ce}g^{df}$$

$$+ \frac{1}{2}g^j{}_a\kappa_{jcd}\kappa_{ief}g^{ce}\Delta g^{df} + \frac{1}{2}\Delta\gamma^{jk}\kappa_{jcd}\kappa_{ike}g^{cd}n^e n_a$$

$$+ \frac{1}{2}\gamma^{jk}\Delta\kappa_{jcd}\kappa_{ike}g^{cd}n^e n_a + \frac{1}{2}\gamma^{jk}\kappa_{jcd}\Delta\kappa_{ike}g^{cd}n^e n_a$$

$$+ \frac{1}{2}\gamma^{jk}\kappa_{jcd}\kappa_{ike}\Delta g^{cd}n^e n_a + \frac{1}{2}\gamma^{jk}\kappa_{jcd}\kappa_{ike}g^{cd}\Delta n^e n_a$$

$$+ \frac{1}{2}\gamma^{jk}\kappa_{jcd}\kappa_{ike}g^{cd}n^e\Delta n_a - \Delta\gamma^{jk}\gamma^{mn}\kappa_{jma}\kappa_{ikn}$$

$$- \gamma^{jk}\Delta\gamma^{mn}\kappa_{jma}\kappa_{ikn} - \gamma^{jk}\gamma^{mn}\Delta\kappa_{jma}\kappa_{ikn} - \gamma^{jk}\gamma^{mn}\kappa_{jma}\Delta\kappa_{ikn}$$

$$+ \frac{1}{2}(\Delta\kappa_{icd}\kappa_{0be}n_a + \kappa_{icd}\Delta\kappa_{0be}n_a + \kappa_{icd}\kappa_{0be}\Delta n_a) \times \left(g^{cb}g^{de} + \frac{1}{2}g^{be}n^c n^d\right)$$

$$+ \frac{1}{2}\kappa_{icd}\kappa_{0be}n_a\left(\Delta g^{cb}g^{de} + g^{cb}\Delta g^{de} + \frac{1}{2}(\Delta g^{be}n^c n^d + g^{be}\Delta n^c n^d + g^{be}n^c\Delta n^d)\right)$$

$$- (\Delta\kappa_{icd}\kappa_{0ba}n^c + \kappa_{icd}\Delta\kappa_{0ba}n^c + \kappa_{icd}\kappa_{0ba}\Delta n^c) \times \left(g^{bd} + \frac{1}{2}n^b n^d\right)$$

$$- \kappa_{icd}\kappa_{0ba}n^c\left(\Delta g^{bd} + \frac{1}{2}\Delta n^b n^d + \frac{1}{2}n^b\Delta n^d\right)$$

$$+ \frac{1}{2}\gamma_2\left(\Delta n_a g^{cd} + n_a\Delta g^{cd} - 2\delta^c_a\Delta n^d\right)C_{icd} + \frac{1}{2}\gamma_2\left(n_a g^{cd} - 2\delta^c_a n^d\right)\Delta C_{icd},$$

where ΔC_{icd} is the perturbed 3-index constraint as defined in Eq. (4.59).

Finally, the perturbation to the time part of the 2-index constraint is

$$\Delta C_{0a} \equiv -2\Delta n^b S_{ba} - 2n^b \Delta S_{ba} + \Delta n_a S_{bc} g^{bc} + n_a \Delta S_{bc} g^{bc} + n_a S_{bc} \Delta g^{bc} \quad (4.79)$$

$$+ \frac{1}{2}\Big(\Delta g_a^i g^{bc} \partial_i \kappa_{0bc} + g_a^i \Delta g^{bc} \partial_i \kappa_{0bc} + g_a^i g^{bc} \partial_i \Delta\Big)\kappa_{0bc} - \Delta\gamma^{ij}\partial_i \kappa_{0ja} - \gamma^{ij}\partial_i \Delta\kappa_{0ja}$$

$$- \Delta\gamma^{ij} n^b \partial_i \kappa_{jba} - \gamma^{ij}\Delta n^b \partial_i \kappa_{jba} - \gamma^{ij} n^b \partial_i \Delta\kappa_{jba}$$

$$+ \frac{1}{2}\Big(\Delta n_a g^{bc}\gamma^{ij}\partial_i \kappa_{jbc} + n_a \Delta g^{bc}\gamma^{ij}\partial_i \kappa_{jbc} + n_a g^{bc}\Delta\gamma^{ij}\partial_i \kappa_{jbc} + n_a g^{bc}\gamma^{ij}\partial_i \Delta\kappa_{jbc}\Big)$$

$$+ \Delta n_a \gamma^{ij}\partial_i H_j + n_a \Delta\gamma^{ij}\partial_i H_j + n_a \gamma^{ij}\partial_i \Delta H_j$$

$$+ \Big(\Delta g_a^i \kappa_{ijb}\gamma^{jk}\kappa_{kcd} + g_a^i \Delta\kappa_{ijb}\gamma^{jk}\kappa_{kcd} + g_a^i \kappa_{ijb}\Delta\gamma^{jk}\kappa_{kcd} + g_a^i \kappa_{ijb}\gamma^{jk}\Delta\kappa_{kcd}\Big)$$

$$\times \Big(g^{bd} n^c - \frac{1}{2}g^{cd} n^b\Big)$$

$$+ g_a^i \kappa_{ijb}\gamma^{jk}\kappa_{kcd}\Big(\Delta g^{bd} n^c + g^{bd}\Delta n^c - \frac{1}{2}\Delta g^{cd} n^b - \frac{1}{2}g^{cd}\Delta n^b\Big)$$

$$- \Delta g_a^i n^b \partial_i H_b - g_a^i \Delta n^b \partial_i H_b - g_a^i n^b \partial_i \Delta H_b$$

$$+ \Delta\gamma^{ij}\kappa_{icd}\kappa_{jba} g^{bc} n^d + \gamma^{ij}\Delta\kappa_{icd}\kappa_{jba} g^{bc} n^d +$$

$$\gamma^{ij}\kappa_{icd}\Delta\kappa_{jba} g^{bc} n^d + \gamma^{ij}\kappa_{icd}\kappa_{jba}\Delta g^{bc} n^d + \gamma^{ij}\kappa_{icd}\kappa_{jba} g^{bc}\Delta n^d$$

$$- \frac{1}{2}\Big(\Delta n_a \gamma^{ij}\gamma^{mn}\kappa_{imc}\kappa_{njd} g^{cd} + n_a \Delta\gamma^{ij}\gamma^{mn}\kappa_{imc}\kappa_{njd} g^{cd} + n_a \gamma^{ij}\Delta\gamma^{mn}\kappa_{imc}\kappa_{njd} g^{cd}$$

$$+ n_a \gamma^{ij}\gamma^{mn}\Delta\kappa_{imc}\kappa_{njd} g^{cd} + n_a \gamma^{ij}\gamma^{mn}\kappa_{imc}\Delta\kappa_{njd} g^{cd} + n_a \gamma^{ij}\gamma^{mn}\kappa_{imc}\kappa_{njd}\Delta g^{cd}\Big)$$

$$- \frac{1}{4}\Big(\Delta n_a \gamma^{ij}\kappa_{icd}\kappa_{jbe} g^{cb} g^{de} + n_a \Delta\gamma^{ij}\kappa_{icd}\kappa_{jbe} g^{cb} g^{de}$$

$$+ n_a \gamma^{ij}\Delta\kappa_{icd}\kappa_{jbe} g^{cb} g^{de}$$

$$+ n_a \gamma^{ij}\kappa_{icd}\Delta\kappa_{jbe} g^{cb} g^{de} + n_a \gamma^{ij}\kappa_{icd}\kappa_{jbe}\Delta g^{cb} g^{de} + n_a \gamma^{ij}\kappa_{icd}\kappa_{jbe} g^{cb}\Delta g^{de}\Big)$$

$$+ \frac{1}{4}\Big(\Delta n_a \kappa_{0cd}\kappa_{0be} g^{cb} g^{de} + n_a \Delta\kappa_{0cd}\kappa_{0be} g^{cb} g^{de}$$

$$+ n_a \kappa_{0cd}\Delta\kappa_{0be} g^{cb} g^{de} + n_a \kappa_{0cd}\kappa_{0be}\Delta g^{cb} g^{de} + n_a \kappa_{0cd}\kappa_{0be} g^{cb}\Delta g^{de}\Big)$$

$$- \Delta\gamma^{ij} H_i \kappa_{0ja} - \gamma^{ij}\Delta H_i \kappa_{0ja} - \gamma^{ij} H_i \Delta\kappa_{0ja} - \Delta n^b \gamma^{ij}\kappa_{0bi}\kappa_{0ja}$$

$$- n^b \Delta\gamma^{ij}\kappa_{0bi}\kappa_{0ja} - n^b \gamma^{ij}\Delta\kappa_{0bi}\kappa_{0ja} - n^b \gamma^{ij}\kappa_{0bi}\Delta\kappa_{0ja}$$

$$- \frac{1}{4}\Big(\Delta g_a^i \kappa_{icd} n^c n^d \kappa_{0be} g^{be} + g_a^i \Delta\kappa_{icd} n^c n^d \kappa_{0be} g^{be}$$

$$+ g_a^i \kappa_{icd}\Delta n^c n^d \kappa_{0be} g^{be} + g_a^i \kappa_{icd} n^c \Delta n^d \kappa_{0be} g^{be}$$

$$+ g_a^i \kappa_{icd} n^c n^d \Delta\kappa_{0be} g^{be} + g_a^i \kappa_{icd} n^c n^d \kappa_{0be}\Delta g^{be}\Big) \ldots$$

$$
\begin{aligned}
\ldots &+ \frac{1}{2}\Big(\Delta n_a \kappa_{0cd}\kappa_{0be}g^{ce}n^d n^b + n_a \Delta\kappa_{0cd}\kappa_{0be}g^{ce}n^d n^b \\
&\quad + n_a \kappa_{0cd}\Delta\kappa_{0be}g^{ce}n^d n^b + n_a \kappa_{0cd}\kappa_{0be}\Delta g^{ce}n^d n^b \\
&+ n_a \kappa_{0cd}\kappa_{0be}g^{ce}\Delta n^d n^b + n_a \kappa_{0cd}\kappa_{0be}g^{ce}n^d \Delta n^b \Big) \\
&+ \Delta g^i_a \kappa_{icd}\kappa_{0be}n^c n^b g^{de} + g^i_a \Delta\kappa_{icd}\kappa_{0be}n^c n^b g^{de} \\
&+ g^i_a \kappa_{icd}\Delta\kappa_{0be}n^c n^b g^{de} + g^i_a \kappa_{icd}\kappa_{0be}\Delta n^c n^b g^{de} \\
&+ g^i_a \kappa_{icd}\kappa_{0be}n^c \Delta n^b g^{de} + g^i_a \kappa_{icd}\kappa_{0be}n^c n^b \Delta g^{de} - \Delta\gamma^{ij}\kappa_{iba}n^b \kappa_{0je}n^e \\
&- \gamma^{ij}\Delta\kappa_{iba}n^b \kappa_{0je}n^e - \gamma^{ij}\kappa_{iba}\Delta n^b \kappa_{0je}n^e \\
&- \gamma^{ij}\kappa_{iba}n^b \Delta\kappa_{0je}n^e - \gamma^{ij}\kappa_{iba}n^b \kappa_{0je}\Delta n^e \\
&- \frac{1}{2}\Big(\Delta\gamma^{ij}\kappa_{icd}n^c n^d \kappa_{0ja} + \gamma^{ij}\Delta\kappa_{icd}n^c n^d \kappa_{0ja} + \gamma^{ij}\kappa_{icd}\Delta n^c n^d \kappa_{0ja} \\
&\quad + \gamma^{ij}\kappa_{icd}n^c \Delta n^d \kappa_{0ja} + \gamma^{ij}\kappa_{icd}n^c n^d \kappa_{0ja} + \gamma^{ij}\kappa_{icd}n^c n^d \Delta\kappa_{0ja} \Big) \\
&- \Delta\gamma^{ij}H_i \kappa_{jba}n^b - \gamma^{ij}\Delta H_i \kappa_{jba}n^b \\
&- \gamma^{ij}H_i \Delta\kappa_{jba}n^b - \gamma^{ij}H_i \kappa_{jba}\Delta n^b + \Delta g^i_a \kappa_{icd}H_b g^{bc}n^d + g^i_a \Delta\kappa_{icd}H_b g^{bc}n^d \\
&+ g^i_a \kappa_{icd}\Delta H_b g^{bc}n^d + g^i_a \kappa_{icd}H_b \Delta g^{bc}n^d + g^i_a \kappa_{icd}H_b g^{bc}\Delta n^d \\
&+ \gamma_2\Big(\Delta\gamma^{id}C_{ida} + \gamma^{id}\Delta C_{ida} - \frac{1}{2}\Big(\Delta g^i_a g^{cd}C_{icd} + g^i_a \Delta g^{cd}C_{icd} + g^i_a g^{cd}\Delta C_{icd} \Big) \Big) \\
&+ \frac{1}{2}\Big(\Delta n_a \kappa_{0cd}g^{cd}H_b n^b + n_a \Delta\kappa_{0cd}g^{cd}H_b n^b + n_a \kappa_{0cd}\Delta g^{cd}H_b n^b \\
&+ n_a \kappa_{0cd}g^{cd}\Delta H_b n^b + n_a \kappa_{0cd}g^{cd}H_b \Delta n^b \Big) \\
&- \Delta n_a \gamma^{ij}\kappa_{ijc}H_d g^{cd} - n_a \Delta\gamma^{ij}\kappa_{ijc}H_d g^{cd} - n_a \gamma^{ij}\Delta\kappa_{ijc}H_d g^{cd} \\
&- n_a \gamma^{ij}\kappa_{ijc}\Delta H_d g^{cd} - n_a \gamma^{ij}\kappa_{ijc}H_d \Delta g^{cd} \\
&+ \frac{1}{2}\Big(\Delta n_a \gamma^{ij}H_i \kappa_{jcd}g^{cd} + n_a \Delta\gamma^{ij}H_i \kappa_{jcd}g^{cd} + n_a \gamma^{ij}\Delta H_i \kappa_{jcd}g^{cd} \\
&+ n_a \gamma^{ij}H_i \Delta\kappa_{jcd}g^{cd} + n_a \gamma^{ij}H_i \kappa_{jcd}\Delta g^{cd} \Big),
\end{aligned}
$$

where ΔS_{ab} is the perturbation to the source term as given by Eq. (4.50). We combine Eqs. (4.78) and (4.79) into one overall constraint,

$$
\Delta C_{ab} = \left(\Delta C_{0a}, \Delta C_{ia} \right). \tag{4.80}
$$

4.B Code tests

In order to have confidence in our dCS metric perturbation evolution results, we perform a suite of tests to check the accuracy of our metric perturbation evolution

code. For each test, we check the convergence of the perturbed constraints derived in Sec. 4.3. Note that the results of these tests do not contain new physics, but rather serve as a check of our implementation of the metric perturbation evolution equations (Eqs. (4.25), (4.26), and (4.27)).

Multipolar wave evolution

We first evolve a multipolar wave in the transverse-traceless gauge on a flat background [196, 171]. This evolution takes place on a domain with only one (outer) boundary, where we set the boundary condition given in Eq. (4.74). We wish to test the numerical evolution against the analytic solution. However, some of the terms in the evolution equations we are testing will vanish because the analytic solution has symmetries. To remove these symmetries, we perform a coordinate transformation of the form

$$r \rightarrow a\bar{r} + (a_0 - a)\frac{\bar{r}^3}{R^2}, \tag{4.81}$$

where $r \equiv \sqrt{x^2 + y^2 + z^2}$ in Cartesian grid coordinates, R and a_0 are constants, and $a(t)$ is a (time-dependent) function. We add an additional coordinate translation of the form

$$\bar{x}^i \rightarrow \bar{x}^i + C^i, \tag{4.82}$$

for some vector C^i.

We evolve an outgoing $l = 2, m = 2$ multipolar wave. This has a Gaussian profile, with an initial width of $1\,M$, amplitude of 0.01, and center of $10\,M$. For the transformations given in Eqs. (4.81) and (4.82), we choose $R = 40\,M$, $a_0 = 1.3$, $a(t) = 1 + 0.001t^2/M^2$ and $C^i = (2.0, -4.0, 3.0)\,M$. We evolve on a grid of nested spherical shells around a filled sphere, with an outer boundary of $R = 35\,M$. Each shell has 8 radial spectral basis functions and 4 angular spectral basis functions at the lowest resolution, with 4 more basis functions added in each direction as we increase resolution. We find that the perturbed constraints, shown in Fig. 4.9, converge exponentially, and that the perturbed variables shown in Fig. 4.10 evolve toward zero (as the data leaves the domain) in a convergent way. Additionally, we check that our results converge to the known analytic solution.

Small data on Schwarzschild

We perform a test where we initially set each component of Δg_{ab} to be a different number close to machine precision (10^{-16}) at each point on the domain, thus seeding
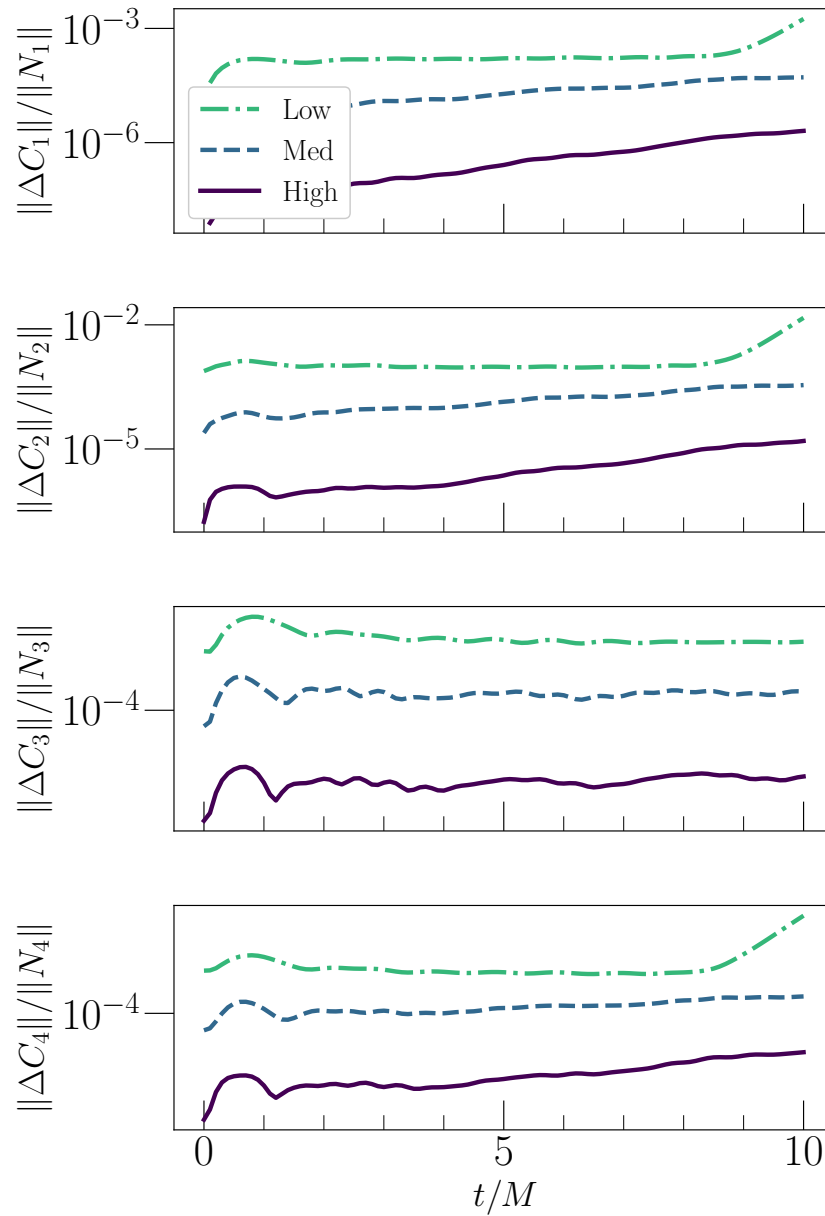
Figure 4.9: Constraints for evolution of a transformed multipolar wave perturbation on flat space, as described in Sec. 4.B. For each constraint ΔC_A, we compute the L2 norm of the constraint over the entire computational domain ($\|\Delta C_1\|$ for the 1-index constraint, for example) and divide by the L2 norm of its normalization factor ($\|N_A\|$) (cf. Sec. 4.3). We see that the constraints converge exponentially with numerical resolution.
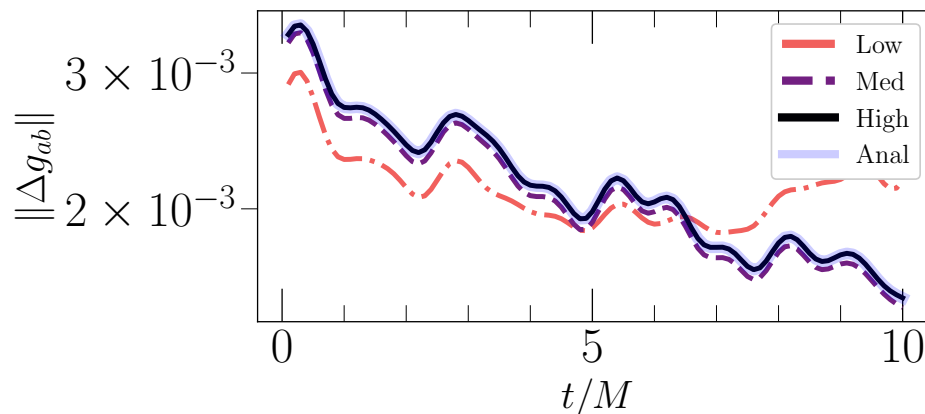
Figure 4.10: Behavior of Δg_{ab} for the multipolar wave test described in Sec. 4.B for low, medium, and high resolution. We see that the value of the metric perturbation decreases as the wave propagates toward $R \to \infty$ (and leaves the computational domain), and that with increasing resolution the behavior of the variables converges to the highest-resolution value. We additionally plot the analytical solution for the behavior of the multipolar wave, which sits on top of the highest-resolution result.

any instabilities that might be present. We apply filtering to the spectral scheme in order to minimize the growth of high-frequency modes [190] and choose damping parameters γ_0 and γ_2 to be larger close to the horizon. We check that as the evolution progresses, the constraints and the values of Δg_{ab} and $\Delta \kappa_{abc}$ remain close to numerical truncation error. This in particular tests the constraint-damping capabilities of the code. We show the behavior of the perturbed variables in Fig. 4.11. We see that the solution remains at roundoff level. There is linear growth in Δg_{ab}, but the level of this growth decreases towards zero with increasing resolution.
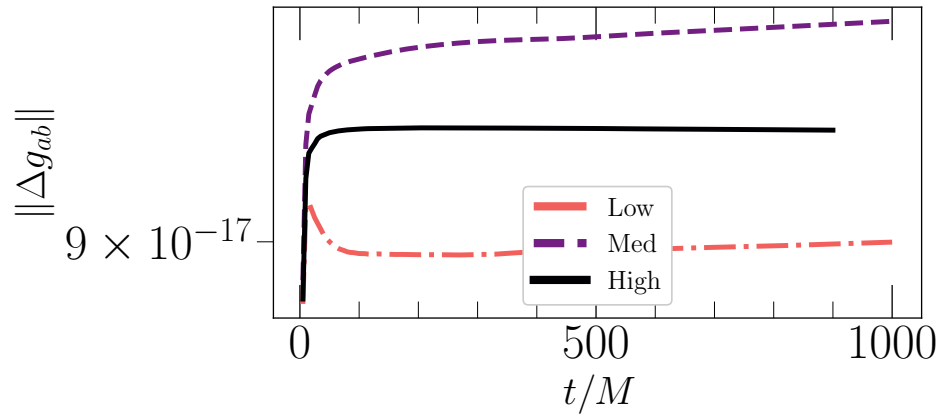
Figure 4.11: Behavior of Δg_{ab} for the small data on Schwarzschild test described in Sec. 4.B. We see that with increasing time, the field with initial magnitude of $\sim 10^{-16}$ remains close to roundoff error.

Chapter 5

BINARY BLACK HOLE COLLISIONS IN DYNAMICAL CHERN-SIMONS GRAVITY

Abstract

We produce the first numerical relativity binary black hole gravitational waveforms in a higher-curvature theory beyond general relativity. In particular, we study head-on collisions of binary black holes in order-reduced dynamical Chern-Simons gravity. This is a precursor to producing beyond-general-relativity waveforms for inspiraling binary black hole systems that are useful for gravitational wave detection. Head-on collisions are interesting in their own right, however, as they cleanly probe the quasi-normal mode spectrum of the final black hole. We thus compute the leading-order dynamical Chern-Simons modifications to the damping time and frequency of the post-merger gravitational radiation. We consider equal-mass systems, with equal spins oriented along the axis of collision, resulting in remnant black holes with spin. We find that there are modifications to the damping time and frequency of the quasi-normal mode spectrum that behave as a power law with spin. We discuss these results in the context of testing general relativity with gravitational wave observations.

5.1 Introduction

At some length scale, Einstein's theory of general relativity (GR) must break down and be reconciled with quantum mechanics in a beyond-GR theory of gravity. Binary black hole (BBH) mergers probe the strong-field, non-linear regime of gravity, and gravitational waves from these systems could thus contain signatures of such a theory. Current and future gravitational wave detectors have the power to test GR [43], and BBH observations from LIGO and Virgo have given a roughly 96% agreement with GR [14, 6].

These tests of GR, however, are presently null-hypothesis and parametrized tests [216, 14], which use gravitational waveforms produced in GR with numerical relativity. An open problem is the simulation of BBH systems through full inspiral, merger, and ringdown in beyond-GR theories. Waveform predictions from such simulations

would allow us to perform *model-dependent* tests and to parametrize the behavior at merger in beyond-GR theories.

In this study, we consider dynamical Chern-Simons (dCS) gravity, a beyond-GR effective field theory that adds a scalar field coupled to spacetime curvature to the Einstein-Hilbert action, and has origins in string theory, loop quantum gravity, and inflation [18, 95, 192, 134, 204]. Computing the evolution of a binary system requires first specifying suitable initial conditions. Because the well-posedness of the initial value problem in full dCS gravity is unknown [74], we work instead in a well-posed *order-reduction scheme*, in which we perturb the metric and scalar field around a GR background [146]. The leading-order modification to the spacetime metric, and hence gravitational radiation, occurs at second order, which is precisely the order we consider in this study, building on our previous work [146, 143, 142].

While our ultimate goal is to produce full inspiral-merger-ringdown waveforms relevant for astrophysical BBH systems, in this study we consider the leading-order dCS corrections to binary black hole head-on collisions. Such configurations, while less astrophysically relevant than orbiting binaries, serve as a proof of principle for our method of producing BBH waveforms in a beyond-GR theory [142], and are fast and efficient to run. Head-on collisions also contain interesting science in their own right, as they cleanly probe the quasi-normal mode (QNM) spectrum of the post-merger gravitational radiation [24, 23, 35, 181]. In this study, we thus produce the first BBH waveforms in a higher-curvature beyond-GR theory, and probe the leading-order dCS modification to the QNM spectrum of a head-on BBH collision.

Roadmap and conventions

This chapter is organized as follows. We give an overview of our methods in Sec. 5.2, and refer the reader to previous papers, [142] and [143], as well as Appendices 5.A and 5.B, for technical details. We discuss fitting perturbed quasi-normal modes in Sec. 5.3. We present and discuss our results, including quasi-normal mode fits, in Sec. 5.4. We discuss the implications of this study on testing GR in Sec. 5.5. We conclude in Sec. 5.6.

We set $G = c = 1$ throughout. Quantities are given in terms of units of M, the sum of the Christodolou masses of the background black holes at a given relaxation time [56]. Latin letters in the beginning of the alphabet $\{a, b, c, d \ldots\}$ denote 4-dimensional spacetime indices, while Latin letters in the middle of the alphabet $\{i, j, k, l, \ldots\}$ denote 3-dimensional spatial indices (present in the appendices). g_{ab}

refs to the spacetime metric with connection $\Gamma^a{}_{bc}$, while γ_{ij} (used in the appendices) refers to the spatial metric from a 3+1 decomposition with corresponding timelike unit normal one-form n_a (cf. [40] for a review of the 3+1 ADM formalism).

5.2   Methods

Order-reduced dynamical Chern-Simons gravity

Full details about order-reduced dynamical Chern-Simons gravity and our methods to simulate black hole spacetimes in this theory are given in [142, 143, 146]. Here we only briefly summarize.

The full dCS action takes the form

$$S \equiv \int d^4x \sqrt{-g} \left(\frac{m_{\text{pl}}^2}{2} R - \frac{1}{2}(\partial\vartheta)^2 - \frac{m_{\text{pl}}}{8}\ell^2\vartheta \, {}^*RR \right) . \tag{5.1}$$

The first term is the Einstein-Hilbert action of GR, with the Planck mass denoted by m_{pl}. The second term in the action is a kinetic term for the scalar field. The third term, meanwhile, couples ϑ to spacetime curvature via the Pontryagin density,

$$^*RR \equiv {}^*R^{abcd}R_{abcd} , \tag{5.2}$$

where $^*R^{abcd} = \frac{1}{2}\epsilon^{abef}R_{ef}{}^{cd}$ is the dual of the Riemann tensor, and $\epsilon^{abcd} \equiv -[abcd]/\sqrt{-g}$ is the fully antisymmetric Levi-Civita tensor. This coupling is governed by a coupling constant ℓ, which has dimensions of length, and physically represents the length scale below which quantum gravity effects become important.

The equations of motion for ϑ and g_{ab} have the form

$$\Box\vartheta \equiv \nabla_a\nabla^a\vartheta = \frac{m_{\text{pl}}}{8}\ell^2 \, {}^*RR , \tag{5.3}$$

and

$$m_{\text{pl}}^2 G_{ab} + m_{\text{pl}}\ell^2 C_{ab} = T_{ab}^\vartheta , \tag{5.4}$$

where

$$C_{ab} \equiv \epsilon_{cde(a}\nabla^d R_{b)}{}^c\nabla^e\vartheta + {}^*R^c{}_{(ab)}{}^d\nabla_c\nabla_d\vartheta , \tag{5.5}$$

and T_{ab}^ϑ is the stress energy tensor for a canonical, massless Klein-Gordon field

$$T_{ab}^\vartheta = \nabla_a\vartheta\nabla_b\vartheta - \frac{1}{2}g_{ab}\nabla_c\vartheta\nabla^c\vartheta . \tag{5.6}$$

Because of C_{ab} in Eq. (5.4), the equation of motion is different from that of a metric in GR sourced by a scalar field.

C_{ab}, as given in Eq. (5.5), contains third derivatives of the metric, and it is thus unknown whether dCS has a well-posed initial value formulation [74]. We work instead in well-posed order-reduced dCS, in which we perturb the metric and scalar field about an arbitrary GR spacetime and obtain perturbed equations of motion. In particular, using an order-counting parameter ε, we can write

$$g_{ab} = g_{ab}^{(0)} + \sum_{k=1}^{\infty} \varepsilon^k h_{ab}^{(k)}, \tag{5.7}$$

$$\vartheta = \sum_{k=0}^{\infty} \varepsilon^k \vartheta^{(k)}. \tag{5.8}$$

Each order in ε leads to an equation of motion with the same principal part as GR. Order ε^0 gives the Einstein field equations of general relativity for $g_{ab}^{(0)}$, the background GR metric. The leading-order dCS correction to the scalar field occurs at order ε^1 (cf. [146]) and takes the form of a sourced wave equation

$$\Box^{(0)} \vartheta^{(1)} = \frac{m_{\text{pl}}}{8} \ell^2 \, {}^*RR^{(0)}, \tag{5.9}$$

where $\Box^{(0)}$ is the d'Alembertian operator of the background and $RR^{(0)}$ is the Pontryagin density of the background.

The leading-order dCS correction to the spacetime metric, which will produce the leading-order dCS correction to the gravitational radiation, occurs at order ε^2 (cf. [146]), and takes the linear form

$$m_{\text{pl}}^2 G_{ab}^{(0)}[h_{ab}^{(2)}] = -m_{\text{pl}} \ell^2 C_{ab}^{(1)} + T_{ab}^{(\vartheta(1))}, \tag{5.10}$$

where $G_{ab}^{(0)}$ is the linearized Einstein field equation operator of the background, and

$$T_{ab}^{(\vartheta(1))} \equiv \nabla_a^{(0)} \vartheta^{(1)} \nabla_b^{(0)} \vartheta^{(1)} - \frac{1}{2} g_{ab}^{(0)} \nabla_c^{(0)} \vartheta^{(1)} \nabla^{c(0)} \vartheta^{(1)}, \tag{5.11}$$

where $\nabla_a^{(0)}$ denotes the covariant derivative associated with $g_{ab}^{(0)}$. Meanwhile,

$$C_{ab}^{(1)} \equiv \epsilon_{cde(a} \nabla^{d(0)} R_{b)}{}^{c(0)} \nabla^{e(0)} \vartheta^{(1)} \tag{5.12}$$
$$+ \, {}^*R^c{}_{(ab)}{}^{d(0)} \nabla_c^{(0)} \nabla_d^{(0)} \vartheta^{(1)}.$$

To produce beyond-GR gravitational waveforms, our goal is thus to evolve Eq. (5.10), to obtain the leading-order dCS correction to the spacetime metric and corresponding gravitational radiation.

Scaled variables

We can scale out the ℓ dependence by defining code variables

$$h_{ab}^{(2)} \equiv \frac{\ell^4}{8} \Delta g_{ab}, \quad \vartheta^{(1)} \equiv \frac{m_{\text{pl}}}{8} \ell^2 \Delta \vartheta \,. \tag{5.13}$$

With these substitutions, Eq. (5.9) becomes

$$\Box^{(0)} \Delta \vartheta = {}^*RR^{(0)} \,. \tag{5.14}$$

Eq. (5.10) similarly becomes

$$G_{ab}^{(0)}[\Delta g_{ab}] = -C_{ab}^{(1)}(\Delta \vartheta) + \frac{1}{8} T_{ab}^{(1)}(\Delta \vartheta) \,. \tag{5.15}$$

where $T_{ab}^{(1)}(\Delta \vartheta)$ refers to the Klein-Gordon stress-energy tensor in Eq. (5.11) computed from $\Delta \vartheta$ instead of $\vartheta^{(1)}$, and $C_{ab}^{(1)}(\Delta \vartheta)$ similarly refers to the C-tensor in Eq. (5.12) computed with $\Delta \vartheta$ instead of $\vartheta^{(1)}$.

We thus need to solve Eqs. (5.14) and (5.15) only once for each BBH background configuration, and then multiply our results for Δg_{ab} and $\Delta \vartheta$ by appropriate powers of ℓ/GM and factors of 8 afterward.

Evolution

To evolve the first-order dCS metric perturbation, we evolve three systems of equations simultaneously: one for the GR background BBH spacetime, one for the scalar field $\Delta \vartheta$ (cf. Eq. (5.14)) sourced by the background curvature, and one for the metric perturbation Δg_{ab} (cf. Eq. (5.15)), sourced by the background curvature and $\Delta \vartheta$. We evolve all variables concurrently, on the same computational domain.

All variables are evolved using the Spectral Einstein Code [198], a pseudo-spectral code. The GR BBH background is evolved using a well-posed generalized harmonic formalism, with details given in [122, 178, 190, 104]. The first-order scalar field is evolved using the formalism detailed in [146]. Finally, the metric perturbation is evolved using the formalism given in [142], a well-posed perturbed analogue of the generalized harmonic formalism. When evolving the metric perturbation, we have the freedom to choose a perturbed gauge, which we choose to be a harmonic gauge.

We give details on perturbed gauge choices in Appendix 5.A. We use the boundary conditions detailed in [69, 172, 146, 142].

The GR BBH evolution governs the shape of the spectral domain, with an initial grid with two excision regions (one for each black hole), and a final, post-merger grid with one excision region [104]. The outer boundary is chosen to be $\sim 700\,M$. The background GR variables govern the adaptive mesh refinement [190]. This is justified, as high gradients in the background will source higher gradients in both the scalar field and the metric perturbation. For all of the evolved variables, in spherical subdomains we filter the top four tensor spherical harmonics, while we use an exponential Chebyshev filter in the radial direction [190]. We similarly filter the variables in subdomains with other topologies according the the prescriptions in [190]. For the constraint damping parameters (cf. [122, 142]), we choose the standard values for BBH simulations.

Initial data

To perform an evolution, we must generate initial data for the background (metric) fields, the scalar field, and the metric perturbation. The background initial data for a BBH system are given by a constraint-satisfying superposition of black hole metrics in Kerr-Schild coordinates [127, 149]. The scalar field initial data are given by a superposition of slow-rotation solutions [146, 214, 210]. The constraint-satisfying initial data for Δg_{ab} are generated using the methods outlined in [143]. For head-on collisions, we start with a separation of $25\,M$, assuming that the contributions to the gravitational radiation and energy flux from times $t \lesssim 25\,M$ are negligible.

In this study, we will consider axisymmetric configurations where the background spins of the black holes are oriented along $\hat{x}$, the axis along which they are colliding. Moreover, we will choose configurations where the two spins have the same orientation along the axis of collision so that the system has a reflection symmetry for $x \to -x$ (recall that spin is a pseudo-vector). We illustrate this configuration in Fig. 5.1. We consider equal mass, equal spin configurations, with dimensionless spins χ between 0.1 and 0.8, in steps of 0.1. Kerr with $\chi \neq 0$ is not a solution of dCS, and hence the initial configurations will have a non-zero dCS metric perturbation [214]. However, Schwarzschild is a solution of the theory, and hence we do not consider $\chi = 0.0$, as there will be no metric perturbation in that case.

As a check, we also consider the opposite configuration to Fig. 5.1, where the spins have opposite orientations. For the equal mass, equal spin systems considered in
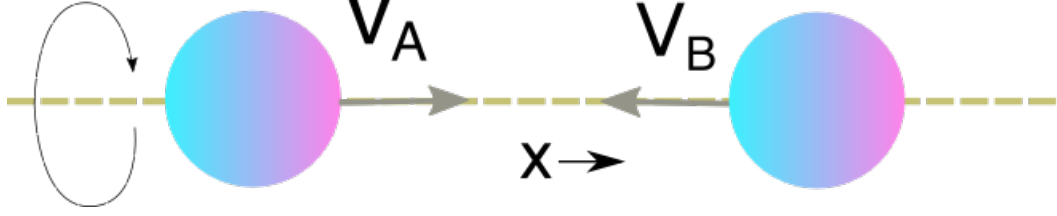
Figure 5.1: The black hole configurations considered in this study. The two black holes (denoted by spheres) merge along the x axis (as schematically shown by their velocities, V_A and V_B). The black holes have equal spins, both oriented in the $+x$ direction, as shown schematically by the gradient on each sphere. The system, as shown by the black arrow on the left, is fully symmetric about the x axis, and additionally has a reflection symmetry $x \rightarrow -x$.

this study, the final remnant in this case (for all spins) is a Schwarzschild black hole. As Schwarzschild is a solution of dCS, there is no final dCS metric perturbation or scalar field in the spacetime.

Wave extraction

In the order reduction scheme, Ψ_4, the Newman-Penrose scalar measuring the outgoing gravitational radiation, is expanded about a GR solution as

$$\Psi_4 = \Psi_4^{(0)} + \sum_{k=1}^{\infty} \varepsilon^k \Psi_4^{(k)} . \qquad (5.16)$$

If we substitute the expanded metric given in Eq. 5.7 into the expression for Ψ_4 (cf. Sec. 5.B), we can match the terms order-by-order. $\Psi_4^{(1)}$, the first-order correction, will have pieces linear in $h_{ab}^{(1)}$. Recalling, however, that $h_{ab}^{(1)} = 0$, $\Psi_4^{(1)}$ vanishes. $\Psi_4^{(2)}$, the second-order correction, will have pieces quadratic in $h_{ab}^{(1)}$, which will similarly vanish, and pieces linear in $h_{ab}^{(2)}$. Thus, the leading-order correction to the gravitational radiation will be linear in the leading-order correction to the spacetime metric.

In practice, we compute $\Delta\Psi_4$, the leading-order correction to the gravitational radiation linear in the leading-order correction to the spacetime metric Δg_{ab} using the methods detailed in Appendix 5.B. The resulting waveform is related to $\Psi_4^{(2)}$ via (cf. Eq. (5.13))

$$\Psi_4^{(2)} = \frac{\ell^4}{8} \Delta\Psi_4 . \qquad (5.17)$$

Throughout the evolution, we extract $\Psi_4^{(0)}$ and $\Delta\Psi$ on a set of topologically spherical shells of various radii using the methods given in [193]. We similarly extract the

scalar field $\Delta\vartheta$ radiation on these spherical shells (cf. [146]). $\Psi_4^{(0)}$ and $\Delta\Psi_4$ are then extrapolated to infinity as a power series in $1/R$ (where R is the radius of the spherical shell) using the methods given in [193, 56].

5.3 Perturbations to quasi-normal modes

Once we have obtained $\Psi_4^{(0)}$, the background gravitational radiation, and $\Psi_4^{(2)}$, the leading order dynamical Chern-Simons correction to the gravitational radiation, we can begin to analyze these quantities. As discussed in Sec. 5.1, head-on BBH collisions cleanly probe the quasi-normal mode spectrum of the post-merger space-time. We are thus most interested in fitting for the QNM spectrum of $\Psi_4^{(0)}$, and the leading-order correction to this spectrum in $\Psi_4^{(2)}$.

Quasi-normal modes in general relativity

A GR QNM waveform takes the form of a damped sinusoid

$$\Psi_{4(l,m,n)}(t) = \tilde{A}_{(l,m,n)} e^{-i\tilde{\omega}_{(l,m,n)}t} \,. \tag{5.18}$$

Here, l and m label the spherical harmonic under consideration, while n refers to the overtone, ordered by largest damping time. The quantities $\tilde{A}$ and $\tilde{\omega}$ are the complex amplitude and frequency of the (l, m, n) mode under consideration. We can write $\tilde{\omega}$ in terms of a real frequency, ω, and a damping time, τ, to give

$$\tilde{\omega} = \omega - i/\tau \,. \tag{5.19}$$

Let us similarly write

$$\tilde{A} = A e^{i\theta} \,. \tag{5.20}$$

where $A \equiv |\tilde{A}|$ is the norm of $\tilde{A}$, and θ is the complex phase of $\tilde{A}$. Then we obtain

$$\Psi_4 = A\cos(-\omega t + \theta)e^{-t/\tau} - iA\sin(-\omega t + \theta)e^{-t/\tau} \,. \tag{5.21}$$

Since the GR background gravitational radiation is comprised of QNMs, we can use the form above to fit for $\Psi_4^{(0)}$. The quantities $\omega^{(0)}$ and $\tau^{(0)}$ are known from perturbation theory for each (l, m, n) [182]. Our fit thus determines two free parameters: $A^{(0)}$, and $\theta^{(0)}$ as

$$\Psi_4^{(0)} = A^{(0)}\cos(-\omega^{(0)}t + \theta^{(0)})e^{-t/\tau^{(0)}} \tag{5.22}$$

$$- iA^{(0)}\sin(-\omega^{(0)}t + \theta^{(0)})e^{-t/\tau^{(0)}} \,.$$

Perturbed quasi-normal modes

Let us now consider how to fit $\Psi_4^{(2)}$ after the merger. The QNM frequency, damping time, and amplitude will all be corrected from the background values as

$$\omega = \omega^{(0)} + \sum_{k=1}^{\infty} \varepsilon^k \omega^{(k)}, \quad \tau = \tau^{(0)} + \sum_{k=1}^{\infty} \varepsilon^k \tau^{(k)}, \tag{5.23}$$

$$A = A^{(0)} + \sum_{k=1}^{\infty} \varepsilon^k A^{(k)}, \quad \theta = \theta^{(0)} + \sum_{k=1}^{\infty} \varepsilon^k \theta^{(k)}. \tag{5.24}$$

Recall that the leading-order correction to the gravitational radiation is $\Psi_4^{(2)}$, which is linear in $h_{ab}^{(2)}$ and has a coupling factor of $(\ell/GM)^4$. Thus, the leading-order correction to ω will be $\omega^{(2)}$, as computed from a linearization of Eq. (5.18), with a coupling factor of $(\ell/GM)^4$. $\Psi_4^{(2)}$, the leading-order dCS correction to the gravitational radiation will thus be parametrized by and linear in $\{\omega^{(2)}, \tau^{(2)}, A^{(2)}, \theta^{(2)}\}$.

Let us focus on the real part of Eq. (5.22). Computing the leading-order perturbation to this expression gives us the form

$$\begin{aligned}
\mathrm{Re}(\Psi_4^{(2)}) = {} & A^{(2)} \cos(-\omega^{(0)}t + \theta^{(0)})e^{-t/\tau^{(0)}} \\
& - \theta^{(2)} A^{(0)} \sin(-\omega^{(0)}t + \theta^{(0)})e^{-t/\tau^{(0)}} \\
& + t\omega^{(2)} A^{(0)} \sin(-\omega^{(0)}t + \theta^{(0)})e^{-t/\tau^{(0)}} \\
& + t\frac{\tau^{(2)}}{(\tau^{(0)})^2} A^{(0)} \cos(-\omega^{(0)}t + \theta^{(0)})e^{-t/\tau^{(0)}},
\end{aligned} \tag{5.25}$$

which can be more compactly written as

$$s \equiv \sin(-\omega^{(0)}t + \theta^{(0)}), \tag{5.26}$$

$$c \equiv \cos(-\omega^{(0)}t + \theta^{(0)}), \tag{5.27}$$

$$\mathrm{Re}(\Psi_4^{(2)}) = e^{-t/\tau^{(0)}} \times \left[A^{(2)}c - \theta^{(2)}A^{(0)}s \right. \tag{5.28}$$

$$\left. + tA^{(0)} \left(\omega^{(2)}s + \frac{\tau^{(2)}}{(\tau^{(0)})^2}c \right) \right].$$

The imaginary part is similarly modified as

$$\mathrm{Im}(\Psi_4^{(2)}) = -e^{-t/\tau^{(0)}} \times \left[A^{(2)}s + \theta^{(2)}A^{(0)}c \right. \tag{5.29}$$

$$\left. + tA^{(0)} \left(-\omega^{(2)}c + \frac{\tau^{(2)}}{(\tau^{(0)})^2}s \right) \right].$$

We thus see both an amplitude modification to the background QNM spectrum from the $A^{(2)}$ and $\theta^{(2)}$ terms, and a modification linear in time from the $\omega^{(2)}$ and $\tau^{(2)}$ terms. We fit precisely the functional form in Eqs. (5.28) and (5.29) to the $\Psi_4^{(2)}$ obtained from the simulation. Our fit determines four free parameters: $\{A^{(2)}, \theta^{(2)}, \omega^{(2)}, \tau^{(2)}\}$; the other free parameters $\{A^{(0)}, \theta^{(0)}\}$ in Eqs. (5.28) and (5.29) are determined by the fit to $\Psi_4^{(0)}$ using Eq. (5.22). *Note that this is different from simply fitting a damped sinusoid to $\Psi_4^{(2)}$.*

Scaling

Because the simulations (cf. Sec. 5.2) are independent of the coupling parameter ℓ/GM, the resulting waveforms for $\vartheta^{(1)}$ and $\Psi_4^{(2)}$ have the coupling scaled out. We will thus report our results as

$$\vartheta^{(1)}(\ell/GM)^{-2}, \quad \Psi_4^{(2)}(\ell/GM)^{-4}, \tag{5.30}$$

$$\omega^{(2)}(\ell/GM)^{-4}, \quad \tau^{(2)}(\ell/GM)^{-4}, \tag{5.31}$$

and so on.

Much of the QNM literature reports $\tilde{\omega}$ in terms of its real and imaginary parts, $\tilde{\omega} = \text{Re}(\omega) + i\text{Im}(\omega)$, without invoking a damping time τ. We can transform our results for τ into $\text{Im}(\omega)$ as

$$\text{Im}(\omega^{(0)}) = \frac{1}{\tau^{(0)}} . \tag{5.32}$$

Similarly, given $\Delta\tau$, we can perturb the above expression to give

$$(\text{Im}(\omega))^{(2)} = -\frac{1}{(\tau^{(0)})^2}\tau^{(2)} . \tag{5.33}$$

Mass and spin definitions

Since $\tau^{(0)}$ and $\omega^{(0)}$ are (by the no-hair theorem) dependent only on M and χ, the mass and dimensionless spin of the final black hole in GR, we should similarly expect $\omega^{(2)}$ and $\tau^{(2)}$ to be dependent on some final mass and final spin. In the full dCS theory, we expect the mass and spin of a dCS black hole to be modified with respect to those of a GR black hole (recall that Kerr is not a solution of the theory [214]). The formulae used to compute mass and spin, because they are derived using properties of GR (cf. [40]), may themselves be modified in the full dCS theory. If we had access to the full theory, we could parametrize the QNM spectra in terms of χ_{dCS} and M_{dCS}, as well as ℓ/GM. Since we are working in an order-reduction scheme, we can instead linearize the formulae used to compute the spin and mass of the final

background black hole, and compute the corrected mass and spin. In this study, however, we choose to parametrize the QNM spectra in terms of the Christodoulou mass and dimensionless spin of the final background black hole, which we will call M_{final} and χ_{final}.

Fitting window

When fitting for $\Psi_4^{(0)}$ and $\Psi_4^{(2)}$, we must be careful about the time window of the post-merger waveform used for the fit. For $\Psi_4^{(0)}$, if we choose a starting time t_{start} too close to merger, then our assumption that each mode can be fit by a function of the form in Eq. (5.18) breaks down [47]. The later we choose t_{start}, the less data are available to perform the fit. However, in [91], the authors found that, when including *overtones*, the post-merger spectrum could be fit with QNMs as early as the peak of the gravitational waveform. We similarly fit enough overtones so that we can faithfully choose t_{start} to be the peak of the gravitational waveform.

At later times in the waveform, numerical noise begins to dominate, and thus we must be careful choosing the end of the window, t_{end}. Choosing a time window for the fit is complicated by the *secular regime of validity* of the perturbative scheme. The form of $\Psi_4^{(2)}$ given in Eqs. (5.28) and (5.29) is a valid first term in a perturbative expansion for times $t < \tau^{(0)}$ and $t < 1/\omega^{(0)}$. Thus, there is a trade-off in choosing t_{end} late enough to have enough data to compute $\omega^{(2)}$ and $\tau^{(2)}$, while choosing t_{end} early enough to still be within this regime of validity.

Particular and homogenous solutions

$\Psi_4^{(2)}$ after merger is driven by both the dCS scalar field $\vartheta^{(1)}$, and the background spacetime. Suppose the scalar field has decayed away such that $\vartheta^{(1)} = 0$ some time after merger. Then $h_{ab}^{(2)}$ would be driven by the approximately Kerr background spacetime. In other words, it would be a metric perturbation on Kerr, and hence should have the QNM spectrum of a pure Kerr spacetime (as does $\Psi_4^{(0)}$). The presence of a non-zero $\vartheta^{(1)}$, however, drives $\Psi_4^{(2)}$ away from this regime. In the $\vartheta^{(1)} = 0$ case, $\Psi_4^{(2)}$ is dominated by a *homogenous* solution of Eq. (5.10), while $\Psi_4^{(2)}$, when driven by $\vartheta^{(1)}$, is dominated by a *particular* solution. In the language of solutions of linear equations, the particular solution describes the response to driving the system with the scalar perturbation, whereas the homogeneous solution describes the free oscillations of the perturbed final black hole.

Such post-merger behavior was observed in [207] for Einstein-dilaton-Gauss-Bonnet gravity. We can use our numerical results to investigate when $\Psi_4^{(2)}$ is driven by a

particular versus homogenous solution.

QNMs in full dCS gravity

In [137], the authors investigated QNMs of Schwarzschild black holes in full dCS gravity. For zero spin, the system is well-posed, and thus can be solved in the full theory, without working in an order-reduction or other perturbative scheme. The radial parts of the scalar and gravitational QNMs for each mode are governed by a set of *fully coupled* ODEs of the form (cf. Eqs. 2.8 and 2.9 in [137]),

$$\frac{d^2}{dr_*^2}\begin{pmatrix}\vartheta\\\Psi\end{pmatrix} = \begin{pmatrix}V_{11} & V_{12}\\V_{21} & V_{22}\end{pmatrix}\begin{pmatrix}\vartheta\\\Psi\end{pmatrix},\tag{5.34}$$

where r_* is a function of the radial coordinate r, ϑ is the *full* dCS scalar field QNM, Ψ is the (full) dCS gravitational QNM, and the V_{ij} are coefficients dependent on r and the dCS coupling parameter. Solving for QNMs of ϑ and Ψ thus involves diagonalizing V.

In the order reduction scheme, however, $h_{ab}^{(2)}$, the leading-order dCS metric perturbation does not back-react onto the scalar field $\vartheta^{(1)}$. Thus, the QNMs of $\vartheta^{(1)}$ are independent of the QNMs of $\Psi^{(2)}$. The ODEs governing the radial part of the system thus take the form

$$\frac{d^2}{dr^2}\begin{pmatrix}\vartheta^{(1)}\\\Psi^{(2)}\end{pmatrix} = \begin{pmatrix}W_{11} & 0\\W_{21} & W_{22}\end{pmatrix}\begin{pmatrix}\vartheta^{(1)}\\\Psi^{(2)}\end{pmatrix}.\tag{5.35}$$

This matrix is already triangular. This distinguishes our order-reduction approach from the approach used in [137].

Practical considerations

To perform these fits, we use `scipy.optimize.curvefit` [109], a non-linear least-squares method. We fit a sum of overtones to each mode (l, m). We can shift $\Psi_4^{(0)}$ and $\Psi_4^{(2)}$ to align at the peaks for each mode, effectively setting $\Delta\theta^{(2)}$ to zero. We compute errors in our estimates of the parameters by considering the fitted values for a medium numerical resolution simulation and a high numerical resolution simulation (for the same initial configuration).

5.4 Results

Waveforms

During each simulation, we extract $\Psi_4^{(0)}$, the Newman-Penrose scalar measuring the outgoing gravitational radiation of the background spacetime, decomposed into

spin-weight -2 spherical harmonics labelled by (l, m). Similarly, we extract and decompose $\Psi_4^{(2)}$, the leading-order dCS correction to the gravitational radiation. Since the computational domain is of finite extent, both quantities are extrapolated to $R \rightarrow \infty$. We additionally extract $\vartheta^{(1)}$, the scalar field, decomposed into spherical harmonics. *In all cases, the spherical harmonics are oriented along the collision axis of the black holes, which we will call $\hat{x}$.*

We show the dominant modes of $\Psi_4^{(0)}$ for a representational case with $\chi = 0.1\hat{x}$ in Fig. 5.2. We similarly show the dominant modes of $\Psi_4^{(2)}$ for this configuration in Fig. 5.3. Recall that the physical gravitational radiation includes a coupling factor $(\ell/GM)^4$, which is scaled out in the numerical computation, and thus we report the waveforms as $(\ell/GM)^{-4}\Psi_4^{(2)}$. This configuration is axisymmetric about the $\hat{x}$ axis, and thus we expect only $m = 0$ modes to be excited. Since the spins have the same orientation, there is reflection symmetry about the $\hat{y} - \hat{z}$ plane, so we expect only the $l =$ even modes to be excited. Recall that we can write $\Psi_4^{(0)} = \text{Re}(\Psi_4^{(0)})e_+ + i\text{Im}(\Psi_4^{(0)})e_\times$, where the polarization tensor e_+ is symmetric in $z \rightarrow -z$ and $e_\times$ is anti-symmetric in $z \rightarrow -z$ (for propagation along x). Since the configuration has an $x \rightarrow -x$ reflection symmetry, there should be power only in the real part of $\Psi_4^{(0)}$. On the other hand, for $\Psi_4^{(2)}$, there is an excitation in the imaginary part of the dominant modes; we will discuss this in more detail in Sec. 5.4.

Finally, we plot the dominant modes of $\vartheta^{(1)}$, the leading-order dCS scalar field for this configuration in Fig. 5.4. Because the scalar field around each black hole takes the form of a dipole oriented around $\hat{x}$ (cf. [210]), and the spins are pointing in the same direction (cf. Fig. 5.1), we expect power only in the odd l modes. Because of the axisymmetry of the configuration, we expect only the $m = 0$ modes to be excited. We see the $(1, 0)$ mode asymptotes to a value that corresponds to the remnant dipolar profile of the scalar field on the final black hole.

Regime of validity

As discussed in Sec. 5.2, the leading-order scalar field $\Delta\vartheta$ and metric perturbation Δg_{ab} as computed from the code are independent of the coupling constant ℓ/GM. In order to make our results physically meaningful, we must multiply the leading-order scalar field by $(\ell/GM)^2$ and the leading-order metric correction by $(\ell/GM)^4$. Similarly, we must multiply the computed leading-order correction to the gravitational radiation, $\Delta\Psi$, by a factor of $(\ell/GM)^4$.

Recall, however, that the order-reduction scheme is perturbative. The modifications
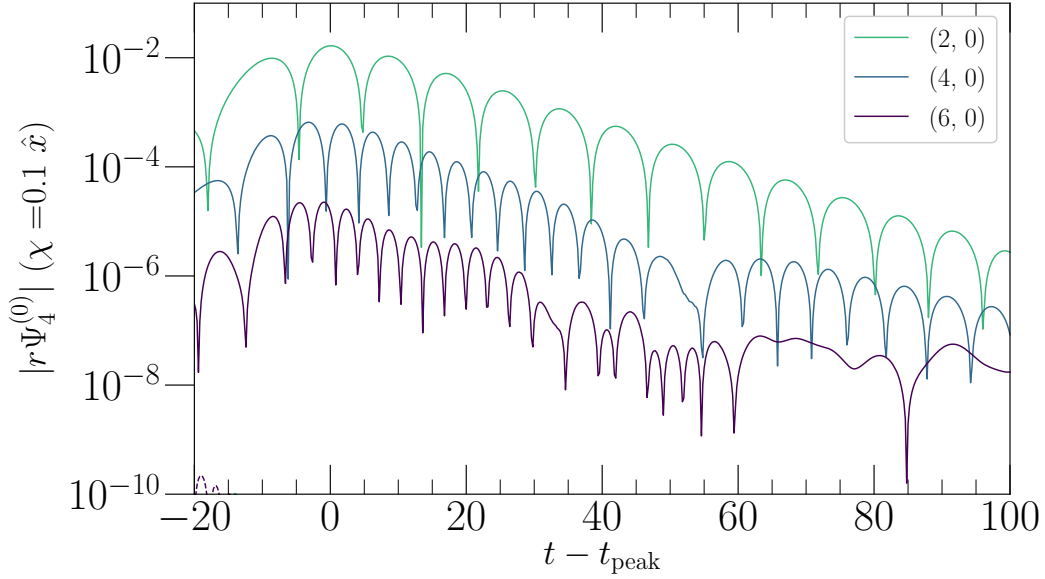
Figure 5.2: Dominant modes of the background gravitational radiation, shown in terms of the Newman-Penrose scalar $\Psi_4^{(0)}$ (scaled with radius r) for a head-on collision with $\chi = 0.1$ along the axis of the collision (cf. Fig. 5.1). Each color corresponds to a different mode. For each mode and color, the solid lines represent the absolute value of the real part of the mode, while there is no power in the imaginary part. We resolve up to the $l = 6$ mode. We choose the reference time t_{peak} to correspond to the peak time of the $(2, 0)$ mode of $\Psi_4^{(0)}$.

to the spacetime must actually form a convergent perturbation series around GR. We thus require that g_{ab}, the background metric, have a larger magnitude than $h_{ab}^{(2)}$ at each point in the spacetime:

$$\|h_{ab}^{(2)}\| \sim C\|g_{ab}^{(0)}\|, \tag{5.36}$$

for some tolerance C. This gives an *instantaneous regime of validity*. Following Eq. (5.15), we can compute

$$\frac{1}{8}(\ell/GM)^4\|\Delta g_{ab}\| \sim C\|g_{ab}^{(0)}\| \tag{5.37}$$

and hence

$$\left|\frac{\ell}{GM}\right|_{\text{max}} \sim C^{1/4}\left(\frac{8\,\|g_{ab}\|}{\|\Delta g_{ab}\|}\right)_{\text{min}}^{1/4} \tag{5.38}$$

In practice, the ratio is taken point-wise on the computational domain. We choose $C = 0.1$ as a rough tolerance.
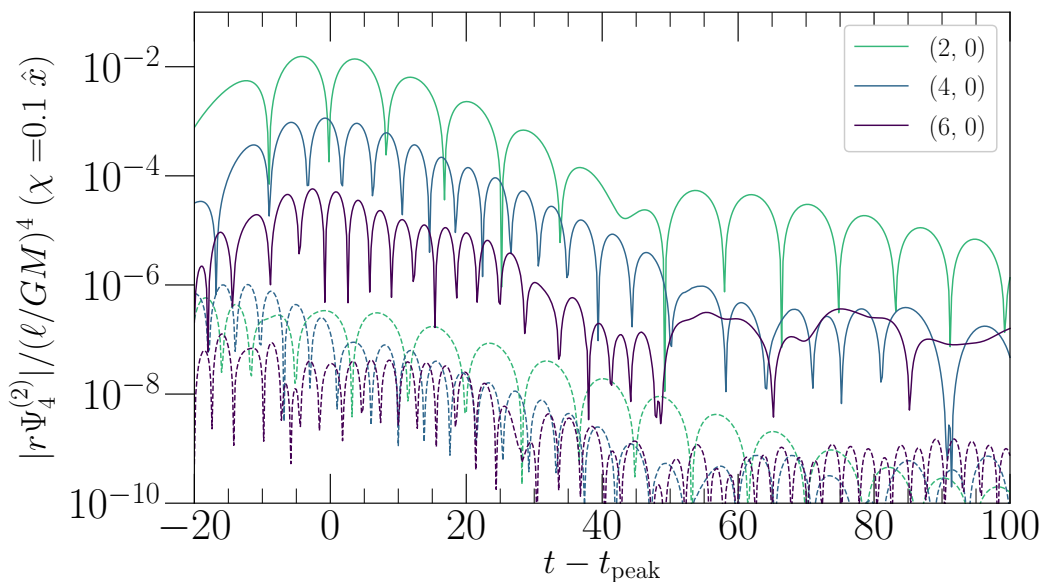
Figure 5.3: Same as Fig. 5.2, but for the leading-order dCS gravitational radiation, $\Psi_4^{(2)}$, with the dCS coupling factor $(\ell/GM)^4$ scaled out. Here, there is power in the imaginary part of each mode, which we show with dashed lines. t_{peak} is again chosen to correspond to the peak time of the $(2, 0)$ mode of $\Psi_4^{(0)}$.

We show the regime of validity for a $\vec{\chi} = 0.7\hat{x}$ head-on collision in Fig. 5.5. ℓ/GM takes its smallest allowed value in the strong-field region, outside the apparent horizon of each black hole. We see that closer to merger, where there is power in the metric perturbation, the maximal allowed value of ℓ/GM decreases. After merger, the maximal allowed value of ℓ/GM increases as the dCS metric perturbation partially radiates away, and the final constant value is governed by the strength of the dCS metric perturbation around the final black hole.

We show the behavior of the minimum allowed value of ℓ/GM, over the entire simulation, as a function of final dimensionless spin χ_{final} in Fig. 5.6. The regime of validity decreases with spin, as the magnitude of Δg_{ab} increases with spin. This scaling serves as a proxy for the allowed values of ℓ/GM when considering gravitational waveforms.

Quasi-normal mode fits

We perform the quasi-normal mode fits detailed in Sec. 5.3 to $\Psi_4^{(0)}$ and $\Psi_4^{(2)}$. We fit three overtones to each (l, m) mode. For $\Psi_4^{(0)}$, we use the perturbation theory results for $\omega^{(0)}$, the GR QNM frequency, and $\tau^{(0)}$, the GR damping time [182], and
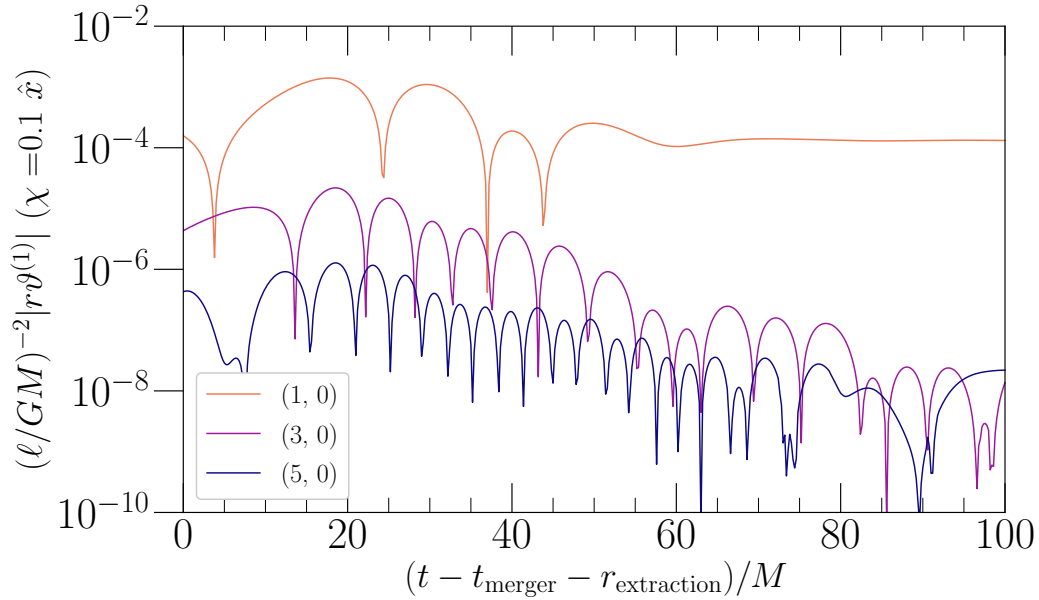
Figure 5.4: Same as Fig. 5.2, but for the leading-order dCS scalar field $\vartheta^{(1)}$, with the coupling $(\ell/GM)^2$ scaled out. We show the dominantly excited modes of the scalar field. Because the scalar field is extracted at finite radius, the time axis corresponds to the time relative to merger, corrected by the finite extraction radius. The $(1, 0)$ mode, asymptotes to a value corresponding to the dipolar profile of the scalar field around the remnant black hole.

fit for the the QNM amplitudes (cf. Eq. (5.22)). From $\Psi_4^{(2)}$, we extract $\omega^{(2)}$, the leading-order dCS correction to the QNM frequency, and $\tau^{(2)}$, the leading-order correction to the QNM damping time, as well as the leading-order corrections to the QNM amplitudes (cf. Eqs. (5.28) and (5.29)). We tabulate all of our fit results in Tables 5.1 and 5.2.

We show representative fits in Fig. 5.7. We find that for head-on collisions, we can most successfully fit each mode from the peak of the waveform using three overtones. We set $t_{\text{end}} = 25\,M$ after the peak. We take a closer look at this fit in Fig. 5.8, where we give an illustration of this linear-in-time behavior of $\Psi_4^{(2)}$. We see that the coefficients of the sine and cosine terms are lines, which range over about an order of magnitude over the time fitting window.

For each of the configurations, the final Christodolou mass of the background spacetime is $M_{\text{final}} = 0.9896$. However, χ_{final}, the final background spin, varies with configuration, and we include these values in Tables 5.1 and 5.2.

We plot the values of $\tau^{(2)}_{(2,0,0)}(\ell/GM)^{-4}$, the leading-order dCS correction to the
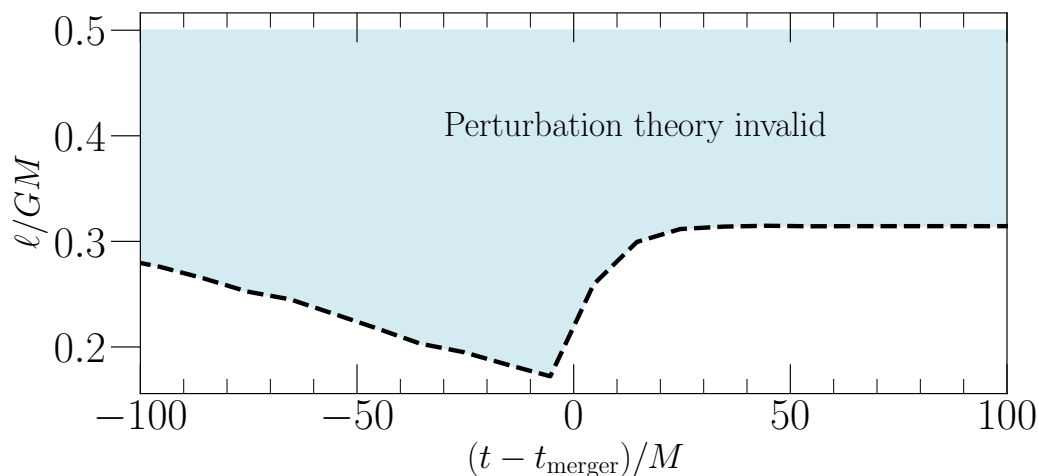
Figure 5.5: The instantaneous regime of validity for a head-on $\vec{\chi} = 0.7\hat{x}$ collision, as a function of coordinate time from merger. On each slice of the simulation, we compute ℓ/GM, the maximum allowed value of the dCS coupling constant according to Eq. (5.38). The blue region above the dashed line corresponds to the values of the coupling constant that are not allowed by perturbation theory. Note that this coupling constant appears as ℓ^2 in the dCS action (cf. Eq. (5.1)), and as ℓ^4 in front of the leading-order dCS modification to the gravitational radiation.
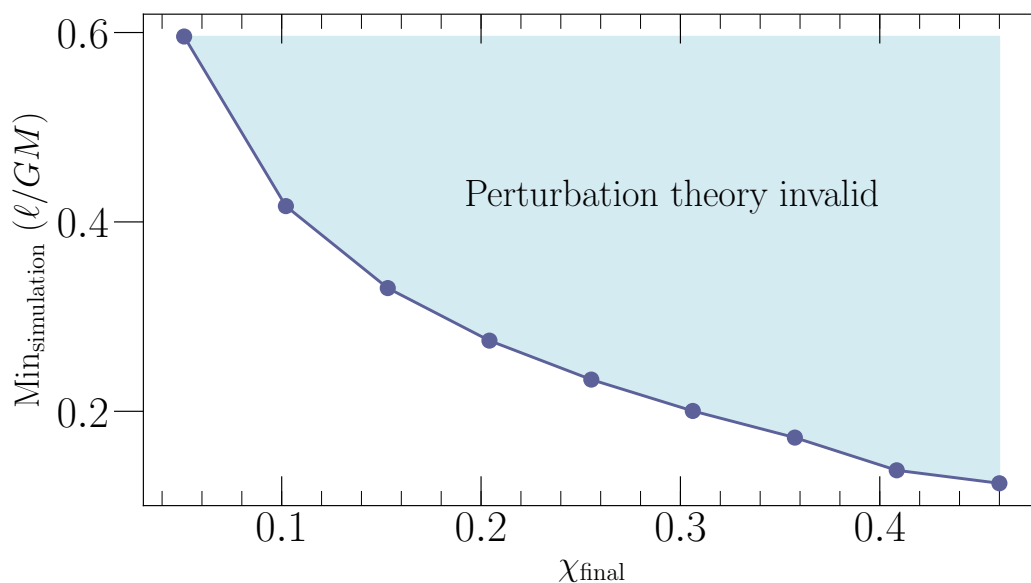
Figure 5.6: Behavior of the regime of validity with the dimensionless spin χ_{final} of the final background black hole. We compute the minimum of ℓ/GM (cf. Eq. (5.38)) over each simulation. The coupling constant achieves its minimum allowed value during the merger phase, and thus this regime of validity is a conservative estimate.
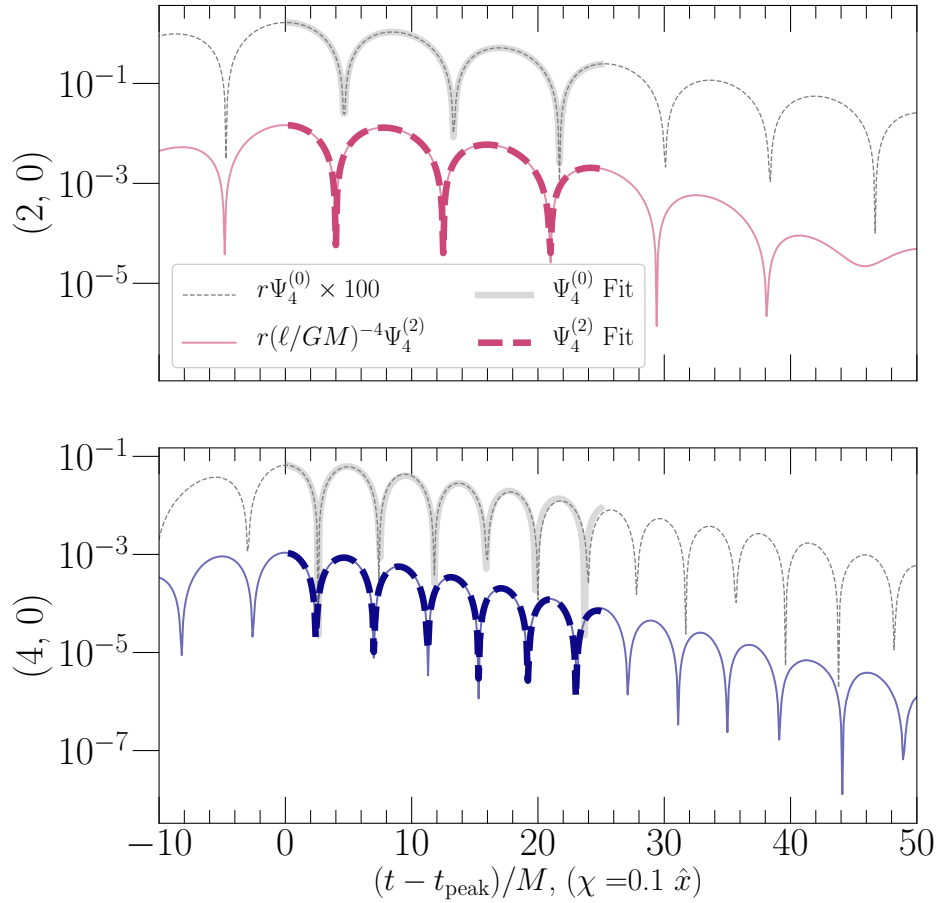
Figure 5.7: Fits for $\Psi_4^{(2)}$, the leading-order dCS gravitational radiation, using the formulae in Eqs. (5.28) and (5.29), for a configuration with $\chi = 0.1$ on each hole. Each panel corresponds to one of the dominant modes of the radiation, fit to the three least-damped overtones. The solid colored lines correspond to the real part of $\Psi_4^{(2)}$. We perform a fit for $\Psi_4^{(2)}$, shown in thick dashed colored lines. For reference, we have plotted the real part of $\Psi_4^{(0)}$ (multiplied by a factor to make it easier to see in this figure) in dashed grey. The QNM fit to $\Psi_4^{(0)}$ is shown by the solid, thick grey line.
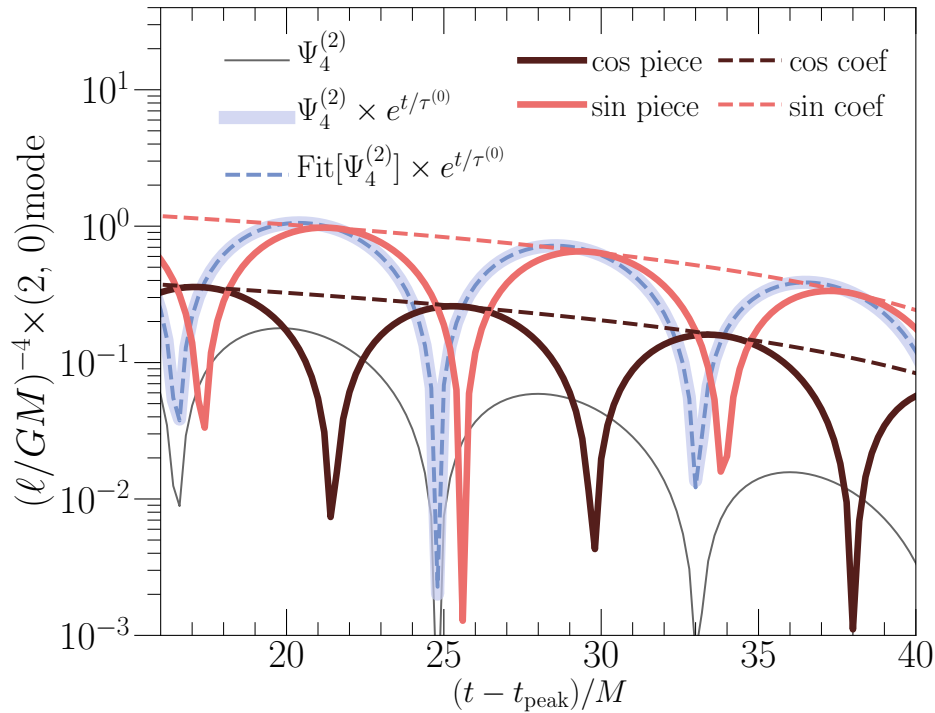
Figure 5.8: The linear-in-time pieces of $\Psi_4^{(2)}$, the leading-order dCS modification to the waveform for least-damped overtone of the $(2, 0)$ mode. The grey line corresponds to $\Psi_4^{(2)}$ as given by the numerical relativity simulation. Because $\Psi_4^{(2)}$ has an overall factor of $e^{-t/\tau^{(0)}}$, we multiply this factor out, showing $\Psi_4^{(2)} \times e^{t/\tau^{(0)}}$ in the thick, solid blue line. We show the fit to $\Psi_4^{(2)}$, similarly multiplied by this factor, in the dashed blue line sitting right on top. The resulting waveform then only depends on factors of the form $(a + bt)\cos(\omega^{(0)}t + \theta^{(0)})$, $(c + dt)\sin(\omega^{(0)}t + \theta^{(0)})$. We separate the sine and cosine terms, showing each in a solid maroon and pink line. We then divide out these terms by sine and cosine, leaving only the linear-in-time $(a + bt)$ and $(c + dt)$ behavior (shown in the corresponding dashed lines).

damping time of the least-damped $(2, 0)$ mode of the gravitational radiation, and $\omega_{(2,0,0)}^{(2)}(\ell/GM)^{-4}$, the leading-order dCS correction to the frequency, as functions of χ_{final} in Figs. 5.9 and 5.10. We see that $\tau^{(2)}(\ell/GM)^{-4}$ and $\omega^{(2)}(\ell/GM)^{-4}$ behave as a power law with spin. This behavior can be expected by considering analytical results in dCS theory. In the slow-rotation approximation, the horizon (and hence the light ring) is modified at quadratic order in spin [210], while containing no modifications at first order in spin [214]. We additionally plot $\tau^{(2)}(\ell/GM)^{-4}$ and $\omega^{(2)}(\ell/GM)^{-4}$ for the $(4, 0, 0)$ mode in Figs. 5.11 and 5.12. Again, we see that these quantities behave as a power law with spin.
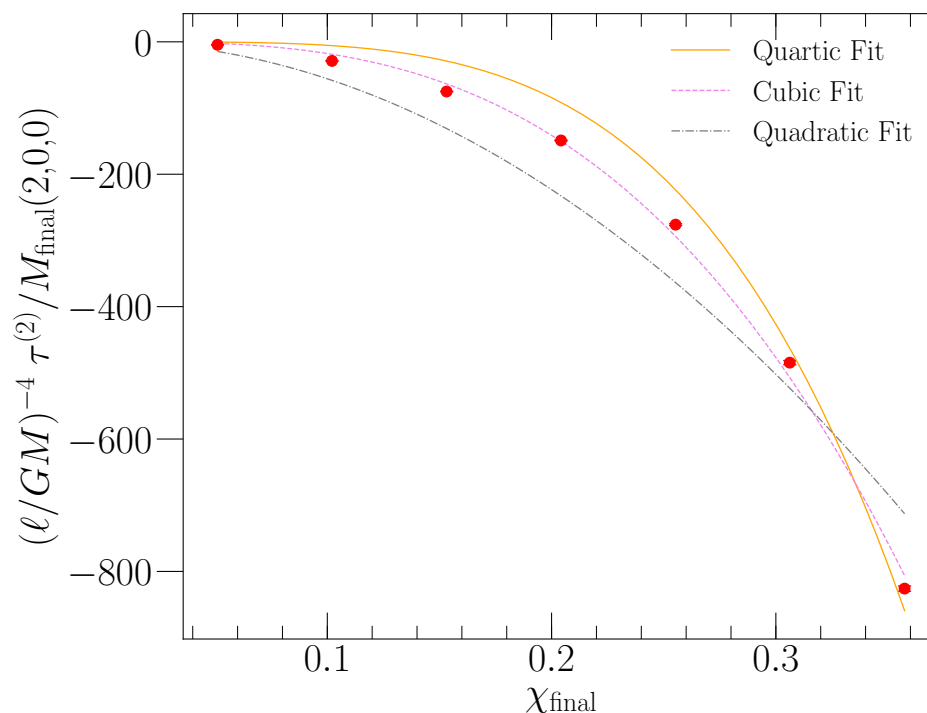
Figure 5.9: Fitted $\tau^{(2)}_{(2,0,0)}$, the leading-order dCS modification, with the dCS coupling scaled out, to the $(2, 0, 0)$ mode QNM damping time, as a function of dimensionless spin χ_{final} of the final background black hole. The error bars on the quantity are computed by considering $\tau^{(2)}$ for numerical simulations with different resolutions (cf. 5.4). We see that $\tau^{(2)}$ increases as a power law with spin. Note that these large values of $\tau^{(2)}(\ell/GM)^{-4}$ must be multiplied by a small, appropriate value of $(\ell/GM)^4$ to have physical meaning.

Let us consider the sources of error in these computations. In each of Figs. 5.9 and 5.11, as well as the tabulated values in Tables 5.1 and 5.2, the error bars on a fitted quantity Q are computed by comparing the value of Q for two simulations with different numerical resolutions (cf. Sec. 5.4). The error bars on the fits for $\tau^{(2)}$, and $\omega^{(2)}$ increase with l, being lowest for the $(2, 0)$ mode, and highest for the $(6, 0)$ mode. Higher modes are more difficult to resolve numerically [198, 178], and thus it takes higher resolution for the error bars on the $(6, 0)$ mode to decrease to those on the $(2, 0)$ mode at lower resolution. The errors also increase with the spin of the system. This is because it is more difficult to resolve higher spin systems numerically [129, 128].
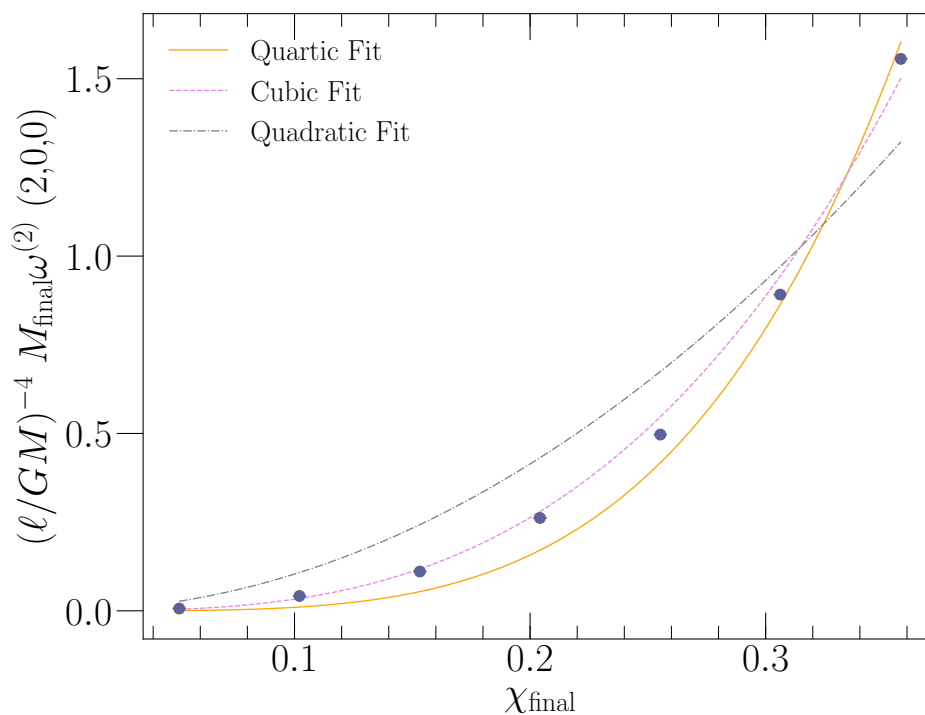
Figure 5.10: Fitted $\omega^{(2)}_{(2,0,0)}$, the leading-order dCS modification, with the dCS coupling scaled out, to the $(2,0,0)$ mode QNM frequency, as a function of dimensionless spin χ_{final} of the final background black hole. The error bars on the quantity are computed by considering $\omega^{(2)}$ for numerical simulations with different resolutions (cf. 5.4). We see that $\omega^{(2)}$ increases as a power law with spin. Note that these large values of $\omega^{(2)}(\ell/GM)^{-4}$ must be multiplied by a small, appropriate value of $(\ell/GM)^4$ to have physical meaning.

Particular and homogeneous solutions

There is interesting behavior later on in the $\Psi_4^{(2)}$ waveforms. As we can see from Fig. 5.3, for example, there is a kink that occurs in $\Psi_4^{(2)}$ around $40\,M$ after the peak time (in the $(2,0)$ mode). This kink is convergent with resolution and is present with and without adaptive mesh refinement. Later in the waveform, after the kink, both $\Psi_4^{(2)}$ and $\Psi_4^{(0)}$ are well-described by damped sinusoids, and have the same decay time and frequency. In other words, $\Psi_4^{(2)}$ has the same QNM spectrum as $\Psi_4^{(0)}$, a QNM perturbation on a pure Kerr spacetime. This suggests that $\Psi_4^{(2)}$ switches from being dominantly driven by the dCS scalar field, to being dominantly driven by the GR background, as postulated in Sec. 5.3. In other words, the early post-merger dCS waveform correction is dominated by a *particular solution*, whereas later it is dominated by a *homogeneous solution*.
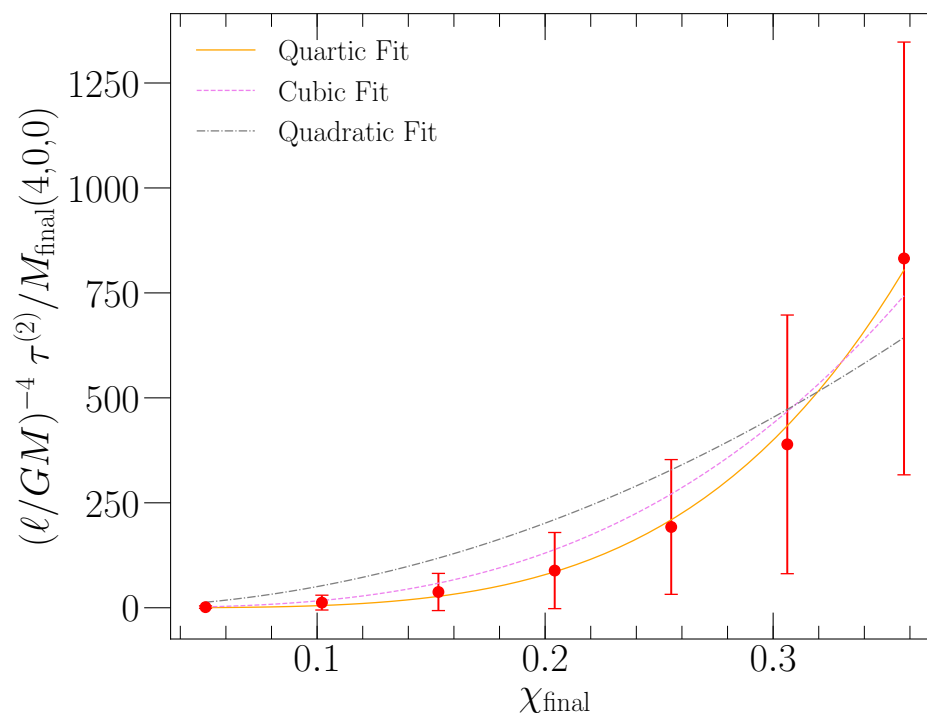
Figure 5.11: Similar to Fig. 5.9, but for $\tau^{(2)}_{(4,0,0)}$, the leading-order dCS modification to the QNM damping time of the $(4, 0)$ mode of the gravitational radiation.

We illustrate this behavior schematically in Fig. 5.13. We consider the slopes of the logarithms of $\Psi_4^{(0)}$ and $\Psi_4^{(2)}$, which is equivalent to finding a decay time for each. Note that this is not the same as the perturbed fits for $\Psi_4^{(2)}$ given in Eqs. (5.28) and (5.29), which we use to extract $\tau^{(2)}$ and $\omega^{(2)}$. After the kink, the decay times are the same. In other words, the leading order dCS modification to the gravitational radiation is the same as a GR QNM spectrum on Kerr.

We can corroborate this interpretation by looking at the scalar field in the strong field region, whose dynamics drives the radiative part of $h_{ab}^{(2)}$. As the scalar field settles down, it no longer the dominant source driving $h_{ab}^{(2)}$, and the metric perturbation is dominantly driven by the Kerr background. However, making this interpretation more precise would be tricky: we must keep in mind that mapping between the strong-field region and a gravitational waveform at infinity requires utmost care (cf. [47]).
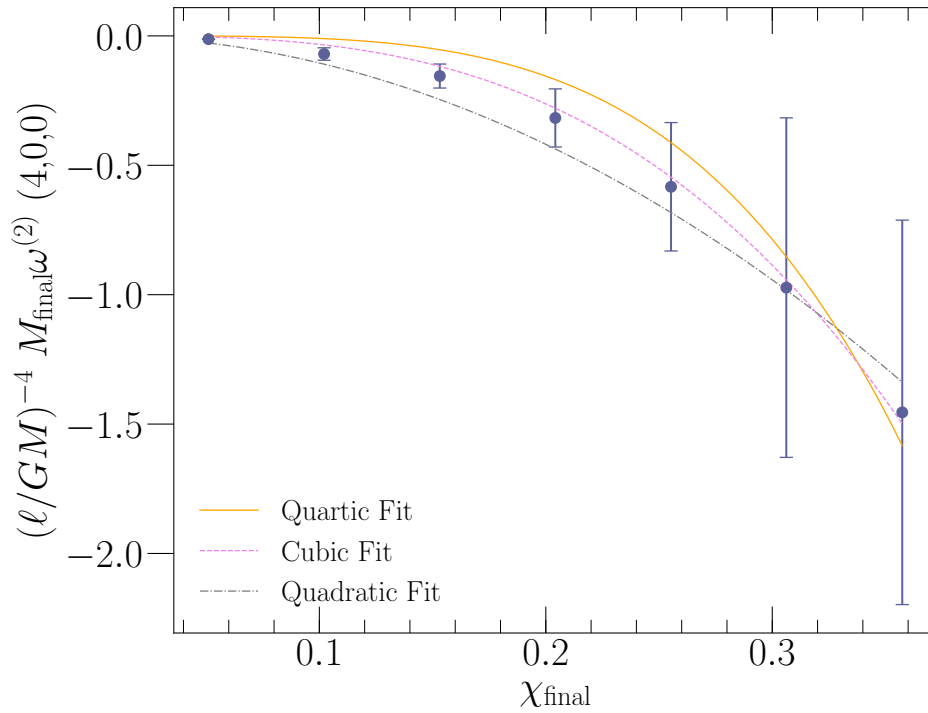
Figure 5.12: Similar to Fig. 5.10, but for $\omega^{(2)}_{(4,0,0)}$, the leading-order dCS modification to the QNM frequency of the $(4, 0)$ mode of the gravitational radiation.

5.5 Implications for testing general relativity

Let us now discuss this work in the context of testing GR with gravitational wave observations. Suppose that we were to observe a post-merger gravitational wave, given by Ψ_4. To third-order accuracy, we can model this wave as

$$\Psi_4 = \Psi_4^{(0)} + \Psi_4^{(2)} + \mathcal{O}((\ell/GM)^6).\tag{5.39}$$

If we were to fit a damped exponential as in Eq. (5.18) to the observed Ψ_4 (without using a modified functional form like Eq. (5.28)), to leading order the ω and τ of this fit would be

$$\omega_{(l,m,n)} = \omega^{(0)}_{(l,m,n)} + \omega^{(2)}_{(l,m,n)} + \mathcal{O}((\ell/GM)^6).\tag{5.40}$$

From perturbation theory, we know the GR values $\omega^{(0)}_{(l,m.n)}$ and $\tau^{(0)}_{(l,m,n)}$ for each $\{\chi_{\text{final}}, M_{\text{final}}\}$. From the numerical methods presented in this study, given a $\{\chi_{\text{final}}, M_{\text{final}}\}$, we can also compute theoretical values in dCS for $(\ell/GM)^{-4}\omega^{(2)}_{(l,m,n)}$ and $(\ell/GM)^{-4}\tau^{(2)}_{(l,m,n)}$.

Let us first suppose that $\ell = 0$, meaning that there is no modification from GR. In GR, assuming the no-hair theorem is true, the frequency and damping time for
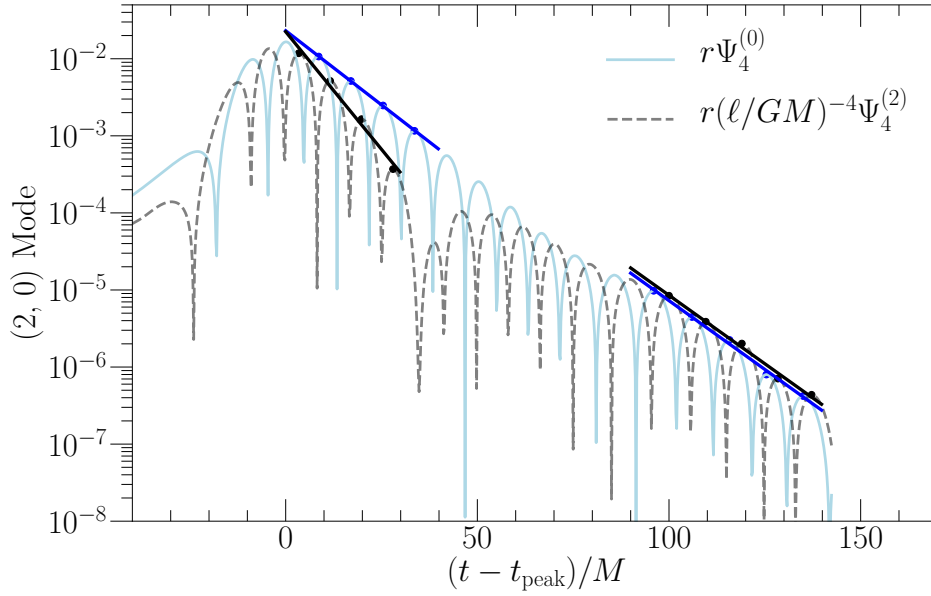
Figure 5.13: The real parts of $\Psi_4^{(2)}$ (with the dCS coupling scaled out) and $\Psi_4^{(0)}$ after merger for $\chi = 0.1\hat{x}$. We fit a line to the peaks of the gravitational waveform during various stages of the post-merger waveform (black for $\Psi_4^{(2)}$, blue for $\Psi_4^{(0)}$). Early on in the waveform, $\Psi_4^{(2)}$ and $\Psi_4^{(0)}$ have different damping times if modeled by damped sinusoids, whereas later in the waveform, they have the same damping time. This suggests that at late times, $\Psi_4^{(2)}$ is well-modeled as a QNM on a pure Kerr background.

each mode of ringdown should be parametrized purely by the mass, M_{final}, and spin, χ_{final}, of the final black hole. Given two observed modes, we can check that the fitted $\omega_{(l,m,n)} = \omega_{(l,m,n)}^{(0)}$ and $\tau_{(l,m,n)} = \tau_{(l,m,n)}^{(0)}$ are consistent with the predicted GR values for M_{final} and χ_{final} [43, 94, 14, 111, 216].

Checking non-degeneracy: projected

Now let us consider the degeneracy of dCS modifications to GR. Consider the 4-dimensional parameter space $\mathbb{P}$ of $\{M\omega^{(0)}, \tau^{(0)}/M, M\omega^{(2)}, \tau^{(2)}/M\}$ for a given mode. GR solutions exist purely in the $M\omega^{(0)} - \tau^{(0)}/M$ 2-dimensional submanifold $\mathbb{S}_{\text{GR}}$ of this space, with coordinates $\{M_{\text{final}}, \chi_{\text{final}}\}$ on the manifold. Suppose at some point (M_1, χ_1) on $\mathbb{S}_{\text{GR}}$, we introduce a dCS deviation with some coupling $(\ell/GM)^4$. In other words, we will have

$$\omega(\chi_1, M_1) = \omega^{(0)}(\chi_1, M_1) + (\ell/GM)^4 \Delta\omega(\chi_1, M_1), \qquad (5.41)$$

$$\tau(\chi_1, M_1) = \tau^{(0)}(\chi_1, M_1) + (\ell/GM)^4 \Delta\tau(\chi_1, M_1), \qquad (5.42)$$

$\chi_{1,2}$	χ_{final}	$(\ell/GM)^{-4}$ $\omega^{(2)}_{(2,0,0)}M_{final}$	$(\ell/GM)^{-4}$ $\omega^{(2)}_{(2,0,1)}M_{final}$	$(\ell/GM)^{-4}$ $\omega^{(2)}_{(2,0,2)}M_{final}$	$(\ell/GM)^{-4}$ $\tau^{(2)}_{(2,0,0)}/M_{final}$	$(\ell/GM)^{-4}$ $\tau^{(2)}_{(2,0,1)}/M_{final}$	$(\ell/GM)^{-4}$ $\tau^{(2)}_{(2,0,2)}/M_{final}$	$(\ell/GM)^4$
0.1	0.05106	$6.(1)\times10^{-3}$	$-1.0(1)\times10^{-1}$	$-2.1(3)\times10^{0}$	$-4.4(2)\times10^{0}$	$8.(1)\times10^{0}$	$3.1(4)\times10^{1}$	1.26×10^{-1}
0.2	0.1021	$4.1(2)\times10^{-2}$	$-6.9(5)\times10^{-1}$	$-1.3(5)\times10^{1}$	$-2.8(1)\times10^{1}$	$5.4(2)\times10^{1}$	$1.9(1)\times10^{2}$	3.01×10^{-2}
0.3	0.1532	$1.1(5)\times10^{-1}$	$-1.9(5)\times10^{0}$	$-3.5(2)\times10^{1}$	$-7.5(7)\times10^{1}$	$1.3(1)\times10^{2}$	$5.1(1)\times10^{2}$	1.18×10^{-2}
0.4	0.2042	$2.6(5)\times10^{-1}$	$-6.1(2)\times10^{0}$	$-7.0(2)\times10^{1}$	$-1.4(4)\times10^{2}$	$3.0(1)\times10^{2}$	$1.0(5)\times10^{3}$	5.68×10^{-3}
0.5	0.2553	$4.9(6)\times10^{-1}$	$-1.1(6)\times10^{1}$	$-1.2(5)\times10^{2}$	$-2.7(1)\times10^{2}$	$5.6(1)\times10^{2}$	$1.9(1)\times10^{3}$	2.97×10^{-3}
0.6	0.3062	$8.9(2)\times10^{-1}$	$-2.1(1)\times10^{1}$	$-2.2(1)\times10^{2}$	$-4.8(3)\times10^{2}$	$9.7(2)\times10^{2}$	$3.4(2)\times10^{3}$	1.61×10^{-3}
0.7	0.3574	$1.5(2)\times10^{0}$	$-4.1(1)\times10^{1}$	$-3.8(1)\times10^{2}$	$-8.2(4)\times10^{2}$	$1.6(2)\times10^{3}$	$5.7(3)\times10^{3}$	8.79×10^{-4}

Table 5.1: Fitted QNM parameters for each head-on collision configuration considered in this study. All configurations have mass ratio $q = 1$ and final background Christodolou mass $M_{final} = 0.9896$. The first column corresponds to the (equal) initial spins of the background black holes, which are oriented in the same direction along the axis of collision (cf. Fig. 5.1). The second column corresponds to the dimensionless spin χ_{final} of the final background black hole. The third, fourth, and fifth columns correspond to the leading-order dCS correction to the QNM frequency of the $(2, 0)$ mode, $\omega^{(2)}_{(2,0)}$ (multiplied by the final background mass, and with the dCS coupling scaled out), for the $n = 0, 1, 2$ overtones. The sixth, seventh, and eighth column similarly correspond to $\tau^{(2)}_{(2,0)}$, the leading-order dCS correction to the QNM damping time (divided by the final background mass and with the dCS coupling scaled out) for the $n = 0, 1, 2$ overtones. We provide a maximum allowed value of $(\ell/GM)^4$ for each configuration (cf. Sec. 5.4) in the last column. In order to be physically meaningful, the dCS QNM parameters must be multiplied by this factor

$\chi_{1,2}$	χ_{final}	$(\ell/GM)^{-4}$ $\omega^{(2)}_{(4,0,0)}M_{final}$	$(\ell/GM)^{-4}$ $\omega^{(2)}_{(4,0,1)}M_{final}$	$(\ell/GM)^{-4}$ $\omega^{(2)}_{(4,0,2)}M_{final}$	$(\ell/GM)^{-4}$ $\tau^{(2)}_{(4,0,0)}/M_{final}$	$(\ell/GM)^{-4}$ $\tau^{(2)}_{(4,0,1)}/M_{final}$	$(\ell/GM)^{-4}$ $\tau^{(2)}_{(4,0,2)}/M_{final}$	$(\ell/GM)^4$
0.1	0.05106	$-1.2(5)\times10^{-2}$	$4.(2)\times10^{-2}$	$8.5(1)\times10^{-2}$	$1.(3)\times10^{0}$	$-7.(1)\times10^{-1}$	$-6.(3)\times10^{-1}$	1.26×10^{-1}
0.2	0.1021	$-6.(2)\times10^{-2}$	$2.(2)\times10^{-1}$	$4.8(8)\times10^{-1}$	$1.(1)\times10^{1}$	$-5.(1)\times10^{0}$	$-4.2(7)\times10^{0}$	3.01×10^{-2}
0.3	0.1532	$-1.5(4)\times10^{-1}$	$5.(5)\times10^{-1}$	$1.2(2)\times10^{0}$	$3.(4)\times10^{1}$	$-1.2(4)\times10^{1}$	$-1.0(3)\times10^{1}$	1.18×10^{-2}
0.4	0.2042	$-3.(1)\times10^{-1}$	$1.(1)\times10^{0}$	$2.5(6)\times10^{0}$	$8.(9)\times10^{1}$	$-2.8(1)\times10^{1}$	$-2.2(6)\times10^{1}$	5.68×10^{-3}
0.5	0.2553	$-5.(2)\times10^{-1}$	$1.(2)\times10^{0}$	$4.(1)\times10^{0}$	$1.(1)\times10^{2}$	$-5.6(2)\times10^{1}$	$-4.(1)\times10^{1}$	2.97×10^{-3}
0.6	0.3062	$-9.(6)\times10^{-1}$	$2.(3)\times10^{0}$	$7.(2)\times10^{0}$	$3.(3)\times10^{2}$	$-1.0(1)\times10^{2}$	$-8.(1)\times10^{1}$	1.61×10^{-3}
0.7	0.3574	$-1.4(7)\times10^{0}$	$2.(8)\times10^{0}$	$1.2(5)\times10^{1}$	$8.(5)\times10^{2}$	$-1.8(1)\times10^{2}$	$-1.6(3)\times10^{2}$	8.79×10^{-4}

Table 5.2: Same as Table 5.1, but for the $(4, 0)$ mode.

where we have explicitly written out the dependence on the coupling constant with $\Delta\omega \equiv (\ell/GM)^{-4}\omega^{(2)}$ and $\Delta\tau \equiv (\ell/GM)^{-4}\tau^{(2)}$. If dCS modifications and GR are degenerate, then this modification will move purely within $\mathbb{S}_{GR}$. However, if dCS modifications and GR are non-degenerate, then the new point will be off $\mathbb{S}_{GR}$ in $\mathbb{P}$. The dCS modifications will form a 3-dimensional submanifold of $\mathbb{P}$, $\mathbb{S}_{dCS}$, with coordinates $\{M_{final}, \chi_{final}, \ell/GM\}$.

Let us now consider this statement in the context of our numerical results. For simplicity, let us first consider holding M_{final} constant in the comparisons. In Fig. 5.14, we plot values of $M_{final}\omega_{(2,0,0)}$ and $\tau_{(2,0,0)}/M_{final}$ for various spins. We
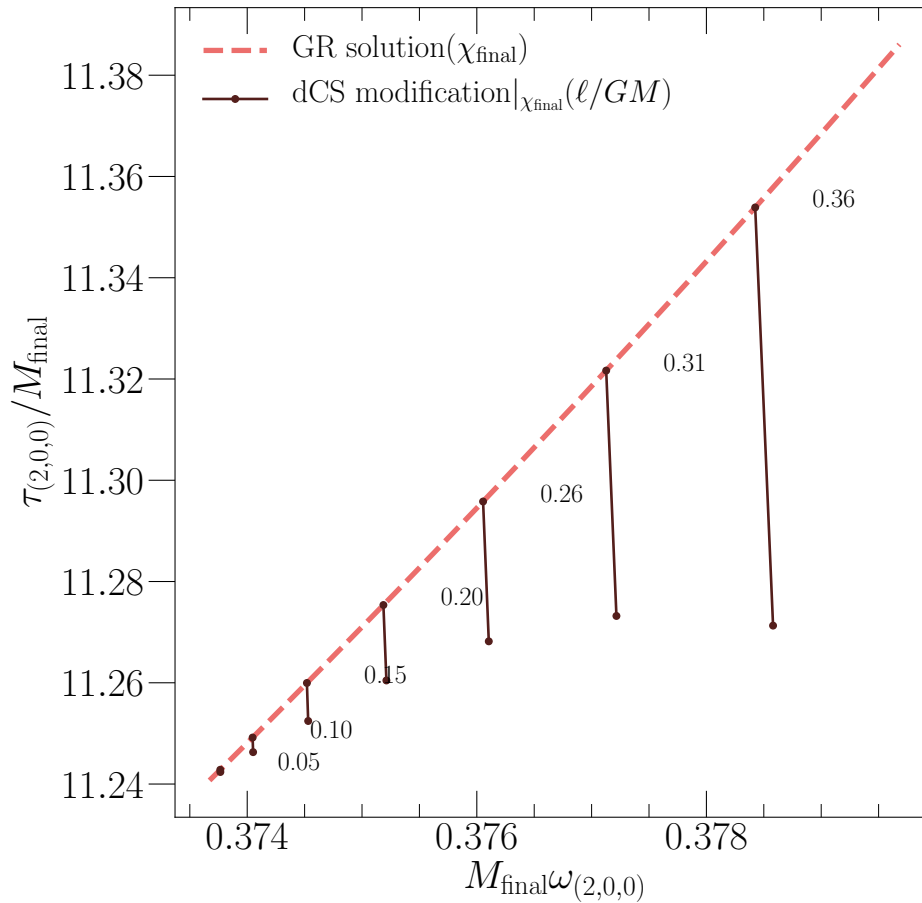
Figure 5.14: Probing degeneracy of GR and dCS-corrected QNM spectra. We show the values of $M_{\text{final}}\omega$ and τ/M_{final} for the $(2,0,0)$ mode of the post-merger gravitational radiation. If there is no dCS modification, i.e. $\ell = 0$, then for fixed final mass M_{final}, the GR QNM solutions form a curve parametrized by χ_{final} in the plane. We show this line in dashed pink. For each χ_{final}, we introduce a dCS modification using the $\omega^{(2)}$ and $\tau^{(2)}$ that we have computed in this study. This modification depends on the coupling parameter (ℓ/GM) and thus forms a line parametrized by (ℓ/GM) in the $M_{\text{final}}\omega - \tau/M_{\text{final}}$ plane. We show these lines for each χ_{final} (labelled by the values of the final dimensionless spin) in solid maroon lines. Here we choose a conservative maximum value of $(\ell/GM)^4 = 10^{-4}$ for each spin. We see that this modification does not purely lie along the GR solution, and hence GR and dCS-corrected QNM spectra are non-degenerate.

similarly plot $M_{\text{final}}\omega_{(4,0,0)}$ and $\tau_{(4,0,0)}/M_{\text{final}}$ in Fig. 5.15. For $\ell = 0$, we can use perturbation theory to compute the values of $\omega = \omega^{(0)}$ and $\tau = \tau^{(0)}$ in GR. Holding M_{final} fixed, the GR solutions form a curve L_{GR} in the $\omega - \tau$ plane, parametrized by χ_{final}.
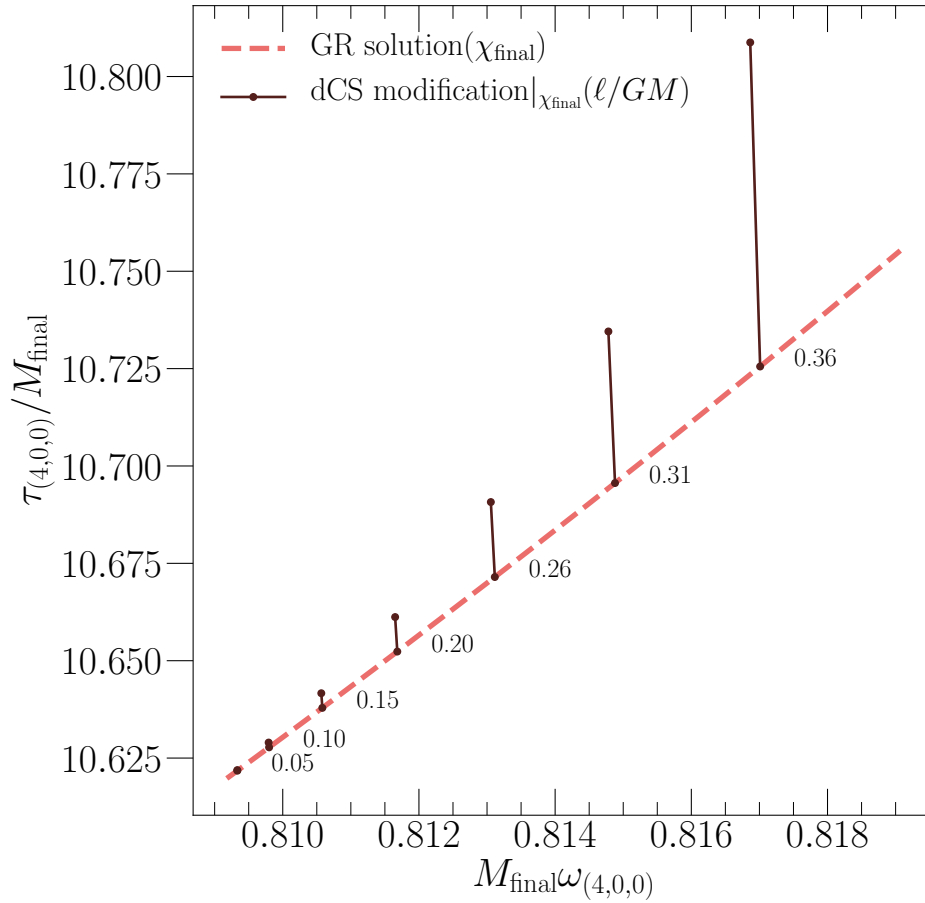
Figure 5.15: Same as Fig. 5.14, but for the $(4, 0, 0)$ mode of the gravitational radiation.

Now let us introduce $\ell \neq 0$. For each simulation that we have performed, with a given χ_{final} (recall all of the M_{final} are equal), we compute $\omega(\chi_{\text{final}})$ and $\tau(\chi_{\text{final}})$ via Eqs. (5.41) and (5.42) using our results for $\Delta\omega = (\ell/GM)^{-4}\omega^{(2)}$ and $\Delta\tau = (\ell/GM)^{-4}\tau^{(2)}$. This computation requires specifying a value of (ℓ/GM). If we vary (ℓ/GM) over an allowed range (cf. Sec. 5.4), for each χ_{final} we obtain a line $L_{\text{dCS}}(\chi_{\text{final}})$ in the $M_{\text{final}}\omega - \tau/M_{\text{final}}$ plane parametrized by (ℓ/GM).

If the dCS corrections to the quasi-normal mode spectrum were degenerate with GR, then $L_{\text{dCS}}(\chi_{\text{final}})$ would lie purely along L_{GR}. In other words, the resulting QNM spectrum for χ_{final} would be degenerate with that of GR for some other spin χ'. However, we see in Figs. 5.14 and 5.15 that in all cases $L_{\text{dCS}}(\chi_{\text{final}})$ does *not* lie purely along L_{GR}, meaning that the QNM spectra are non-degenerate. This in turn means that dCS modifications to QNM spectra can in principle be observed (in the

limit of infinite signal-to-noise ratio).

Note that we have held M_{final} fixed, given that all of our simulations have the same final mass. If we allowed M_{final} to vary as well, then we would have to carefully consider the full space $\mathbb{P}$ parametrized by $\{M\omega^{(0)}, \tau^{(0)}/M, M\omega^{(2)}, \tau^{(2)}/M\}$, and ask whether the dCS solutions deviate from the $M\omega^{(0)} - \tau^{(0)}/M$ submanifold $\mathbb{S}_{\text{GR}}$.

Checking non-degeneracy: full case

We can perform a more rigorous analysis, checking for full degeneracy, rather than the simpler check that holds M_{final} fixed. Let us think about the 3-dimensional space p with coordinates $\{\chi, M, \varepsilon^2\}$ (where ε is our dCS order-reduction parameter). Suppose we observe k QNMs, which gives us $2k$ quantities (ω and τ for each mode). Let q be the $2k$-dimensional space q with these coordinates.

Let us consider the map $\phi : p \rightarrow q$, which maps each set of parameters $\{\chi, M, \varepsilon^2\}$ to the QNM values. The image $\phi(p)$ will form a 3-dimensional submanifold of q, and the tangent space of the image will be spanned by the pushforwards of $\{\partial/\partial\chi, \partial/\partial M, \partial/\partial\varepsilon^2\}$. That is, $\{\phi_*\partial/\partial\chi, \phi_*\partial/\partial M, \phi_*\partial/\partial\varepsilon^2\}$.

Non-degeneracy in this context means that the dimension of the span of

$$\{\phi_*\partial/\partial\chi, \phi_*\partial/\partial M, \phi_*\partial/\partial\varepsilon^2\} \tag{5.43}$$

is 3. This can be checked by looking at the rank of the $3 \times 2k$ dimensional matrix

$$D \equiv \begin{bmatrix} \Big| & \Big| & \Big| \\ \phi_*\frac{\partial}{\partial\chi} & \phi_*\frac{\partial}{\partial M} & \phi_*\frac{\partial}{\partial\varepsilon^2} \\ \Big| & \Big| & \Big| \end{bmatrix} . \tag{5.44}$$

Let us consider how to evaluate this matrix, working at $\varepsilon^2 = 0$ for each χ_{final} and M_{final} for which we have performed a head-on collision. Suppose we are considering some mode with QNM frequency ω_{lmn} and damping time τ_{lmn}. This will give us two rows in the matrix D.

Let us first compute

$$\frac{\partial}{\partial\chi}\omega_{lmn} = \frac{1}{M_{\text{final}}}\frac{\partial}{\partial\chi}(\omega_{lmn}M_{\text{final}}), \tag{5.45}$$

$$\frac{\partial}{\partial\chi}\tau_{lmn} = M_{\text{final}}\frac{\partial}{\partial\chi}(\tau_{lmn}/M_{\text{final}}) \tag{5.46}$$

This can be done by computing the values of $\omega_{lmn}M_{\text{final}}$ and $\tau_{lmn}/M_{\text{final}}$ from perturbation theory [182], varying only χ around χ_{final}, and then taking a numerical derivative. We work with a step-size of 10^{-10}, which is comparable to the accuracy of [182].

Now let us compute the $\partial/\partial M$ column. For fixed χ_{final} and $\ell^4 = 0$, the dependence on M is

$$\frac{d}{dM}\omega_{lmn} = \frac{-\omega_{lmn}}{M_{\text{final}}}, \tag{5.47}$$

$$\frac{d}{dM}\tau_{lmn} = \tau_{lmn}M_{\text{final}}. \tag{5.48}$$

Finally, for the last column, for fixed $\chi_{\text{final}}, M_{\text{final}}$, we have

$$\frac{d}{d\varepsilon^2}\omega_{lmn} = \frac{\Delta\omega_{lmn}}{M_{\text{final}}}, \frac{d}{d\varepsilon^2}\tau_{lmn} \qquad\qquad = \Delta\tau_{lmn}M_{\text{final}} \tag{5.49}$$

where $\Delta\omega_{lmn}$ and $\Delta\tau_{lmn}$ are the quantities we compute from our numerical fits.

We put the matrix D together with these values. Note that the ω rows all have a factor of $1/M_{\text{final}}$, while the τ rows have a factor of M_{final}. We evaluate the rank of this matrix using a singular-value decomposition (SVD) [109]. For all values of $\{\chi_{\text{final}}, M_{\text{final}}\}$ in our head-on collisions dataset, we find that the rank of D is 3. The lowest singular value is $10^{-2} - 10^{-1}$, while the condition numbers (the 2-norm, computed from the SVD) are of order 10^3.

5.6 Conclusion

In this study, we have produced the first beyond-GR BBH gravitational waveforms in full numerical relativity for a higher-curvature theory. We have considered head-on collisions of BBHs in dynamical Chern-Simons gravity. While these are not likely to be astrophysically relevant configurations, they serve as a proof of principle of our ability to produce beyond-GR waveforms [142]. Future work in this program thus involves adding initial orbital angular momentum to the system and producing beyond-GR gravitational waveforms for inspiraling systems. We have previously evolved the leading order dCS scalar field for an inspiraling BBH background [146], and can use our (fully-general) methods given in [143] and [142] to produce initial data for and evolve an inspiraling BBH system.

We have also studied modifications to the post-merger BBH head-on collision QNM spectra. We found that at leading order, the damping time of each QNM receives a modification that increases with the spin of the final black hole in a power law.

The frequency of each QNM receives a similar modification. When performing inspiraling BBH simulations, we can repeat the analysis outlined in this paper to learn about the dCS modification to the QNM spectrum of an astrophysically revelant system. These results can then be applied to beyond-GR tests of BBH ringdowns [14, 216].

5.A   Choosing a perturbed gauge

Throughout this appendix, as well as Appendix 5.B, we use the notation developed in [142], and standard 3+1 ADM decomposition notation [40]. Recall that g_{ab} refers to the 4-dimensional spacetime metric, while γ_{ij} refers to the 3-dimensional spatial metric. ΔQ is the leading-order perturbation to quantity Q.

The generalized harmonic evolution for the background follows from the equation

$$\Gamma_a = -H_a, \tag{5.50}$$

where $\Gamma_a \equiv g^{bc}\Gamma_{bca}$, and H_a is known as the *gauge source function* (cf. [122] for more details). Throughout the evolution, the *gauge constraint*,

$$C_a \equiv H_a + \Gamma_a = 0, \tag{5.51}$$

must be satisfied.

When generating initial data for g_{ab} and $\partial_t g_{ab}$, we are free to choose $\partial_t \alpha$ and $\partial_t \beta^i$, the initial time derivatives of the lapse and shift. These quantities appear in Γ_a, so choosing them is equivalent to choosing initial values of H_a, via Eq. (5.51). For example, for initial data in equilibrium, we can set $\partial_t \alpha = 0$ and $\partial_t \beta^i = 0$, and set H_a to initially satisfy Eq. (5.51). Alternatively, we can choose to work in a certain gauge, such as harmonic gauge with $H_a = 0$, and set $\partial_t \alpha$ and $\partial_t \beta^i$ to satisfy Eq. (5.51).

As the evolution progresses, we can either leave H_a fixed, or continuously "roll" it into a different gauge, with the restriction that it contains only up to first derivatives of g_{ab} to ensure well-posedness. In practice, for BBH in GR, we work in a *damped harmonic gauge*, with H_a specified using the methods given in [190].

The perturbed generalized harmonic evolution takes a similar form as Eq. (5.50), with

$$\Delta\Gamma_a = -\Delta H_a, \tag{5.52}$$

where $\Delta\Gamma_a$ is the first-order perturbation to Γ_a, and ΔH_a is a perturbed gauge source function. Similar to Eq. (5.51), we have a perturbed gauge constraint,

$$\Delta C_a \equiv \Delta\Gamma_a + \Delta H_a = 0\,. \tag{5.53}$$

At the start of the evolution, we similarly have the freedom to choose ΔH_a, provided that it contains no higher than first derivatives of Δg_{ab}, and satisfies the perturbed gauge constraint Eq. (5.53). When solving for perturbed initial data (cf. [143]), we similarly have the freedom to choose $\partial_t\Delta\alpha$ and $\partial_t\Delta\beta^i$, the time derivatives of the perturbed lapse and shift. An easy choice, for example, is to work in a perturbed harmonic gauge,

$$\Delta H_a = 0\,. \tag{5.54}$$

Let us now work out how to set $\partial_t\Delta\alpha$ and $\partial_t\Delta\beta^i$ in order to satisfy Eq. (5.53) for some desired perturbed gauge source function ΔH_a. Let us first consider the unperturbed case, setting $\partial_t\alpha$ and $\partial_t\beta^i$ for some gauge source function H_a. We will work with the κ_{abc} variable, which is the fundamental variable encoding the spatial and time derivatives of the metric (cf. [142]) as

$$\kappa_{iab} \equiv \partial_i g_{ab}\,, \tag{5.55}$$

$$\kappa_{0ab} \equiv -n^c \partial_c g_{ab}\,, \tag{5.56}$$

where n^c denotes the timelike unit normal vector. We can use our freedom to set $\partial_t\beta^i$ and $\partial_t\alpha$ to modify κ_{abc} to satisfy $\Gamma_a = -H_a$ as

$$\kappa_{00i} = -\alpha H_i + \beta^k \kappa_{0ki} - \alpha\gamma^{jk}\Gamma_{ijk} - \frac{1}{2}\alpha n^a n^b \kappa_{iab}\,, \tag{5.57}$$

where Γ_{ijk} is the spatial Christoffel symbol of the first kind, and

$$\kappa_{000} = -2\alpha H_0 + 2\beta^j(\kappa_{00j} + \alpha H_j) \tag{5.58}$$
$$- \beta^j \beta^k \kappa_{0jk} - \alpha^2 \gamma^{jk}\kappa_{0jk} - 2\alpha^2 \gamma^{jk} n^a \kappa_{jka}\,,$$

where κ_{00j} in the above expression is given by Eq. (5.57). We can then use this modified κ_{abc} to compute Γ_a and ensure that Eq. (5.51) is satisfied for $H_a = H_a$.

Perturbing Eqs. (5.57) and (5.58), we can get an expression for a modified $\Delta\kappa_{abc}$ to satisfy Eq. (5.53) for some desired perturbed gauge source function ΔH_a. We thus

obtain

$$\Delta\kappa_{00i} = -\Delta\alpha H_i - \alpha\Delta H_i \tag{5.59}$$
$$+ \Delta\beta^k \kappa_{0ki} + \beta^k \Delta\kappa_{0ki}$$
$$- \Delta\alpha\gamma^{jk}\Gamma_{ijk} - \alpha\Delta\gamma^{jk}\Gamma_{ijk} - \alpha\gamma^{jk}\Delta\Gamma_{ijk}$$
$$- \frac{1}{2}\Delta\alpha n^a n^b \kappa_{iab} - \frac{1}{2}\alpha\Delta n^a n^b \kappa_{iab}$$
$$- \frac{1}{2}\alpha n^a \Delta n^b \kappa_{iab} - \frac{1}{2}\alpha n^a n^b \Delta\kappa_{iab},$$

and

$$\Delta\kappa_{000} = -2\Delta\alpha H_0 - 2\alpha\Delta H_0 \tag{5.60}$$
$$+ 2\Delta\beta^j(\kappa_{00j} + \alpha H_j)$$
$$+ 2\beta^j(\Delta\kappa_{00j} + \Delta\alpha H_j + \alpha\Delta H_j)$$
$$- \Delta\beta^j\beta^k \kappa_{0jk} - \beta^j\Delta\beta^k \kappa_{0jk} - \beta^j\beta^k \Delta\kappa_{0jk}$$
$$- 2\alpha\Delta\alpha\gamma^{jk}\kappa_{0jk} - \alpha^2\Delta\gamma^{jk}\kappa_{0jk} - \alpha^2\gamma^{jk}\Delta\kappa_{0jk}$$
$$- 4\alpha\Delta\alpha\gamma^{jk}n^a\kappa_{jka} - 2\alpha^2\Delta\gamma^{jk}n^a\kappa_{jka}$$
$$- 2\alpha^2\gamma^{jk}\Delta n^a\kappa_{jka} - 2\alpha^2\gamma^{jk}n^a\Delta\kappa_{jka}.$$

Note that this computation also uses the gauge source function of the background, H_a. Assuming that the background is in a satisfactory gauge, we set H_a to the initial background gauge source function. All of the perturbed quantities in Eqs. (5.59) and (5.60) are given in [142].

In this study, we choose to work in a perturbed harmonic gauge, with $\Delta H_a = 0$.

5.B Computing perturbed gravitational radiation

The outgoing gravitational radiation of a spacetime is encoded in the Newman-Penrose scalar Ψ_4. In order to compute the leading-order correction to the binary black hole background radiation due to the metric perturbation Δg_{ab}, we need to compute $\Delta\Psi_4$, the leading-order correction to Ψ_4.

Ψ_4, a scalar, is computed on a topologically spherical surface from a rank-two tensor U_{ij}, contracted with a tetrad (in our case, a coordinate tetrad that converges to a quasi-Kinnersley tetrad at large radii). U_{ij} on a surface with normal vector $\hat{n}^i$ takes the form

$$U_{ij} = (P_i^m P_j^n - \frac{1}{2}P_{ij}P^{mn})(E_{mn} - \epsilon_m{}^{kl}\hat{n}_l B_{kn}), \tag{5.61}$$

where E_{ij} is the electric Weyl tensor, B_{ij} is the magnetic Weyl tensor, ϵ_{ijk} is the (spatial) Levi-Civita tensor, and the projection operators are given by

$$P^{ij} = \gamma^{ij} - \hat{n}^i \hat{n}^j, \tag{5.62}$$

$$P_{ij} = \gamma_{ij} - \hat{n}_i \hat{n}_j, \tag{5.63}$$

$$P^i_j = \gamma^i_j - \hat{n}^i \hat{n}_j. \tag{5.64}$$

Here, the vector $\hat{n}^i$ and the one form $\hat{n}_i$ are normalized using $N \equiv \sqrt{\gamma^{ij} n_i n_j}$ with $n^i = \gamma^{ij} n_j$.

In order to perturb Ψ_4, let us write the electric and magnetic Weyl tensors in Eq. (5.61) in terms of the extrinsic curvature K_{ij},

$$
\begin{aligned}
U_{ij} = (P^m_i P^n_j - \frac{1}{2} P_{ij} P^{mn}) \times \\
\left(R_{mn} + \gamma^{kl}(K_{mn}K_{kl} - K_{mk}K_{ln}) \right. \\
\left. - \hat{n}^k(D_k K_{mn} - D_{(m}K_{n)k}) \right),
\end{aligned} \tag{5.65}
$$

where R_{ij} is the spatial Ricci tensor, and D_i is the spatial covariant derivative associated with γ_{ij}.

Perturbing Eq. (5.65), we obtain

$$
\begin{aligned}
\Delta U_{ij} = (P^m_i P^n_j - \frac{1}{2} P_{ij} P^{mn}) \times \\
\left(\Delta R_{mn} + \Delta\gamma^{kl}(K_{mn}K_{kl} - K_{mk}K_{ln}) \right. \\
+ \gamma^{kl}(\Delta K_{mn}K_{kl} + K_{mn}\Delta K_{kl} \\
- \Delta K_{mk}K_{ln} - K_{mk}\Delta K_{ln}) \\
- \hat{n}^k(\Delta(D_k K_{mn}) - \Delta(D_{(m}K_{n)k}) \\
\left. - \Delta\hat{n}^k(D_k K_{mn} - D_{(m}K_{n)k}) \right) \\
+ (\Delta P^m_i P^n_j + P^m_i \Delta P^n_j \\
- \frac{1}{2}\Delta P_{ij} P^{mn} - \frac{1}{2} P_{ij}\Delta P^{mn}) \times U_{mn}.
\end{aligned} \tag{5.66}
$$

All of the perturbed quantities Δg^{ij}, ΔK_{ij}, $\Delta(D_k K_{ij})$, and ΔR_{ij} are given in terms of the perturbation to the spatial metric, $\Delta\gamma_{ij} = \Delta g_{ij}$, its spatial derivative $\partial_k \Delta\gamma_{ij} = \partial_k \Delta g_{ab}$, and its time derivative, $\partial_t \Delta\gamma_{ij} = \partial_t \Delta g_{ij}$ in [143]. Note that since we use a first-order scheme, we have access to Δg_{ab}, $\partial_c \Delta g_{ab}$ throughout the evolution (cf. [142]).

Let us now work through the perturbations to the normal vectors and projection operators. Because we want the perturbation to the gravitational radiation to be extracted on the same surface as the background gravitational radiation, we will hold the unnormalized one-form to the surface, n_i, fixed. That is, $\Delta n_i = 0$. From this, we can then compute

$$\Delta N = \Delta(\gamma^{ij} n_i n_j)^{1/2} = \frac{1}{2} \Delta \gamma^{ij} n_i n_j (\gamma^{ij} n_i n_j)^{-1/2} \tag{5.67}$$
$$= \frac{1}{2N} \Delta \gamma^{ij} n_i n_j \,,$$

and

$$\Delta \hat{n}_i = -\frac{n_i}{N^2} \Delta N = -\frac{\hat{n}_i}{N} \Delta N \,, \tag{5.68}$$

$$\Delta n^i = \Delta \gamma^{ij} n_j = \Delta \gamma^{ij} \hat{n}_j N \,, \tag{5.69}$$

$$\Delta \hat{n}^i = \frac{\Delta n^i}{N} - \frac{n^i}{N^2} \Delta N \tag{5.70}$$
$$= \frac{\Delta \gamma^{ij} n_j}{N} - \frac{n^i}{N^2} \Delta N$$
$$= \Delta \gamma^{ij} \hat{n}_j - \frac{\hat{n}^i}{N} \Delta N \,.$$

We can then perturb the projection operators,

$$\Delta P^{ij} = \Delta \gamma^{ij} - \Delta \hat{n}^i \hat{n}^j - \hat{n}^i \Delta \hat{n}^j \,, \tag{5.71}$$

$$\Delta P_{ij} = \Delta \gamma_{ij} - \Delta \hat{n}_i \hat{n}_j - \hat{n}_i \Delta \hat{n}_j \,, \tag{5.72}$$

$$\Delta P^i_j = \Delta \gamma^i_j - \Delta \hat{n}^i \hat{n}_j - \hat{n}^i \Delta \hat{n}_j \,, \tag{5.73}$$

where $\Delta \gamma^i{}_j = \Delta \gamma^{ik} \gamma_{kj} + \gamma^{ik} \Delta \gamma_{kj}$.

Once we obtain ΔU_{mn}, we use the same tetrad to generate $\Delta \Psi_4$ from ΔU_{ij} as we do for Ψ_4.

Chapter 6

NUMERICAL RELATIVITY SIMULATION OF GW150914 BEYOND GENERAL RELATIVITY

Abstract

We produce the first numerical relativity gravitational waveform from an inspiraling binary black hole system in a higher-curvature theory beyond general relativity. We simulate a system with parameters consistent with GW150914, in order-reduced dynamical Chern-Simons gravity through full inspiral, merger, and ringdown. We compute the leading-order dynamical Chern-Simons correction to the gravitational radiation. We find that the dynamical Chern-Simons correction to the inspiral part of the gravitational waveform exhibits a beating frequency pattern, sourced by the leading-order dynamical Chern-Simons scalar field and binary black hole background. We additionaly compute the leading-order dynamical Chern-Simons modifications to the post-merger quasi-normal mode spectrum.

6.1 Introduction

Binary black hole mergers probe the strong-field, non-linear regime of gravity, and thus serve as test beds for Einstein's theory of general relativity. At some length scale, general relativity (GR) must break down and be reconciled with quantum mechanics in a theory beyond general relativity. While GR has been consistent with all weak-field tests to date [206], gravitational wave signatures from BBHs, by virtue of probing the strong-field region of gravity, may contain signatures of a beyond-GR theory.

GW150914, the first binary black hole observation by LIGO, was found to have a roughly 96% agreement with GR [6, 12], within statistical uncertainties. The final remnant's mass and spin were consistent with GR predictions [14], and the dominant ringdown quasi-normal mode was consistent with GR predictions. The inspiral part of the signal was further tested against waveform models containing parametrized deviations from GR [12]. These are all null-hypothesis and parametrized tests.

As Yunes et al. argue in [216], the potential for GW150914 to test beyond-GR physics is *severely limited* by the lack of understanding of BBH coalescences in

beyond-GR theories. In other words, in order to most effectively test GR, we must have access to BBH waveforms not only in GR, but also in beyond-GR theories. The most accurate BBH waveforms in GR come from numerical relativity, the practice of precisely numerically solving the equations governing spacetime. Our goal is thus to produce beyond-GR waveforms in numerical relativity.

In this study, we will consider dynamical Chern-Simons (dCS) gravity, a beyond-GR effective field theory that adds a scalar field coupled to spacetime curvature to the Einstein-Hilbert action of GR, and has origins in string theory, loop quantum gravity, and inflation [18, 95, 192, 134, 204]. The action of this theory takes the form

$$S \equiv \int d^4 x \sqrt{-g} \left(\frac{m_{\mathrm{pl}}^2}{2} R - \frac{1}{2} (\partial \vartheta)^2 - \frac{m_{\mathrm{pl}}}{8} \ell^2 \vartheta \, {}^*\!RR \right) , \qquad (6.1)$$

where g_{ab} is the spacetime metric, m_{pl} is the Planck mass, and ϑ is the dCS scalar field, which couples to spacetime curvature via the Pontryagin density, ${}^*\!RR \equiv {}^*\!R^{abcd} R_{abcd}$. This coupling is governed by a constant ℓ, which has dimensions of length, and physically represents the length scale below which quantum gravity effects become important.

The well-posedness of the initial value problem in full dCS gravity is unknown [74], and we work instead in a well-posed *order-reduction scheme*, in which we perturb the metric and scalar field around a GR background [146]. The leading-order dCS scalar field occurs at first order in this perturbative expansion, while the leading-order dCS modification to the spacetime metric occurs at second-order. Our goal is to compute the leading (second)-order dCS modification to the GR gravitational radiation of a BBH background.

We have previously computed the leading-order dCS modification to the gravitational radiation in BBH *head-on* collisions [145]. In this study, we use the methods of [145] to revisit GW150914 and compute the leading-order dCS modification to the gravitational radiation for this system.

Conventions

Please refer to [145, 142, 143, 146] for additional technical details of the order-reduction scheme, leading-order dCS scalar field evolution, and initial data generation for and evolution of the leading-order dCS correction to the spacetime metric. Quantities are given in terms of units of M, the sum of the Christodolou masses of the background black holes at a given relaxation time [56].

6.2 Results

Simulation parameters

While there is a distribution of mass and spin parameters consistent with GW150914 [12, 118], we choose to use the parameters of SXS:BBH:0305, as given in the Simulating eXtreme Spacetimes (SXS) catalog [188]. This simulation was used in Fig. 1 of the GW150914 detection paper [10], as well a host of follow-up studies [126, 47, 91]. The simulation has relaxed dimensionless spins (measured $640\,M$ into the simulation) $\chi_A = 0.330\hat{z}$ and $\chi_B = -0.440\hat{z}$, aligned and anti-aligned with the orbital angular momentum, and relaxed masses of $0.5497\,M$ and $0.4502\,M$, leading to a mass ratio of 1.221. The relaxed eccentricity is $\sim 7 \times 10^{-4}$. The black holes merge at $t = 3688\,M$, forming a common horizon after ~ 15 orbits. The remnant has final Christodolou mass $0.9525\,M$ and dimensionless spin 0.692 purely in the $\hat{z}$ direction.

Waveforms

In order-reduced dCS, the gravitational radiation encoded in the Newman-Penrose scalar Ψ_4 is modified from the GR value $\Psi_4^{(0)}$ as (cf. [145])

$$\Psi_4 = \Psi_4^{(0)} + \Psi_4^{(2)} + O(\ell^6), \tag{6.2}$$

where $\Psi_4^{(2)}$ is the leading-order dCS correction to the gravitational radiation, which occurs at second-order in the order reduction scheme.

We compute and decompose $\Psi_4^{(0)}$ and $\Psi_4^{(2)}$ into a basis of spin weight -2 spherical harmonics labelled by (l, m) [193, 56]. The dominant modes of $\Psi_4^{(0)}$ are $(2, 2)$ and $(3, 3)$. We plot these modes in Fig. 6.1.

We similarly plot the $(2, 2)$ mode of $\Psi_4^{(2)}$, the leading-order dCS correction to the gravitational radiation, and the subdominant $(3, 3)$ mode in Fig. 6.2. As discussed in [145], the leading-order dCS modification to the spacetime metric, as computed from the simulation, is independent of the coupling parameter ℓ. To be physically meaningful, the result must be multiplied by a factor of $(\ell/GM)^4$. We thus present all of our results as $(\ell/GM)^{-4}\Psi_4^{(2)}$, with the coupling scaled out.

For completeness, we present the dominant $(2, 1)$ and $(3, 2)$ modes of the leading-order dCS scalar field $\vartheta^{(1)}$, decomposed into spherical harmonics and scaled out by the coupling $(\ell/GM)^2$ in Fig. 6.3. We similarly present the $(1, 0)$ mode, which is non-radiative until merger, in Fig. 6.4. These mode excitations are consistent with the results that we saw in [146], where we evolved the $\vartheta^{(1)}$ in a variety of
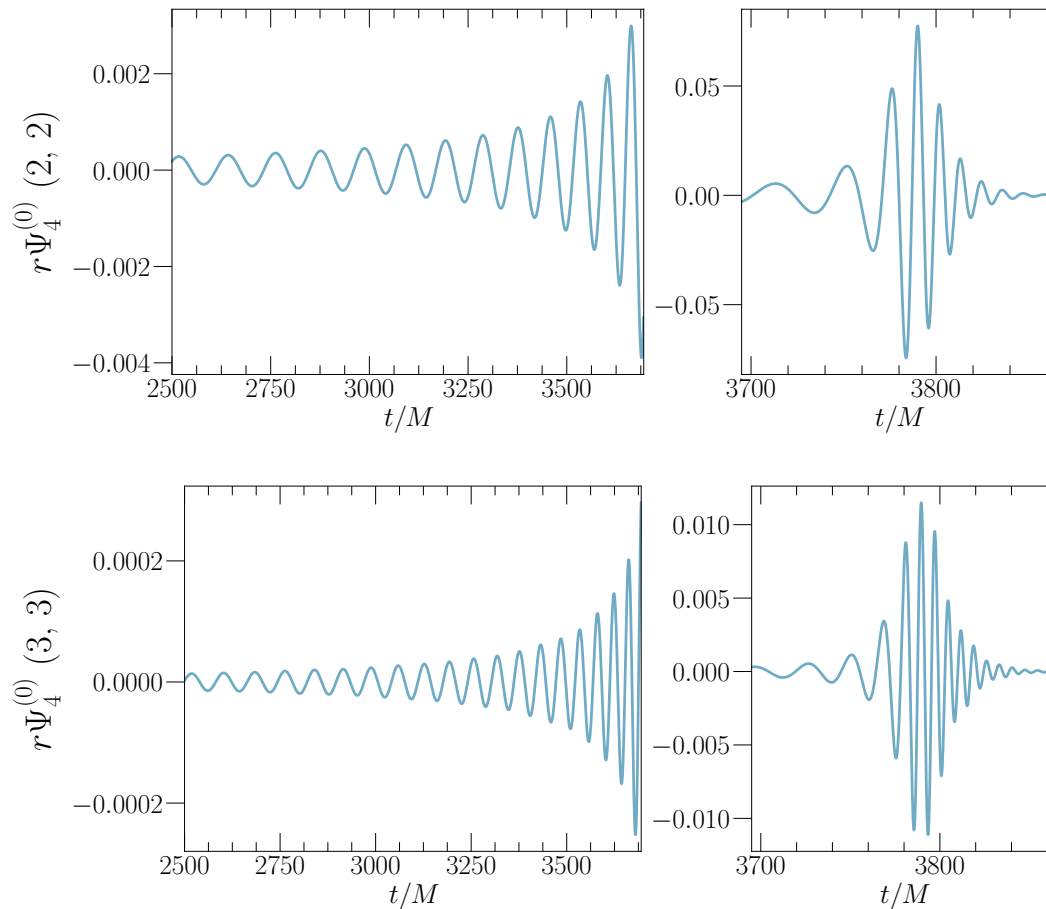
Figure 6.1: GR background gravitational radiation, given by the Newman-Penrose scalar $\Psi_4^{(0)}$, as a function of simulation coordinate time. We show the $(2, 2)$ mode (**top**), the dominant mode of the background gravitational radiation for this configuration (cf. Sec. 6.2) and the subdominant $(3, 3)$ mode (**bottom**). We separate the inspiral and ringdown parts in this figure in order to give a closer look at each behavior.

BBH backgrounds. These results are similarly consistent with the PN waveforms for $\vartheta^{(1)}$ computed in [212], where the $(l, l-1)$ modes are dominant. The numerical background Pontryagin density, $^*RR^{(0)}$, which sources $\vartheta^{(1)}$ similarly has excitations in the $(l, l-1)$ modes.

Regime of validity

Instantaneous regime of validity

Since we work in a perturbative scheme, there is a maximum value that the coupling ℓ/GM is allowed to take so that the leading-order correction to the spacetime metric
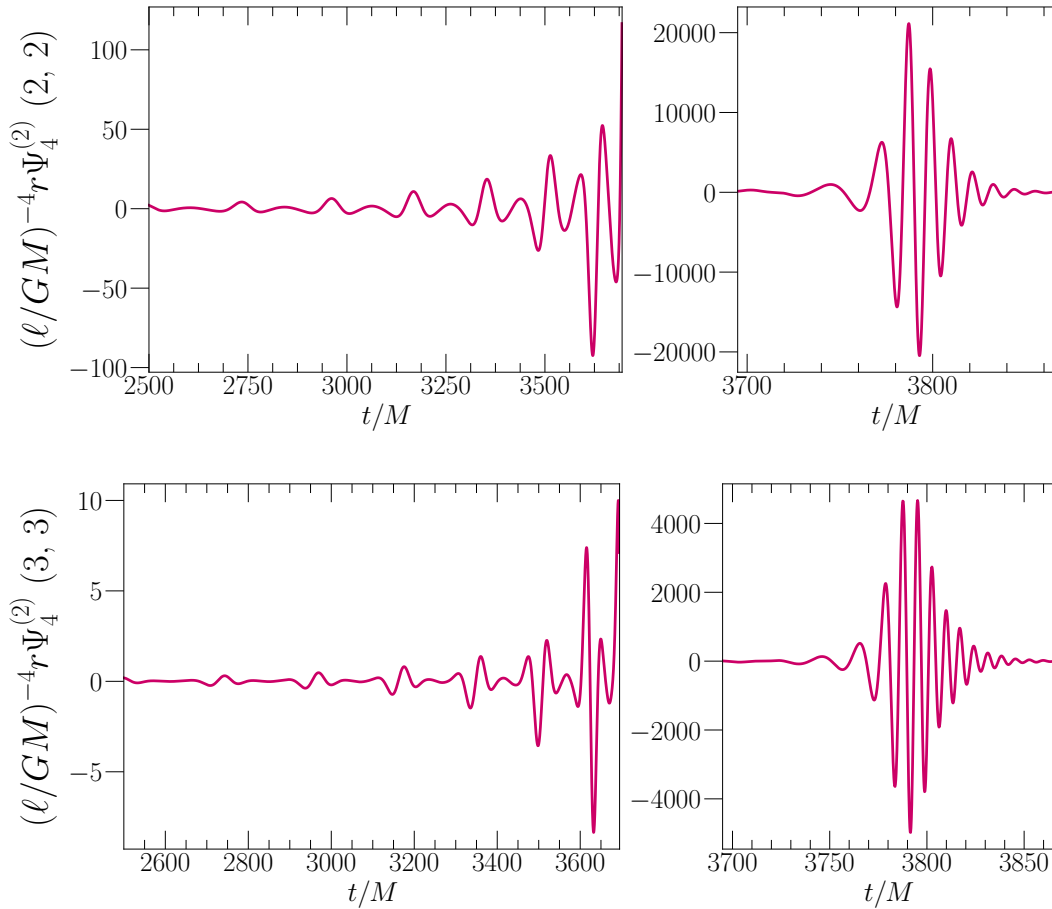
Figure 6.2: Leading-order dCS correction to the gravitational radiation, $\Psi_4^{(2)}$. We show the $(2, 2)$ mode (**top**), the dominant mode of the background gravitational radiation for this configuration (cf. Sec. 6.2), and the subdominant $(3, 3)$ mode (**bottom**). We separate the inspiral and ringdown parts in this figure in order to give a closer look at each behavior. Note that the (small) dCS coupling, $(\ell/GM)^4$ is scaled out, and to have physical meaning, these (large) values must be multiplied by appropriate values of this coupling constant (cf. Sec. 6.2).
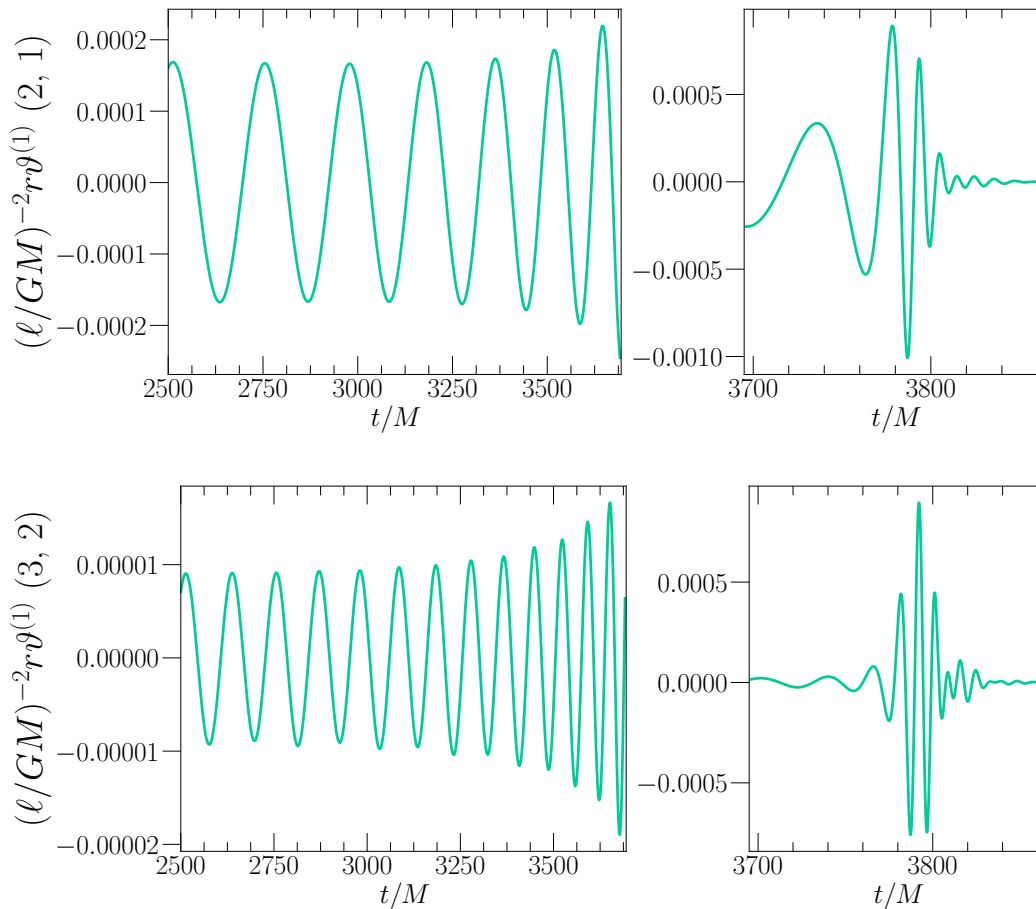
Figure 6.3: Leading-order dCS scalar field, $\vartheta^{(1)}$, decomposed into spherical harmonics. We show the dominant $(2,1)$ (**top**) and $(3,2)$ (**bottom**) modes. We separate the inspiral and ringdown parts in this figure in order to give a closer look at each behavior. Note that the dCS coupling, $(\ell/GM)^2$ is scaled out, and to have physical meaning, these values must be multiplied by appropriate values of this coupling constant.

is smaller than the background metric. This is known as an *instantaneous regime of validity* and is computed using the formalism in [145]. We show the regime of validity for this GW150914 simulation in Fig. 6.5. ℓ/GM attains its minimum value at merger, where strong-field effects play a significant role.

dCS modification to the inspiral

Let us take a closer look at the inspiral part of the $\Psi_4^{(2)}$ waveforms, which we zoom into in Fig. 6.6. In the GR case (cf. Fig. 6.1), there is one frequency governing the inspiral. However, we see in the $(2,2)$ mode of $\Psi_4^{(2)}$ that there are two frequencies (with two distinct peak amplitudes). In the $(3,3)$ mode, we see three frequencies
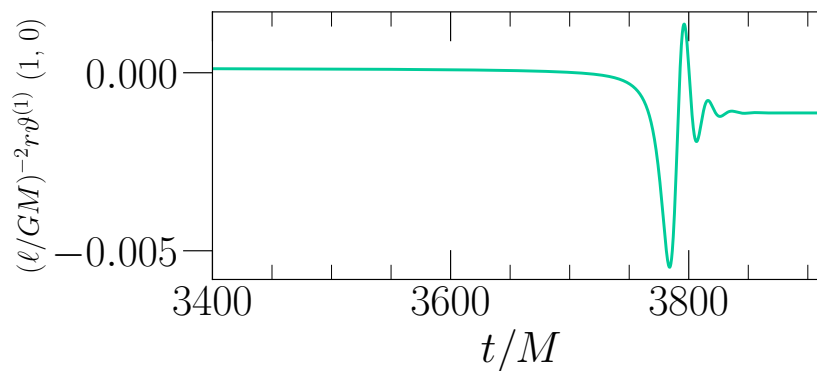
Figure 6.4: $(1, 0)$ mode of the leading-order dCS scalar field, $\vartheta^{(1)}$. As previously found in [146], this mode is non-radiative throughout the inspiral but shows a burst of dipolar radiation at merger.
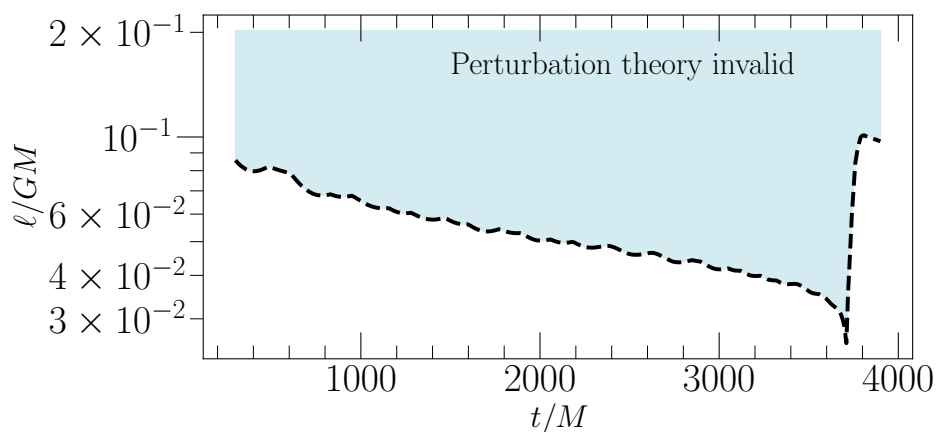
Figure 6.5: Instantaneous regime of validity as a function of simulation coordinate time. The vertical axis corresponds to the maximum allowed value of the dCS coupling constant ℓ/GM by perturbation theory. The dashed black line separates the region excluded by perturbation theory (light blue) from that allowed by perturbation theory (white). We see that the allowed value of ℓ/GM decreases as the system approaches merger.
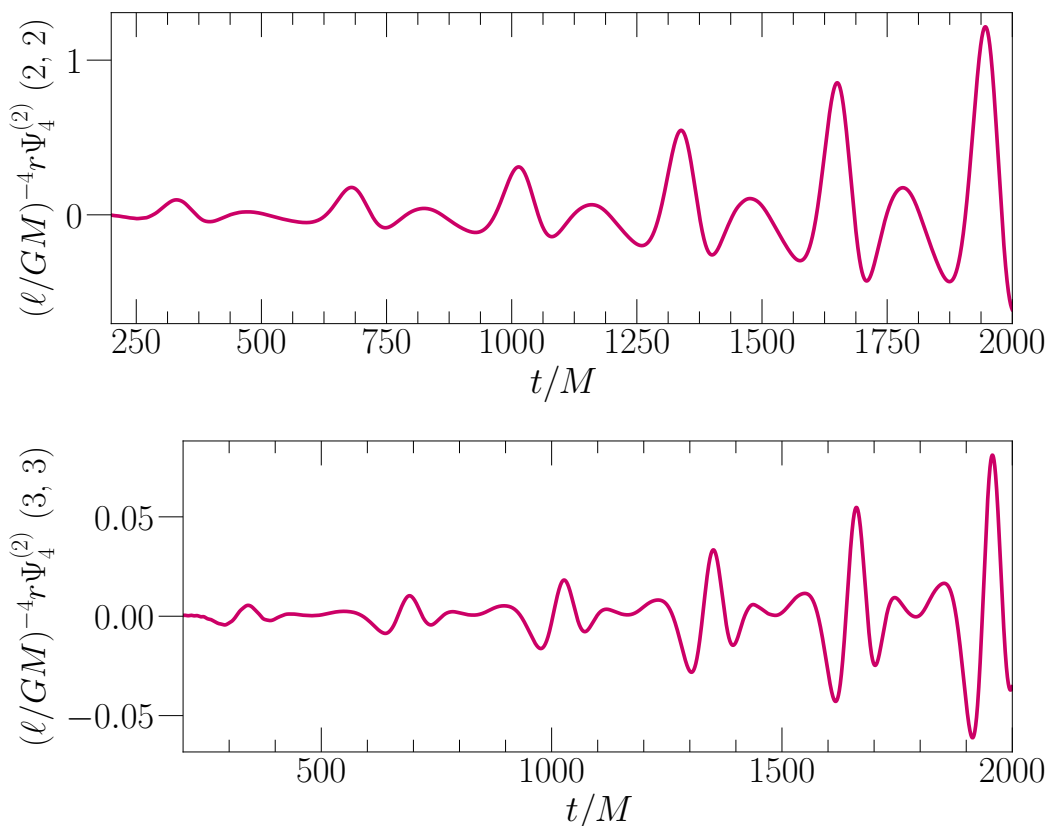
Figure 6.6: Zoomed-in view of the dominant modes of $\Psi_4^{(2)}$ during the inspiral. We see that the $(2, 2)$ mode (**top**) has two distinct frequencies, with a large peak followed by a smaller peak followed by a large peak again in a n A-B-A-B type pattern. The $(3, 3)$ mode (**bottom**), meanwhile, has three distinct frequencies, with a large peak followed by a small peak followed by a medium peak, in an A-B-C-A-B-C type pattern.

(with three distinct peak amplitudes).

These patterns look like characteristic beats, and we conjecture that the interference comes from the background and the scalar field, both of which source leading-order correction to the metric. In Fig. 6.7, we show the $\Psi_4^{(0)}$ waveform and the $\vartheta^{(1)}$ waveform overlaid on the $\Psi_4^{(2)}$ waveform for a given l. We see that the peaks in the $l = 2$ case align with a ratio of $1 : 2$, while in the $l = 3$ case, they align with a ratio of $2 : 3$. We see similar patterns in other spin configurations, for example with a mass ratio $q = 1$ and spins of 0.1 both in the $+\hat{z}$ direction.
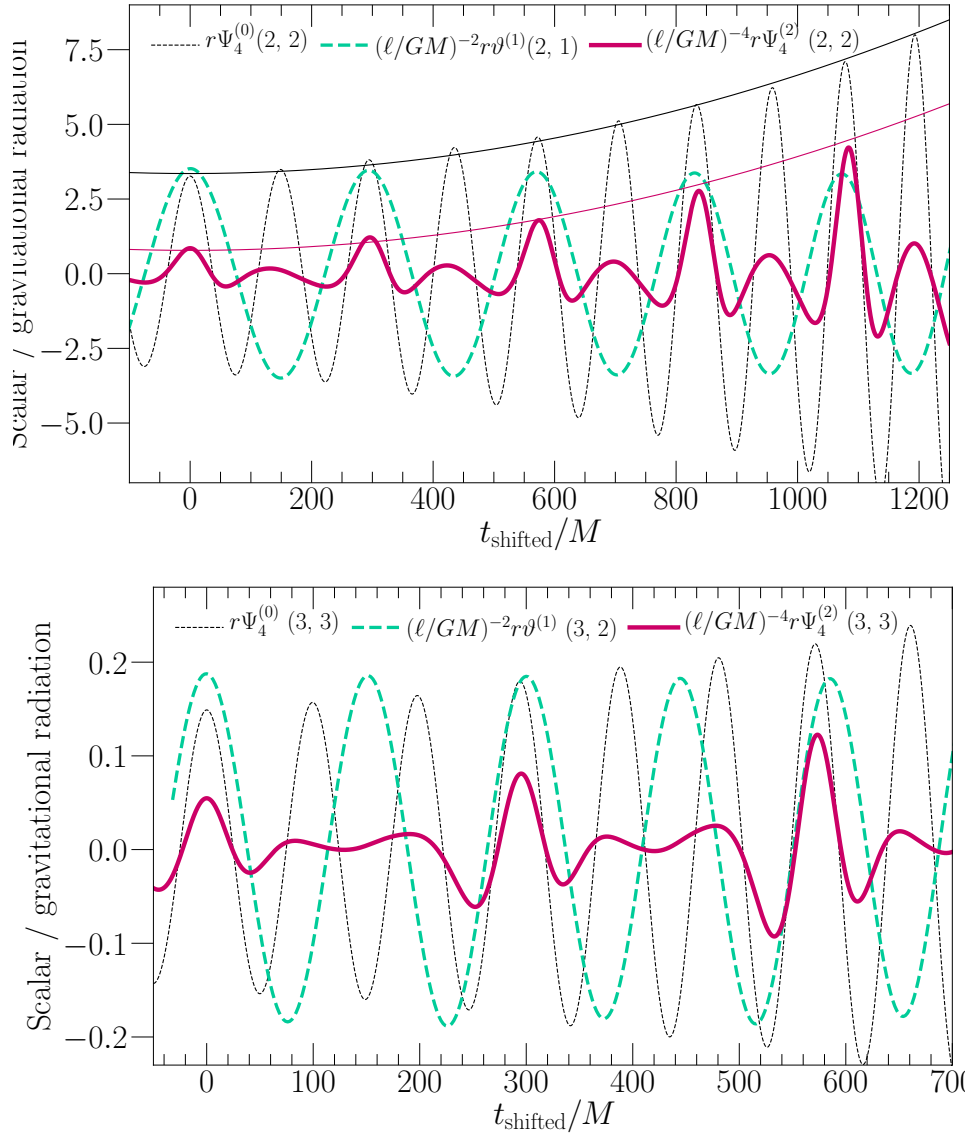
Figure 6.7: $\Psi_4^{(0)}$, $\vartheta^{(0)}$, and $\Psi_4^{(2)}$, aligned by peak and overlaid on one another. We show the $l = 2$ modes (with $m = 2$ for the gravitational waveforms and $m = 1$ for the scalar waveform) in the **top** panel, and the $l = 3$ modes (with $m = 3$ for the gravitational waveforms and $m = 2$ for the scalar waveform) in the **bottom** panel. We see an interference ratio of $1/2$ in the top panel, and $2/3$ in the bottom panel.

dCS modification to the ringdown

Let us now consider the dCS modifications to the ringdown portion of the waveform. Following the analysis detailed in [145], we fit $\Psi_4^{(0)}$ of each mode to obtain the background GR QNM frequency, $\omega^{(0)}$, and damping time, $\tau^{(0)}$. We similarly fit $\Psi_4^{(2)}$ using the functional form based on the linearization of a damped exponential to obtain $\omega^{(2)}$ and $\tau^{(2)}$, the leading-order dCS corrections to the QNM frequency
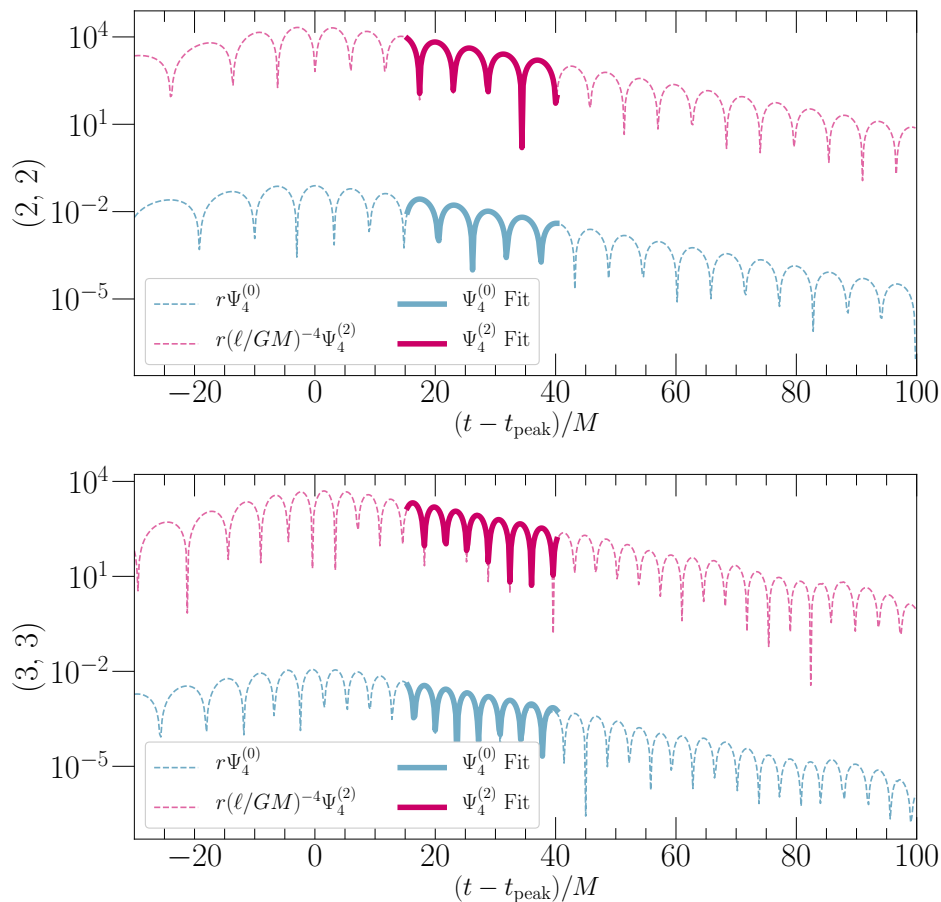
Figure 6.8: QNM fits to the post-merger gravitational radiation, for the dominant $(2, 2)$ (**top**) and $(3, 3)$ (**bottom**) modes. We show the GR background gravitational radiation, $\Psi_4^{(0)}$, by a dashed blue line, and show a fitted damped exponential by the overlayed solid, thick line. We show leading-order dCS correction to the post-merger gravitational radiation in the dashed pink line. The overlayed solid pink line shows our fit to the leading-order modification to the QNM spectrum (cf. [145] for the exact functional form).

and damping time. We show these fits for the dominant $(2, 2)$ and $(3, 3)$ modes of the gravitational radiation in Fig. 6.8.

6.3 Conclusion

In this study, we have revisited GW150914, the first LIGO binary black hole gravitational wave detection, and have computed the leading-order correction to the gravitational radiation in dynamical Chern-Simons gravity. This is the first numerical relativity simulation of a BBH system in a higher-curvature theory beyond general relativity through full inspiral, merger, and ringdown. We have found that

the leading-order dCS correction to the inspiral part of the waveform exhibits a frequency beating pattern sourced by the GR background and the dCS scalar field. We have additionally computed the leading-order dCS corrections to the ringdown QNM spectrum.

Future work in this program includes performing dCS simulations for further LIGO and Virgo detections [9]. In order to allow for beyond-GR parameter estimation, we also aim to produce surrogate model for the modified waveforms [118, 50]. The methods outlined in [146, 143, 142, 145] can be applied to other higher-curvature beyond-GR theories, including Einstein-dilaton-Gauss-Bonnet gravity, where the leading-order scalar field modification has previously been computed [207].

Chapter 7

ON CHOOSING THE START TIME OF BINARY BLACK HOLE RINGDOWN

[1]   Swetha Bhagwat et al. "On choosing the start time of binary black hole ringdowns". In: *Phys. Rev.* D97.10 (2018), p. 104065. DOI: 10.1103/PhysRevD.97.104065. arXiv: 1711.00926 [gr-qc].

Abstract

The final stage of a binary black hole merger is ringdown, in which the system is described by a Kerr black hole with quasinormal mode perturbations. It is far from straightforward to identify the time at which the ringdown begins. Yet determining this time is important for precision tests of the general theory of relativity that compare an observed signal with quasinormal mode descriptions of the ringdown, such as tests of the no-hair theorem. We present an algorithmic method to analyze the choice of ringdown start time in the observed waveform. This method is based on determining how close the strong field is to a Kerr black hole (*Kerrness*). Using numerical relativity simulations, we characterize the Kerrness of the strong-field region close to the black hole using a set of local, gauge-invariant geometric and algebraic conditions that measure local isometry to Kerr. We produce a map that associates each time in the gravitational waveform with a value of each of these Kerrness measures; this map is produced by following outgoing null characteristics from the strong and near-field regions to the wave zone. We perform this analysis on a numerical relativity simulation with parameters consistent with GW150914- the first gravitational wave detection. We find that the choice of ringdown start time of 3 ms after merger used in the GW150914 study [14] to test general relativity corresponds to a high dimensionless perturbation amplitude of $\sim 7.5 \times 10^{-3}$ in the strong-field region. This suggests that in higher signal-to-noise detections, one would need to start analyzing the signal at a later time for studies that depend on the validity of black hole perturbation theory.

7.1   Introduction

The quasi-normal mode (QNM) spectrum seen during the ringdown of a perturbed black hole (BH) is determined by the Teukolsky equation; it carries the signature

of the BH potential along with the BH horizon and asymptotic boundary conditions [194, 159, 195]. The recent detections of binary black hole (BBH) gravitational wave (GW) signals by LIGO (the Laser Interferometer Gravitational-Wave Observatory) [10, 5, 4, 16, 7] allow us to begin to probe this QNM signature [14]. The QNM spectrum in a gravitational-wave observation allows us to perform tests of the no-hair theorem. This theorem states that vacuum, asymptotically flat, stationary, axisymmetric, uncharged BHs are completely characterized by two parameters: the mass and the spin [132, 135, 76, 94, 111]. This allows us to constrain modified theories of gravity that violate the no-hair theorem [43, 216]. Observing the QNM spectrum in GWs can be used to validate the BH uniqueness theorem. This theorem states that the exterior geometry of a vacuum, asymptotically flat, stationary, axisymmetric, uncharged BH must be Kerr [132, 130].

However, testing the no-hair and uniqueness theorems relies on observing GWs from the QNM perturbative regime (without additional transients remaining from the inspiral). This requires an appropriate choice of start time of this regime.[1] Identifying this time in the signal is mathematically an ill-defined problem, since QNMs form an incomplete and non-orthogonal basis [141, 200]. Hence, the conventions for choosing the start time of the ringdown have varied in the literature. Berti et al. [44] and Baibhav et al. [33] chose the start time based on maximizing the energy contained in the QNM. London et al. [124] used 10 M after the peak of the dominant mode of Ψ_4 (the Newman-Penrose scalar that encodes outgoing radiation) for fitting to NR waveforms.[2] Kamaretsos et al. [110] chose 10 M after the peak luminosity of the dominant mode of the waveform, while Thrane et al. [199] proposed a loudness-dependent start time. In the GW150914 testing general relativity (GR) paper [14], different start times were used to perform the QNM analysis shown in Fig. 5 of that paper, and the results were consistent with GR when the start time was picked as 3 ms (or later) after the merger.

None of these methods use information from the strong field to motivate the start times. The strong field refers to the region near the BHs (typically within a radius of few M), where the scale of the curvature is much smaller than the wavelength of a gravitational wave. In this paper, we develop an algorithmic method for validating choices of the start time of ringdown using strong-field features. Specifically,

---

[1]While conventions in the literature vary, in this paper, by "ringdown", we explicitly mean the part of the post-merger gravitational waveform that can be described in terms of QNMs.

[2] Since vacuum GR is a scale-invariant theory, it is convenient to express distance and time in terms of source mass by setting $G = c = 1$. Explicitly, 1 $M = M_{BH} \times G/c^3$ seconds, where M_{BH} is the mass of the BH.

we measure the *Kerrness*, or closeness to Kerr, in the strong-field region of an NR simulation ringdown, and use null characteristics to map Kerrness onto the GW at asymptotic future null infinity, $\mathcal{I}^+$. We then demonstrate this method on a GW150914-like system. However, this method is generic, and this procedure can be carried out for any BBH system.

Determining Kerrness in the strong-field regime is non-trivial, since one needs a coordinate-invariant way of identifying a metric as Kerr. Necessary and sufficient conditions for a gauge-invariant characterization of local isometry to a Kerr manifold were proposed by García-Parrado Gómez-Lobo in [93].[3] We use this set of algebraic and geometric conditions to provide a numerical measure of Kerrness. Previous studies have used multipole moments of the BH apparent horizon [152], horizon spin measurement comparisons [178], or Petrov classification [34, 59, 150] to characterize ringdown spacetimes. Our work is the first set of conditions that completely characterizes a spacetime as isometric to a Kerr manifold. We study the violation of these conditions post-merger in the strong field of a BBH simulation.

Connecting the strong-field region to the wave zone is a challenge, as the simulation gauge is different from the gauge in which GWs are observed. There is no straightforward way to transform between these gauges. Furthermore, establishing simultaneity between events is not possible in the GR framework, and thus there is no direct map between an event in the strong-field region and a point on the waveform. We therefore devise a scheme to approximately associate the two frames. The association used in this study is of a cause-effect nature: we follow the outgoing null characteristics from the strong-field region to the wave zone using a Cauchy Characteristic Extraction scheme (CCE) [100, 101, 99], and associate events in the strong field to the wave zone. However, given that GR is a nonlinear theory, the source associated with a particular feature in the GW signal may not be well localized in the spacetime. Nevertheless, one would expect that the source dynamics that dominantly contribute to certain features in the waveform be localizable to a certain extent. Several such approximate localizations have been performed in linear perturbation theory [163, 63].

This paper is organized as follows. Sec. 7.2 presents the theoretical methods used in this paper, and Sec. 7.3 discusses their implementation in NR simulations. Sec. 7.4 then presents and discusses the results of applying these methods to an NR simulation with GW150914-like parameters. We conclude in Sec. 7.5. Figs. 7.15 and 7.22

---

[3]Throughout this text, *isometry* refers to the smooth mapping of manifolds equipped with metrics.

are the flagship figures, presenting our major results. The results are quantitatively summarized in Table 7.3.

Conventions

We work with the standard 3+1 decomposition of NR (cf. [40] for an introduction). In this paper, g_{ab} refers to the spacetime metric, n^a refers to the timelike unit normal vector, γ_{ij} refers to the spatial metric on each slice, D_i is the covariant derivative with respect to γ_{ij}, and K_{ij} refers to the extrinsic curvature. We set $G = c = 1$ and express all quantities in terms of M, the sum of the Christodoulou Masses of the two BHs at the start of the simulation. Latin letters at the start of the alphabet, $\{a, b, c, d\}$, refer to (4-dimensional) spacetime indices, while Latin letters in the middle of the alphabet, $\{i, j, k, l, m, n\}$ are (3-dimensional) spatial indices. We denote complex conjugation by an overbar (e.g. $\bar{A}$). To avoid confusion among the multiple meanings of "data" in this paper, we refer to the vacuum data $\{\gamma_{ij}, K_{ij}\}$ on a spatial slice simply as "a slice".[4] Similarly, rather than being purely geometric, a "slicing" in our case is a foliation equipped with a coordinate chart.

7.2 Theory

Characterizing strong-field Kerrness

First, we explain our method of measuring Kerrness in the strong-field region and develop a method to map it onto $\mathcal{I}^+$. Secs. 7.2 and 7.2 discuss theoretically characterizing Kerrness in the strong-field region, while Secs. 7.2, 7.2, and 7.2 discuss mapping strong-field information onto the wave zone via null characteristics.

Overview and historical background

Our overall goal in this section is to evaluate *Kerrness*: how close a numerical BH ringdown spacetime is to being locally isometric to the Kerr spacetime. In order to evaluate the Kerrness of a spacetime, we first need a set of theoretical conditions to evaluate whether a spacetime *is* isometric to Kerr. We can then turn these conditions into a set of *measures*, where deviation from zero indicates being farther from being locally isometric to Kerr. In a numerical simulation, one would evaluate these measures on spatial slices of a simulation. To characterize Kerrness in the strong-field region, one needs local quantifiers evaluated close to the BH, as opposed to looking at regions far away, which are contaminated by gravitational radiation.

---

[4]*Vacuum data* means that the spatial metric, γ_{ij}, and the extrinsic curvature K_{ij} satisfy a set of constraint equations corresponding to the decomposition of the vacuum Einstein equations.
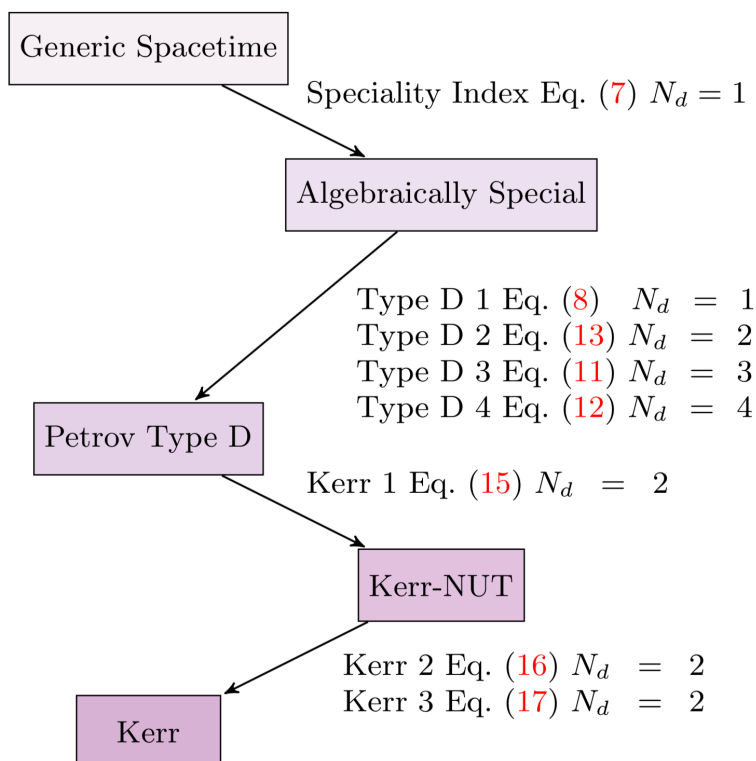
Figure 7.1: The set of conditions for a slice to be locally isometric to Kerr. The nodes refer to the resulting type of spacetime when the conditions on each edge, given by their name and equation in the text, are met. For example, a spacetime must meet all four of the conditions specified in the edge from Algebraically Special to Petrov Type D to belong to the type D subset of algebraically special spacetimes. In numerical applications, the failure of these Kerrness conditions to be met gives a set of respective Kerrness measures, where larger measures denote greater deviation from Kerr. For each measure, we give N_d, the number of numerical derivatives beyond the first derivatives of the metric needed to evaluate it, which corresponds to the numerical noise level in the measure, with higher derivative powers giving more numerical noise.

Consequently, we seek a point-wise measure and do not use global measures on a slice such as those proposed in [30, 32, 31].

Uniquely characterizing a spacetime as Kerr has been historically challenging—until recently, one could only classify spacetimes up to a Petrov type, which gives a weaker classification that admits several manifolds besides Kerr. The Petrov classification uses algebraic properties of the Weyl tensor C_{abcd} based on the four principal null directions (PNDs), by solving the eigenbivector problem (cf. [187] for a review)

$$\frac{1}{2}C^{ab}{}_{cd}X^{cd} = \lambda X^{ab}, \tag{7.1}$$

where eigenbivectors $X^{ab}_{(\alpha)}$ have eigenvalues $\lambda_{(\alpha)}$. The degeneracies of the PNDs give a unique algebraic classification of a spacetime. A spacetime with no repeated PNDs is fully general (Petrov Type I). A spacetime with at least one repeated PND is *algebraically special*. The Kerr metric belongs to a particular class of algebraically special spacetimes, the set of type D spacetimes, which have two double PNDs. A necessary condition for the manifold to be locally isometric to Kerr is to be type D.

Campanelli et al. [59] used this approach to analyze a numerical BBH ringdown. They determined the degeneracies between the PNDs by solving the eigenbivector problem and measuring the difference between eigenvalues. Their analysis found that the spacetime first numerically settled to type II, which has only one double PND, and then to type D. Owen [150] later showed that this measure was sensitive to the choice of tetrad used to compute the Weyl scalars needed to solve the characteristic equation. He proposed a new measure, less-sensitive to the choice of tetrad, and showed that the spacetime settled to type D without first settling to type II.

A type D spacetime can then be shown to be locally isometric to Kerr through additional conditions. Kerr belongs to the Kerr-NUT subset of type D spacetimes. One needs to show that a spacetime is Kerr-NUT and then constrain the acceleration and the NUT parameters. We give more information on Kerr-NUT spacetimes and the various parameters in Appendix 7.A. Ref. [59] investigated the asymptotic behavior of the acceleration and the NUT parameter on a BBH simulation and showed they were constrained to be those of Kerr.

In this study, we do not solve the eigenbivector problem, but rather use a set of local algebraic and geometric conditions recently proposed by García-Parrado Gómez-Lobo [93] to show that a spacetime is locally isometric to Kerr. These conditions

are formulated in a fully covariant way and thus avoid the complications in [59] and [150] due to tetrad choice.

Necessary and sufficient Kerrness conditions

To characterize a spatial Cauchy slice as isometric to Kerr, we first check if the slice is algebraically special. Next, we use two geometric conditions to check for the existence of Killing vectors (KVs) on the slice, and we impose two algebraic conditions to verify that the slice containing the KVs is type D. Then, we check the properties of the KVs and further classify the slice into the Kerr-NUT subfamily. Finally, imposing conditions on the acceleration and NUT parameters, we completely characterize the slice as locally isometric to Kerr. These conditions are summarized in Fig. 7.1.

All algebraic conditions are expressed in terms of electric and magnetic parts of the Weyl tensor, C_{abcd}, as

$$E_{ab} \equiv +C_{acbd}n^c n^d \,, \tag{7.2}$$

$$B_{ab} \equiv -{}^*C_{acbd}n^c n^d \,, \tag{7.3}$$

where the left dual of the Weyl tensor is defined as ${}^*C^{abcd} \equiv \frac{1}{2}\epsilon^{abef}C_{ef}{}^{cd}$. For a vacuum spacetime, these spatial tensors can be more readily evaluated on a slice as

$$E_{ij} = K_{ij}K^k{}_k - K_i{}^k K_{jk} + {}^{(3)}R_{ij} \,, \tag{7.4}$$

$$B_{ij} = -\epsilon_{kl(i}D^k K^l_{j)} \,, \tag{7.5}$$

where ${}^{(3)}R_{ij}$ is the spatial Ricci tensor evaluated from γ_{ij}. These can be combined into a complex quantity as

$$\mathcal{E}_{ij} \equiv \frac{1}{2}\left(E_{ij} - iB_{ij}\right) \,. \tag{7.6}$$

In [93], the algebraic condition for a slice to be locally algebraically special is given in Eq. 85 as

$$\textbf{Speciality Index: } 6b^2 - a^3 = 0 \,, \tag{7.7}$$

where

$$a \equiv 16\mathcal{E}_{ij}\mathcal{E}^{ij} \,,$$

$$b \equiv -64\mathcal{E}^k_i\mathcal{E}^{ij}\mathcal{E}_{jk} \,.$$

This condition is equivalent to the speciality index in the Petrov classification literature (cf. Eq. 4.13 of [187]).

Recall that algebraic speciality corresponds to having one double PND, and hence is a weaker condition than being type D, which corresponds to having two double PNDs. A *necessary* algebraic condition for a slice to be type D is given in Theorem 4 of [93] as

$$\textbf{Type D 1}: \frac{a}{12}\gamma_{ij} - \frac{b}{a}\mathcal{E}_{ij} - 4\mathcal{E}_i{}^k\mathcal{E}_{jk} = 0, \tag{7.8}$$

which makes use of 4-dimensional algebraic conditions proven in [86] and orthogonally splits these onto the spatial slice. Here we have called the condition "Type D 1" purely for bookkeeping purposes, in order to label each of the type D conditions.

The three *sufficient* conditions for a slice to be type D consist of two geometric conditions involving KVs and one algebraic condition which also includes the KV. As proven in Theorem 2 of [93], a vacuum type D spacetime has a complex KV field ξ^a which satisfies an algebraic condition

$$\Xi_{ab} = \frac{27}{2}w^{\frac{11}{3}}\xi_a\xi_b, \tag{7.9}$$

where Ξ_{ab} is derived from the Weyl tensor, and

$$w \equiv -\frac{b}{2a}. \tag{7.10}$$

However, one must show that a KV field exists on the slice in the first place, and then that it satisfies the properties given in Eq. (7.9). The necessary and sufficient geometric conditions for a slice to contain a KV field are known as Killing Initial Data (KID), and for a vector $\xi^a = Yn^a + Y^a$, are given as

$$\textbf{Type D 3}: D_{(i}Y_{j)} - YK_{ij} = 0, \tag{7.11}$$

$$\textbf{Type D 4}: D_iD_jY - \mathcal{L}_{Y^l}K_{ij} \tag{7.12}$$

$$- Y(^{(3)}R_{ij} + KK_{ij} - 2K_{il}K^l_j) = 0.$$

Satisfying these conditions guarantees that a KV field exists on the slice—note that these two conditions say nothing so far about type D.

We can then relate this KV field ξ^a to the condition on the KV in a type D spacetime given in Eq. (7.9) by requiring

$$\textbf{Type D 2} : \mathcal{E}_{pj}(\Omega^2 + \Omega_l \Omega^l), \tag{7.13}$$

$$- 2\Omega^l \left(i\mathcal{E}^k_{(p} \varepsilon_{j)lk}\Omega + \mathcal{E}_{l(p}\Omega_{j)} \right)$$

$$+ \gamma_{pj} \left(\frac{1}{2} w\Omega^2 + \Omega^l \left(-\frac{1}{2} w\Omega_l + \mathcal{E}_{lk}\Omega^k \right) \right)$$

$$+ \frac{1}{2} w\Omega_p \Omega_j - \frac{27}{2} w^{11/3} Y_p Y_j = 0,$$

where Eq. (7.13) is the orthogonal splitting of Eq. (7.9), and

$$\Omega_j \equiv D_k w, \tag{7.14}$$

$$\Omega \equiv K^{jk}\mathcal{E}_{jk} - wK - 16i\frac{w}{a}\mathcal{E}^{jk}\varepsilon_{kpl}D^l\mathcal{E}^p_j,$$

$$Y \equiv (w\Omega_j\Omega^j + 2\mathcal{E}_{jk}\Omega^j\Omega^k)^{1/2}w^{-11/6},$$

$$Y_j \equiv \frac{\Omega(2\mathcal{E}_{jk}\Omega^k + w\Omega_j) - 2i\varepsilon_{jkl}\mathcal{E}_p{}^l\Omega^p\Omega^k}{27Yw^{11/3}}.$$

This procedure is shown in Theorem 6 of [93].[5]

Type D 3 and Type D 4 are independent geometric conditions that depend on the complex KV ξ^a and show that the slice is KID. Type D 1 is a purely algebraic condition that informs us of the behavior of the PNDs. Type D 2 ties in the algebraic and geometric conditions, thereby completing the classification into type D. Speciality Index, meanwhile, is an independent algebraic condition.

In order to then show that an algebraically special, type D slice is locally isometric to Kerr, we must also show that it belongs to the Kerr-NUT subset of type D spacetimes. Kerr-NUT spacetimes have the symmetry property of two commuting KVs [187] - one spacelike and timelike, and thus if we impose this geometric condition on KV ξ^a as defined above, we arrive at the condition given in Theorem 8 of [93],[6]

$$\textbf{Kerr 1} : \text{Im}(Y\bar{Y}_j) = 0. \tag{7.15}$$

In order to further show that a slice is locally isometric to Kerr, we must place constraints on the parameters characterizing Kerr-NUT spacetimes. We summarize

---

[5]The Type D 2 condition has a $+$ in the second term where [93] has a $-$. The sign error has been confirmed by the author of [93]. Similarly, The factor of $\frac{1}{27}$ in the definition of Y_j is not included in [93], but is in the corresponding Mathematica notebook [92].

[6]However, this has a typographical error (confirmed by the author [92]), and should include $\bar{Y}_j$, the complex conjugate, as given Eq. (7.15).

the parameters involved in Type D spacetimes in Appendix 7.A. We require that λ, the NUT parameter, vanish, and ϵ, which is related to the acceleration of the BH, be greater than zero. These conditions are given in Theorem 8 of [93] as

$$\textbf{Kerr 2} : Z^3 \bar{w}^8 \in \mathbb{R}^- , \tag{7.16}$$

for the condition $\lambda = 0$, where $Z \equiv \nabla_a w \nabla^a w$, and

$$\textbf{Kerr 3} : -|Z|^2 + 18\text{Re}(w^3 \bar{Z}) > 0 , \tag{7.17}$$

for $\epsilon > 0$. However, the above expression only holds outside of the ergoregion [92] in Kerr. This condition is thus impractical to use in the this study, since it involves finding the ergoregion, and masking this region would introduce high levels of numerical error within a spectral code.

Thus, for a slice to be locally isometric to Kerr, it must satisfy all of the above conditions, which are summarized in Fig. 7.1. Since the vacuum spacetime at the start of a ringdown may be fully general, the left hand sides of the Kerrness conditions will not necessarily be zero on some slices. Instead, the Kerrness conditions turn into a set of *Kerrness measures*, where larger deviation from zero indicates a larger deviation from being isometric to Kerr.

Connecting strong-field information to $\mathcal{I}^+$
Motivation

Having characterized the Kerrness in the strong-field region, we connect this information to the GWs at $\mathcal{I}^+$. We develop a framework to map the evolution of the Kerrness measures computed during a post-merger simulation to the evolution of the post-merger waveform in the asymptotic frame. This provides a procedure to validate the choices of start time of ringdown when analyzing a gravitational-wave signal.

Just after the two BHs merge, the newly formed BH is expected to be highly distorted. The dynamics of the BH can be explained only via a full numerical simulation. At $\mathcal{I}^+$, where the GWs are observed, these strong-field dynamics are responsible for features in a small region close to the peak of the GW amplitude. Once the excitation amplitude in the strong-field region decays to a level when linear perturbation theory is valid the spacetime dynamics and the associated waveform is governed by the Teukolsky equation [194, 159, 195]. At $\mathcal{I}^+$, the waveform appears as a sum of exponentially damped sinusoids with a specific QNM frequency spectrum

Figure 7.2: Prescription for connecting the strong-field information to the asymptotic frame dynamics. The colored cylinder represents the region of spacetime that is evolved by the Cauchy code. The vertical green line within the cylinder indicates the direction of coordinate time. The horizontal lines represent time slices. The details of the location of time slices depend on the gauge choice. The pink boundary of the cylinder depicts the worldtube from where the CCE is performed. The purple lines with unit slope illustrate the null characteristics along which the information on the worldtube is propagated to (the solid blue line) $\mathcal{I}^+$. In our procedure of associating information in the source frame with the asymptotic frame, we identify all the points along a characteristic by an equivalence. The solid green line in the cylinder acts as a source to the waveform feature at τ_0 observed at $\mathcal{I}^+$.

(with power-law tails that are usually very weak). Beyond this rough picture, the association of the specifics in the strong-field dynamics to the waveform is not well understood, especially during the merger and post-merger phases.

Understanding this association is crucial because several strong-field tests of GR rely on BH perturbation theory and thus, on identifying the perturbative regime in the waveform. These tests include the no-hair theorem test, consistency tests of the QNM spectrum with the inspiral parameters, and the area theorem test. The start of ringdown in the GW is mathematically ill-defined as damped sinusoids form an incomplete and non-orthogonal basis [141, 200]. Therefore, it is important that we validate the choices of start times in the data analysis of ringdown guided by the strong-field information, where the validity of perturbation theory can be better understood.

Conceptual challenges

Mathematically, GR being a non-linear theory does not allow for unambiguous localization of sources of GWs. However, to a certain extent, one expects that the dominant source of a particular feature in the wave zone be localizable to a relatively small region of the spacetime in the past light cone. For instance, studies like [163, 113] identify the dominant source for the peak of the waveform during the plunge of a test particle into a Schwarzschild BH with the particle crossing the light-ring.[7] Furthermore, the last few cycles of the BBH GW signal are associated with the dynamics of a linearly perturbed BH [197, 36, 60]. However, one needs to bear in mind that these studies are performed using linear perturbation theory where such localizations are better defined. For example, if one adds a massive particle instead of a test particle in the former case and makes the problem non-linear, one would get some additional source contributions from self-force, thus making the source localization trickier.

In the case of BBH post-merger, identifying specific events as a source of the features in the waveform cannot be done unambiguously owing to the non-linear dynamics from merger. However, drawing intuition from analytical linear perturbation theory, we expect the region within the support of the analytical effective BH potential to contribute significantly to the waveform at $\mathcal{I}^+$. Thus, we argue that even in a non-

---

[7]The light-ring is the orbit of a massless particle around the BH, which corresponds to the peak of the BH potential located at $3\,M$ in Boyer-Lindquist coordinates for a Schwarzschild BH.

linear case, a small region in the spacetime around the BH containing the strong-field dynamics, can be associated as a dominant source of features in the GW.

Another challenge in performing this association is that the notion of simultaneity in GR is not absolute, which means that all spacelike slicings of the spacetime are equally valid. In numerical simulations however, we have to make a gauge choice. In our case, this choice is made by the Cauchy evolution code. The spatial features corresponding to a particular timeslice are gauge dependent. We choose to monitor the Kerrness on a spatial coordinate 2-sphere in the strong-field region, instead of computing a volume integral over the source region in a timeslice.[8]

We attempt to present a mathematically rigorous validation for the start time of RD. However, we caution the reader that this association may be affected by gauge choices, and in particular, is dependent on the radius of the 2-sphere we monitor, especially in the strong-field region.

Forming a source-effect association via null characteristics

Given these challenges, we propose the following association scheme. We evaluate the Newman-Penrose scalar Ψ_4, which measures the outgoing gravitational radiation, on a given slice of the simulation. Ψ_4 is obtained from the Weyl tensor as

$$\Psi_4 \equiv -C_{abcd}k^a\bar{m}^b k^c \bar{m}^d \,, \tag{7.18}$$

where k^a is a radially ingoing null vector, and the complex vector m^a is formed from spatial vectors orthogonal to the radially ingoing and outgoing null vectors (cf. [40] for more detail). By looking at Ψ_4 evaluated on the simulation, we infer a 2-sphere radius that lies within the strong-field region, containing and generating significant radiative fields. This 2-sphere acts like an effective source for the GW seen at $\mathcal{I}^+$. We evaluate a surface integral of the Kerrness measures at each time slice during the ringdown on this 2-sphere. Then, we connect the evolution of the Kerrness measures on this surface to the associated features in the GW by following the outgoing null characteristics emanating from this 2-sphere. The details of this procedure are described below.

The GWs emanating from a source propagate to $\mathcal{I}^+$ along outgoing null rays (since the spacetime is curved, a small portion of GWs also travel inside the light cone). We utilize this in constructing an association between strong-field information and

---

[8]By doing so, the gauge effect is limited to uncertainty of picking the 2-sphere, thereby avoiding contribution of gauge effects through the entire volume region.

the features on the GW. We associate a feature on the GW to a 2-sphere in the strong-field region at a given time (in the simulation coordinates) if they lie on the same outgoing null hypersurface. This 2-sphere can thus be interpreted as an effective source producing the point on the waveform. The choice of 2-sphere should be close to the region generating GWs rather than farther out, as we are interested in monitoring the region with a strong support of the BH potential. Measuring Kerrness of such a surface would give an insight into validity of perturbation theory in the region that acts as a dominant source of the GWs.

A framework that is naturally suited for such connections is Cauchy Characteristic Extraction (CCE). CCE foliates the spacetime into a family of outgoing null hyper-surfaces and formulates Einstein's equations as an initial-boundary value problem in a 2+2 characteristic decomposition. The mathematical details of this formalism can be found in [48, 99]. CCE performs a characteristic evolution using the metric data on a timelike boundary of the Cauchy region (known as the worldtube), and propagates it to $\mathcal{I}^+$. At $\mathcal{I}^+$ the radiation information is obtained as the Bondi news function $\mathcal{N}$ [55]. The GW strain can then be obtained from $\mathcal{N}$ by a time integration,

$$h(t) = \int_{-\infty}^{t} \mathcal{N}(t')dt' . \tag{7.19}$$

A key feature of this scheme is that each point at $\mathcal{I}^+$ corresponds to a null hypersur-face, which in turn corresponds to a particular (coordinate) time label on the world tube.

We can thus associate the average of the Kerrness on a 2-sphere to spherical har-monic modes at $\mathcal{I}^+$. We choose to average the quantities, rather than modally decompose them, in order to obtain a single number, which makes the interpretation and presentation of results easier. We illustrate this in Fig. 7.2. Here, τ_0 marks a specific timeslice (horizontal solid green line) in the Cauchy evolution region in a gauge chosen by the Cauchy code. The intersection of this timeslice with the world-tube boundary is a spatial (topological) 2-sphere. The information on this 2-sphere is propagated to $\mathcal{I}^+$ along a null hypersurface labeled (solid purple line) as τ_0. The radiation feature carries the time stamp τ_0 at $\mathcal{I}^+$, which, roughly speaking, arises from the 2-sphere defined by the intersection of timeslice τ_0 and the worldtube in the simulation and thus, we identify them to be associated.

Having established a framework to associate information on a 2-sphere in the strong-field region to the waveform at $\mathcal{I}^+$, we now discuss the choice of the 2-sphere

used in this study. Motivated by analytical studies of test particles plunging into Schwarzschild BHs [163, 113], one might want to inspect the 2-sphere associated with the peak of effective BH potential. However, locating it during the merger in a numerical simulation is non-trivial (if at all well-defined) and is beyond the scope of this paper. Furthermore, CCE cannot be performed from an arbitrarily small worldtube close to the horizon. This limitation arises because CCE is formulated in light-cone coordinates. In the regions very close to the horizon, light-cone coordinates can form caustics, leading to coordinate singularities. Because of these constraints, we choose the worldtube radius corresponding to the smallest coordinate 2-sphere that is accessible to our procedure, but we visually verify that it contains strong-field dynamics by plotting Ψ_4 in Figs. 7.16.

Inferring perturbation amplitudes via Kerrness
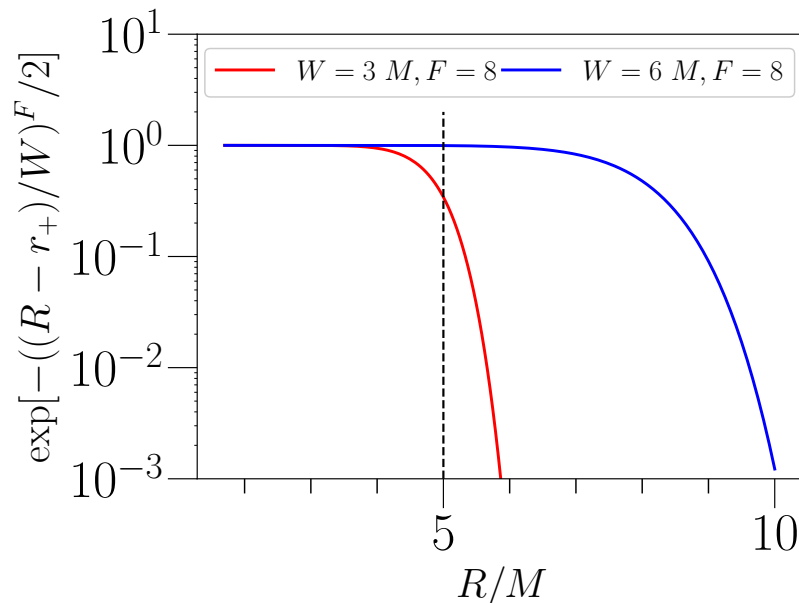
Figure 7.3: Envelope function from Eq. (7.21), for two choices of width and falloff parameters, $\{W, F\}$. We show how the envelope parameters affect an extraction radius of $R = 5\,M$ (marked by the dashed black line). For our chosen values of $\{W = 6\,M, F = 8\}$, the envelope is at ~ 1 and $R = 5\,M$, while for $\{W = 3\,M, F = 8\}$, the envelope affects the perturbation amplitude at $R = 5\,M$. We have checked that using a smaller envelope does not change the qualitative behavior of our results.

In order to give physical meaning to the values of the Kerrness measures outlined in Sec. 7.2, we can compare their values (on a post-merger spacetime, for example) to those on a single BH with a known analytic perturbation. Specifically, we can compare the Kerrness measures during ringdown to those on a $l = m = 2$ spheroidal
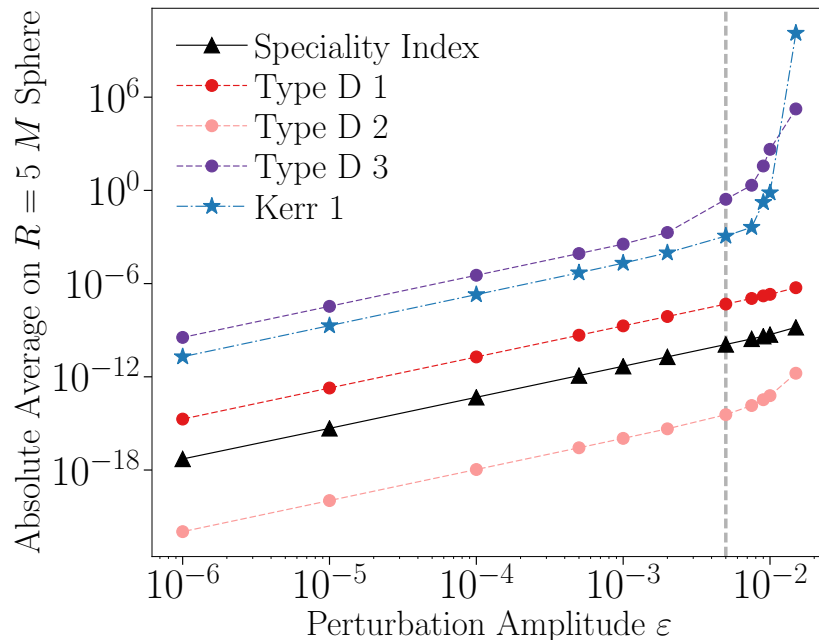
Figure 7.4: Behavior of absolute Kerrness measures with perturbation amplitude ε. We compute this on an $l = m = 2$ QNM perturbed Kerr BH with the same mass and spin as the final remnant in the BBH simulation we consider in this paper. We average each measure on a coordinate 2-sphere of $R = 5\,M$. Note that we do not plot Type D 4 due to the high level of numerical noise in the measure, but it behaves similarly to Type D 3. The behavior is initially quadratic with ε for all measures. At larger amplitudes $\varepsilon \geq 5 \times 10^{-3}$, Type D 2, D 3, D 4 and Kerr 1 show higher-power dependence, and hence non-linearity. We show this $\varepsilon_{\text{crit}} \sim 5 \times 10^{-3}$ by a dashed vertical line. The lines between the points are only used to visually connect them (rather than being fits).

QNM perturbed Kerr BH of the same final mass and spin, with varying dimensionless perturbation amplitude ε. This will provide a true physical comparison, as linearly-perturbed type D spacetimes are fully generic type I, and thus the Kerrness measures on the perturbed spacetime are expected to be nonzero [26]. This comparison will allow us to infer the perturbation amplitude to which a particular coordinate time corresponds. We can then map this inferred amplitude onto the waveform using the methods in Sec. 7.2.

Given the initial masses and spins, we can generate initial data for a perturbed BH (including all the relevant modes). In this study, we choose to use the initial data consisting of only (2,2) mode as this is the dominant mode of the system. We have fitting formula for relative mode amplitudes in the perturbative regime, and thus we can extract an overall amplitude factor and call that ε.

Kerrness measures on perturbed metrics

The perturbed metric is generated on a single slice for each ε by solving the Teukolsky equation and reconstructing the metric perturbation h_{ab} using a Hertz-potential formalism [213, 125] (cf. [197] for a general review). The resulting perturbation h_{ab} is then added to the background metric to give

$$\tilde{g}_{ab} = g_{ab}^{\text{Kerr}} + \varepsilon h_{ab}, \tag{7.20}$$

which is correct to linear order. The constraint equations for the metric $\tilde{g}_{ab}$ are then solved to give a fully constraint-satisfying metric g_{ab} in Kerr-Schild coordinates using the extended conformal thin-sandwich formalism (cf. [40]). This introduces some nonlinear effects into the perturbed metric. Furthermore, the asymptotic radial behavior leads to blow-up of the solution at large radii [147]. Thus, before solving for g_{ab}, we multiply h_{ab} by an envelope of the form

$$f_{\text{Envelope}}(R) = \exp[-((R - r_+)/W)^F/2], \tag{7.21}$$

where r_+ is the radius of the outer horizon of the BH, W is the width, and F is the falloff of the envelope. Since the mapping of the Kerrness measures onto the waveform occurs at $R = 5\,M$, as will be discussed in Sec. 7.3, and the horizon typically has outer radius $R_+ \sim 1.7\,M$, we choose $W = 6\,M$ to give $f_{\text{Envelope}}(5\,M) \sim 1$ so as to minimally affect the perturbation at the extraction radius. Additionally, we choose $F = 8$ in order to counteract the steep growth of the perturbation with radius. We plot the envelope in Fig. 7.3. In practice, the metric perturbation is generated using an extension of the code used in East et al. [78], but with the QNM solution rather than an ingoing GW solution and using the full radial dependence.

Fig. 7.4 shows the behavior of the Kerrness measures averaged on a 2-sphere of $R = 5\,M$ with ε on a BH of the same final mass and spin as the simulation outlined in Sec. 7.3. The theoretical behavior of the Kerrness measures with perturbation amplitude is unknown [92, 107], and thus this is the first (numerical) computation of the behavior. We first check that the measures converge to finite values with numerical resolution, thus representing real physical values. The Kerrness measures increase quadratically for small ε, then show higher-order effects for large ε. Type D 2 grows to (best-fit) quartic, Type D 3 and Kerr 1 become cubic, while Speciality and Type D 1 remain quadratic at $\varepsilon \sim 10^{-2}$, the largest amplitude for which we can solve for g_{ab} before violating the constraints. In particular, the steep increase of the Type D 3 and Kerr 1 measures, which come from geometric conditions on KVs,

indicates that at large enough perturbation amplitude, the slice fails to have even an approximate KV. Since the perturbation we are introducing is not axisymmetric, it makes sense that at large ε the slice loses this KV symmetry.

The linear perturbation regime corresponds to the region where the measures increase quadratically with ε, while the non-linear regime approximately begins where one can see higher-power behavior. In this case, we see the transition from quadratic behavior around $\varepsilon_{\text{critical}} \sim 5 \times 10^{-3}$, suggesting that this is the approximate start of the nonlinear regime. In practice, one can normalize all of the ε values in this paper by $\varepsilon_{\text{critical}}$. However, we do not do this for readability of the figures.

However, there are some sources of error in the g_{ab} analysis. The areal radius of the perturbed metric on a coordinate 2-sphere of radius $R = 5\,M$ changes slightly with perturbation amplitude, changing by $10^{-2}\,M$ between $\varepsilon = 10^{-6}$ and 10^{-2}. Thus, a coordinate-radius measure comparison does not happen on exactly the same 2-sphere. Solving for g_{ab} changes the values of the mass and spin from the parameters used in creating g_{ab}^{Kerr}. At the largest perturbation amplitude $\varepsilon = 10^{-2}$, the dimensionless spin changes by .003, while the mass changes by .008 M. We keep these errors in mind when computing the Kerrness values of the strong-field region in terms of ε and mapping them to the waveform for the binary case in Sec. 7.4.

Mapping onto the waveform

A perturbation amplitude ε is associated with each timeslice of a post-merger spacetime in the strong-field region by the procedure described above. Since the procedure developed in 7.2 allows us to associate simulation timeslices with the gravitational waveform at $\mathcal{I}^+$, we can map the perturbation amplitude associated with each timeslice to the corresponding parts of the waveform at $\mathcal{I}^+$. This gives an insight into deciding which portion of the waveform at $\mathcal{I}^+$ can be modeled as being generated by linearly perturbed Kerr manifold, thus providing validation of start times chosen in data analysis that rely on perturbative description of Kerr.

Outline of method

For quick reference, we now concisely provide an outline of the algorithmic procedure developed in this paper. This also serves as a step-by-step plan that we can apply to future BBH detections.

1. Performing an NR simulation with waveform parameters inferred from parameter estimation, and saving the metric data,

2. Generating worldtube data for various extraction radii and performing CCE from the inner-most possible radius,

3. Evaluating the Kerrness measures on the metric data at this radius for BBH ringdown,

4. Evaluating the Kerrness measures on QNM perturbed data with the same final mass and spin, and inferring corresponding perturbation amplitude from the Kerrness values,

5. Mapping the Kerrness measures and inferred perturbation amplitudes to the waveform via null-characteristics,

6. Using these results to validate choices for the start time of ringdown in detector data analysis.

Measuring Kerrness on the horizon

In addition to local measures throughout a spatial slice discussed in Sec. 7.2, Kerrness can also be evaluated on the post-merger apparent horizon (AH). Owen describes a multipolar horizon analysis in [152], finding that the multipolar structure of a final BBH remnant was that of Kerr. Probing the multipolar structure also serves as a test of the no-hair theorem [197].

This formalism involves computing the mass multipole moments I_α of the horizon as

$$I_\alpha = \oint y_\alpha R dA, \tag{7.22}$$

where R is the scalar curvature of the horizon, dA is the metric volume element on the AH, and α labels generalized (non-axisymmetric) scalar spherical harmonics y_α. These generalized spherical harmonics are computed from the eigenvalue problem

$$\Delta y_\alpha = \lambda(\alpha) y_\alpha, \tag{7.23}$$

where Δ is the operator $\Delta \equiv g^{AB} \nabla_A \nabla_B$ on the AH, and λ is its eigenvalue. In analogy with axisymmetric spherical harmonics Y_{lm}, an effective l is defined for the eigenvalues as

$$\lambda = -\frac{l_{\text{eff}}(l_{\text{eff}} + 1)}{r^2}, \tag{7.24}$$

where r is the areal radius of the horizon. Since the l_{eff} values are time-dependent, we refer to a given multipole by its final value.

As discussed in [152], the multipole moments that are zero on a Kerr BH either immediately vanish due to the symmetry of the AH, or decay to zero from their excited values as the remnant BH settles to Kerr. The multipole moments that do not vanish on Kerr are functions of the mass and spin, and reach these values with increasing coordinate time. We use the code implemented and tested in [152] to compute the multipole moments. However, since the multipole moments are features of the horizon, we cannot map their behavior onto the waveform at $\mathcal{I}^+$. Moreover, CCE cannot be performed close to the horizon, as discussed in Sec. 7.2. Nevertheless, we can compare the qualitative behavior of the multipole moments with those of the Kerrness measures as done in Sec. 7.4.

7.3 Numerical implementation

Description of simulation

We apply the methods outlined Sec. 7.2 to the numerical simulation presented in Fig. 1 of [10], with similar parameters to GW150914, the first LIGO detection. The simulation is performed, and the methods are applied using SpEC, the Spectral Einstein Code. The waveforms and parameters are available in `SXS:BBH:0305` in the SXS Public Catalog [1]. The simulation has initial mass ratio $q = 1.221$, and dimensionless spins $\chi_A = (0, 0, 0.33)$ and $\chi_B = (0, 0, -0.44)$. The initial orbital frequency is $\Omega_0 = 0.017$. The final (post-merger) BH has dimensionless spin $\chi_C \simeq (0, 0, 0.69)$ (within numerical error, as measured using the techniques in [178]) and mass $0.952\,M$. The inspiral proceeds for $3694.4\,M$ until the formation of a fully-resolved common AH. The visible part of the post-merger waveform on a linear scale has a temporal duration of $\sim 61\,M$.

Within a BBH simulation, the metric equations are evolved in a damped harmonic gauge [190, 120], with excision boundaries just inside the apparent horizons [104, 177] and minimally-reflective, constraint-preserving boundary conditions on the outer boundary [172]. The spectral grid used during the inspiral of the simulation has an excised region for each BH. Once a common AH forms, the simulation proceeds for a few M before switching to a new grid, in which there is one excision region for the new AH [104]. For this simulation, the grid-switch happens at $3696.9\,M$. For more information on the code, see [126].

Implementation of Kerrness measures

We discuss the numerical implementation of the Kerrness measures outlined in Sec. 7.2 and summarized in Fig. 7.1, on an NR BBH post-merger. Note that these measures will not be zero even on a numerical Kerr spacetime, due to the resolution of the simulation.
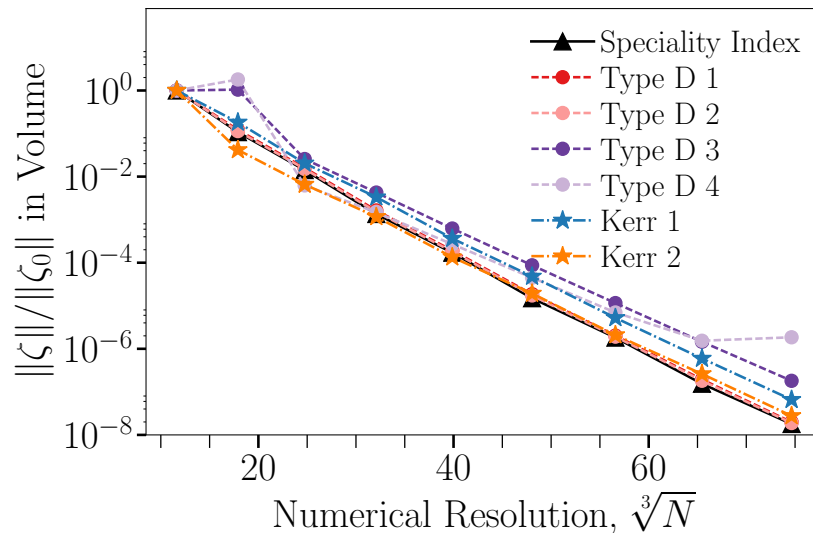
Figure 7.5: Convergence of Kerrness measures on a numerical BH in Kerr-Schild coordinates with dimensionless spin $\chi = (0.2, 0.3, 0.4)$. We observe exponential convergence towards the theoretical value of zero with numerical resolution. For each measure ζ, we present $\|\zeta\|/\|\zeta_0\|$, the L2 norm over the spatial slice normalized by the L2 norm of the lowest resolution. The resolution is expressed $\sqrt[3]{N}$, where N is the number of spectral collocation points in the domain.

In order to quantify the Kerrness measures at each point, we convert the complex tensors into scalars. We contract a tensor A^{ij}, a vector B^i, and a scalar C as

$$S_A = A^{ij}\bar{A}_{ij} \qquad S_B = B^i\bar{B}_i \quad S_C = C\bar{C}, \tag{7.25}$$

where raising and lowering occurs using the spatial metric γ_{ij}.[9] Throughout the rest of the paper, all of the measures will refer to their respective scalars generated using Eq. (7.25).

Because our simulations are performed using spectral methods, we expect errors to converge exponentially with increasing numerical resolution [160]. In Fig. 7.5, we

---

[9]The Kerr 2 measure given in Eq. (7.16) requires that the imaginary part be zero, while the real part be ≥ 0. Hence, when evaluating Kerr 2, we measure the deviation of the imaginary part from zero, and the deviation of the real part from being positive (hence only including negative values).

plot the Kerrness measures as a function of resolution for a single Kerr black hole; we see that the measures decay exponentially towards zero as expected.

SpEC solves a first-order formulation of the Einstein equations, and therefore evolves both the spacetime metric and variables corresponding to its time and spatial derivatives [121]. The metric and first derivatives are available to the accuracy of the numerical simulation on each slice. Kerrness measures that require additional numerical derivatives, however, will have greater numerical noise and a higher numerical noise floor. The highest numerical order derivative needed to evaluate each measure is given in Fig. 7.1. Type D 4, which requires four numerical derivatives, is the noisiest measure and has a higher noise floor than the other measures, as shown in Fig. 7.5.

Map from source to $\mathcal{I}^+$ - implementation

In our study, we use a CCE implementation in SpEC (cf. [38], in prep). This implementation uses a no ingoing and outgoing radiation condition on the initial null hypersurface of the characteristic evolution. This means that the code treats the spacetime outside the worldtube as initially free of any gravitational radiation from the past.[10] Usually the CCE worldtube is placed at a large radius, and the CCE evolution begins at the start of the numerical simulation during early inspiral. However, here we begin CCE only at the merger portion of the Cauchy evolution, and in addition, we place the CCE worldtube at a very small radius. This means that extracted waveform does not contain contribution coming from the inspiral part of the dynamics.

By decreasing the radius of the extraction worldtube progressively by $1\,M$, we find the smallest radius of the worldtube that our procedure can be applied to occurs at a coordinate radius of $R = 5\,M$. For a radius of $R = 3\,M$, the CCE procedure can not be performed, presumably due to the formation of caustics. At $R = 4\,M$, we get a very glitchy and unreliable extraction of the news function.

However, performing the CCE from such small radii gives rise to an additional complication. Since time stamps on the waveform at $\mathcal{I}^+$ are induced by the simulation coordinates, the news function obtained is not necessarily in an inertial gauge. In a standard CCE scheme, a gauge transformation is applied to the news function in order to obtain it in an inertial gauge. To preserve the map between the time in

---

[10]During the Cauchy evolution, we perform the evolution with a boundary of $R \approx 670\,M$ and we do not neglect the backscatter from the region outside of the CCE extraction radius.
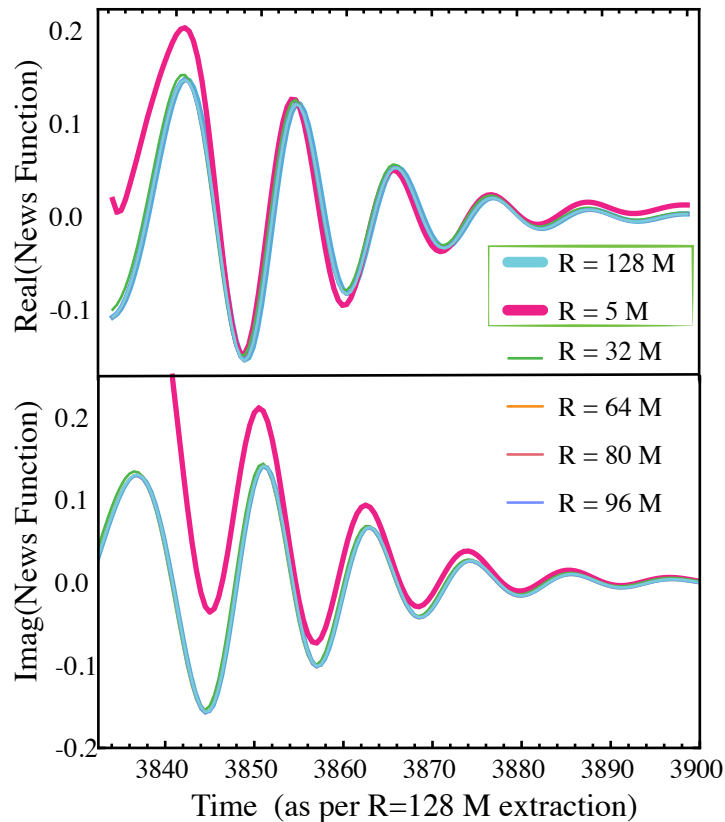
Figure 7.6: The $l = m = 2$ mode of the news function seen at $\mathfrak{I}^+$ extracted from worldtube boundaries of $R = 5\,M$, $32\,M$, $64\,M$, $80\,M$, $96\,M$ and $128\,M$. The horizontal axis corresponds to the time stamps associated with the news function corresponding to CCE from $R = 128\,M$. The **top panel** shows the real part and the **bottom panel** shows the imaginary part of the news function. The alignment of news functions has been done such that the overlap is maximized. The transformation that changes the gauge from a non-inertial to an inertial observer has not been applied to any of the extractions. All of the extractions beginning with $R = 32\,M$ seem to agree with one another (to the point of overlapping with the $R = 128\,M$ line). Notice that the amplitude of the news function extracted from $R = 5\,M$ deviates from the other extractions, especially in the first cycle. Nevertheless, the phase evolution between the news function from extraction radii seem to agree. The primary goal of this figure is to compare the extracted waveforms at $R = 5\,M$ and $R = 128\,M$. Thus, we have bolded and boxed these lines.
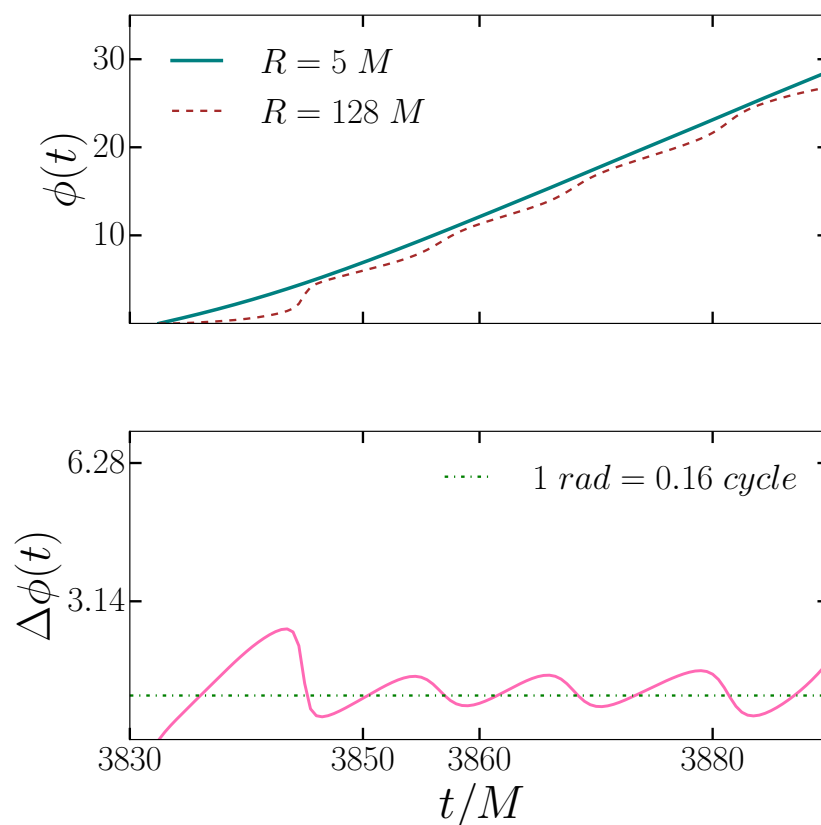
Figure 7.7: The phase discrepancy between the news function extracted from a worldtube radius of $R = 5\,M$ and $R = 128\,M$. The news functions are aligned to maximize the overlap. The **top panel** presents the phase evolution of the news function for each extraction radius. The **bottom panel** shows the fractional difference defined as $\phi_{128} - \phi_5$. Notice that the phase difference is significant at the very beginning but quickly decreases to an acceptable level for our analysis. We notice that the phase difference oscillates about 1 radian, indicating the level of error we introduce by - a) not performing the final gauge transformation, b) imposing no-ingoing condition for CCE.

simulation gauge and the time coordinate on the extracted news function, we do not perform this gauge transformation. We see the effect of the gauge transformation in the waveform at $\mathcal{I}^+$ as a mixing of mode amplitudes. The effect is very small when the worldtube boundary for CCE is large i.e., lies in the weak field region. For instance, for a worldtube boundary of $R = 128\,M$ the effect of this transformation is negligible. To confirm this, we compute the overlap O between the news extracted from $R = 128\,M$ with and without the gauge transformation. The overlap O is defined as:

$$O = \left\langle \widetilde{\mathcal{N}}_1 | \widetilde{\mathcal{N}}_2 \right\rangle = \int_{-\infty}^{\infty} \frac{\widetilde{\mathcal{N}}_1(f) \widetilde{\mathcal{N}}_2^*(f)}{|\widetilde{\mathcal{N}}_1||\widetilde{\mathcal{N}}_2|} \, df, \tag{7.26}$$

where $\widetilde{\mathcal{N}}_{1,2}$ is the frequency domain Fourier-transformed news function, and * denotes complex conjugation for ease of readability, and $||$ is the norm [25].

We find that the mismatch, $1 - O$, is $\sim 10^{-6}$. This overlap computation uses only the merger and post-merger parts of the news function for the dominant ($l = m = 2$) spin-weighted spherical mode. However, for a worldtube radius of $R = 5\,M$, there could be significant amplitude deviations between the waveforms in the simulation-coordinate-induced gauge and the inertial gauge. Because of technical difficulties in the code implementation, we could not apply the gauge transformation to an extraction from $R = 5M$ and quantify the difference.

Furthermore, before the non-inertial to inertial gauge transformation, every point on $\mathcal{I}^+$ at the same timestamp on the waveform corresponds to the same null hypersurface and therefore to the same simulation coordinate time. After the transformation, this is no longer true: the waveform seen at different sky directions with the same timestamp on the waveform corresponds to different null hypersurfaces and therefore different values of simulation coordinate time. This happens because the choice of the 2-sphere is gauge-dependent. Therefore, we omit the gauge transformation, as the aim in this paper is to connect the near-zone to the wave zone, requiring us to retain the timestamps.

Additionally, the initial no-ingoing radiation condition neglects gravitational radiation coming from the inspiral. This may be significant for extraction done at small radii, where the initial CCE null hypersurface connects the strong-field region close to merger to $\mathcal{I}^+$ and may contain significant radiation from the inspiral. This could contribute towards the discrepancy between the $R = 128\,M$ and $R = 5\,M$ waveforms.

To assess this difference, we compare the news function obtained by extraction performed from $R = 5\,M$ with the extractions performed from the worldtubes of larger radii, all without the gauge transformation. The result of this is presented in Figure 7.6. We observe that all the extractions from radii greater than $32\,M$ converge with radius, indicating that the effect of the gauge transformation is insignificant at these radii. Further, the extraction from $R = 5\,M$ has a significant amplitude discrepancy with the other extractions, particularly in its first cycle. Therefore, we would ideally wish to map the strong-field information computed on the 2-sphere at a coordinate radius of $R = 5\,M$ on the news function that has been extracted from a larger radius like $R = 128\,M$.

We do this mapping in two steps. First, we map the strong-field information computed on the 2-sphere at a coordinate radius of $R = 5\,M$ onto the CCE performed from a worldtube of $R = 5\,M$ using the framework described above. Next, we note that the phase evolution of extraction from $R = 5\,M$ agrees with the extractions from larger radii.[11] We verify this in Fig. 7.7. Then we align the news function extracted from $R = 5\,M$ to the extraction from larger radii as shown in Fig. 7.6. The alignment is done such that the overlap O between the CCE extracted news function from different world tube radii is maximized. The maximum normalized O between the news function extracted from $R = 128\,M$ and $R = 5\,M$ is 0.82. Incidentally, this alignment is equivalent to aligning the real part of the news function at its global minima (or global maxima of the absolute value). Table 7.1 lists the time shifts that have been applied in order to align the news function extracted from a radius R_i with extraction done at $R = 128\,M$.

Worldtube radius	Alignment shift wrt $R = 128\,M$
$R = 5\,M$	$132.5\,M$
$R = 32\,M$	$96.5\,M$
$R = 64\,M$	$62.5\,M$
$R = 128\,M$	$0\,M$

Table 7.1: The shift in the time axis performed to align the news functions extracted from different radii in Fig. 7.6. The alignment has been done such that the overlap between the news function extracted from different worldtube radii with the extraction from $R = 128\,M$ is maximized.

Using this alignment, we map the time stamps on the $R = 5\,M$ to those on $R = 128\,M$. From this, we infer the mapping of strong-field information at $R = 5\,M$ on

---

[11]The time-derivative of the phase gives the instantaneous frequency of the gravitational radiation.

to the extraction done from $R = 128\,M$, thus mapping the strong-field information onto the news function as seen in near inertial gauge.

We summarize our algorithm for mapping the strong-field information onto the news function:

1. Perform CCE from worldtube with radius of the 2-sphere that lies in the strong-field region (whose evolution you wish to map on to the news function seen at $\mathcal{J}^+$) without the final non-inertial to inertial gauge transformation. The time stamps on this extracted news function are induced by the time coordinates in the simulation, thus providing a natural map between the evolution of the strong-field region and the wave zone.

2. Perform CCE from a large worldtube radius where the effect of the non-inertial to inertial gauge transformation is negligible.

3. Align the news functions obtained in steps 1 and 2 such that the overlap between the waveform is maximized.

4. Use this alignment to map the time stamps of the news function extracted in step 1 to that in step 2. The 2-sphere chosen in step 1 at the timeslice marked with the simulation time coordinate can be associated as the dominant source of the feature at $\mathcal{J}^+$ with the same time stamp.

7.4   Results

We now present the results of performing the analysis outlined in Secs. 7.2 and 7.3 on the GW150914-like simulation detailed in Sec. 7.3. Sec. 7.4 presents the behavior of the multipole moments of the AH, which provides a comparison for the Kerrness measures on the simulation volume. Sec. 7.4 discusses the results of evaluating the Kerrness measures on the post-merger spacetime and mapping them onto the waveform at $\mathcal{J}^+$, presenting them in terms of the percentage decrease from their peak values. Sec. 7.4 presents the results of comparing the Kerrness measures on the post-merger spacetime to values on perturbed data, in order to infer the perturbation amplitude in the strong-field region, and mapping them onto the waveform, presenting them in terms of the inferred perturbation amplitude ε. The percentage decrease from the peak value and ε can then be used to estimate the overall level of Kerrness and validate choices for the start time of ringdown. Finally, in Sec. 7.4, we discuss the implications of these results on analyzing ringdown in GW data, and in Sec. 7.4,

we compare our results to the ringdown start times chosen in the GW150914 testing GR study [14].

Horizon behavior and multipolar analysis on BBH ringdown

As a first measure of Kerrness, we apply the horizon multipolar analysis outlined in [152] and summarized in Sec. 7.2 to the simulation described in Sec. 7.3. Fig. 7.8 presents the behavior of the AH. The areal mass of the AH, given by $\sqrt{A/16\pi}$ where A is the proper area of the AH, sharply settles to a final value. The minimum and maximum radii are initially noisy, as the AH is initially peanut shaped, but they decrease exponentially with coordinate time, showing a settling of the AH to the final state. However, the radii are coordinate-dependent measures, and thus to check if the BH settles to Kerr it is more instructive to look at the AH multipole moments.

Fig. 7.8 shows the behavior of the initially non-vanishing quadrupole and hexade-cupole moments, labeled by their corresponding l_{eff} at the final time, as given in Eq. (7.24). The quadrupole moments correspond to $l_{\text{eff}} \sim 2$ and the hexadecapole moments correspond to $l_{\text{eff}} \sim 4$. The multipole moments behave as expected for a generic simulation remnant settling to a Kerr BH. As explained in [152], two of the five quadrupole moments immediately vanish by reflection symmetry, while two others exponentially go to zero (eventually hitting a numerical noise floor) as the final remnant settles to Kerr. Four of the nine possible hexadecupole moments immediately vanish from reflection symmetry, while four go exponentially to zero as the remnant settles to Kerr. Note that the $l = 1$ and $l = 3$ moments vanish on Kerr due to symmetry. As in [152], one quadrupole moment ($l_{\text{eff}} = 2.1$) and one hexadecupole moment ($l_{\text{eff}} = 4.17$), both corresponding to $m = 0$, do not vanish, but rather attain a constant value in line with that of a Kerr BH of the same final mass and spin.

The multipolar behavior thus confirms that the final state of the AH is that of a Kerr BH. This serves as an independent test of Kerrness, and thus one would expect the Kerrness measures presented in Sec. 7.2 to also show the strong-field region exponentially settling to Kerr. This also serves as numerical evidence for BH uniqueness, as the final remnant of a BBH merger is indeed Kerr, as also discussed in [152]. Similarly, since the final multipolar structure can be described completely by the mass and spin, this serves as numerical validation of the no-hair theorem.
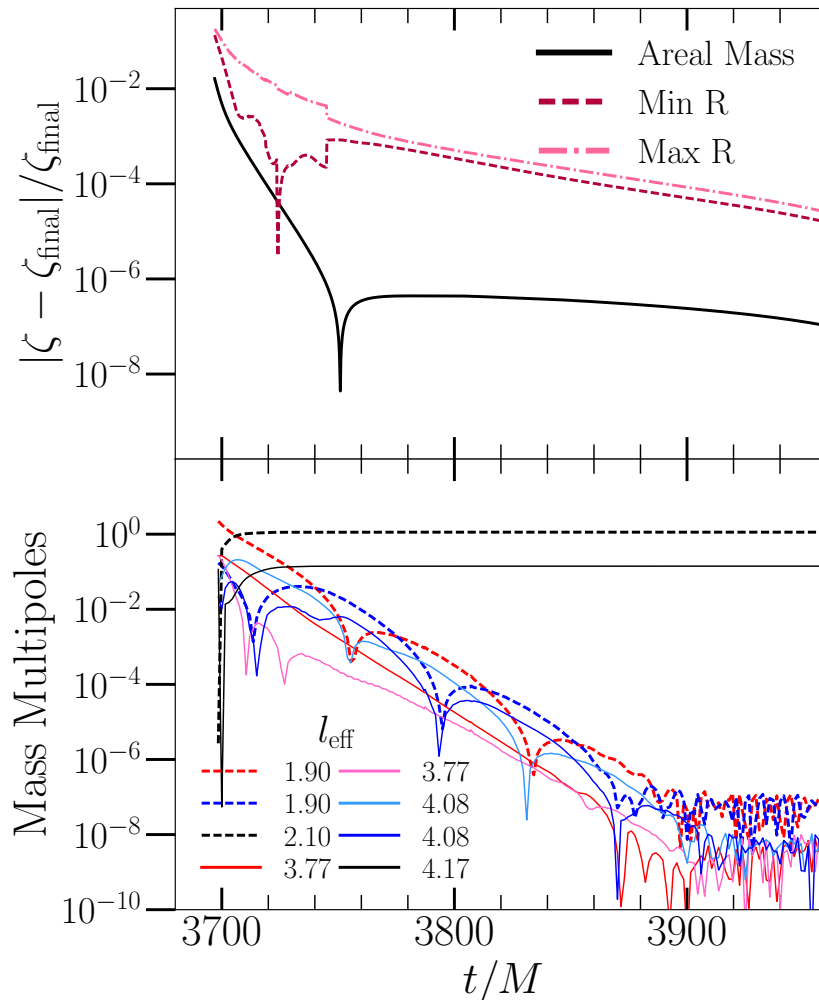
Figure 7.8: Settling of the post-merger AH as a function of coordinate time. The **top panel** shows the areal mass quickly attaining a constant value and the minimum and maximum radii R of the horizon exponentially settling to final values. Each quantity ζ is presented as $|\zeta - \zeta_{\text{final}}|/\zeta_{\text{final}}$ where ζ_{final} is the value at the final time of the simulation. The **bottom panel** shows the behavior of the initially excited AH mass multipoles, labeled by the l_{eff} given in Eq. (7.24) at the final time. The initially excited quadruple moments ($l_{\text{eff}} \sim 2$) are shown by the dashed lines, while the initially excited hexadecupole moments ($l_{\text{eff}} \sim 4$) are shown by the solid lines. As discussed in the text, two of the quadruple moments and four of the hexadecupole moments, as well as the $l \sim 1$ and $l \sim 3$ moments immediately vanish due to symmetry. Thus, we do not plot them in this figure. The excited multipoles either exponentially decay or reach constant values consistent with the values expected for Kerr [152].
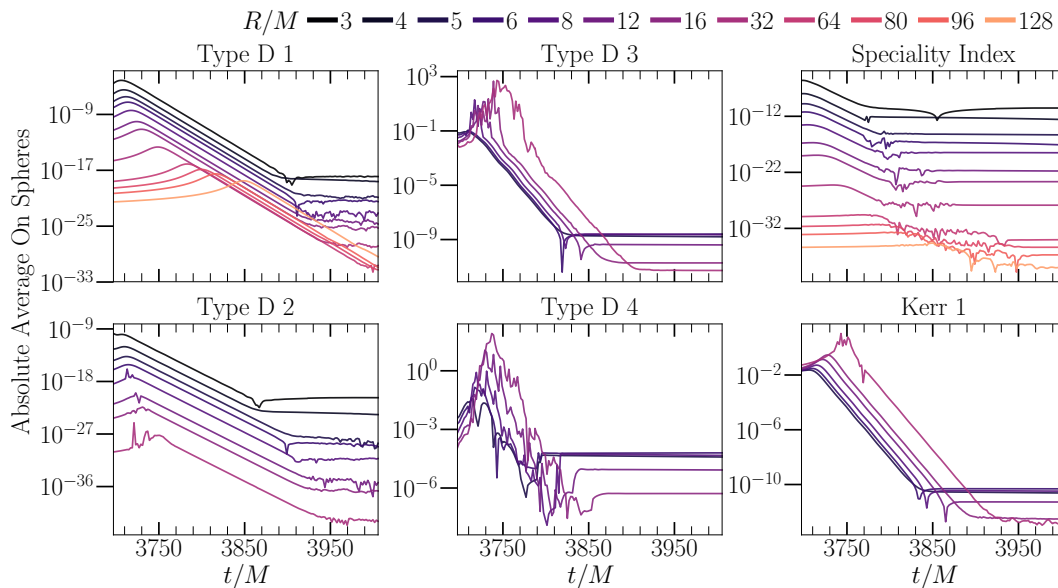
Figure 7.9: Behavior of absolute Kerrness measures with coordinate time on BBH post-merger spacetime. The measures are averaged on a variety of concentric nested coordinate 2-spheres of radii R around the BH, as indicated by the colors. Larger values *within each subplot* mean that the 2-sphere is farther from being locally isometric to Kerr. For measures that involve higher-order numerical derivatives, we present the results only at radii where they are at least somewhat well resolved. All plots, however, include $R = 5\,M$, the radius we use to map Kerrness onto the waveform. Type D 4 is particularly noisy, as it contains the highest number of numerical derivatives. The measures exponentially decay as the spacetime approaches Kerr, ultimately reaching a numerical noise floor. We observe that the peak of each measure moves outwards with radius, indicating propagation of non-Kerrness.

Measuring and mapping Kerrness onto the waveform

The goal in this section is to validate choices of the start time of ringdown using Kerrness measures on the GW150914-like system described in Sec. 7.3. We now present the results of evaluating the Kerrness measures outlined in Secs. 7.2 and 7.3 (and summarized in Fig. 7.1) in the strong-field region and mapping them onto the waveform at $\mathcal{I}^+$ using the procedure given in 7.3. These measures are evaluated point-wise on each slice, and we map the value on a 2-sphere at a radius of $R = 5\,M$ onto the news function. Recall that larger values of the Kerrness measures indicate greater deviation from being locally isometric to Kerr.

Fig. 7.9 shows the Kerrness measures averaged at various coordinate radii on each slice of the post-merger spacetime, presented as a function of coordinate time. All of the measures decay exponentially toward zero, showing that the spacetime approaches an isometry to Kerr. This confirms the results of the multipolar analysis

in Sec. 7.4. Additionally, this serves as a numerical verification of BH uniqueness, as the final state of a BBH merger is isometric to Kerr. The behavior of the measures at large radii (such as $R = 128\,M$ in this case) is especially interesting to the question of BH uniqueness, which is particularly concerned with the *domain of outer communication* [107].

Fig. 7.10 shows the behavior of the Speciality Index, an algebraic measure (Type D 1) and a geometric measure (Kerr 1) in the volume, as a function of increasing coordinate time. We see a distinct quadrupolar pattern in all our measures (the equatorial plane has a modal pattern that corresponds to $|m| = 2$), consistent with the dominant mode of gravitational radiation. Furthermore, the Speciality Index and Type D 1 measures, which determine properties of the PNDs, settle first further from the BH, while the geometric Kerr 1 measure, which is determined by properties of the KV, first settles closer to the BH.

The Kerr 2 measure, which constrains the NUT parameter, is effectively constant throughout the ringdown, as shown in Fig. 7.11. Since the NUT parameter is one of the hairs of a generic type D manifold, Fig. 7.11 confirms that a NUT charge is not generated during a BBH merger. We thus do not include it further in our analysis.

Of these measures, two are algebraic constraints—Type D 1 and Type D 2—and three are geometric constraints on the KV, Type D 3, Type D 4, and Kerr 1. In Fig. 7.9, we see that all the algebraic measures decay in a similar fashion and all the geometric measures decay similarly. Type D 4, which requires 4 numerical derivatives, is visibly noisier than the other measures. This measure checks if the vector identified as (Y, Y_j) satisfies the Killing equation and is crucial for a rigorous mathematical characterization of Kerr manifold. However, all geometric measures depend on the same Killing vector, and we observe that Type D 4 has a similar decay property as Type D 3 and Kerr 1. Thus, we do not include the noisier Type D 4 in our analysis, rather treating Type D 3 as a proxy for both.

Each measure at each radius in Fig. 7.9 eventually reaches a floor. This is confirmed to be a numerical noise floor in Fig. 7.12, where the floor is shown to exponentially converge to zero with numerical resolution. The radial behavior of the Kerrness measures stems from the radial behavior of the Weyl tensor and the metric quantities. For example, for a stationary background, $E_{ij} \sim R^{-3}$ and $B_{ij} \sim R^{-4}$, and thus Speciality Index given in Eq. (7.7) should be $\sim R^{-18}$, which we indeed observe.

The analysis outlined in Sec. 7.3 requires the Kerrness measures to be extracted
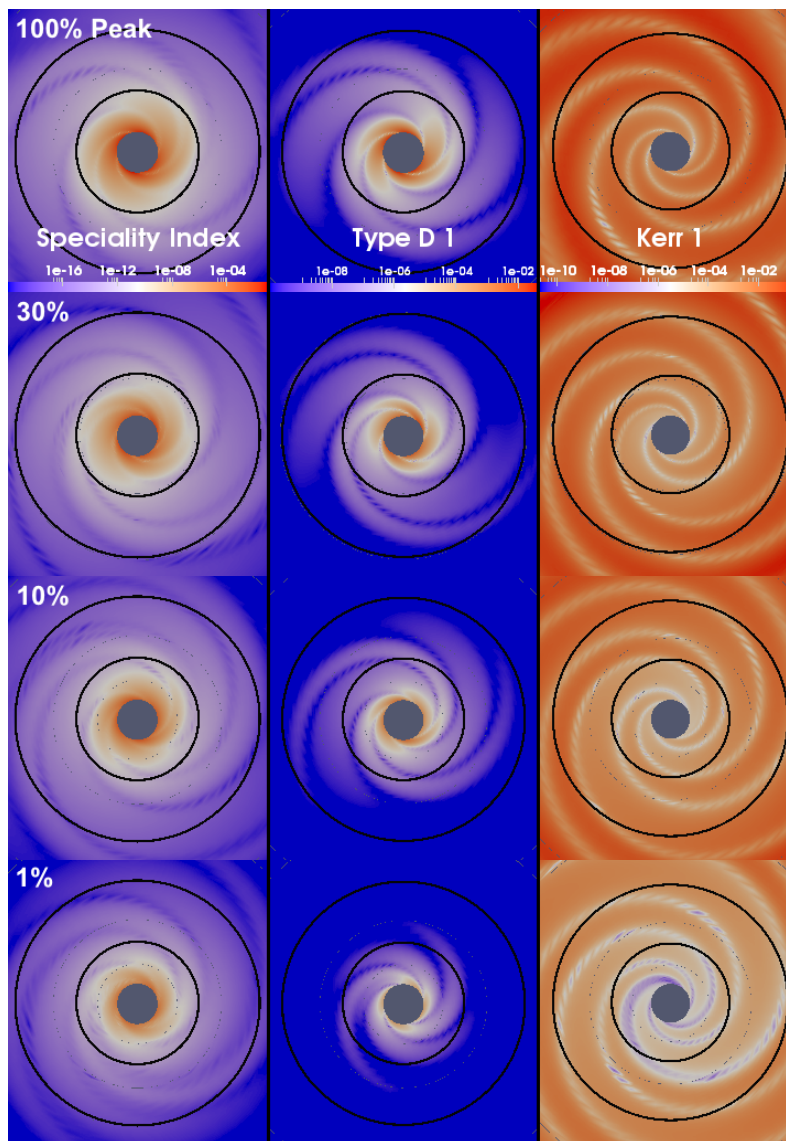
Figure 7.10: Absolute Kerrness measures on slices of the BBH post-merger space-time. The data is presented in the equatorial plane, with the gray region corresponding to the excised BH. The black circles correspond to coordinate radii $R = 5\,M$ and $R = 10\,M$. The columns correspond to Speciality Index, Type D 1, and Kerr 1, and the rows (from top to bottom) correspond to coordinate times at which the each measure at $R = 5\,M$ achieves 100%, 30%, 10%, and 1% of the combined peak value. The quadrupolar pattern (with $|m| = 2$) in all three measures is consistent with the dominant quadrupolar radiation (recall that these are absolute measures, and hence do not distinguish between positive and negative values). Notice that the algebraic measures—Speciality Index and Type D 1—settle outward-in, whereas Kerr 1, a geometric measure, settles inward-out. Additionally, the structures in the measures are visible even at 1% of the peak value. We can compare these measures to Ψ_4 (in Figs. 7.16) to infer their sensitivity to the spacetime curvature features.
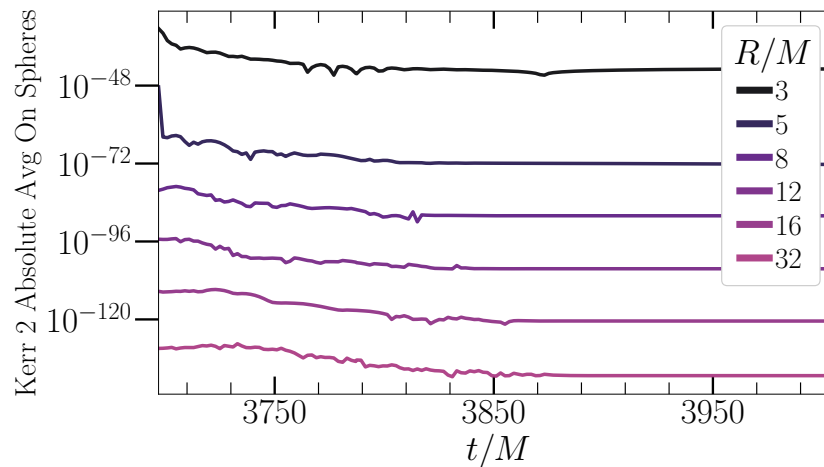
Figure 7.11: Kerr 2 measure throughout the post-merger BBH simulation, averaged on a variety of coordinate 2-spheres of radius R. The values remain relatively constant and low, indicating that no NUT charge is gained during ringdown.

at $R = 5\,M$ in order to map them to the news function. Fig. 7.10 shows that the Kerrness measures have strong support at $R = 5\,M$, thus justifying the choice of radius as being in the near field.[12]

The Kerrness measures quantify the violation of the conditions for a manifold to be isometric to Kerr and therefore, they need not have the same dimensions and sensitivities. Thus, one cannot compare the absolute magnitudes of these measures with each other and directly translate their value into statements on validity of start time of perturbative regime. In order to normalize and combine them into an overall measure of Kerrness, we use the concomitant percentage decrease from their peak values.

We present the percentage decrease of each of these measures from their peak values mapped on to the news function in Fig. 7.13 and Fig. 7.14. In the bottom panels of these figures, the news function is plotted as a function of time. On the same time axis, the top panel depicts the corresponding evolution of the Kerrness measure in the strong-field region. The waveform feature in the bottom panel at a particular time coordinate is associated to the timeslice carrying the same time label, via source-effect association outlined in Sec. 7.2. In the bottom panel, the Kerrness value at this time characterizes the deviation from Kerr.

---

[12]The measures at $R = 3\,M$ in Fig. 7.9 behave similarly to those at $R = 5\,M$ indicating that $R = 3\,M$ also behaves like the near field region, but unfortunately we have not been able to perform CCE from this small a radius.
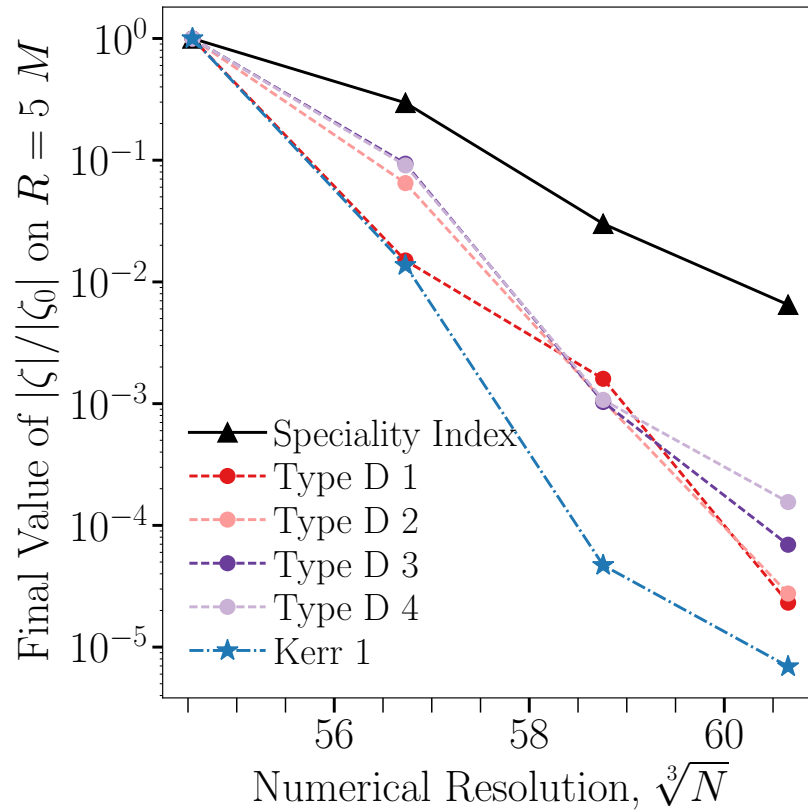
Figure 7.12: Exponential convergence of the noise floor of each Kerrness measure on the final timestep of the BBH simulation. Each measure ζ is presented as an average over a 2-sphere of $R = 5\,M$ (where the measures have settled to a noise floor), normalized by $|\zeta_0|$, the average of the lowest resolution. The resolution is indicated by $\sqrt[3]{N}$, where N is the number of spectral collocation points. The convergence to zero shows that the noise floor observed in Fig. 7.9 is a numerical noise floor, rather than real a physical artifact. We have also tested this convergence behavior on a 2-sphere $R = 5\,M$ and verified that the behavior is consistent (although more noisy).
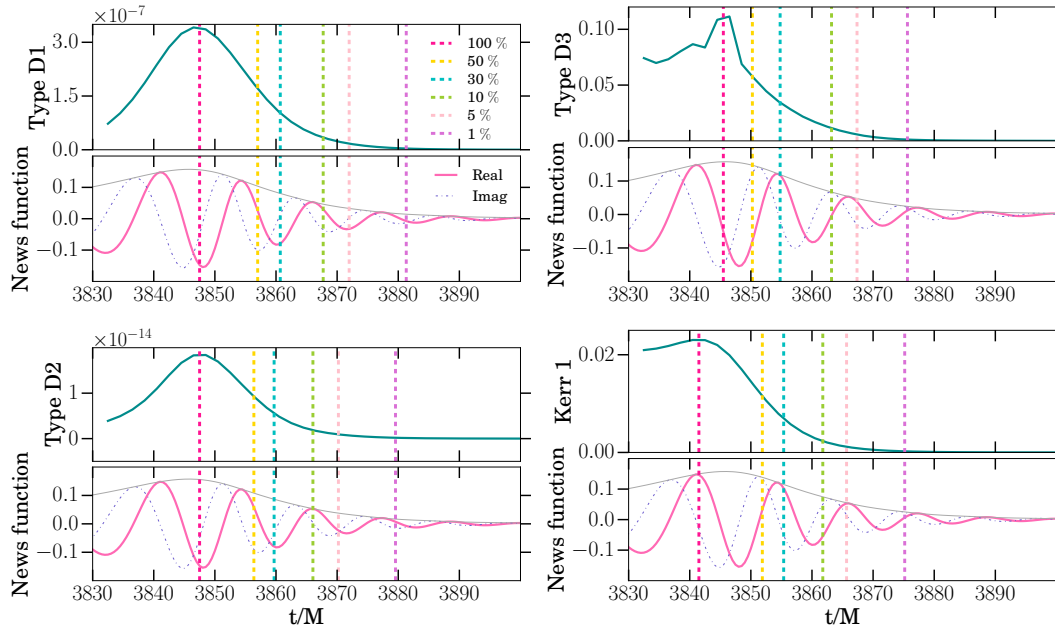
Figure 7.13: Connecting the Kerrness measures in the strong-field to dynamics at $\mathcal{I}^+$ using the procedure described in Sec. 7.3 on the BBH post-merger. The **left panels** map the algebraic measures and the **right panels** map the geometric measures on to the news function. The **top panel** within each subplot corresponds to a Kerrness measure in the strong-field, while the **bottom panel** shows the news function at $\mathcal{I}^+$. The purpose of plotting the news function directly below each Kerrness measure is to emphasize that the top and bottom panels are mapped to the same time axis. The dashed lines of different colors indicate the % decrease from the peak value of the respective Kerrness measures. The horizontal axis corresponds to the simulation coordinate time induced on the news function extracted from a world tube radius of $R = 128\,M$. Furthermore, unlike the strong-field result plots that aim at rigorous characterization of isometry to Kerr, here we aim at providing insight into validating the start time of ringdown for data analysis. Therefore, these plots are on linear scale as opposed to logarithmic scale. Notice that the curves on the left panel decay more slowly than those on the right; Type D 1 is the slowest to decay, closely followed by Type D 2. Also, recall that we cannot compare the magnitude of the top part of each of these panels as they are dimensionally different.
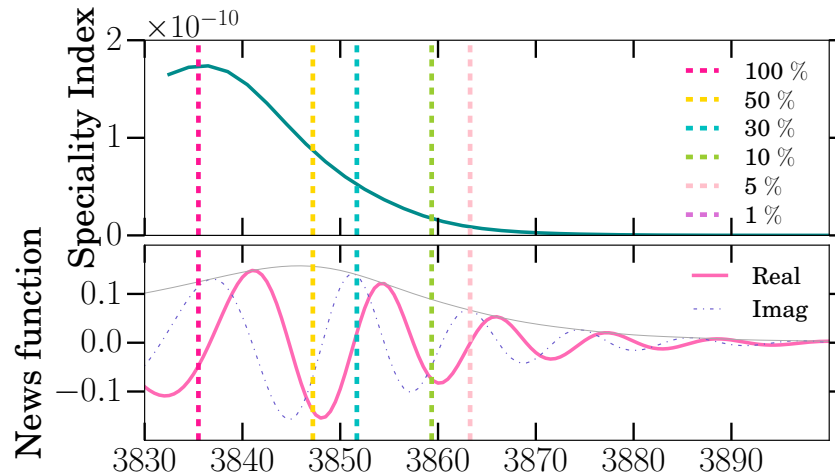
Figure 7.14: This figure is similar to Fig. 7.13 but for Speciality Index. We plot this separately as it is an independent measure and decays rapidly compared to the other measures. Further, we do not indicate the 1% of peak line because of numerical noise (cf. Fig. 7.9), which leads to unreliable root finding for time of percentage decrease.

In these figures, we delineate 6 lines marking the percentage decrease from the peak value of each of the Kerrness measures as a function of time—both in the strong-field region and on the news function at $\mathcal{I}^+$. As stated before, these measures have different decay properties and so do not decay to a particular percentage of their peak value at the same time. The difference between the time at which measures decay to a particular percent is tabulated in Table 7.2.

% of peak value	Spread in time	Combined % Time
100 %	12 M	1.5 M
50 %	9.8 M	11 M
30 %	9 M	14.7 M
10 %	8.3 M	21.7 M
5 %	8.7 M	25.9 M
1 %	6.1 M	35.3 M

Table 7.2: The spread in the time for given % of the peak value of Kerrness measures computed using all the measures. The combined % time refers to the value of the dashed lines in Fig. 7.15 and corresponds to the time at which all the measures have at least decayed to the indicated % relative to the time at which the peak amplitude of news function occurs.

We present the combined percentage decrease from the peak value on the news function in Fig. 7.15. The shaded bands correspond to spread in percentage decay
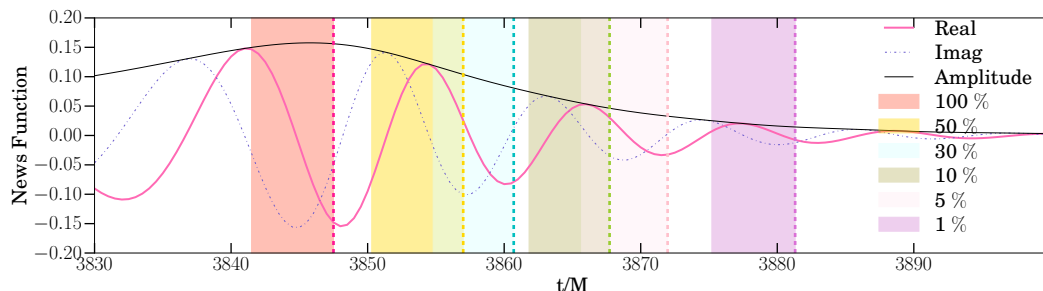
Figure 7.15: The concomitant decrease of all of our Kerrness measures. The dashed lines indicate the time at which all the measures decay to at least the indicated % of peak. The bands color the region in which different measures decrease to the indicated % of peak. Notice that there is about half a cycle spread in each of these bands. Therefore, the dashed lines provide a conservative idea of the validity of the choice of the start time for data analysis. We have specifically included the spread of these bands as a quantifier of error bounds in the statements of validity made further in this paper. Furthermore, one could shrink the right boundary of these shaded bands if one combines the Kerrness measures with appropriate weights based on their sensitivity to the spacetime curvature and the final remnant's effective potential.

on the news function. The widths of these bands are given in Table 7.2. The solid line at the end of each band marks the time when all these measures have decayed to the indicated percentages, and this can be used to conservatively choose the start time.

Furthermore, in this figure, we do not include the Speciality Index. The Speciality Index is an independent measure that quantifies if the manifold is algebraically special. Since this is the weakest condition in our Kerrness characterization scheme, we see that it gets satisfied earliest on the post-merger simulation from Fig. 7.14. The 1% of peak line which occurs unexpectedly late arises because of numerical reasons. We assert this by looking at the nearly flat nature of Speciality Index curves in Fig. 7.9 at late times, very close to the numerical noise floor.

We observe that all measures decay to $\sim 50\%$ of their peak value within half a cycle from the peak of the news function. Further, in approximately one cycle, all the measures are reduced to $\sim 30\%$ of their peak values. The spread in each of the bands is about $\sim 10\,M$ when we include all the Kerrness measures in computing the band, and this shrinks to $\sim 6\,M$ when we exclude Speciality Index.

We combine the measures with equal weights, thereby presenting a conservative result. Furthermore, we have repeated our analysis with larger worldtube radii and

confirmed that our results for the spread do not change significantly. For instance, using $R = 128\,M$ results in a time shift of about $+4\,M$ relative to the $R = 5\,M$ results, and this positive time shift monotonically decreases with radius for $R = 32$, 64 and $80\,M$.

Estimating and mapping the perturbation amplitude onto the waveform
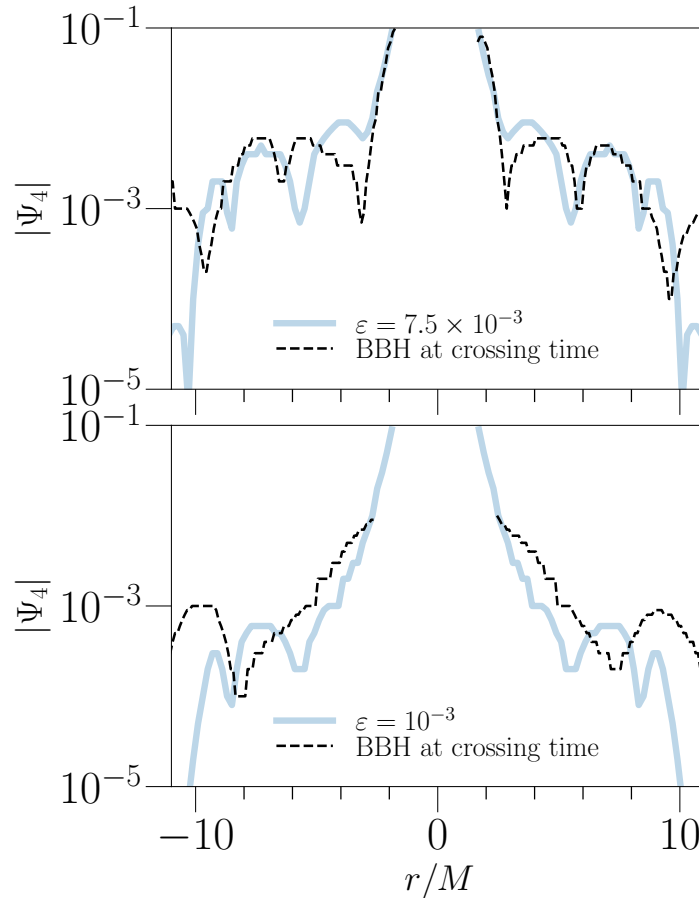
Figure 7.16: Ψ_4 in on the x-axis (in the equatorial plane) for both a single BH with an $l = m = 2$ perturbation of amplitude $\varepsilon = 7.5 \times 10^{-3}$ (**top panel**) and $\varepsilon = 10^{-3}$ (**bottom panel**), and for the BBH ringdown at times that achieve the same Kerrness. For all cases, Kerrness is matched on a coordinate 2-sphere of $R = 5\,M$. The x-axis of the plot shows the radius, and includes the data within the Gaussian envelope of width $R = 8\,M$, as described in Fig. 7.3. Note that this is only meant to show qualitative agreement between Ψ_4 on both slices, as the quantity is still subject to coordinate tetrad effects in the strong-field region. Notice that although the two systems look similar, the mapping does have some imperfections. Recall, however, that it is ultimately the invariant Kerrness measures that determine the mapping between the perturbation amplitude and the BBH merger-ringdown time.

In order to provide a physical understanding for the values of the measures in the

strong-field region shown in Figs. 7.9 and 7.10, we can compare the values to those on an initial slice of a perturbed Kerr BH with the same final mass and spin as the BBH simulation, as outlined in Sec. 7.2. We can then map the inferred strong-field perturbation amplitude ε onto the waveform using the procedure outlined in Secs. 7.2 and 7.3. This procedure involves the following steps:

1. Generate perturbed Kerr manifolds for a range of amplitudes ε.

2. Compute the Kerrness measures at $R = 5\,M$ on these slices.

3. Compute the Kerrness measures at $R = 5\,M$ on the post-merger BBH simulation (verifying that the gauge-invariant areal radii of the $R = 5\,M$ coordinate 2-spheres are approximately (within $0.01\,M$ in our case) equal for the single-BH and the BBH case). If the areal radii do not match, then choose a different surface on the perturbation slice such that the two areal radii agree.

4. Identify the coordinate time in the post-merger BBH simulation at which the Kerrness measures at $R = 5\,M$ agree with those on the perturbed Kerr slice for a given ε — this gives a *crossing time* for this ε.

5. Use this crossing time to map the inferred ε onto the waveform.

Fig. 7.17 shows the inferred ε for the BBH ringdown simulation as a function of coordinate time in the simulation. The gauge-invariant areal radii at $R = 5\,M$ on the BBH simulation slices and on the metric perturbation are within $10^{-2}\,M$. The values of the Kerrness measures on the perturbed data vary quadratically with ε, as shown in Fig. 7.4. At higher values of ε, they obtain higher-power dependence, as discussed in Sec. 7.2. Each Kerrness measure decays through various ε as the simulation progresses. Type D 1 and Type D 2, the two algebraic conditions, have comparable crossing times for a given ε, while the two geometric KV conditions, Type D 3 and Kerr 1, also have comparable crossing times. Speciality Index crosses around $10\,M$ before the other measures, in part because it is a weaker condition that the others. Each crossing time has an intrinsic $2\,M$ spread due to sampling, and not all measures cross each ε due to numerical noise floors, leading to spreads in crossing time.

In Fig. 7.16, we qualitatively check the spacetime features by comparing Ψ_4 corresponding to $\varepsilon = 7.5 \times 10^{-3}$ and 10^{-3} on the perturbed Kerr metric with the corresponding timeslice during the post-merger simulation. The crossing time spread
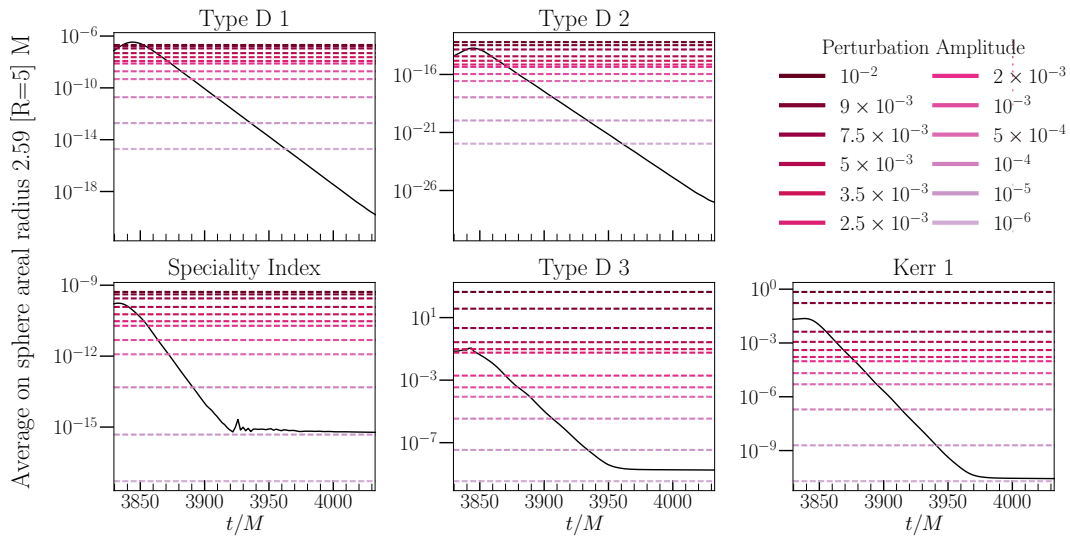
Figure 7.17: Comparison of the Kerrness measures during the BBH post-merger to the values of the Kerrness measures on an $l = m = 2$ QNM perturbed Kerr BH of various perturbation amplitudes ε, with the same mass and spin parameters. The measures are averaged on a 2-sphere of coordinate radius $R = 5\,M$, which corresponds to comparable areal radii of $\sim 2.59\,M$ in both systems. The measures evaluated on the BBH slices are shown by solid black lines, decaying as a function of time. The Kerrness measures for the perturbed metric are presented as horizontal dashed red lines, one for each ε. The times at which the BBH curves intersect the Kerrness values for a given ε Kerr perturbation give a scale for the BBH Kerrness measures as the post-merger progresses. These times, known as *crossing times* are then mapped onto the waveform, and used to validate the start time of ringdown. Note that the measures have different crossing times. The time axes are shifted to agree with the timestamps of the GW at $R = 128\,M$, as explained in Table 7.1.

for a particular ε arises because of the imperfect mapping between an analytically perturbed Kerr BH and the post-merger spacetime. Therefore, unlike in an ideal mapping, the combined crossing times will have a spread. In particular, the difference in the features between the post-merger and the perturbed Kerr slice indicates a difference in symmetry and explains the larger spread in the crossing time between the KV-dependent measures. We see that the spread in the combined crossing times using only algebraic measures is much smaller than when we include the geometric measures.

We next map the inferred perturbation amplitude to the news function, using a procedure similar to the one in the previous section, and present the result in Fig. 7.18. The top panel of the figure indicates the crossing time for the Speciality Index, the middle panel for the algebraic measures, and the bottom panel shows
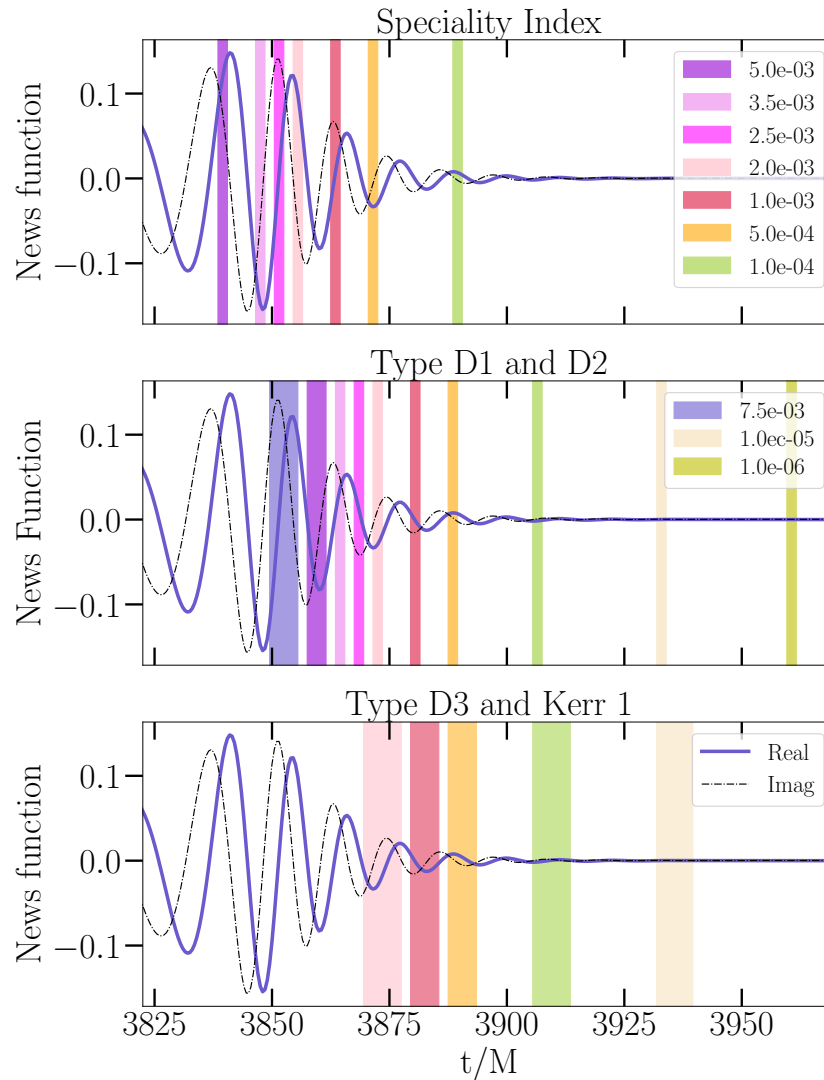
Figure 7.18: Mapping the inferred perturbation amplitude close to the BH onto the news function. The **top panel** shows the spread in the crossing times computed using just the Speciality Index, the **middle panel** uses only the algebraic measures and the **bottom panel** utilizes only the geometric measures. Notice that amplitudes larger than 2×10^{-3} do cross the post-merger timeslices when computed using the geometric measures and that the crossing time spreads in them are relatively large, suggesting a difference in the symmetry of a perturbed Kerr metric and the post-merger BBH spacetime. However, this does not seem to be reflected when we just consider the algebraic measures as they have a relatively small spread in the crossing time. The spread in the crossing time of the Speciality Index is equal to the sampling rate.

that for geometric measures. The spread in the crossing time for the algebraic measures decreases from $\sim 6\,M$ at the start, to our sampling rate, $2\,M$. This occurs because at the very start of post-merger, the system is not yet in a perturbative regime and therefore, our mapping contains a larger error. Geometric measures are more drastically affected by the imperfections in the mapping, indicating the differences in the symmetries of the two systems. On including the geometric measures, the crossing time spreads to $\sim 8\,M$. We confirm that the spread of the crossing times calculated using the algebraic measures is always contained within the spread of crossing times calculated using the geometric measures.

As the signal decays from the peak to a barely-visible amplitude on a linear scale ($\sim 3 - 4$ cycles) at $\mathcal{I}^+$, the corresponding perturbation in the strong-field region decreases by an order of magnitude. The peak of the news function corresponds to a perturbation amplitude of $\sim 7.5 \times 10^{-3}$. Further, it takes about 2 cycles in the wave zone for the perturbation amplitude to decay to half its peak value. Also, by the time the perturbation amplitude decays by an order of magnitude, there is hardly any power left in the signal.

Implication of the start time on data analysis

From news to h

In order to compare the Kerrness measures on the GW to the loss in signal-to-noise ratio (SNR) at the times used in [14], we must first calculate the strain h from the news function, and then calculate the merger time. As outlined in Sec. 7.3, h can be calculated by integrating the CCE news function. One can also independently calculate h using the Regge-Wheeler-Zerilli (RWZ) (cf. [173] for details on the method) [169, 217, 218, 138] method and then extrapolating it in powers of the extraction radius (cf. [56] for details). The RWZ method and extrapolation have been implemented and tested in SpEC [56, 193], and the strain calculated by this method was presented in the GW150914 detection paper [10]. This method, however, has a different retarded time axis [56] than the CCE news function. Thus, we differentiate the RWZ strain to get a news function, and shift it to align in phase with the CCE news function. We check the CCE results by comparing the output of the two methods, presenting the results in Fig. 7.19.

In the GW150914 testing GR study [14], t_{merger} is defined as the point at which the quadrature sum of the $h_\times$ and h_+ polarizations of the most-probable, or *maximum a posteriori* (MAP) waveform, produced by Effective-One-Body (SEOBNRv4) tem-

plate [168] is maximal. For this study, we use the $l = m = 2$ spin-weighted spherical harmonic mode of the MAP waveform, as this is the least-damped QNM. In this study, rather than using the EOBNR waveform, we calculate t_{merger} based on the time of maximum amplitude of the time-shifted RWZ strain, as

$$t_{\text{merger}} \equiv \{t | h^2(t) = \max_{t'}(h^2(t'))\}, \tag{7.27}$$

where

$$h^2 \equiv \text{Real}(h)^2 + \text{Imag}(h)^2 . \tag{7.28}$$

We find $t_{\text{merger}} = 3839.0 \pm 0.1 \, M$.
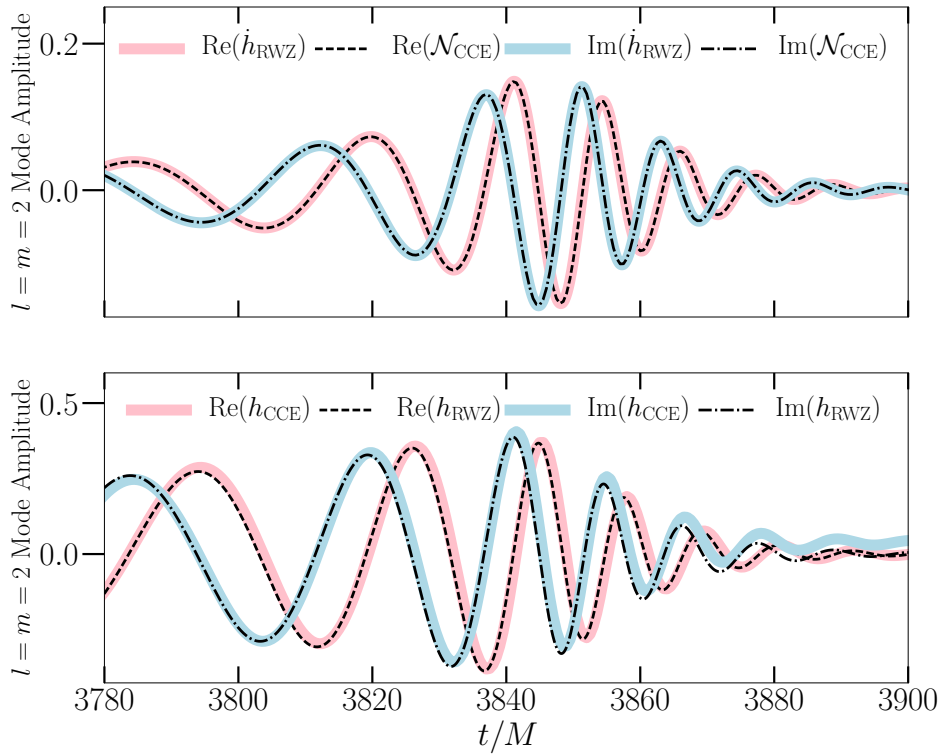
Figure 7.19: Comparison between the strain h calculated using CCE and RWZ methods. All waveforms are presented in terms of the $l = m = 2$ mode. We use the fact that the strain is the integral of the news function to crosscheck the methods. The **top panel** shows the CCE news function $\mathcal{N}_{\text{CCE}}$ compared to $\dot{h}_{\text{RWZ}}$, the derivative of the RWZ strain. The **bottom panel** shows h_{CCE}, the integral of the CCE news function, compared to the RWZ strain h_{RWZ}. We find good agreement until late times, when h_{CCE} begins to drift, likely due to the numerical integration scheme used.
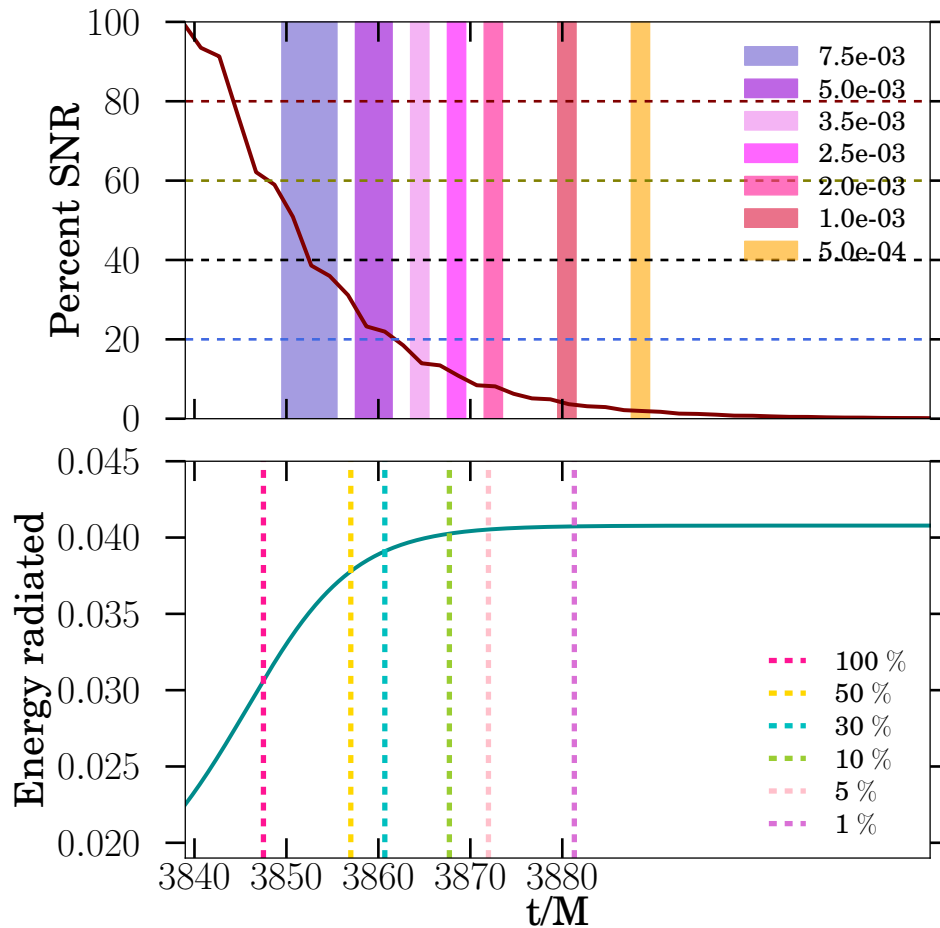
Figure 7.20: The **top panel** of this figure shows the percentage decrease of SNR from the peak value. The % SNR is set to 100 at t_{merger}. For this plot, we evaluate Eq. (7.29) with varying lower bounds for the integration. The dashed horizontal lines correspond to $\{80, 60, 40, 20\}\%$ SNR. On the same plot, we mark the perturbation amplitude bands for a direct comparison between perturbation amplitude and statistical error. Notice that by the time the perturbation amplitude near the BH decreases by an order of magnitude, there is only a few percent of SNR left in the signal, emphasizing the sharp trade-off between the systematic biases arising from modeling the post-merger as perturbed Kerr and the statistical uncertainty arising due to exponentially decay of signal amplitude. The **bottom panel** shows the total energy radiated in units of M during the merger-ringdown. This is calculated by integrating Eq. (7.31). Again, we have plotted the concomitant percentage decrease of the Kerrness measures from their peak values for an easy comparison between the statistical and systematic errors associated with the choice of the start time of ringdown. In particular, the constant settling in the total radiated energy occurs between the time when the Kerrness measures have decayed to $5 - 1\%$ of their peak values, implying that at these times the GW is very weak in amplitude.

No. of cycles	% SNR	% Kerrness	$\varepsilon/10^{-3}$
peak	60	100	7.5
$\frac{1}{2}$ cycle	30 - 40	40 - 50	7.5
1 cycle	20 - 25	35 - 30	5
$1\frac{1}{2}$ cycles	10 - 20	8 - 12	3.5
2 cycles	~ 10	7 - 5	2 - 2.5
$2\frac{1}{2}$ cycles	< 10	~ 1	1 - 2
3 cycles	< 5	< 1	0.5 - 1

Table 7.3: Summary of our results. The first column counts the number of cycles from the peak of the news function. The second column presents the drop in SNR with start time chosen in the data analysis. SNR is normalized to have 100% when the data analysis starts at the peak of the waveform ($h(t)$) i.e., at 3839 M. The third column shows the concomitant percentage decrease in the Kerrness measures from the peak value (similar to Fig. 7.15). Further, in the last column, we present the perturbation amplitude inferred by the crossing times computed with Type D 1 and D 2 measures (similar to middle panel of Fig. 7.18.)
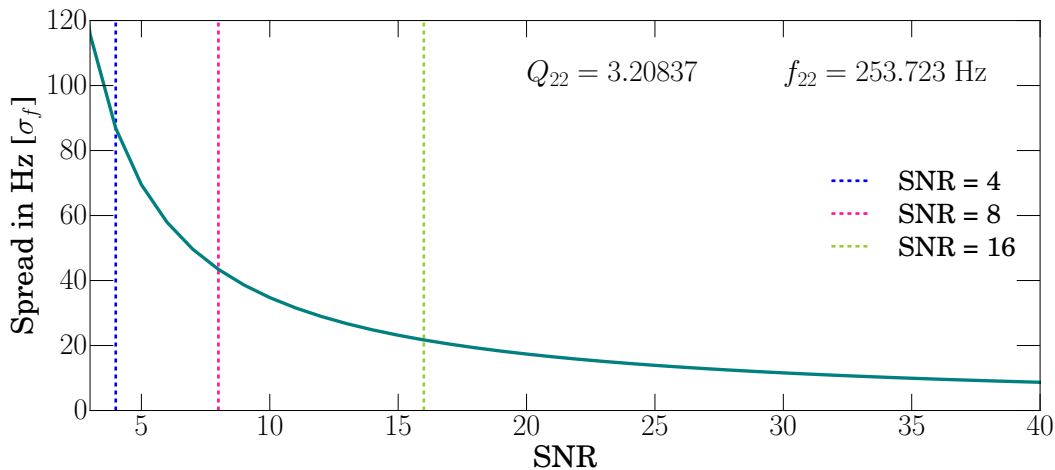
Figure 7.21: Spread in estimation of dominant mode frequency as a function of SNR. We present the spread, σ_f in the estimation of frequency calculated using Fisher information matrix formalism. We should the increase in spread with decreasing SNR, providing the rough intuition on the implication of Fig. 7.20 on parameter estimation.

Start time and the SNR

While picking too early a start time for an analysis that relies on being in ringdown gives inaccurate and biased results, picking a start time too late leads to a large statistical error. Since the amplitude of the signal decays exponentially with time, the SNR in ringdown decreases as exponential-squared with the start time. Consequently, the spread in the posteriors during estimation of ringdown parameters,

which goes inversely proportional to match-filtered SNR, increases and gives rise to large statistical uncertainties. Therefore, one must chose an optimal middle ground considering both these factors.

In the top panel of Fig. 7.20, we show the percentage decrease in match-filtered SNR with the start time of the ringdown. A match-filtered SNR is a noise-weighted scalar product between the signal and the template and is defined as

$$\text{SNR} = 4 \int_0^\infty \frac{\tilde{h}_1^*(f')\tilde{h}_2(f')}{S_h(f')} df' = \langle h_1 | h_2 \rangle, \tag{7.29}$$

where * denotes complex conjugation for ease of readability. Here, $h_1(t)$ corresponds to a ringdown waveform that is tapered at t_{merger} and acts as a signal. We filter this against the template, $h_2(t)$, which is tapered with varying start time. Further, $S_h(f)$ corresponds to power spectral density (PSD) of aLIGO at design sensitivity [119]. However, since we present our results in terms of ratios, our analysis remains valid to any detector noise curve. Then, a Fourier transform is taken to evaluate Eq. (7.29). Here we use only the $l = m = 2$ spin-weighted spherical harmonic mode of the RWZ strain waveform computed in Sec. 7.4. The system is considered to be optimally oriented with respect to the detector for this calculation.

The tapering is done with a tanh window function defined as

$$\mathfrak{W}(t) = \tanh[\alpha_0(t - t_0)]/2. \tag{7.30}$$

t_0 is the time around which the tapering is centered, and it is set to the start time of the perturbative regime. α_0 is set to 10 in making the top panel of Fig. 7.20. Furthermore, we confirm that our results do not change significantly with the tuning parameter α_0 using $\alpha_0 = \{2, 5, 10, 20\}\ M^{-1}$.

We then present percentage decrease of SNR in the top panel of Fig. 7.20 by defining 100% for start time at t_{merger}. Further, on this same plot, we also indicate the amplitude of perturbation in the strong-field region (as calculated using the algebraic measures) at the start time, giving an insight into how statistical and systematic errors vary with the choice of start time.

The bottom panel of Fig. 7.20 presents the total energy radiated through the merger-ringdown as a function of time. This indicates the strength of GW signal and is calculated by integrating [175]

$$\frac{dE}{dt} = \lim_{r \to \infty} \frac{r^2}{16\pi} \oint \left| \int_{-\infty}^t \Psi_4 dt' \right|^2 d\Omega. \tag{7.31}$$

Furthermore, on the same plot, we mark the percentage decrease of the Kerrness measures from their peak values, providing a comparison between the strength of the signal left for performing the analysis versus Kerrness evaluated in the strong-field region.

To impress the sharp trade-off in systematic and statistical uncertainties in choosing the start time of the ringdown and, to provide an intuition of implication of Fig. 7.20, we present the spread in estimation of dominant QNM frequency, f_{22} in Fig. 7.21. For this, we calculate the spread using the Fisher information matrix formalism similar to that in Eq. 4.1a of [45], for a GW150914-like system. In particular, we set f_{22} to 253.7 Hz and the quality factor, Q_{22} to 3.2. However, we emphasize that this is a rough estimate intended only to provide intuition and, we plan to follow this up by a rigorous Bayesian parameter estimation in the future.

We present the interplay between the systematic and statistical uncertainty concisely in Table 7.3. Furthermore, we find that by the time the news function peaks, the SNR has already dropped down to 60%. However, at this time, the algebraic Kerrness measures are at their peak value. We also observe that by about a cycle of news function, there is less than 20 percent SNR left in the signal. Therefore, there seems to be a sharp trade-off between the systematic modeling error and statistical uncertainties.

Comparison with GW150914 testing GR paper

The test of consistency of ringdown of the GW150914 signal with the analytically predicted QNM frequency is given in Fig. 5 of [14]. The analysis chooses various start times of ringdown, namely t_{merger} + 0, 1, 3, 5, 6.5 ms. At a start time of t_{merger} + 3 ms (or later), parameter estimation of the dominant QNM in ringdown is consistent with predictions using initial masses and spins.

A time of 3 ms for the system corresponds to $9.4\,M$ from t_{merger}. In our analysis, $t_{\text{merger}} = 3839\,M$ (cf. Eq. (7.27)), while the peak of the news function occurs at $3846\,M$. Thus, 3 ms corresponds to $2.4\,M$ after the peak of the news function. In this region, as shown in Fig. 7.22, the perturbation amplitude is $\gtrsim 7.5 \times 10^{-3}$. Our analysis indicates that this corresponds to a relatively large deviation from Kerr. Recall that Fig. 7.4 suggests that $\varepsilon = 5 \times 10^{-3}$ is the approximate start of the nonlinear regime.

With a start time of t_{merger} + 3 ms, the SNR was about 8.5, and the spread in the estimate of QNM frequency was roughly 40 Hz [14]. Because of this low SNR and
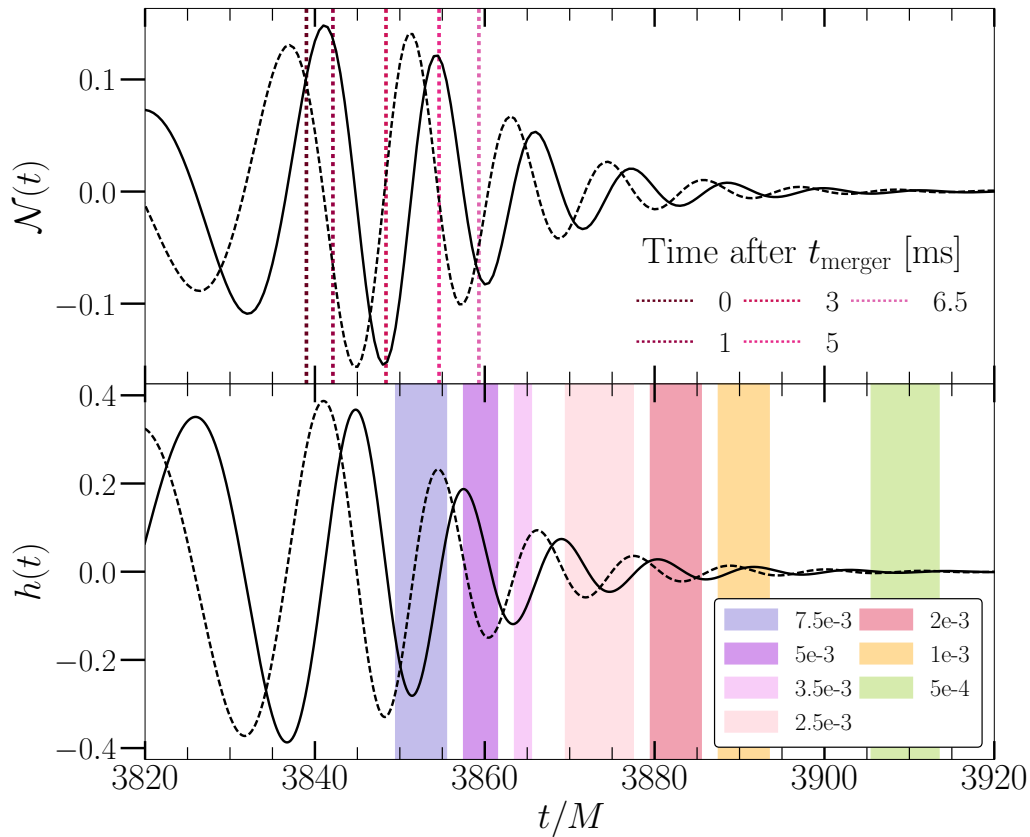
Figure 7.22: Comparison of the times chosen in the testing GR study of GW150914 [14]. Here, we make statements about their validity to perform tests that rely on the perturbative nature of the BH. Specifically, we propose that a plot of this nature be done for future detections, especially if the SNR is high, to gain an insight into the inferred strong-field perturbation amplitudes corresponding to different choices of ringdown start time. The dotted line in the **top panel** shows different choices of start time for performing tests on the detector data. The **bottom panel** shows what each time choice corresponds to in the simulation gauge. Although a practical choice of start time to perform tests like no-hair theorem tests should be decided based on the interplay between the statistical and systematic uncertainty, a plot of this nature gives significant understanding of the results of such tests. For instance, in the case of GW150914, had the signal been much louder than what we observed, this plot suggests that we *could* get biased results due to large inferred perturbation amplitude in the strong-field leading to errors in modeling the post-merger as a perturbed BH at 3 ms.

high spread, the GW150914 testing GR analysis may not have been sensitive to the large non-Kerrness we see close to the BH. However, in the case of higher SNR, where the analysis is sensitive to the systematics of the ringdown model, our study suggests picking a later start time.

Our analysis uses geometric and algebraic conditions to identify isometry to Kerr. However, these conditions do not directly measure the deviation of the curvature BH potential from that of Kerr. Since the QNM are intrinsic tests of the BH potential along with the boundary conditions, deviation of QNM frequencies will depend on details of the BH potential, and thus are not directly quantified in our measures. Additionally, the parameters used in this study correspond to `SXS:BBH:0305` waveform used in the GW150914 detection paper [10], which are slightly different from those of the MAP waveform used in the testing GR paper.

7.5   Conclusion

In this study, we present a method for validating choices of the time at which a BBH GW signal can be considered to enter the ringdown stage. This is done by computing algebraic and geometric measures of Kerrness in the strong-field region of an NR simulation of a BBH ringdown, and then associating each point on the asymptotic-frame waveform with a particular value of these Kerrness measures. Thus, for each point on the asymptotic-frame waveform there is an estimate for how close the BH spacetime is to Kerr spacetime. This is the first time this set of measures, proposed in [93], is evaluated in the strong-field region. This is also the first time measures of Kerrness in the strong-field region are mapped onto the waveform. We outline this method in Secs. 7.2 and 7.3, and implement this analysis in Sec. 7.4 on a GW150914-like NR simulation.

We observe that after merger, the Kerrness measures of a BBH ringdown simulation decrease exponentially with coordinate time in the simulation, eventually settling to a numerical noise floor, as shown in Fig. 7.9. This decay is consistent with measuring Kerrness using multipole moments of the apparent horizon, as in Fig. 7.8 and [152]. In all cases, the measures on the final slice of the simulation indicate that the final remnant is a Kerr BH, thus providing numerical consistency with the BH uniqueness theorem. Moreover, we find that the final state in the multipolar analysis depends just on mass and spin, which serves as a confirmation of the no-hair theorem in the strong-field region. Additionally, as shown in Fig. 7.10, the Kerrness measures have a quadrupolar (with $|m| = 2$) structure consistent with the dominant

gravitational radiation. The geometric measures, which rely on the existence of a Killing vector field, first decay to zero close to the horizon, then later they decay at larger radii as gravitational radiation propagates out. On the other hand, algebraic measures, which depend on principal null directions, first decay to zero at larger radii, before decaying near the BH. We also see that the NUT parameter remains zero during merger and ringdown, as shown in Fig. 7.11.

These gauge-independent Kerrness measures are crucial to the nonlinear stability analysis of Kerr, as they quantify the deviation from being isometric to Kerr. The analytical behavior of these measures with perturbation amplitude is unknown [107, 92]. Through this study, we provide insights into their numerical behavior in Fig. 7.4. We find that all of these measures scale quadratically with ε for low amplitude perturbations, but acquire higher-order nonlinearities for larger perturbation amplitudes. Furthermore, in Figs. 7.9 and 7.10, we provide the radial behavior of these measures, up to a large radius of $R = 128\,M$. For a BBH simulation, we track these measures starting from merger, where linear perturbation theory is not expected to hold. Despite the large initial excitation, our study shows that the BBH ringdown simulation evolves to a final Kerr state, providing a numerical validation of the nonlinear stability of Kerr.

To connect the Kerrness measures in the strong-field region to the asymptotic waveform at $\mathcal{I}^+$, we use CCE, which evolves Einstein's equations on a foliation of outgoing null hypersurfaces. A null characteristic evolution can be done only in a region free from caustics. We demonstrate that CCE results using a worldtube at $R = 5\,M$ are consistent with those done from larger radii. This implies that during ringdown, caustics only exist very close to the BH. Furthermore, we show that the map between the strong-field region and the wave zone can be extended all the way in to $R = 5\,M$.

Although caustics do not form, we see in Figs. 7.10 and 7.16 strong features in the curvature quantity Ψ_4 in the region enclosed by $R \sim 10\,M$. This implies that our extraction radius choice of $R = 5\,M$ lies within the strong-field and within the support of the BH potential.

In Fig. 7.13, we label each point of the BBH ringdown waveform with the percentage decrease of the Kerrness measures in the strong-field region relative to their maximum values. In order to give a physical interpretation of the values of the Kerrness measures, we compare them throughout the post-merger spacetime to those evaluated on a $l = m = 2$ QNM perturbed Kerr BH of the same final mass and

spin. From this we infer the amplitude of BH perturbation during ringdown and map onto a particular point in the BBH ringdown waveform; this is marked on the BBH ringdown waveform in Fig. 7.18.

As the BBH simulation proceeds after merger, the strong-field region starts looking like Kerr, indicating the validity of perturbative analysis. However, as time progresses, the amplitude of the ringdown decreases, leading to a rapid decay in SNR in a GW detection. We find that by the time the Kerrness measures decrease to 50% of their peak values, there is only about 20% SNR left in the signal. In terms of perturbation amplitude close to the BH, this maps to an amplitude between $7.5 - 5 \times 10^{-3}$. This occurs after $1 - 1.5$ cycles of the news function, which corresponds to $\sim 16.4\,M$ after t_{merger}. Additionally, we find that the start time of ringdown used in [14], $t_{\mathrm{merger}} + 3$ ms, corresponds to an amplitude of 7.5×10^{-3}. Our results also agree with the start time proposed in [176]. In future detections with higher SNR, where the statistical noise is significantly smaller, one may need to choose a later start time to perform precision tests of GR such as no-hair theorem tests.

A future extension to this project would be to investigate methods that allow us to perform similar source-asymptotic frame associations for smaller radii. For instance, the light ring would be an interesting region to monitor, as it is crucial to the QNM structure. This can perhaps be done numerically through ray-tracing methods such as those used in [53] and [54] to understand the evolution of the peak of the BH potential (if it forms). Another possible technique could be to try performing CCE from smaller radii after the high amplitude of the initial excitation has reduced. Additionally, being able to perform this association at smaller radii would allow one to understand the propagation of perturbations very close to the BH horizon onto the waveform; these are expected to be redshifted and appear on the waveform with a large time delay.

Another avenue of future work would be investigating the effects of implementing a more realistic condition on the initial null hypersurface by relaxing the no-ingoing-waves condition used in performing CCE. In addition, we can study the trade-off involved in choosing an earlier ringdown time, which will decrease the spread in recovered ringdown parameter posterior distributions and increase the systematic errors that arise because of deviations from Kerr in the strong-field region.

The methods used in this paper can be applied to future BBH detections in order to guide the choice of the start time of ringdown. For the sake of quick reference to the

procedure described in this paper, we concisely enumerated the steps in Sec. 7.2. Note that the results of this paper approximately hold for any equal mass system with an appropriate mass rescaling (cf. footnote 2) and effective spin near zero. The analysis presented, however, is fully generic and holds for all spins and masses. Our method would better allow one to perform precision tests of GR that depend on being in perturbative regime, such as tests of the no-hair theorem and area theorem. With this procedure, we provide an algorithmic way to check whether an unexpected deviation in a QNM analysis is due to not being in the perturbative regime, rather than due to a violation of GR or corresponding theorems.

For future detections, we plan to repeat this analysis using an NR simulation with the MAP waveform parameters.

7.A Kerr-NUT parameters

In this appendix, we provide a review of the parameters of the Kerr-NUT solution. The Kerr family of vacuum solutions is unique when one imposes axisymmetry, stationarity and regularity on the BH horizon along with asymptotic flatness. However, if one allows for generalization by relaxing the asymptotic flatness condition, one arrives at a family of solutions called Kerr-NUT. This solution is a part of the broader family of Einstein-Maxwell type D solutions. This generalized family of spacetimes is parameterized by 6 parameters (potentially 7 if one includes the cosmological constant Λ). In Table 7.4, we summarize the parameters, as well as their physical meaning and symbols used in various texts.

The general Einstein-Maxwell Type D solution (including cosmological constant Λ) has the form given in Eq. 21.11 of [187], with parameters m, l, γ, ε, e, and g. m refers to the mass parameter (closely related to the mass of the BH), γ is related to the angular momentum parameter a (closely related to the spin of the BH), ε is related to the acceleration b, e is the electric charge, g is the magnetic charge, and l is known as the NUT parameter. As outlined in [155], the mass and the NUT parameter form a complex quantity, as do the angular momentum and the acceleration, similarly to the electric and magnetic charges. In [155], ε and γ do not appear in the curvature quantities, and are called kinematical parameters, while the others are dynamical parameters.

As shown in Table 21.1 of [187], setting all of the parameters to zero except for m, a (and hence γ and ε), and e yields the Kerr-Newman solution, while also setting $a = 0$ yields the Reissner-Nordstrom solution. Kerr-Taub-NUT metrics, meanwhile, are

parametrized by mass, spin, and l, with $l \neq 0$, and are thought to be unphysical [19]. The vacuum BBH case considered in this study, meanwhile, sets $e = 0$ and $g = 0$, since there are no electric or magnetic charges at the start of the simulation, and no sourcing of them during the simulation.

An accelerating and rotating BH with a NUT charge will have non-zero m, l, a, and b, with $a > l$. A Kerr solution with a NUT charge will then have $b = 0$. An accelerating and rotating BH, meanwhile, will have $l = 0$. Finally, the Kerr solution has both $l = 0$ and $b = 0$. An illustration of this is provided in Fig. 1 of [96]. The condition $l = 0$ gives the Kerr 2 condition considered in this paper, given in Eq. (7.16).

After setting $l = 0$, the parameters m, ε and γ are related to the mass and spin of a BH are as follows,

$$\text{mass} = \frac{m}{\varepsilon^{\frac{3}{2}}} \quad \text{and} \quad \text{spin} = \frac{2\sqrt{|\gamma|}}{\varepsilon}. \tag{7.32}$$

Since, $\varepsilon > 0$ and $m > 0$ for a Kerr BH, the condition that $b = 0$ gives $\varepsilon > 0$, which corresponds to the Kerr 3 condition given in Eq. (7.17).

	Stephani [187]	García-Parrado [93]	Plebanski [155]	Griffiths [96]
Cosmological constant	Λ		λ	
Mass parameter	m	μ	m	m
NUT parameter	l	λ	n	n
Angular momentum parameter	γ	γ	γ	k
Acceleration parameter	ε	ϵ	ϵ	ϵ
Electric charge	e		e	e
Magnetic charge	g		g	g

Table 7.4: Parameters of the family of the Einstein-Maxwell type D solutions, presented with physical meanings in the rows and naming conventions in various literature in the columns. These parameters do not measure the physical quantities directly but are intimately connected to the physical quantities they describe. For instance, Eq. (7.32) shows how the mass and spin of a BH are related to the mass parameter and the angular momentum parameter.

BIBLIOGRAPHY

[1]   http://www.black-holes.org/waveforms.

[2]   Michael Boyle et al. "The SXS Collaboration catalog of binary black hole simulations". In: (2019). arXiv: 1904.04831 [gr-qc].

[3]   J. Aasi et al. "Advanced LIGO". In: *Class. Quant. Grav.* 32 (2015), p. 074001. DOI: 10.1088/0264-9381/32/7/074001. arXiv: 1411.4547 [gr-qc].

[4]   B. P. Abbott et al. "Binary Black Hole Mergers in the first Advanced LIGO Observing Run". In: *Phys. Rev.* X6.4 (2016), p. 041015. DOI: 10.1103/PhysRevX.6.041015. arXiv: 1606.04856 [gr-qc].

[5]   B. P. Abbott et al. "GW151226: Observation of Gravitational Waves from a 22-Solar-Mass Binary Black Hole Coalescence". In: *Phys. Rev. Lett.* 116.24 (2016), p. 241103. DOI: 10.1103/PhysRevLett.116.241103. arXiv: 1606.04855 [gr-qc].

[6]   B. P. Abbott et al. "GW170814: A Three-Detector Observation of Gravitational Waves from a Binary Black Hole Coalescence". In: *Phys. Rev. Lett.* 119.14 (2017), p. 141101. DOI: 10.1103/PhysRevLett.119.141101. arXiv: 1709.09660 [gr-qc].

[7]   B. P. Abbott et al. "GW170814: A Three-Detector Observation of Gravitational Waves from a Binary Black Hole Coalescence". In: *Phys. Rev. Lett.* 119 (14 Oct. 2017), p. 141101. DOI: 10.1103/PhysRevLett.119.141101. URL: https://link.aps.org/doi/10.1103/PhysRevLett.119.141101.

[8]   B. P. Abbott et al. "GW170817: Observation of Gravitational Waves from a Binary Neutron Star Inspiral". In: *Phys. Rev. Lett.* 119.16 (2017), p. 161101. DOI: 10.1103/PhysRevLett.119.161101. arXiv: 1710.05832 [gr-qc].

[9]   B. P. Abbott et al. "GWTC-1: A Gravitational-Wave Transient Catalog of Compact Binary Mergers Observed by LIGO and Virgo during the First and Second Observing Runs". In: (2018). arXiv: 1811.12907 [astro-ph.HE].

[10] B. P. Abbott et al. "Observation of Gravitational Waves from a Binary Black Hole Merger". In: *Phys. Rev. Lett.* 116.6 (2016), p. 061102. DOI: 10.1103/PhysRevLett.116.061102. arXiv: 1602.03837 [gr-qc].

[11] B. P. Abbott et al. "Observation of Gravitational Waves from a Binary Black Hole Merger". In: *Phys. Rev. Lett.* 116 (6 Feb. 2016), p. 061102. DOI: 10.1103/PhysRevLett.116.061102. URL: http://link.aps.org/doi/10.1103/PhysRevLett.116.061102.

[12] B. P. Abbott et al. "Properties of the Binary Black Hole Merger GW150914". In: *Phys. Rev. Lett.* 116.24 (2016), p. 241102. DOI: 10.1103/PhysRevLett.116.241102. arXiv: 1602.03840 [gr-qc].

[13] B. P. Abbott et al. "Prospects for Observing and Localizing Gravitational-Wave Transients with Advanced LIGO, Advanced Virgo and KAGRA". In: *Living Rev. Rel.* 21.1 (2018), p. 3. DOI: 10.1007/s41114-018-0012-9,10.1007/lrr-2016-1. arXiv: 1304.0670 [gr-qc].

[14] B. P. Abbott et al. "Tests of general relativity with GW150914". In: *Phys. Rev. Lett.* 116.22 (2016), p. 221101. DOI: 10.1103/PhysRevLett.116.221101, 10.1103/PhysRevLett.121.129902. arXiv: 1602.03841 [gr-qc].

[15] B. P. Abbott et al. "Tests of General Relativity with the Binary Black Hole Signals from the LIGO-Virgo Catalog GWTC-1". In: (2019). arXiv: 1903.04467 [gr-qc].

[16] Benjamin P. Abbott et al. "GW170104: Observation of a 50-Solar-Mass Binary Black Hole Coalescence at Redshift 0.2". In: *Phys. Rev. Lett.* 118.22 (2017). [Erratum: Phys. Rev. Lett.121,no.12,129901(2018)], p. 221101. DOI: 10.1103/PhysRevLett.118.221101,10.1103/PhysRevLett.121.129901. arXiv: 1706.01812 [gr-qc].

[17] A. A. Abdujabbarov, L. Rezzolla, and B. J. Ahmedov. "A coordinate independent characterization of a black hole shadow". In: *Mon. Not. Roy. Astron. Soc.* 454.3 (2015), pp. 2423–2435. DOI: 10.1093/mnras/stv2079. arXiv: 1503.09054 [gr-qc].

[18] Stephon Alexander and Nicolas Yunes. "Chern-Simons Modified General Relativity". In: *Phys. Rept.* 480 (2009), pp. 1–55. DOI: 10.1016/j.physrep.2009.07.002. arXiv: 0907.2562 [hep-th].

[19] Alikram N. Aliev, Hakan Cebeci, and Tekin Dereli. "Kerr-Taub-NUT spacetime with Maxwell and dilaton fields". In: *Phys. Rev. D* 77 (12 June 2008), p. 124022. DOI: 10.1103/PhysRevD.77.124022. URL: https://link.aps.org/doi/10.1103/PhysRevD.77.124022.

[20] Yacine Ali-Haïmoud and Yanbei Chen. "Slowly-rotating stars and black holes in dynamical Chern-Simons gravity". In: *Phys. Rev.* D84 (2011), p. 124033. DOI: 10.1103/PhysRevD.84.124033. arXiv: 1110.5329 [astro-ph.HE].

[21] Luis Alvarez-Gaume and Edward Witten. "Gravitational Anomalies". In: *Nucl. Phys.* B234 (1984), p. 269. DOI: 10.1016/0550-3213(84)90066-X.

[22] P. Amaro-Seoane et al. "Laser Interferometer Space Antenna". In: *ArXiv e-prints* (Feb. 2017). arXiv: 1702.00786 [astro-ph.IM].

[23] Peter Anninos et al. "Headon collision of two black holes: Comparison of different approaches". In: *Phys. Rev.* D52 (1995), pp. 4462–4480. DOI: 10.1103/PhysRevD.52.4462. arXiv: gr-qc/9505042 [gr-qc].

[24] Peter Anninos et al. "The Collision of two black holes". In: *Phys. Rev. Lett.* 71 (1993), pp. 2851–2854. DOI: 10.1103/PhysRevLett.71.2851. arXiv: gr-qc/9309016 [gr-qc].

[25] Theocharis A. Apostolatos. "Search templates for gravitational waves from precessing, inspiraling binaries". In: *Phys. Rev. D* 52 (2 July 1995), pp. 605–620. DOI: 10.1103/PhysRevD.52.605. URL: https://link.aps.org/doi/10.1103/PhysRevD.52.605.

[26] Bernardo Araneda and Gustavo Dotti. "Petrov type of linearly perturbed type D spacetimes". In: *Class. Quant. Grav.* 32.19 (2015), p. 195013. DOI: 10.1088/0264-9381/32/19/195013. arXiv: 1502.07153 [gr-qc].

[27] M. Armano et al. "Sub-Femto- g Free Fall for Space-Based Gravitational Wave Observatories: LISA Pathfinder Results". In: *Phys. Rev. Lett.* 116.23 (2016), p. 231101. DOI: 10.1103/PhysRevLett.116.231101.

[28] R. Arnowitt, S. Deser, and C. W. Misner. "Dynamical Structure and Definition of Energy in General Relativity". In: *Phys. Rev.* 116 (5 Dec. 1959), pp. 1322–1330. DOI: 10.1103/PhysRev.116.1322. URL: https://link.aps.org/doi/10.1103/PhysRev.116.1322.

[29] Dimitry Ayzenberg and Nicolas Yunes. "Black Hole Shadow as a Test of General Relativity: Quadratic Gravity". In: (2018). arXiv: 1807.08422 [gr-qc].

[30] Thomas Backdahl and Juan A. Valiente Kroon. "A geometric invariant measuring the deviation from Kerr data". In: *Phys. Rev. Lett.* 104 (2010), p. 231102. DOI: 10.1103/PhysRevLett.104.231102. arXiv: 1001.4492 [gr-qc].

[31] Thomas Backdahl and Juan A. Valiente Kroon. "Constructing 'non-Kerrness' on compact domains". In: *J. Math. Phys.* 53 (2012), p. 042503. DOI: 10.1063/1.3702569. arXiv: 1111.6019 [gr-qc].

[32] Thomas Backdahl and Juan A. Valiente Kroon. "On the construction of a geometric invariant measuring the deviation from Kerr data". In: *Annales Henri Poincare* 11 (2010), pp. 1225–1271. DOI: 10.1007/s00023-010-0063-2. arXiv: 1005.0743 [gr-qc].

[33] Vishal Baibhav et al. "Black Hole Spectroscopy: Systematic Errors and Ringdown Energy Estimates". In: (2017). arXiv: 1710.02156 [gr-qc].

[34] J. Baker and M. Campanelli. "Making use of geometrical invariants in black hole collisions". In: *Phys. Rev. D* 62.12, 127501 (Dec. 2000), p. 127501. DOI: 10.1103/PhysRevD.62.127501. eprint: gr-qc/0003031.

[35] John G. Baker et al. "Gravitational waves from black hole collisions via an eclectic approach". In: *Class. Quant. Grav.* 17 (2000), pp. L149–L156. DOI: 10.1088/0264-9381/17/20/102. arXiv: gr-qc/0003027 [gr-qc].

[36] John Baker, Manuela Campanelli, and Carlos O. Lousto. "The Lazarus project: A pragmatic approach to binary black hole evolutions". In: *Phys. Rev. D* 65 (4 Jan. 2002), p. 044001. DOI: 10.1103/PhysRevD.65.044001. URL: https://link.aps.org/doi/10.1103/PhysRevD.65.044001.

[37] Tessa Baker, Dimitrios Psaltis, and Constantinos Skordis. "Linking Tests of Gravity On All Scales: from the Strong-Field Regime to Cosmology". In: *Astrophys. J.* 802 (2015), p. 63. DOI: 10.1088/0004-637X/802/1/63. arXiv: 1412.3455 [astro-ph.CO].

[38] Kevin Barkett and Mark Scheel. In: (2017). Forthcoming.

[39] Thomas W. Baumgarte, Niall O Murchadha, and Harald P. Pfeiffer. "The Einstein constraints: Uniqueness and non-uniqueness in the conformal thin sandwich approach". In: *Phys. Rev.* D75 (2007), p. 044009. DOI: 10.1103/PhysRevD.75.044009. arXiv: gr-qc/0610120 [gr-qc].

[40] Thomas W. Baumgarte and Stuart L. Shapiro. *Numerical Relativity: Solving Einstein's Equations on the Computer*. Cambridge University Press, 2010. DOI: 10.1017/CBO9781139193344.

[41] K. Becker, M. Becker, and J. H. Schwarz. *String theory and M-theory: A modern introduction*. Cambridge University Press, 2006.

[42] Carl M. Bender and Steven A. Orszag. *Advanced mathematical methods for scientists and engineers*. International Series in Pure and Applied Mathematics. McGraw-Hill Book Co., New York, 1978, pp. xiv+593. ISBN: 0-07-004452-X.

[43] Emanuele Berti et al. "Testing General Relativity with Present and Future Astrophysical Observations". In: *Class. Quant. Grav.* 32 (2015), p. 243001. DOI: 10.1088/0264-9381/32/24/243001. arXiv: 1501.07274 [gr-qc].

[44] Emanuele Berti et al. "Inspiral, merger and ringdown of unequal mass black hole binaries: A Multipolar analysis". In: *Phys. Rev.* D76 (2007), p. 064034. DOI: 10.1103/PhysRevD.76.064034. arXiv: gr-qc/0703053 [GR-QC].

[45] Emanuele Berti et al. "Matched-filtering and parameter estimation of ringdown waveforms". In: *Phys. Rev.* D76 (2007), p. 104044. DOI: 10.1103/PhysRevD.76.104044. arXiv: 0707.1202 [gr-qc].

[46] Emanuele Berti et al. "Numerical simulations of single and binary black holes in scalar-tensor theories: circumventing the no-hair theorem". In: *Phys. Rev.* D87.12 (2013), p. 124020. DOI: 10.1103/PhysRevD.87.124020. arXiv: 1304.2836 [gr-qc].

[47] Swetha Bhagwat et al. "On choosing the start time of binary black hole ringdowns". In: *Phys. Rev.* D97.10 (2018), p. 104065. DOI: 10.1103/PhysRevD.97.104065. arXiv: 1711.00926 [gr-qc].

[48] N. Bishop et al. "Cauchy-characteristic extraction in numerical relativity". In: *ArXiv General Relativity and Quantum Cosmology e-prints* (May 1997). eprint: gr-qc/9705033.

[49] Jonathan Blackman et al. "Numerical relativity waveform surrogate model for generically precessing binary black hole mergers". In: *Phys. Rev.* D96.2 (2017), p. 024058. DOI: 10.1103/PhysRevD.96.024058. arXiv: 1705.07089 [gr-qc].

[50] Jonathan Blackman et al. "A Surrogate Model of Gravitational Waveforms from Numerical Relativity Simulations of Precessing Binary Black Hole Mergers". In: *Phys. Rev.* D95.10 (2017), p. 104023. DOI: 10.1103/PhysRevD.95.104023. arXiv: 1701.00550 [gr-qc].

[51] Jonathan Blackman et al. "Fast and Accurate Prediction of Numerical Relativity Waveforms from Binary Black Hole Coalescences Using Surrogate Models". In: *Phys. Rev. Lett.* 115.12 (2015), p. 121102. DOI: 10.1103/PhysRevLett.115.121102. arXiv: 1502.07758 [gr-qc].

[52] Luc Blanchet and Thibault Damour. "Radiative gravitational fields in general relativity I. general structure of the field outside the source". In: *Phil. Trans. Roy. Soc. Lond.* A320 (1986), pp. 379–430. DOI: 10.1098/rsta.1986.0125.

[53] Andy Bohn, Lawrence E. Kidder, and Saul A. Teukolsky. "Parallel adaptive event horizon finder for numerical relativity". In: *Phys. Rev.* D94.6 (2016), p. 064008. DOI: 10.1103/PhysRevD.94.064008. arXiv: 1606.00437 [gr-qc].

[54] Andy Bohn et al. "What does a binary black hole merger look like?" In: *Class. Quant. Grav.* 32.6 (2015), p. 065002. DOI: 10.1088/0264-9381/32/6/065002. arXiv: 1410.7775 [gr-qc].

[55] H. Bondi, M. G. J. van der Burg, and A. W. K. Metzner. "Gravitational Waves in General Relativity. VII. Waves from Axi-Symmetric Isolated Systems". In: *Proceedings of the Royal Society of London. Series A, Mathematical and Physical Sciences* 269.1336 (1962), pp. 21–52. ISSN: 00804630. URL: http://www.jstor.org/stable/2414436.

[56] Michael Boyle and Abdul H. Mroue. "Extrapolating gravitational-wave data from numerical simulations". In: *Phys. Rev.* D80 (2009), p. 124045. DOI: 10.1103/PhysRevD.80.124045. arXiv: 0905.3177 [gr-qc].

[57] Richard Brito, Alessandra Buonanno, and Vivien Raymond. "Black-hole Spectroscopy by Making Full Use of Gravitational-Wave Modeling". In: *Phys. Rev.* D98.8 (2018), p. 084038. DOI: 10.1103/PhysRevD.98.084038. arXiv: 1805.00293 [gr-qc].

[58] David Brizuela, Jose M. Martin-Garcia, and Guillermo A. Mena Marugan. "xPert: Computer algebra for metric perturbation theory". In: *Gen. Rel. Grav.* 41 (2009), pp. 2415–2431. DOI: 10.1007/s10714-009-0773-2. arXiv: 0807.0824 [gr-qc].

[59] Manuela Campanelli, Carlos O. Lousto, and Yosef Zlochower. "Algebraic Classification of Numerical Spacetimes and Black-Hole-Binary Remnants". In: *Phys. Rev.* D79 (2009), p. 084012. DOI: 10.1103/PhysRevD.79.084012. arXiv: 0811.3006 [gr-qc].

[60] Manuela Campanelli et al. "Imposition of Cauchy data to the Teukolsky equation. III. The rotating case". In: *Phys. Rev. D* 58 (8 Sept. 1998), p. 084019. DOI: 10.1103/PhysRevD.58.084019. URL: https://link.aps.org/doi/10.1103/PhysRevD.58.084019.

[61] Bruce A. Campbell et al. "Gravitational dynamics with Lorentz Chern-Simons terms". In: *Nucl. Phys.* B351 (1991), pp. 778–792. DOI: 10.1016/S0550-3213(05)80045-8.

[62] Alejandro Cárdenas-Avendaño et al. "The exact dynamical Chern–Simons metric for a spinning black hole possesses a fourth constant of motion: A dynamical-systems-based conjecture". In: *Class. Quant. Grav.* 35.16 (2018), p. 165010. DOI: 10.1088/1361-6382/aad06f. arXiv: 1804.04002 [gr-qc].

[63] V. Cardoso, E. Franzin, and P. Pani. "Is the Gravitational-Wave Ringdown a Probe of the Event Horizon?" In: *Physical Review Letters* 116.17, 171101 (Apr. 2016), p. 171101. DOI: 10.1103/PhysRevLett.116.171101. arXiv: 1602.07309 [gr-qc].

[64] Sean M. Carroll. *Spacetime and geometry: An introduction to general relativity*. 2004. ISBN: 0805387323.

[65] Gregorio Carullo et al. "Empirical tests of the black hole no-hair conjecture using gravitational-wave observations". In: *Phys. Rev.* D98.10 (2018), p. 104020. DOI: 10.1103/PhysRevD.98.104020. arXiv: 1805.04760 [gr-qc].

[66] Lin-Yuan Chen, Nigel Goldenfeld, and Y. Oono. "The Renormalization group and singular perturbations: Multiple scales, boundary layers and reductive perturbation theory". In: *Phys. Rev.* E54 (1996), pp. 376–394. DOI: 10.1103/PhysRevE.54.376. arXiv: hep-th/9506161 [hep-th].

[67] Yvonne Choquet-Bruhat. "Beginnings of the Cauchy problem". In: (2014). arXiv: 1410.3490 [gr-qc].

[68] Michael I. Cohen, Harald P. Pfeiffer, and Mark A. Scheel. "Revisiting Event Horizon Finders". In: *Class. Quant. Grav.* 26 (2009), p. 035005. DOI: 10.1088/0264-9381/26/3/035005. arXiv: 0809.2628 [gr-qc].

[69] Gregory B. Cook and Harald P. Pfeiffer. "Excision boundary conditions for black-hole initial data". In: *Phys. Rev. D* 70.10 (Nov. 2004), p. 104016. DOI: 10.1103/PhysRevD.70.104016.

[70] Neil J. Cornish and Tyson B. Littenberg. "BayesWave: Bayesian Inference for Gravitational Wave Bursts and Instrument Glitches". In: *Class. Quant. Grav.* 32.13 (2015), p. 135012. DOI: 10.1088/0264-9381/32/13/135012. arXiv: 1410.3835 [gr-qc].

[71] Neil Cornish et al. "Gravitational Wave Tests of General Relativity with the Parameterized Post-Einsteinian Framework". In: *Phys. Rev.* D84 (2011), p. 062003. DOI: 10.1103/PhysRevD.84.062003. arXiv: 1105.2088 [gr-qc].

[72] Robert Delbourgo and Abdus Salam. "The gravitational correction to pcac". In: *Phys. Lett.* 40B (1972), pp. 381–382. DOI: 10.1016/0370-2693(72)90825-8.

[73] Terence Delsate, Carlos Herdeiro, and Eugen Radu. "Non-perturbative spinning black holes in dynamical Chern-Simons gravity". In: (2018). arXiv: 1806.06700 [gr-qc].

[74] Térence Delsate, David Hilditch, and Helvi Witek. "Initial value formulation of dynamical Chern-Simons gravity". In: *Phys. Rev.* D91.2 (2015), p. 024027. DOI: 10.1103/PhysRevD.91.024027. arXiv: 1407.6727 [gr-qc].

[75] J. Dexter and P. C. Fragile. "Tilted black hole accretion disc models of Sagittarius A*: time-variable millimetre to near-infrared emission". In: *Monthly Notices of the Royal Astronomical Society* 432 (July 2013), pp. 2252–2272. DOI: 10.1093/mnras/stt583. arXiv: 1204.4454 [astro-ph.HE].

[76] O. Dreyer et al. "Black-hole spectroscopy: testing general relativity through gravitational-wave observations". In: *Classical and Quantum Gravity* 21 (Feb. 2004), pp. 787–803. DOI: 10.1088/0264-9381/21/4/003. eprint: gr-qc/0309007.

[77] Sergei Dyda, Eanna E. Flanagan, and Marc Kamionkowski. "Vacuum Instability in Chern-Simons Gravity". In: *Phys. Rev.* D86 (2012), p. 124031. DOI: 10.1103/PhysRevD.86.124031. arXiv: 1208.4871 [gr-qc].

[78] William E. East, Fethi M. Ramazanoğlu, and Frans Pretorius. "Black Hole Superradiance in Dynamical Spacetime". In: *Phys. Rev.* D89.6 (2014), p. 061503. DOI: 10.1103/PhysRevD.89.061503. arXiv: 1312.4529 [gr-qc].

[79] Tohru Eguchi and Peter G. O. Freund. "Quantum Gravity and World Topology". In: *Phys. Rev. Lett.* 37 (1976), p. 1251. DOI: 10.1103/PhysRevLett.37.1251.

[80] EHT Collaboration and others. "First M87 Event Horizon Telescope Results. I. The Shadow of the Supermassive Black Hole," in: *Astrophys. J. Lett.* 875.L1 (2019), p. 064008. DOI: 10.3847/2041-8213/ab0ec7.

[81] EHT Collaboration and others. "First M87 Event Horizon Telescope Results. VI. The Shadow and Mass of the Central Black Hole". In: *Astrophys. J. Lett.* 875.L1 (2019), p. 064008. DOI: 10.3847/2041-8213/ab1141.

[82] Albert Einstein. "The Foundation of the General Theory of Relativity". In: *Annalen Phys.* 49.7 (1916). [Annalen Phys.354,no.7,769(1916)], pp. 769–822. DOI: 10.1002/andp.200590044,10.1002/andp.19163540702.

[83] Solomon Endlich et al. "An effective formalism for testing extensions to General Relativity with gravitational waves". In: (2017). arXiv: 1704.01590 [gr-qc].

[84] H. Falcke and S. B. Markoff. "Toward the event horizon—the supermassive black hole in the Galactic Center". In: *Class. Quant. Grav.* 30 (2013), p. 244003. DOI: 10.1088/0264-9381/30/24/244003. arXiv: 1311.1841 [astro-ph.HE].

[85] Heino Falcke. "Imaging black holes: past, present and future". In: *J. Phys. Conf. Ser.* 942.1 (2017), p. 012001. DOI: 10.1088/1742-6596/942/1/012001. arXiv: 1801.03298 [astro-ph.HE].

[86] Joan Josep Ferrando, Juan Antonio Morales, and Juan Antonio SÃ¡ez. "Covariant determination of the Weyl tensor geometry". In: *Classical and Quantum Gravity* 18.22 (2001), p. 4939. URL: http://stacks.iop.org/0264-9381/18/i=22/a=315.

[87] Helmut Friedrich. "On the hyperbolicity of Einstein's and other gauge field equations". In: *Comm. Math. Phys.* 100.4 (1985), pp. 525–543. URL: https://projecteuclid.org:443/euclid.cmp/1104114004.

[88] Helmut Friedrich, Istvan Racz, and Robert M. Wald. "On the rigidity theorem for space-times with a stationary event horizon or a compact Cauchy horizon". In: *Commun. Math. Phys.* 204 (1999), pp. 691–707. DOI: 10.1007/s002200050662. arXiv: gr-qc/9811021 [gr-qc].

[89] Chad R. Galley and Ira Z. Rothstein. "Deriving analytic solutions for compact binary inspirals without recourse to adiabatic approximations". In: *Phys. Rev.* D95.10 (2017), p. 104054. DOI: 10.1103/PhysRevD.95.104054. arXiv: 1609.08268 [gr-qc].

[90] David Garfinkle, Frans Pretorius, and Nicolas Yunes. "Linear Stability Analysis and the Speed of Gravitational Waves in Dynamical Chern-Simons Modified Gravity". In: *Phys. Rev.* D82 (2010), p. 041501. DOI: 10.1103/PhysRevD.82.041501. arXiv: 1007.2429 [gr-qc].

[91] Matthew Giesler et al. "Black hole ringdown: the importance of overtones". In: (2019). arXiv: 1903.08284 [gr-qc].

[92] Alfonso García-Parrado Gómez-Lobo. Private communication.

[93] Alfonso García-Parrado Gómez-Lobo. "Vacuum type D initial data". In: *Class. Quant. Grav.* 33.17 (2016), p. 175005. DOI: 10.1088/0264-9381/33/17/175005. arXiv: 1602.08075 [gr-qc].

[94] S. Gossan, J. Veitch, and B. S. Sathyaprakash. "Bayesian model selection for testing the no-hair theorem with black hole ringdowns". In: *Phys. Rev.* D85 (2012), p. 124056. DOI: 10.1103/PhysRevD.85.124056. arXiv: 1111.5819 [gr-qc].

[95] Michael B. Green and John H. Schwarz. "Anomaly Cancellation in Supersymmetric D=10 Gauge Theory and Superstring Theory". In: *Phys. Lett.* 149B (1984), pp. 117–122. DOI: 10.1016/0370-2693(84)91565-X.

[96] J. B. Griffiths and Jiri Podolsky. "Accelerating and rotating black holes". In: *Class. Quant. Grav.* 22 (2005), pp. 3467–3480. DOI: 10.1088/0264-9381/22/17/008. arXiv: gr-qc/0507021 [gr-qc].

[97] D. Grumiller, W. Kummer, and D. V. Vassilevich. "Dilaton gravity in two-dimensions". In: *Phys. Rept.* 369 (2002), pp. 327–430. DOI: 10.1016/S0370-1573(02)00267-3. arXiv: hep-th/0204253 [hep-th].

[98] Carsten Gundlach. "Pseudospectral apparent horizon finders: An Efficient new algorithm". In: *Phys. Rev.* D57 (1998), pp. 863–875. DOI: 10.1103/PhysRevD.57.863. arXiv: gr-qc/9707050 [gr-qc].

[99] C. J. Handmer, B. Szilágyi, and J. Winicour. "Spectral Cauchy characteristic extraction of strain, news and gravitational radiation flux". In: *Classical and Quantum Gravity* 33.22, 225007 (Nov. 2016), p. 225007. DOI: 10.1088/0264-9381/33/22/225007. arXiv: 1605.04332 [gr-qc].

[100] Casey J. Handmer and B. Szilágyi. "Spectral Characteristic Evolution: A New Algorithm for Gravitational Wave Propagation". In: *Class. Quant. Grav.* 32.2 (2015), p. 025008. DOI: 10.1088/0264-9381/32/2/025008. arXiv: 1406.7029 [gr-qc].

[101] Casey J. Handmer, Béla Szilágyi, and Jeffrey Winicour. "Gauge Invariant Spectral Cauchy Characteristic Extraction". In: *Class. Quant. Grav.* 32.23 (2015), p. 235018. DOI: 10.1088/0264-9381/32/23/235018. arXiv: 1502.06987 [gr-qc].

[102] James Healy, Carlos O. Lousto, and Yosef Zlochower. "Remnant mass, spin, and recoil from spin aligned black-hole binaries". In: *Phys. Rev.* D90.10 (2014), p. 104004. DOI: 10.1103/PhysRevD.90.104004. arXiv: 1406.7295 [gr-qc].

[103] James Healy et al. "Late Inspiral and Merger of Binary Black Holes in Scalar-Tensor Theories of Gravity". In: *Class. Quant. Grav.* 29 (2012), p. 232002. DOI: 10.1088/0264-9381/29/23/232002. arXiv: 1112.3928 [gr-qc].

[104] Daniel A. Hemberger et al. "Dynamical Excision Boundaries in Spectral Evolutions of Binary Black Hole Spacetimes". In: *Class. Quant. Grav.* 30 (2013), p. 115001. DOI: 10.1088/0264-9381/30/11/115001. arXiv: 1211.6079 [gr-qc].

[105] Michael Holst et al. "Optimal constraint projection for hyperbolic evolution systems". In: *Phys. Rev.* D70 (2004), p. 084017. DOI: 10.1103/PhysRevD.70.084017. arXiv: gr-qc/0407011 [gr-qc].

[106] R. A. Hulse and J. H. Taylor. "Discovery of a pulsar in a binary system". In: 195 (Jan. 1975), pp. L51–L53. DOI: 10.1086/181708.

[107] A. D. Ionescu and S. Klainerman. "On the global stability of the wave-map equation in Kerr spaces with small angular momentum". In: (2014). arXiv: 1412.5679 [math.AP].

[108] Tim Johannsen. "Testing the No-Hair Theorem with Observations of Black Holes in the Electromagnetic Spectrum". In: *Class. Quant. Grav.* 33.12 (2016), p. 124001. DOI: 10.1088/0264-9381/33/12/124001. arXiv: 1602.07694 [astro-ph.HE].

[109] Eric Jones, Travis Oliphant, Pearu Peterson, et al. *SciPy: Open source scientific tools for Python*. 2001. URL: http://www.scipy.org/.

[110] I. Kamaretsos, M. Hannam, and B. S. Sathyaprakash. "Is Black-Hole Ringdown a Memory of Its Progenitor?" In: *Physical Review Letters* 109.14, 141102 (Oct. 2012), p. 141102. DOI: 10.1103/PhysRevLett.109.141102. arXiv: 1207.0399 [gr-qc].

[111] Ioannis Kamaretsos et al. "Black-hole hair loss: learning about binary progenitors from ringdown signals". In: *Phys. Rev.* D85 (2012), p. 024018. DOI: 10.1103/PhysRevD.85.024018. arXiv: 1107.0854 [gr-qc].

[112] Roy P. Kerr. "Gravitational Field of a Spinning Mass as an Example of Algebraically Special Metrics". In: *Phys. Rev. Lett.* 11 (5 Sept. 1963), pp. 237–238. DOI: 10.1103/PhysRevLett.11.237. URL: https://link.aps.org/doi/10.1103/PhysRevLett.11.237.

[113] G. Khanna and R. H. Price. "Black hole ringing, quasinormal modes, and light rings". In: *Phys. Rev. D* 95.8, 081501 (Apr. 2017), p. 081501. DOI: 10.1103/PhysRevD.95.081501. arXiv: 1609.00083 [gr-qc].

[114] Lawrence E. Kidder et al. "SpECTRE: A Task-based Discontinuous Galerkin Code for Relativistic Astrophysics". In: *J. Comput. Phys.* 335 (2017), pp. 84–114. DOI: 10.1016/j.jcp.2016.12.059. arXiv: 1609.00098 [astro-ph.HE].

[115] Lawrence E. Kidder et al. "Boundary conditions for the Einstein evolution system". In: *Phys. Rev.* D71 (2005), p. 064020. DOI: 10.1103/PhysRevD.71.064020. arXiv: gr-qc/0412116 [gr-qc].

[116] Kohkichi Konno, Toyoki Matsuyama, and Satoshi Tanda. "Rotating black hole in extended Chern-Simons modified gravity". In: *Prog. Theor. Phys.* 122 (2009), pp. 561–568. DOI: 10.1143/PTP.122.561. arXiv: 0902.4767 [gr-qc].

[117] Kohkichi Konno and Rohta Takahashi. "Scalar field excited around a rapidly rotating black hole in Chern-Simons modified gravity". In: *Phys. Rev.* D90.6 (2014), p. 064011. DOI: 10.1103/PhysRevD.90.064011. arXiv: 1406.0957 [gr-qc].

[118] Prayush Kumar et al. "Constraining the parameters of GW150914 & GW170104 with numerical relativity surrogates". In: (2018). arXiv: 1808.08004 [gr-qc].

[119] LIGO Scientific Collaboration et al. "Advanced LIGO". In: *Classical and Quantum Gravity* 32.7, 074001 (Apr. 2015), p. 074001. DOI: 10.1088/0264-9381/32/7/074001. arXiv: 1411.4547 [gr-qc].

[120] Lee Lindblom and Béla Szilágyi. "An Improved Gauge Driver for the GH Einstein System". In: *Phys. Rev. D* 80 (2009), p. 084019. eprint: arXiv:0904.4873.

[121] Lee Lindblom et al. "A New generalized harmonic evolution system". In: *Class. Quant. Grav.* 23 (2006), S447–S462. DOI: 10.1088/0264-9381/23/16/S09. arXiv: gr-qc/0512093 [gr-qc].

[122] Lee Lindblom et al. "A New generalized harmonic evolution system". In: *Class. Quant. Grav.* 23 (2006), S447–S462. DOI: 10.1088/0264-9381/23/16/S09. arXiv: gr-qc/0512093 [gr-qc].

[123] L. T. London. "Modeling ringdown II: non-precessing binary black holes". In: (2018). arXiv: 1801.08208 [gr-qc].

[124] Lionel London, Deirdre Shoemaker, and James Healy. "Modeling ringdown: Beyond the fundamental quasinormal modes". In: *Phys. Rev. D* 90 (12 Dec. 2014), p. 124032. DOI: 10.1103/PhysRevD.90.124032. URL: https://link.aps.org/doi/10.1103/PhysRevD.90.124032.

[125] Carlos O. Lousto and Bernard F. Whiting. "Reconstruction of black hole metric perturbations from Weyl curvature". In: *Phys. Rev.* D66 (2002), p. 024026. DOI: 10.1103/PhysRevD.66.024026. arXiv: gr-qc/0203061 [gr-qc].

[126] Geoffrey Lovelace et al. "Modeling the source of GW150914 with targeted numerical-relativity simulations". In: *Class. Quant. Grav.* 33.24 (2016), p. 244002. DOI: 10.1088/0264-9381/33/24/244002. arXiv: 1607.05377 [gr-qc].

[127] Geoffrey Lovelace. "Reducing spurious gravitational radiation in binary-black-hole simulations by using conformally curved initial data". In: *Class. Quantum Grav.* 26 (2009), p. 114002.

[128] Geoffrey Lovelace, Mark.A. Scheel, and Bela Szilagyi. "Simulating merging binary black holes with nearly extremal spins". In: *Phys. Rev.* D83 (2011), p. 024010. DOI: 10.1103/PhysRevD.83.024010. arXiv: 1010.2777 [gr-qc].

[129] Geoffrey Lovelace et al. "Binary-black-hole initial data with nearly-extremal spins". In: *Phys. Rev. D* 78 (2008), p. 084017. DOI: 10.1103/PhysRevD.78.084017.

[130] Marc Mars. "A Space-time characterization of the Kerr metric". In: *Class. Quant. Grav.* 16 (1999), pp. 2507–2523. DOI: 10.1088/0264-9381/16/7/323. arXiv: gr-qc/9904070 [gr-qc].

[131] Andrea Maselli et al. "Geodesic models of quasi-periodic-oscillations as probes of quadratic gravity". In: *Astrophys. J.* 843.1 (2017), p. 25. DOI: 10.3847/1538-4357/aa72e2. arXiv: 1703.01472 [astro-ph.HE].

[132] Pawel O. Mazur. "Black hole uniqueness theorems". In: (2000). arXiv: hep-th/0101012 [hep-th].

[133] Robert McNees, Leo C. Stein, and Nicolás Yunes. "Extremal black holes in dynamical Chern–Simons gravity". In: *Class. Quant. Grav.* 33.23 (2016), p. 235013. DOI: 10.1088/0264-9381/33/23/235013. arXiv: 1512.05453 [gr-qc].

[134] Simone Mercuri and Victor Taveras. "Interaction of the Barbero-Immirzi Field with Matter and Pseudo-Scalar Perturbations". In: *Phys. Rev.* D80 (2009), p. 104007. DOI: 10.1103/PhysRevD.80.104007. arXiv: 0903.4407 [gr-qc].

[135] C.W. Misner, K.S. Thorne, and J.A. Wheeler. *Gravitation*. W.H. Freeman and Company, 1973, pp. 1–1279.

[136] Yosuke Mizuno et al. "The Current Ability to Test Theories of Gravity with Black Hole Shadows". In: *Nat. Astron.* 2.7 (2018), pp. 585–590. DOI: 10.1038/s41550-018-0449-5. arXiv: 1804.05812 [astro-ph.GA].

[137] C. Molina et al. "Gravitational signature of Schwarzschild black holes in dynamical Chern-Simons gravity". In: *Phys. Rev.* D81 (2010), p. 124021. DOI: 10.1103/PhysRevD.81.124021. arXiv: 1004.4007 [gr-qc].

[138] V. Moncrief. "Gravitational perturbations of spherically symmetric systems. I. The exterior problem." In: *Annals Phys.* 88 (1974), pp. 323–342. DOI: 10.1016/0003-4916(74)90173-0.

[139] Abdul H. Mroue et al. "Catalog of 174 Binary Black Hole Simulations for Gravitational Wave Astronomy". In: *Phys. Rev. Lett.* 111.24 (2013), p. 241104. DOI: 10.1103/PhysRevLett.111.241104. arXiv: 1304.6077 [gr-qc].

[140] David A. Nichols et al. "Visualizing Spacetime Curvature via Frame-Drag Vortexes and Tidal Tendexes I. General Theory and Weak-Gravity Applications". In: *Phys. Rev.* D84 (2011), p. 124014. DOI: 10.1103/PhysRevD.84.124014. arXiv: 1108.5486 [gr-qc].

[141] Hans-Peter Nollert. "About the significance of quasinormal modes of black holes". In: *Phys. Rev. D* 53 (8 Apr. 1996), pp. 4397–4402. DOI: 10.1103/PhysRevD.53.4397. URL: https://link.aps.org/doi/10.1103/PhysRevD.53.4397.

[142] Maria Okounkova, Mark A. Scheel, and Saul A. Teukolsky. "Evolving Metric Perturbations in dynamical Chern-Simons Gravity". In: *Phys. Rev.* D99.4 (2019), p. 044019. DOI: 10.1103/PhysRevD.99.044019. arXiv: 1811.10713 [gr-qc].

[143] Maria Okounkova, Mark A. Scheel, and Saul A. Teukolsky. "Numerical black hole initial data and shadows in dynamical Chern-Simons gravity". In: (2018). DOI: 10.1088/1361-6382/aafcdf. arXiv: 1810.05306 [gr-qc].

[144] Maria Okounkova and Leo C. Stein. In: (2017). Forthcoming.

[145] Maria Okounkova et al. "Binary black hole collisions in dynamical Chern-Simons gravity". In: (2009). Forthcoming.

[146] Maria Okounkova et al. "Numerical binary black hole mergers in dynamical Chern-Simons gravity: Scalar field". In: *Phys. Rev.* D96.4 (2017), p. 044020. DOI: 10.1103/PhysRevD.96.044020. arXiv: 1705.07924 [gr-qc].

[147] Amos Ori. "Reconstruction of inhomogeneous metric perturbations and electromagnetic four potential in Kerr space-time". In: *Phys. Rev.* D67 (2003), p. 124010. DOI: 10.1103/PhysRevD.67.124010. arXiv: gr-qc/0207045 [gr-qc].

[148] Serguei Ossokine et al. "Comparing Post-Newtonian and Numerical-Relativity Precession Dynamics". In: *Phys. Rev.* D92.10 (2015), p. 104028. DOI: 10.1103/PhysRevD.92.104028. arXiv: 1502.01747 [gr-qc].

[149] Serguei Ossokine et al. "Improvements to the construction of binary black hole initial data". In: *Class. Quant. Grav.* 32 (2015), p. 245010. DOI: 10.1088/0264-9381/32/24/245010. arXiv: 1506.01689 [gr-qc].

[150] Robert Owen. "Degeneracy measures for the algebraic classification of numerical spacetimes". In: *Phys. Rev.* D81 (2010), p. 124042. DOI: 10.1103/PhysRevD.81.124042. arXiv: 1004.3768 [gr-qc].

[151] Robert Owen et al. "Frame-Dragging Vortexes and Tidal Tendexes Attached to Colliding Black Holes: Visualizing the Curvature of Spacetime". In: *Phys. Rev. Lett.* 106 (2011), p. 151101. DOI: 10.1103/PhysRevLett.106.151101. arXiv: 1012.4869 [gr-qc].

[152]   Robert Owen. "The Final Remnant of Binary Black Hole Mergers: Multipolar Analysis". In: *Phys. Rev.* D80 (2009), p. 084012. DOI: 10.1103/PhysRevD.80.084012. arXiv: 0907.0280 [gr-qc].

[153]   Harald P. Pfeiffer. "The Initial value problem in numerical relativity". In: *Miami Waves 2004: Conference on Geometric Analysis, Nonlinear Wave Equations and General Relativity Coral Gables, Florida, January 4-10, 2004*. 2004. arXiv: gr-qc/0412002 [gr-qc].

[154]   Harald Paul Pfeiffer. "Initial data for black hole evolutions". PhD thesis. Cornell U., Phys. Dept., 2005. arXiv: gr-qc/0510016 [gr-qc]. URL: http://wwwlib.umi.com/dissertations/fullcit?p3104429.

[155]   J.F Plebanski and M Demianski. "Rotating, charged, and uniformly accelerating mass in general relativity". In: *Annals of Physics* 98.1 (1976), pp. 98–127. ISSN: 0003-4916. DOI: http://dx.doi.org/10.1016/0003-4916(76)90240-2. URL: http://www.sciencedirect.com/science/article/pii/0003491676902402.

[156]   E. Poisson and C.M. Will. *Gravity: Newtonian, Post-Newtonian, Relativistic*. Cambridge University Press, 2014. ISBN: 9781107032866. URL: https://books.google.com/books?id=PZ5cAwAAQBAJ.

[157]   J. Polchinski. *String Theory: Volume 1, An Introduction to the Bosonic String*. Cambridge Monographs on Mathematical Physics. Cambridge, England: Cambridge University Press, 1998. ISBN: 9781139457408.

[158]   J. Polchinski. *String Theory: Volume 2, Superstring Theory and Beyond*. Cambridge Monographs on Mathematical Physics. Cambridge, England: Cambridge University Press, 1998. ISBN: 9781139457415. URL: https://books.google.com/books?id=WKatSc5pjOgC.

[159]   W. H. Press and S. A. Teukolsky. "Perturbations of a Rotating Black Hole. II. Dynamical Stability of the Kerr Metric". In: *Astrophys. J.* 185 (Oct. 1973), pp. 649–674. DOI: 10.1086/152445.

[160]   William H. Press et al. *Numerical Recipes 3rd Edition: The Art of Scientific Computing*. 3rd ed. New York, NY, USA: Cambridge University Press, 2007. ISBN: 0521880688.

[161]   Frans Pretorius. "Evolution of binary black hole spacetimes". In: *Phys. Rev. Lett.* 95 (2005), p. 121101. DOI: 10.1103/PhysRevLett.95.121101. arXiv: gr-qc/0507014 [gr-qc].

[162]   Frans Pretorius. "Numerical relativity using a generalized harmonic decomposition". In: *Class. Quant. Grav.* 22 (2005), pp. 425–452. DOI: 10.1088/0264-9381/22/2/014. arXiv: gr-qc/0407110 [gr-qc].

[163] R. H. Price, S. Nampalliwar, and G. Khanna. "Black hole binary inspiral: Analysis of the plunge". In: *Phys. Rev. D* 93.4, 044060 (Feb. 2016), p. 044060. DOI: 10.1103/PhysRevD.93.044060. arXiv: 1508.04797 [gr-qc].

[164] Dimitrios Psaltis. "Testing General Relativity with the Event Horizon Telescope". In: (2018). arXiv: 1806.09740 [astro-ph.HE].

[165] Dimitrios Psaltis and Tim Johannsen. "Sgr A*: The Optimal Testbed of Strong-Field Gravity". In: *J. Phys. Conf. Ser.* 283 (2011), p. 012030. DOI: 10.1088/1742-6596/283/1/012030. arXiv: 1012.1602 [astro-ph.HE].

[166] Dimitrios Psaltis et al. "A General Relativistic Null Hypothesis Test with Event Horizon Telescope Observations of the black-hole shadow in Sgr A*". In: *Astrophys. J.* 814.2 (2015), p. 115. DOI: 10.1088/0004-637X/814/2/115. arXiv: 1411.1454 [astro-ph.HE].

[167] M. Punturo et al. "The third generation of gravitational wave observatories and their science reach". In: *Class. Quant. Grav.* 27 (2010), p. 084007. DOI: 10.1088/0264-9381/27/8/084007.

[168] Michael Pürrer. "Frequency domain reduced order model of aligned-spin effective-one-body waveforms with generic mass-ratios and spins". In: *Phys. Rev.* D93.6 (2016), p. 064041. DOI: 10.1103/PhysRevD.93.064041. arXiv: 1512.02248 [gr-qc].

[169] Tullio Regge and John A. Wheeler. "Stability of a Schwarzschild Singularity". In: *Phys. Rev.* 108 (4 Nov. 1957), pp. 1063–1069. DOI: 10.1103/PhysRev.108.1063. URL: https://link.aps.org/doi/10.1103/PhysRev.108.1063.

[170] Angelo Ricarte and Jason Dexter. "The Event Horizon Telescope: exploring strong gravity and accretion physics". In: *Mon. Not. Roy. Astron. Soc.* 446 (2015), pp. 1973–1987. DOI: 10.1093/mnras/stu2128. arXiv: 1410.2899 [astro-ph.HE].

[171] Oliver Rinne. "Explicit solution of the linearized Einstein equations in TT gauge for all multipoles". In: *Class. Quant. Grav.* 26 (2009), p. 048003. DOI: 10.1088/0264-9381/26/4/048003. arXiv: 0809.1761 [gr-qc].

[172] Oliver Rinne, Lee Lindblom, and Mark A. Scheel. "Testing outer boundary treatments for the Einstein equations". In: *Class. Quant. Grav.* 24 (2007), pp. 4053–4078. DOI: 10.1088/0264-9381/24/16/006. arXiv: 0704.0782 [gr-qc].

[173] Oliver Rinne et al. "Implementation of higher-order absorbing boundary conditions for the Einstein equations". In: *Class. Quant. Grav.* 26 (2009), p. 075009. DOI: 10.1088/0264-9381/26/7/075009. arXiv: 0811.3593 [gr-qc].

[174] Carlo Rovelli. "Loop Quantum Gravity". In: *Living Reviews in Relativity* 1.1 (Jan. 1998), p. 1. ISSN: 1433-8351. DOI: 10.12942/lrr-1998-1. URL: https://doi.org/10.12942/lrr-1998-1.

[175] Milton Ruiz et al. "Multipole expansions for energy and momenta carried by gravitational waves". In: *Gen. Rel. Grav.* 40 (2008), p. 2467. DOI: 10.1007/s10714-007-0570-8,10.1007/s10714-008-0684-7. arXiv: 0707.4654 [gr-qc].

[176] Kazuki Sakai et al. "Estimation of starting times of quasinormal modes in ringdown gravitational waves with the Hilbert-Huang transform". In: *Phys. Rev. D* 96 (4 Aug. 2017), p. 044047. DOI: 10.1103/PhysRevD.96.044047. URL: https://link.aps.org/doi/10.1103/PhysRevD.96.044047.

[177] M. A. Scheel et al. "Improved methods for simulating nearly extremal binary black holes". In: *Class. Quantum Grav.* 32.10, 105009 (May 2015), p. 105009. DOI: 10.1088/0264-9381/32/10/105009. arXiv: 1412.1803 [gr-qc].

[178] Mark A. Scheel et al. "High-accuracy waveforms for binary black hole inspiral, merger, and ringdown". In: *Phys. Rev.* D79 (2009), p. 024003. DOI: 10.1103/PhysRevD.79.024003. arXiv: 0810.1767 [gr-qc].

[179] Mark A. Scheel et al. "Solving Einstein's equations with dual coordinate frames". In: *Phys. Rev.* D74 (2006), p. 104006. DOI: 10.1103/PhysRevD.74.104006. arXiv: gr-qc/0607056 [gr-qc].

[180] Karl Schwarzschild. "On the gravitational field of a mass point according to Einstein's theory". In: *Sitzungsber. Preuss. Akad. Wiss. Berlin (Math. Phys.)* 1916 (1916), pp. 189–196. arXiv: physics/9905030 [physics].

[181] Ulrich Sperhake et al. "Black hole head-on collisions and gravitational waves with fixed mesh-refinement and dynamic singularity excision". In: *Phys. Rev.* D71 (2005), p. 124042. DOI: 10.1103/PhysRevD.71.124042. arXiv: gr-qc/0503071 [gr-qc].

[182] Leo Stein. https://pypi.org/project/qnm/.

[183] Leo C. Stein. "Note on Legendre decomposition of the Pontryagin density in Kerr". In: (2014). arXiv: 1407.0744 [gr-qc].

[184] Leo C. Stein. "Rapidly rotating black holes in dynamical Chern-Simons gravity: Decoupling limit solutions and breakdown". In: *Phys. Rev.* D90.4 (2014), p. 044061. DOI: 10.1103/PhysRevD.90.044061. arXiv: 1407.2350 [gr-qc].

[185] Leo C. Stein and Kent Yagi. "Parametrizing and constraining scalar corrections to general relativity". In: *Phys. Rev.* D89.4 (2014), p. 044026. DOI: 10.1103/PhysRevD.89.044026. arXiv: 1310.6743 [gr-qc].

[186] K. S. Stelle. "Renormalization of Higher Derivative Quantum Gravity". In: *Phys. Rev.* D16 (1977), pp. 953–969. DOI: 10.1103/PhysRevD.16.953.

[187] H. Stephani et al. *Exact Solutions of Einstein's Field Equations*. Cambridge Monographs on Mathematical Physics. Cambridge University Press, 2009. ISBN: 9781139435024. URL: https://books.google.com/books?id=SiWXP8FjTFEC.

[188] *SXS Gravitational Waveform Database*. http://www.black-holes.org/waveforms.

[189] Béla Szilágyi. "Key Elements of Robustness in Binary Black Hole Evolutions using Spectral Methods". In: *Int.J.Mod.Phys.* D23.7 (2014), p. 1430014. DOI: 10.1142/S0218271814300146. arXiv: 1405.3693 [gr-qc].

[190] Béla Szilágyi, Lee Lindblom, and Mark A. Scheel. "Simulations of Binary Black Hole Mergers Using Spectral Methods". In: *Phys. Rev. D* 80 (2009), p. 124010. arXiv: 0909.3557 [gr-qc].

[191] Andrea Taracchini et al. "Effective-one-body model for black-hole binaries with generic mass ratios and spins". In: *Phys. Rev. D* 89 (6 Mar. 2014), p. 061502. DOI: 10.1103/PhysRevD.89.061502. URL: https://link.aps.org/doi/10.1103/PhysRevD.89.061502.

[192] Victor Taveras and Nicolas Yunes. "The Barbero-Immirzi Parameter as a Scalar Field: K-Inflation from Loop Quantum Gravity?" In: *Phys. Rev.* D78 (2008), p. 064070. DOI: 10.1103/PhysRevD.78.064070. arXiv: 0807.2652 [gr-qc].

[193] Nicholas W. Taylor et al. "Comparing Gravitational Waveform Extrapolation to Cauchy-Characteristic Extraction in Binary Black Hole Simulations". In: *Phys. Rev.* D88.12 (2013), p. 124010. DOI: 10.1103/PhysRevD.88.124010. arXiv: 1309.3605 [gr-qc].

[194] S. A. Teukolsky. "Perturbations of a Rotating Black Hole. I. Fundamental Equations for Gravitational, Electromagnetic, and Neutrino-Field Perturbations". In: *Astrophys. J.* 185 (Oct. 1973), pp. 635–648. DOI: 10.1086/152444.

[195] S. A. Teukolsky and W. H. Press. "Perturbations of a rotating black hole. III - Interaction of the hole with gravitational and electromagnetic radiation". In: *Astrophys. J.* 193 (Oct. 1974), pp. 443–461. DOI: 10.1086/153180.

[196] Saul A. Teukolsky. "Linearized quadrupole waves in general relativity and the motion of test particles". In: *Phys. Rev. D* 26 (4 Aug. 1982), pp. 745–750. DOI: 10.1103/PhysRevD.26.745. URL: https://link.aps.org/doi/10.1103/PhysRevD.26.745.

[197] Saul A. Teukolsky. "The Kerr Metric". In: *Class. Quant. Grav.* 32.12 (2015), p. 124006. DOI: 10.1088/0264-9381/32/12/124006. arXiv: 1410.2130 [gr-qc].

[198] *The Spectral Einstein Code (SpEC)*. http://www.black-holes.org/SpEC.html.

[199] E. Thrane, P. Lasky, and Y. Levin. "Challenges testing the no-hair theorem with gravitational waves". In: *ArXiv e-prints* (June 2017). arXiv: 1706. 05152 [gr-qc].

[200] D. W. Tufts and R. Kumaresan. "Estimation of frequencies of multiple sinusoids: Making linear prediction perform like maximum likelihood". In: *Proceedings of the IEEE* 70.9 (Sept. 1982), pp. 975–989. ISSN: 0018-9219. DOI: 10.1109/PROC.1982.12428.

[201] Vijay Varma et al. "High-accuracy mass, spin, and recoil predictions of generic black-hole merger remnants". In: *Phys. Rev. Lett.* 122.1 (2019), p. 011101. DOI: 10.1103/PhysRevLett.122.011101. arXiv: 1809. 09125 [gr-qc].

[202] J. Veitch et al. "Parameter estimation for compact binaries with ground-based gravitational-wave observations using the LALInference software library". In: *Phys. Rev. D* 91 (4 Feb. 2015), p. 042003. DOI: 10.1103/PhysRevD. 91.042003. URL: https://link.aps.org/doi/10.1103/PhysRevD. 91.042003.

[203] R.M. Wald. *General Relativity*. University of Chicago Press, 1984. ISBN: 9780226870328.

[204] Steven Weinberg. "Effective Field Theory for Inflation". In: *Phys. Rev.* D77 (2008), p. 123541. DOI: 10.1103/PhysRevD.77.123541. arXiv: 0804. 4291 [hep-th].

[205] Joel M. Weisberg and Joseph H. Taylor. "Relativistic binary pulsar B1913+16: Thirty years of observations and analysis". In: *ASP Conf. Ser.* 328 (2005), p. 25. arXiv: astro-ph/0407149 [astro-ph].

[206] Clifford M. Will. "The Confrontation between General Relativity and Experiment". In: *Living Rev. Rel.* 17 (2014), p. 4. DOI: 10.12942/lrr-2014-4. arXiv: 1403.7377 [gr-qc].

[207] Helvi Witek et al. "Black holes and binary mergers in scalar Gauss-Bonnet gravity: scalar field dynamics". In: (2018). arXiv: 1810.05177 [gr-qc].

[208] *xAct: Efficient tensor computer algebra for the Wolfram Language*. http: //www.xact.es/.

[209] Kent Yagi, Nicolas Yunes, and Takahiro Tanaka. "Gravitational Waves from Quasi-Circular Black Hole Binaries in Dynamical Chern-Simons Gravity". In: *Phys. Rev. Lett.* 109 (2012), p. 251105. DOI: 10.1103/PhysRevLett. 116.169902. arXiv: 1208.5102 [gr-qc].

[210] Kent Yagi, Nicolas Yunes, and Takahiro Tanaka. "Slowly Rotating Black Holes in Dynamical Chern-Simons Gravity: Deformation Quadratic in the Spin". In: *Phys. Rev.* D86 (2012), p. 044037. DOI: 10.1103/PhysRevD.89. 049902,10.1103/PhysRevD.86.044037. arXiv: 1206.6130 [gr-qc].

[211]   Kent Yagi et al. "Isolated and Binary Neutron Stars in Dynamical Chern-Simons Gravity". In: *Phys. Rev.* D87 (2013), p. 084058. DOI: 10.1103/PhysRevD.87.084058. arXiv: 1302.1918 [gr-qc].

[212]   Kent Yagi et al. "Post-Newtonian, Quasi-Circular Binary Inspirals in Quadratic Modified Gravity". In: *Phys. Rev.* D85 (2012), p. 064022. DOI: 10.1103/PhysRevD.93.029902. arXiv: 1110.5950 [gr-qc].

[213]   Huan Yang, Aaron Zimmerman, and Luis Lehner. "Turbulent Black Holes". In: *Phys. Rev. Lett.* 114 (2015), p. 081101. DOI: 10.1103/PhysRevLett.114.081101. arXiv: 1402.4859 [gr-qc].

[214]   Nicolas Yunes and Frans Pretorius. "Dynamical Chern-Simons Modified Gravity. I. Spinning Black Holes in the Slow-Rotation Approximation". In: *Phys. Rev.* D79 (2009), p. 084043. DOI: 10.1103/PhysRevD.79.084043. arXiv: 0902.4669 [gr-qc].

[215]   Nicolas Yunes and Frans Pretorius. "Fundamental Theoretical Bias in Gravitational Wave Astrophysics and the Parameterized Post-Einsteinian Framework". In: *Phys. Rev.* D80 (2009), p. 122003. DOI: 10.1103/PhysRevD.80.122003. arXiv: 0909.3328 [gr-qc].

[216]   Nicolas Yunes, Kent Yagi, and Frans Pretorius. "Theoretical Physics Implications of the Binary Black-Hole Mergers GW150914 and GW151226". In: *Phys. Rev.* D94.8 (2016), p. 084002. DOI: 10.1103/PhysRevD.94.084002. arXiv: 1603.08955 [gr-qc].

[217]   Frank J. Zerilli. "Effective Potential for Even-Parity Regge-Wheeler Gravitational Perturbation Equations". In: *Phys. Rev. Lett.* 24 (13 Mar. 1970), pp. 737–738. DOI: 10.1103/PhysRevLett.24.737. URL: https://link.aps.org/doi/10.1103/PhysRevLett.24.737.

[218]   Frank J. Zerilli. "Gravitational Field of a Particle Falling in a Schwarzschild Geometry Analyzed in Tensor Harmonics". In: *Phys. Rev. D* 2 (10 Nov. 1970), pp. 2141–2160. DOI: 10.1103/PhysRevD.2.2141. URL: https://link.aps.org/doi/10.1103/PhysRevD.2.2141.